National Technical University of Athens

Laboratory of Aerodynamics
Department of Fluid Mechanics
School of Mechanical Engineering

Computational analysis of transitional and massively separated flows with application to wind turbines

---

Konstantinos Diakakis

A thesis presented for the degree of Doctor of Philosophy

July 2019
Athens

Computational analysis of transitional and massively separated flows with application to wind turbines

Konstantinos Diakakis

A thesis presented for the degree of Doctor of Philosophy

Examination Committee

1. I. Anagnostopoulos, Professor, NTUA, School of Mechanical Engineering
2. D. Bouris, Associate Professor, NTUA, School of Mechanical Engineering
3. K. Giannakoglou*, Professor, NTUA, School of Mechanical Engineering
4. L. Kaiktsis, Professor, NTUA, School of Naval Architecture and Marine Engineering
5. V. Riziotis*, Assistant Professor, NTUA, School of Mechanical Engineering
6. G. Tzabiras, Professor, NTUA, School of Naval Architecture and Marine Engineering
7. S. Voutsinas (Supervisor)*, Professor, NTUA, School of Mechanical Engineering

* *Member of the Advisory Committee*

Acknowledgements

The completion of this thesis would not have been possible without the assistance of many people. I therefore want to take this opportunity to extend my sincere gratitude and appreciation to all those who helped (directly or indirectly).

First and foremost, I would like to thank Professor Spyros Voutsinas for being the best supervisor one could ask for. He was always more than happy to share his vast knowledge and experience and, despite having one of the busiest schedules, was always available to discuss and answer my questions. Through his calmness and composure, he taught me that with patience and determination no problem is unsolvable. It was a great honor to carry out my tenure as a Ph. D. candidate under his guidance and I am sincerely grateful for being given the opportunity to do so.

I would also like to express my gratitude towards the members of the Advisory Committee, Professor Kyriakos Giannakoglou and Associate Professor Vasilis Riziotis, for their comments and suggestions that helped shape the final form of this thesis. Professor Kyriakos Giannakoglou was the one that introduced me to numerical analysis through his teaching during my undergraduate years at NTUA, sparking my interest in algorithms and computational solvers, whereas Associate Professor Vasilis Riziotis introduced me to applied aerodynamics. The theoretical background obtained from these two subjects proved invaluable for the completion of this Ph. D. thesis.

I also want to thank the members of the Examination Committee for reading the thesis and making constructive comments.

Special thanks to Professor Georgios Papadakis, aka Papis, who is the person to whom I owe most of my practical experience on the subject of computational mechanics (be it fluid or not). In addition, his programming skills along with his tips and suggestions helped shape how I think as a programmer. Through his hard work and dedication, he raised the standards in the Aerodynamics Laboratory. He always found the time to discuss and help me with various programming or physics related issues and was never stressful nor rushing. I consider myself lucky to have him as a colleague and collaborator.

Moving on, I would like to thank Giannis Prospathopoulos for his valuable comments on various aspects of this thesis. He also gave many programming suggestions that proved to be very useful, and carried out a great amount of simulations that provided invaluable experience.

Theologos Andronikos and Panagiotis Schinas were awesome office-sharing partners and I would like to thank them for the many hours we shared together and the scientific and general discussions we had.

Many thanks to Marinos Manolesos, Dimitris Manolas and Petros Chasapogiannis for being great collaborators in the Aerodynamics Laboratory through the past five years, as well as to Vaggelis Fillipas and Stelios Polyzos for being great neighbors at work. I would also like to thank Nikos Spyropoulos and Dimitrios Ntouras for the discussions and walks around campus.

Setting co-workers aside, I would first like to thank my sister, Marina. She provided invaluable support throughout these years and I do not feel that words can do her justice. My life would definitely be completely different without her.

Ilias, Dimitris, Chris and Stefanos have been awesome friends and bandmates. Music was always a huge part of my life and helped me escape during the years of this Ph. D. thesis. I am glad to have the opportunity to play music and share my artistic and creative visions with them. Special mention goes to Nikos, who is always up for scientific talks and has been a great friend. Additional special mention goes to Vasilis and Michalis, who have been my friends since childhood.

I would also like to thank my family, who supported me in their own way throughout these years and believed in my goals and ambitions.

Finally, I want to mention Amalia. She has always been caring and supportive, making me feel like every new day can be productive. I don't think I can thank her enough through words.

Contents

This page intentionally left blank

Nomenclature

α	Angle of attack
δ	Boundary layer thickness
δ^*	Displacement thickness
θ	Momentum thickness
H	Shape factor, $\frac{\delta*}{\theta}$
c	Airfoil chord
C_f	Skin friction coefficient, $\tau/(0.5\rho U_\infty^2)$
C_p	Pressure coefficient, $(p_\infty - p)/(0.5\rho U_\infty^2))$
d_w	Distance to nearest wall
λ_θ	Pressure gradient parameter, $(\rho\theta^2/\mu)(dU/ds)$
Ma	Freestream Mach number
μ	Molecular viscosity
μ_t	Eddy viscosity
$\tilde{N}$	Local amplification factor
N_{crit}	Critical amplification factor
α_i	Spatial amplification rate
Ω	Absolute value of vorticity, $(2\Omega_{ij}\Omega_{ij})^{1/2}$
Ω_{ij}	Vorticity tensor, $0.5(\partial u_i/\partial x_j - \partial u_j/\partial x_i)$
R_T	Viscosity ratio, ν_t/ν
Re	Reynolds number based on freestream conditions, $\rho c U_\infty/\mu$
Re_v	Vorticity Reynolds number, $\rho d_w^2 S/\mu$
Re_θ	Reynolds number based on momentum thickness, $\rho\theta U/\mu$
$Re_{\theta t}$	Transition onset momentum thickness Reynolds number
$\tilde{Re}_{\theta t}$	Local transition onset momentum thickness Reynolds number, taken from a transport equation
Re_x	Reynolds number based on distance from the stagnation point, $\rho x U_0/\mu$
ρ	Density
S	Absolute value of strain rate, $(2S_{ij}S_{ij})^{1/2}$
S_{ij}	Strain rate tensor, $0.5(\partial u_i/\partial x_j + \partial u_j/\partial x_i)$
τ	Wall shear stress
Tu	Turbulence intensity, $(2k/3)^{1/2}/U$
k	Turbulent kinetic energy
ω	Turbulent specific dissipation
γ	Intermittency
$\tilde{\gamma}$	Isentropic constant
U	Local velocity
U_e	Boundary layer edge velocity
u^*	Friction velocity
y^+	Distance in wall coordinates, $\rho y u^*/\mu$

This page intentionally left blank

List of Figures

List of Tables

This page intentionally left blank

Abstract

Laminar to turbulent transition and higher fidelity turbulence modeling have been implemented in the parallelized, unstructured mesh, compressible Navier-Stokes solver MaPFlow.

In the case of laminar to turbulent transition, both boundary layer and transport equation approaches were assessed. These include the e^N method and the transport equation models γ-Re_θ , γ and AFT. All approaches were validated against a wide range of cases concerning airfoils, wings/blades and generic fuselage, stemming from both the wind energy and the aeronautics sectors. The focus was on integrated loads and transition locations. In the context of two-dimensional simulations, the boundary layer e^N method and the AFT transport equation model exhibit better performance than the other alternatives. The γ-Re_θ model is also a viable option if Reynolds numbers not higher than $6\ x\ 10^6$ are considered. For Reynolds numbers higher than this limit, the accuracy of the model was found to deteriorate. However, both the e^N method and the AFT model cannot be used to predict crossflow transition in three-dimensional simulations. In such scenarios, the γ-Re_θ model can give accurate results, provided that the Reynolds numbers fall within the aforementioned limit.

In the case of higher fidelity turbulence modeling, both Large Eddy Simulation (LES) and Detached Eddy Simulation (DES) approaches were implemented. LES utilized the Smagorinsky subgrid model. Regarding DES, both Delayed DES (DDES) and Improved Delayed DES (IDDES) variants were considered. The focus was on flow cases with massive separation. Both LES and DES provided more accurate results than the baseline Unsteady Reynolds Averaged Navier Stokes (URANS) simulations when compared to experiments and reference results. Neither LES nor DES were pushed to their limits. DES is considered computationally less demanding, due to wall modeling inside the boundary layer region. Therefore, it is a more viable option than LES for industrial applications. However, due to wall modeling, DES is not expected to perform well in flows where the presence and development of small turbulent scales inside the boundary layer are important. In those cases, LES using fine meshes should be considered.

This page intentionally left blank

Chapter 1

Introduction

1.1 Thesis background

In the early years of aviation, wind tunnel experiments were the primary way via which engineers could gain insight on the flow characteristics and the aerodynamic behavior of bodies in airflow. Long before the advent of computers, aerodynamic designs were mainly based on and verified by experimental tests. However, wind tunnel experiments are not cheap nor are they flexible. Measuring setups are complex to build and maintain and wind tunnels are costly to operate. This sets the financial requirement bar for wind tunnel experiments very high. In addition, most wind tunnels are limited by their technical capabilities, meaning that not every flow case can be adequately tackled in every experimental setup. Furthermore, some types of flows cannot be studied in wind tunnels anyway.

As computers became more powerful, so did the process of simulating flows with the aid of computers. This led to a whole new branch of fluid dynamics called *Computational Fluid Dynamics (CFD)*. In comparison to setting up a wind tunnel experiment, using computers to simulate aerodynamic flows is both cheaper and more flexible because parameters such as flow conditions or body shape can be very easily modified. When a new aerodynamic concept is considered, CFD can help in a significant part of the initial assessment of its aerodynamic behavior, providing useful insight that can decisively guide the course of the design process.

The computational resources that were available in the dawn of CFD were only capable of supporting the simulation of simple, two-dimensional inviscid flows. Nowadays, it is possible to simulate complex, three-dimensional viscous flows with the inclusion of effects such as aeroelasticity or combustion. Given the aforementioned costs of wind tunnel experiments, the need for robust and reliable computational tools that can be used for the prediction of flows is undeniable. Said tools can vary in concept and strategy. There exist potential flow solvers, viscous-inviscid interaction solvers and full Navier-Stokes solvers.

A Navier-Stokes solver, which is what this thesis works on, is broadly characterized by three main aspects that define its prediction capabilities:

- **Arithmetic accuracy**
  Relevant examples are the employed difference schemes for variable reconstruction, the approximate Riemann solvers, the Poisson solvers, the preconditioning for low Mach flows, the time integration for unsteady problems, and various other parts that refer to one or more aspects of the computational solution process.
- **Turbulent flow**
  The application range of Navier-Stokes solvers, which may reach high Reynolds numbers, was greatly widened by the development of turbulence models that enabled the inclusion of the effect of turbulence in flow simulations with relatively low computational cost. However, for a given computational solver the prediction accuracy of a simulation is inherently tied to the capabilities of the utilized turbulence model. This means that the presence of flow phenomena such as separation may vary between different models because of different modeling approaches or model performance.
- **Modeling of transition from laminar to turbulent flow**
  Even though transition may be related to turbulence, it is however treated in a separate way. This occurs because the vast majority of turbulence models used in contemporary Navier-Stokes solvers almost always do not attempt to model transition. The behavior of the transitional process is not as well understood as the behavior of turbulence. This occurs because the process itself is inherently different; transition is essentially a flow stability problem. Therefore, turbulence models and transition models do not necessarily share the same framework. Turbulence modeling and transition modeling are most often tackled in a segregated but loosely coupled manner.

1.2 Thesis scope

The current thesis continues the work of G. Papadakis, who developed the Navier-Stokes solver MaPFlow during his tenure as a PhD candidate in the National Technical University of Athens [23]. Based on what was discussed in the previous paragraph, this thesis aimed to extend the capabilities of MaPFlow in regards to turbulence modeling and transition modeling. Arithmetic accuracy aspects were not investigated.

The objectives were therefore defined as:

- **Implementation of laminar to turbulent transition models**
  Transition is very important not solely from a scientific standpoint. It is inherently tied to the fuel consumption of aircraft and the energy production of wind turbines. By not including the transition process, simulations will always lack important aspects of physics that can drastically alter the predicted aerodynamic behavior.
- **Implementation of higher fidelity turbulence modeling**
  Conventional one and two-equation turbulence models are mainly geared towards predicting averaged flow phenomena, since they utilize Reynolds averaging for the turbulence quantities. The Navier-Stokes framework which utilizes the aforementioned models bears the name Reynolds-averaged Navier-Stokes (RANS). These models do not always cope well with inherently unsteady flows and therefore they have a limited application range. For separated flows, which is an example of unsteady flow with great technological interest, a different, higher fidelity turbulence modeling approach is needed in order to obtain accurate results. The implemented approaches for the simulation of massively separated flows were Large Eddy Simulation (LES) and Detached Eddy Simulation (DES).

1.2.1 Laminar to turbulent transition modeling

In contemporary wind turbines, rotors sometimes have a radius larger than 100 meters. At such cases, high Reynolds numbers appear on the tip of the blade. Most wind tunnels are not suitable for the corresponding flow measurements and thus Navier-Stokes solvers are the only viable tool that can provide aerodynamic results. At this size the roughness on the blade surface, caused by accumulating dirt or erosion, is not enough to trim the boundary layer and bypass the transition process. This leads to the presence of extended laminar regions that have a significant effect on the aerodynamic behavior. A robust and reliable way to predict laminar to turbulent transition is thus deemed very important for the initial wind turbine design. Moreover, in wind turbine aerodynamic simulations accurate representation of separated flow is highly important. In this regard, laminar to turbulent flow transition can have a major effect in the produced results, especially in cases that laminar separation bubbles are present.

Laminar to turbulent transition is a topic that has been tackled in many publications over the years, leading to the development of many different models that attempt to predict the onset of transition. However, implementation of these models in Navier-Stokes solvers unfortunately does not cover the same spectrum as the implementation of turbulence models. This mainly occurs because the mechanisms that drive transition greatly depend on the type of application. In purely aerodynamic flows, transition is typically the result of flow instability (Tollmien-Schlichting waves or crossflow instability in cases of high swept wings), where the resulting exponential growth of two-dimensional waves eventually results in a nonlinear breakdown of turbulence. Transition due to Tollmien-Schlichting waves is often referred to as natural transition [24]. In turbomachinery, however, the main transition mechanism is bypass transition [25] imposed on the boundary layer by high levels of freestream turbulence. Another important transition mechanism is separation-induced transition [26], where a laminar boundary layer separates under the influence of a pressure gradient and transition develops within the separated shear layer, which may or may not reattach. Furthermore, a turbulent boundary layer can relaminarize under the influence of a strong favorable pressure gradient [27]. The importance of transition phenomena in aerodynamic and heat transfer simulations is widely accepted, however the inclusion of all aforementioned mechanisms in a single model poses significant difficulties.

Laminar flow break down, development of instabilities and turbulent spots and transition to fully turbulent flow can, in principle, be simulated with great accuracy using Direct Numerical Simulation (DNS) or Large Eddy Simulation (LES), provided that the discretization is able to resolve the transition process. However, the computational cost of both these approaches renders them impractical for industrial applications. This leaves the RANS equations as the only viable tool for CFD simulations and thus adding transition prediction capabilites to Navier-Stokes solvers is desirable.

The first contribution of this thesis is the implementation of laminar to turbulent transition models in MaPFlow. The previous versions of the solver simulated turbulent flows using one or two-equation turbulence models and assuming that the flow is turbulent everywhere in the domain (fully turbulent approach). This led to the need for the inclusion of the laminar to turbulent transition process. This has been achieved with the implementation of various transition models. The primary objective regarding transition modeling is that it

should be able to provide adequate results for a wide range of flows that are typically encountered in wind turbine applications. The transition models should also work without user interference in regards to topology, i.e. the whole process must be as automated as possible. Conceptually speaking, transition models can be distinguished into two categories:

- Transition models that utilize transport equations
- Transition models that are based on the solution of the boundary layer on the wall surface

Transport equation transition models are more straightforward to implement in the context of a Navier-Stokes solver, since transport equations are already used for the primary variables and the additional turbulence model variables. For the transition models that require the solution of the boundary layer, a separate boundary layer transition module is created that works in conjuction with the Navier-Stokes solver. The Navier-Stokes solver provides the input data for the module, whereas the module returns the required topology regarding laminar and turbulent regions. The Navier-Stokes solver then updates the laminar and turbulent regions and continues the simulation.

1.2.2 Higher fidelity turbulence modeling: LES and DES

The motivation for the implementation of LES and DES in MaPFlow also stems from the wind energy sector. Wind turbines are always designed to work in atmospheric flow conditions. In such cases, freestream velocity variations are very rich and chaotic. If one attempts to tackle this flow problem using averaged methods and without accounting for the presence of the aforementioned variations, then the simulations will not be able to provide accurate predictions of the flow characteristics.

One and two-equation RANS turbulence models, that are typically used in Navier-Stokes solvers for turbulence closure, are not well suited for the representation of unsteady flows. RANS models integrate all turbulent frequencies over the time domain, and therefore can only provide an averaged estimation of the flow field and its turbulent structures. Examples where the conventional turbulence models do not perform well are flows with massive separation, flows with vortex shedding, or flows with turbulent inflow, all of which are of great technological interest.

Similarly to what was discussed for laminar to turbulent transition, DNS can provide very accurate results for highly unsteady separated flows. However, the computational cost of DNS is prohibitively high. Reynolds numbers typically encountered in wind energy applications are most often in the region of millions, therefore they cannot be realistically tackled using DNS. By adopting methods such as LES or DES and utilizing turbulent inflow, small turbulent scales in the simulation are not diffused or averaged. Therefore, a high percentage of the initial velocity fluctuation spectrum is maintained, which in turn can alter the results drastically

Both LES and DES have significantly lower computational cost than DNS. LES can also be aided by the inclusion of wall functions that can reduce the computational cost of a simulation even further. This point is discussed in the work of Balakumar et al [28], where the flow past periodic hills is simulated using both DNS and LES with and without wall modeling. The employed mesh for DNS had 200 million elements whereas for LES it only had approximately 6 million, which is a huge difference. The computational cost for DNS and LES is also theoretically analyzed in Choi et al [29], which is a revision of the landmark paper by Chapman [30] who initially estimated the costs for DNS and LES in 1979. Both works conclude that with realistic computational effort, DNS can only be used for low Reynolds number flows.

Examples of LES and DES of external aerodynamic flows are the works of Mary et al [9], where an airfoil at Reynolds number 2.1 x 10^6 and high angle of attack with in presence of laminar separation is simulated with great success using LES, the works of Strelets [31] and Xu et al [32], who assess the performance of DES for airfoils at very high angles of attack showing that DES outperforms URANS for massively separated flows, and the work of Gilling [33] who simulated airfoils in turbulent inflow using DES. The works of Beaudan et al [34] and Breuer [35] investigated the flow past a circular cylinder with LES, whereas Travin et al [36] tackled the same flow problem with DES. All works were able to get good results when compared to the experiments. Galbraith et al [37] used LES for a low Reynolds airfoil that exhibits large laminar separation bubbles. In atmospheric flow conditions, Troldborg et al [38][39][40] used actuator methods with turbulent inflow for the simulation of wind turbines, concluding that the presence of inflow turbulence can have a significant effect on the produced wake. Breuer et al [41] compared the results from LES, DES and RANS for a flat plate at high angle of attack and showed that DES is able to give results that are close to those from LES. Toms [42] investigated the effect of mesh resolution, inflow turbulence, wall treatment and subgrid-scale model for the flow past a backward facing step, noting that inflow turbulence is the most important contributor to downstream flow evolution. Salvetti [43] et al were able to get good results using coarse LES to simulate the flow past 2D sinusoidal periodic waves.

The second contribution of this thesis is the implementation of higher fidelity turbulence models that can provide better results for highly unsteady flows. This has been achieved with the implementation of the Large

Eddy Simulation and Detached Eddy Simulation approaches. LES and DES differ, although they may initially seem similar. DES is essentially a modified one or two equation turbulence model that includes a RANS and an LES branch that switch based on the local mesh resolution. If the latter is coarse, then DES will use the RANS branch and behave like a standard RANS turbulence model. LES fully resolves the large scales of the flow, while it only models the subgrid scales. This means that LES has a relatively tight margin in regards to mesh resolution. Using a computational mesh with insufficient mesh may lead to significantly inaccurate results.

Both approaches were used in simulations of separated flows, in which the unsteady character is dominant and cannot be adequately represented by conventional turbulence models.

1.3 Thesis outline

This thesis content is presented in the following 6 Chapters:

- Chapter 2 presents the CFD solver MaPFlow, which was the computational tool used in this thesis.
- Chapter 3 contains the implementation of transition models.
- Chapter 4 contains the implementation of LES and DES.
- Chapter 5 presents the results from simulations with free transition.
- Chapter 6 presents the results from simulations with LES and DES.
- Chapter 7 draws a conclusion and gives some future work recommendations.

Chapter 2

CFD solver MaPFlow

2.1 Introduction

It is deemed useful to present the MaPFlow solver in some detail. The starting point of this thesis was the solver as presented in [23]. In Section 2.2 the governing system of equations is defined. With regards to [23], some improvements on spatial discretization have been made. Besides the 2$^{\text{nd}}$ order PLR scheme, the solver may now also utilize 3$^{\text{rd}}$ order schemes, namely MUSCL and QUICK. Spatial discretization is discussed in Section 2.3. Time discretization is discussed in Section 2.4, whereas Section 2.5 formulates the boundary conditions. MaPFlow is equipped with one and two-equation turbulence models which are presented in Section 2.6. Section 2.7 contains the solution of the discrete system of equations whereas Section 2.8 discusses mesh deformation.

2.2 Governing equations

2.2.1 Conservative form

Let D denote a volume of fluid and ∂D its boundary. By integrating the governing equations over D, the following integral form is obtained:

$$\int_D \frac{\partial \vec{U}}{\partial t} dD + \oint_{\partial D} (\vec{F_c} - \vec{F_v}) dS = \int_D \vec{Q} dD \tag{2.1}$$

In (2.1), $\vec{U}$ is the vector of the Conservative Flow Variables,

$$\vec{U} = \begin{pmatrix} \rho \\ \rho u \\ \rho v \\ \rho w \\ \rho E \end{pmatrix} \tag{2.2}$$

where ρ denotes the density, (u, v, w) the three components of the velocity field and E the total energy.

$\vec{F_c}$ and $\vec{F_v}$ denote the Convective and Viscous Fluxes respectively,

$$\vec{F_c} = \begin{pmatrix} \rho V \\ \rho u V + n_x p \\ \rho v V + n_y p \\ \rho w V + n_z p \\ \rho(E + \frac{p}{\rho}) V \end{pmatrix} \tag{2.3}$$

$$\vec{F_v} = \begin{pmatrix} 0 \\ n_x \tau_x x + n_y \tau_x y + n_z \tau_x z \\ n_x \tau_y x + n_y \tau_y y + n_z \tau_y z \\ n_x \tau_z x + n_y \tau_z y + n_z \tau_z z \\ n_x \Theta_x + n_y \Theta_y + n_z \theta_z \end{pmatrix} \tag{2.4}$$

where V is the normal velocity,

$$V = \vec{u} \cdot \vec{n} \tag{2.5}$$

and

$$\begin{aligned}\Theta_x &= u\tau_{xx} + v\tau_{xy} + w\tau_{xz} + k\frac{\partial T}{\partial x}\\ \Theta_y &= u\tau_{yx} + v\tau_{yy} + w\tau_{yz} + k\frac{\partial T}{\partial y}\\ \Theta_z &= u\tau_{zx} + v\tau_{zy} + w\tau_{zz} + k\frac{\partial T}{\partial z}\end{aligned} \tag{2.6}$$

The above system is completed by the constitutive equation of state for perfect gases:

$$p = (\gamma - 1)\rho\left[E - \frac{u^2 + v^2 + w^2}{2}\right] \tag{2.7}$$

2.2.2 Variable Transformations

CFD solvers are formulated using the governing equations (2.1) written in primitive ($\vec{V}$) or characteristic ($\vec{V}_{ch}$) variables,

$$\vec{V} = \begin{pmatrix} \rho \\ u \\ v \\ w \\ p \end{pmatrix} \tag{2.8}$$

Primitive Variables

Starting from the differential form of the governing equations,

$$\frac{\partial \vec{U}}{\partial t} + \frac{\partial \vec{F}_c}{\partial \vec{x}} - \frac{\partial \vec{F}_v}{\partial \vec{x}} = \frac{\partial \vec{Q}}{\partial \vec{x}} \tag{2.9}$$

by neglecting the viscous terms and using the chain rule:

$$\begin{aligned}\frac{\partial \vec{U}}{\partial t} + \frac{\partial \vec{F}_c}{\partial \vec{U}}\frac{\partial \vec{U}}{\partial \vec{x}} &= \frac{\partial \vec{Q}}{\partial \vec{x}}\\ \frac{\partial \vec{U}}{\partial t} + A_c\frac{\partial \vec{U}}{\partial \vec{x}} &= \frac{\partial \vec{Q}}{\partial \vec{x}}\end{aligned} \tag{2.10}$$

the Jacobian of the convective fluxes $A_c = \partial \vec{F}_c / \partial \vec{U}$ is derived.

By introducing the transformation matrix $M = \partial \vec{U} / \partial \vec{V}$, the system of equations is written in Primitive Variables form [44]:

$$\begin{aligned}\frac{\partial \vec{U}}{\partial \vec{V}}\frac{\partial \vec{V}}{\partial t} + A_c\frac{\partial \vec{U}}{\partial \vec{V}}\frac{\partial \vec{V}}{\partial t} &= \frac{\partial \vec{Q}}{\partial \vec{x}}\\ M\frac{\partial \vec{V}}{\partial t} + A_c M\frac{\partial \vec{V}}{\partial t} &= \frac{\partial \vec{Q}}{\partial \vec{x}}\\ \frac{\partial \vec{V}}{\partial t} + M^{-1}A_c M\frac{\partial \vec{V}}{\partial t} &= M^{-1}\frac{\partial \vec{Q}}{\partial \vec{x}}\\ \frac{\partial \vec{V}}{\partial t} + A_p\frac{\partial \vec{V}}{\partial t} &= \frac{\partial \vec{Q_v}}{\partial \vec{x}}\end{aligned} \tag{2.11}$$

The transformation matrix M is defined as:

$$M = \frac{\partial \vec{U}}{\partial \vec{V}} = \begin{bmatrix} 1 & 0 & 0 & 0 & 0 \\ u & \rho & 0 & 0 & 0 \\ v & 0 & \rho & 0 & 0 \\ w & 0 & 0 & \rho & 0 \\ \frac{u^2+v^2+w^2}{2} & \rho u & \rho v & \rho w & \frac{1}{\gamma - 1} \end{bmatrix} \tag{2.12}$$

and its inverse as:

$$M^{-1} = \frac{\partial \vec{V}}{\partial \vec{U}} = \begin{bmatrix} 1 & 0 & 0 & 0 & 0 \\ -\frac{u}{\rho} & \frac{1}{\rho} & 0 & 0 & 0 \\ -\frac{v}{\rho} & 0 & \frac{1}{\rho} & 0 & 0 \\ -\frac{w}{\rho} & 0 & 0 & \frac{1}{\rho} & 0 \\ \frac{\gamma-1}{2}\left(u^2+v^2+w^2\right) & -u(\gamma-1) & -v(\gamma-1) & -w(\gamma-1) & \gamma-1 \end{bmatrix} \tag{2.13}$$

(2.11) has the same form as (2.10) but the Jacobian of the convective fluxes, A_p, is expressed in primitive variables.

Characteristic Variables

Diagonalization of A_c ($A_c = R\Lambda L$, where R, L contain the right and left eigenvectors respectively and Λ the eigenvalues) enables the transformation of (2.10) in characteristic variables. By that, decoupling of the system of equations is achieved.

$$\begin{aligned} \frac{\partial \vec{U}}{\partial t} + L^{-1}\Lambda L\frac{\partial \vec{U}}{\partial \vec{x}} &= \frac{\partial \vec{Q}}{\partial \vec{x}} \\ L\frac{\partial \vec{U}}{\partial t} + \Lambda L\frac{\partial \vec{U}}{\partial \vec{x}} &= L\frac{\partial \vec{Q}}{\partial \vec{x}} \end{aligned} \tag{2.14}$$

By defining $M_{ch} \equiv \partial\vec{U}/\partial\vec{V}_{ch} = L$ the decoupled system is acquired:

$$\frac{\partial \vec{V}_{ch}}{\partial t} + \Lambda\frac{\partial \vec{V}_{ch}}{\partial \vec{x}} = \frac{\partial \vec{Q}_{ch}}{\partial \vec{x}} \tag{2.15}$$

with:

$$\Lambda = \begin{bmatrix} V & 0 & 0 & 0 & 0 \\ 0 & V & 0 & 0 & 0 \\ 0 & 0 & V & 0 & 0 \\ 0 & 0 & 0 & V+c & 0 \\ 0 & 0 & 0 & 0 & V-c \end{bmatrix} \tag{2.16}$$

Depending on the variables chosen the diagonalization of the Jacobian Matrix (A_c for conservative variables,A_p for primitive) will lead to different eigenvectors. However, the eigenvectors can be transformed to the desired variables using the appropriate transformation matrix. For example in between primitive and characteristic variables the following hold:

$$A_p = M^{-1}A_cM = \left(M^{-1}R\right)\Lambda\left(LM\right) = R_p\Lambda L_p \tag{2.17}$$

where $R_p = M^{-1}R$ and $L_p = LM$ are the right and left eigenvectors in primitive variables. Using the inverse transformation matrix enables the transformation from primitive eigenvectors to conservative eigenvectors.

The right eigenvectors in primitive variables are :

$$R_p = \begin{bmatrix} n_x & 0 & n_z & -n_y & -\frac{n_x}{c^2} \\ n_y & -n_z & 0 & n_x & -\frac{n_y}{c^2} \\ n_z & n_y & -n_x & 0 & -\frac{n_z}{c^2} \\ 0 & n_x & n_y & n_z & -\frac{\lambda_1-\lambda_4}{\rho c^2} \\ 0 & -n_x & -n_y & -n_z & \frac{\lambda_1-\lambda_5}{\rho c^2} \end{bmatrix} \tag{2.18}$$

where $\vec{n} = (n_x, n_y, n_z)$ is the unit normal vector, $\lambda_1 = \lambda_2 = \lambda_3 = V$, $\lambda_4 = V + c$ and $\lambda_5 = V - c$.

The left eigenvectors in primitive variables are :

$$L_p = R_p^{-1} = \begin{bmatrix} n_x & n_y & n_z & \frac{\rho}{\lambda_4-\lambda_5} & \frac{\rho}{\lambda_4-\lambda_5} \\ 0 & -n_z & n_y & \frac{\lambda_1-\lambda_5}{\lambda_4-\lambda_5}n_x & \frac{\lambda_1-\lambda_4}{\lambda_4-\lambda_5}n_x \\ n_z & 0 & -n_x & \frac{\lambda_1-\lambda_5}{\lambda_4-\lambda_5}n_y & \frac{\lambda_1-\lambda_4}{\lambda_4-\lambda_5}n_y \\ -n_y & n_x & 0 & \frac{\lambda_1-\lambda_5}{\lambda_4-\lambda_5}n_z & \frac{\lambda_1-\lambda_4}{\lambda_4-\lambda_5}n_z \\ 0 & 0 & 0 & \frac{\rho c^2}{\lambda_4-\lambda_5} & \frac{\rho c^2}{\lambda_4-\lambda_5} \end{bmatrix} \tag{2.19}$$

2.2.3 Low Mach Number Preconditioning

In cases where the local Mach number approaches zero there is large disparity in the wave propagation speeds. The speed of sound (c) becomes very large compared to the flow velocity (V) and completely deteriorates the stability and convergence properties of the system. In such cases the equations should be modified. Low Mach Preconditioning is applied that acts on the time derivatives of the equations and basically modifies the speed of sound to make the two velocities comparable. By that, the convergence and stability characteristics of the system are improved.

Neglecting the viscous terms, and using the Preconditioning Matrix Γ, the system of equations (2.10) takes the following general form:

$$\begin{aligned} \Gamma^{-1}\frac{\partial \vec{U}}{\partial t} + A_c\frac{\partial \vec{U}}{\partial \vec{x}} = \frac{\partial \vec{Q}}{\partial \vec{x}} \Rightarrow \\ \frac{\partial \vec{U}}{\partial t} + \Gamma A_c\frac{\partial \vec{U}}{\partial \vec{x}} = \Gamma\frac{\partial \vec{Q}}{\partial \vec{x}} \Rightarrow \\ \frac{\partial \vec{U}}{\partial t} + A_\Gamma\frac{\partial \vec{U}}{\partial \vec{x}} = \Gamma\frac{\partial \vec{Q}}{\partial \vec{x}} \end{aligned} \tag{2.20}$$

Various forms of the Preconditioning Matrix Γ have been proposed [45][46]. In the present work Eriksson's Preconditioning Matrix [47] has been implemented, based on its successful use in [48].

In primitive variables,

$$\Gamma_p = \begin{bmatrix} 1 & 0 & 0 & 0 & \beta \\ 0 & 1 & 0 & 0 & 0 \\ 0 & 0 & 1 & 0 & 0 \\ 0 & 0 & 0 & 1 & 0 \\ 0 & 0 & 0 & 0 & \alpha \end{bmatrix} \tag{2.21}$$

where

$$\begin{aligned} \alpha &= min(1, M_{local}^2, \kappa_p M_\infty^2) \\ \beta &= (1-\alpha)/c^2 \end{aligned} \tag{2.22}$$

The amount of preconditioning is controlled by α in the sense that it follows the local Mach Number (M_{local}) variations. The parameter κ_p takes values from 3-5. On one hand, its role is to prevent α from approaching zero in stagnant regions and on the other to assure constant α within the boundary layer [49]. It is noted that zero preconditioning and recovery of the original form of the equations is obtained for $\alpha = 1$.

In order to express the preconditioning matrix in conservative or characteristic variables, the appropriate transformation matrix is applied. For example,

$$\begin{aligned} \Gamma_c &= M^{-1}\Gamma_p M \\ M &= \frac{\partial \vec{U}}{\partial \vec{V}} \end{aligned} \tag{2.23}$$

When transforming the preconditioned system in characteristic variables, a new set of modified eigenvalues is obtained,

$$\Lambda_\Gamma = \begin{bmatrix} V & 0 & 0 & 0 & 0 \\ 0 & V & 0 & 0 & 0 \\ 0 & 0 & V & 0 & 0 \\ 0 & 0 & 0 & V'+c' & 0 \\ 0 & 0 & 0 & 0 & V'-c' \end{bmatrix} \tag{2.24}$$

in which the "modified" speed of sound c' and velocity V' are defined as follows:

$$\begin{aligned} V' &= \frac{1}{2}(1+\alpha)V \\ c' &= \frac{1}{2}\sqrt{\left[(1-\alpha)V\right]^2 + 4\alpha c^2} \end{aligned} \tag{2.25}$$

leading to the following expressions for the eigenvalues:

$$
\begin{aligned}
\lambda_1 &= \lambda_2 = \lambda_3 = V \\
\lambda_4 &= \frac{1}{2}\left[(1+\alpha)\,V - \sqrt{\left[(1-\alpha)\,V\right]^2 + 4\alpha c^2}\right] \\
\lambda_5 &= \frac{1}{2}\left[(1+\alpha)\,V + \sqrt{\left[(1-\alpha)\,V\right]^2 + 4\alpha c^2}\right]
\end{aligned}
\tag{2.26}
$$

Since preconditioning changes the eigenvalues, the left and right eigenvectors will also change. The right eigenvectors in primitive variables become:

$$
R_{\Gamma p} = \begin{bmatrix}
n_x & 0 & n_z & -n_y & -\frac{n_x}{c^2} \\
n_y & -n_z & 0 & n_x & -\frac{n_y}{c^2} \\
n_z & n_y & -n_x & 0 & -\frac{n_z}{c^2} \\
0 & n_x & n_y & n_z & -\frac{\lambda_1-\lambda_4}{\alpha\rho c^2} \\
0 & -n_x & -n_y & -n_z & \frac{\lambda_1-\lambda_5}{\alpha\rho c^2}
\end{bmatrix}
\tag{2.27}
$$

while the left eigenvectors in primitive variables become :

$$
L_{\Gamma p} = R_{\Gamma p}^{-1} = \begin{bmatrix}
n_x & n_y & n_z & \frac{\alpha\rho}{\lambda_4-\lambda_5} & \frac{\alpha\rho}{\lambda_4-\lambda_5} \\
0 & -n_z & n_y & \frac{\lambda_1-\lambda_5}{\lambda_4-\lambda_5}n_x & \frac{\lambda_1-\lambda_4}{\lambda_4-\lambda_5}n_x \\
n_z & 0 & -n_x & \frac{\lambda_1-\lambda_5}{\lambda_4-\lambda_5}n_y & \frac{\lambda_1-\lambda_4}{\lambda_4-\lambda_5}n_y \\
-n_y & n_x & 0 & \frac{\lambda_1-\lambda_5}{\lambda_4-\lambda_5}n_z & \frac{\lambda_1-\lambda_4}{\lambda_4-\lambda_5}n_z \\
0 & 0 & 0 & \frac{\alpha\rho c^2}{\lambda_4-\lambda_5} & \frac{\alpha\rho c^2}{\lambda_4-\lambda_5}
\end{bmatrix}
\tag{2.28}
$$

2.2.4 Moving Meshes

In case D changes in time, the time derivative in (2.1) will also act on $D(t)$. In order to pass time derivation into the integral, Reynold's transport theorem is applied:

$$
\begin{aligned}
\frac{\partial}{\partial t}\int_{D(t)} \vec{U}\,dD &= \int_{D(t)} \frac{\partial \vec{U}}{\partial t} + \int_{D(t)} \nabla\left(\vec{U}\otimes\vec{u}_{vol}\right) dD \\
&= \int_{D(t)} \frac{\partial \vec{U}}{\partial t} + \oint_{\partial D(t)} \vec{U}\cdot(\vec{u}_{vol}\cdot\vec{n})\,dS
\end{aligned}
\tag{2.29}
$$

where $\vec{u}_{vol}$ is the velocity that defines the time evolution of $D(t)$.

If $\vec{u}_{mesh}$ denotes the mesh velocity then $\vec{u}_{vol} = \vec{u}_{mesh}$, hence

$$
\int_{D(t)} \frac{\partial \vec{U}}{\partial t} = \frac{\partial}{\partial t}\int_{D(t)} \vec{U}\,dD - \oint_{\partial D(t)} \vec{U}\cdot(\vec{u}_{vol}\cdot\vec{n})\,dS
\tag{2.30}
$$

Substituting the above expression in (2.1), the Arbitrary Lagrangian-Eulerian (ALE) formulation of the governing equations is obtained:

$$
\frac{\partial}{\partial t}\int_{D(t)} \vec{U}\,dD + \oint_{\partial D(t)} (\vec{F}_c - V_g\vec{U}\,dS - \vec{F}_v)\,dS = \int_{D(t)} \vec{Q}\,dD
\tag{2.31}
$$

where $V_g = \vec{u}_{mesh}\cdot\vec{n}$.

In the case of moving meshes the eigenvalues of the system must change in order to account for the mesh velocity and become:

$$
\Lambda = \begin{bmatrix}
V-V_g & 0 & 0 & 0 & 0 \\
0 & V-V_g & 0 & 0 & 0 \\
0 & 0 & V_g & 0 & 0 \\
0 & 0 & 0 & V-V_g+c & 0 \\
0 & 0 & 0 & 0 & V-V_g+c
\end{bmatrix}
\tag{2.32}
$$

The above formulation is consistent for all types of motions since no assumptions about the velocity have been made. Thus, it can be used both for rigid body motions (rotation, translation) and for deforming meshes where the control volume is stretched and twisted.

Rotating frame of reference

In several applications, the solid bodies are rotating. Often it is preferred to formulate the problem in the rotating frame of reference, especially in cases where the relative flow attains a steady state. The governing equations in a rotating frame take the following form (see [44] for details):

$$\frac{\partial \rho}{\partial t} + \nabla \cdot (\rho \vec{u}_r) = 0 \tag{2.33}$$

$$\frac{\partial \rho \vec{u}_r}{\partial t} + \nabla \cdot \left(\rho \vec{u}_r \vec{u}_r + p\vec{I} - \vec{\tau} \right) = -2\rho \left(\vec{\Omega} \times \vec{u}_r \right) - \rho \vec{\Omega} \times (\vec{\Omega} \times \vec{R}) \tag{2.34}$$

$$\frac{\partial E_r}{\partial t} + \nabla \cdot \left[\vec{u}_r \left(E_r + p \right) + \vec{\tau} \cdot \vec{u}_r \right] = 0 \tag{2.35}$$

where

$$\vec{u}_r = \vec{u} - (\vec{\Omega} \times \vec{R}) \tag{2.36}$$

is the relative velocity and

$$E_r = p/(\gamma - 1) + 1/2\rho u_r^2 + 1/2\rho |(\vec{\Omega} \times \vec{R})|^2 \tag{2.37}$$

is the total energy per unit volume in the rotating frame. In the momentum equation, the Coriolis and Centrifugal forces are also added.

A variant of the above formulation is easily obtained by introducing the absolute flow velocity as expressed in the rotating frame:

$$\frac{\partial \rho}{\partial t} + \nabla \cdot \rho \left(\vec{u} - \vec{\Omega} \times \vec{R} \right) = 0 \tag{2.38}$$

$$\frac{\partial \rho \vec{u}}{\partial t} + \nabla \cdot \left[\rho \vec{u} (\vec{u} - \vec{\Omega} \times \vec{R}) + p\vec{I} - \vec{\tau} \right] = -\rho \left(\vec{\Omega} \times \vec{u} \right) \tag{2.39}$$

$$\frac{\partial E}{\partial t} + \nabla \cdot \left[(\vec{u} - \vec{\Omega} \times \vec{R}) (E + p) + \left(\vec{\Omega} \times \vec{R} \right) p + \vec{\tau} \cdot \vec{u} \right] = 0 \tag{2.40}$$

According to [50][51] the absolute velocity formulation results in a more accurate evaluation of the fluxes in Finite Volume solvers.

2.3 Spatial discretization

In MaPFlow the flow variables are calculated and stored at cell centers. Assuming that the cell volume remains constant in time:

$$\frac{\partial}{\partial t} \int_D \vec{U} dD = D \frac{\partial \vec{U}}{\partial t} \tag{2.41}$$

where:

$$\vec{U} = \frac{1}{D} \int_D \vec{U}_{exact} dD \tag{2.42}$$

Thus equation (2.1) becomes:

$$\frac{\partial \vec{U}}{\partial t} = -\frac{1}{D} [\oint_{\partial D} (\vec{F}_c - \vec{F}_v) dS - \int_D \vec{Q} dD] \tag{2.43}$$

The surface integral is approximated by the sum of fluxes through the faces of each cell. The usual assumption is that the flux is evenly distributed over every face and its mean is computed at its center. For cell I, (2.43) takes the form:

$$\frac{d\vec{U}_I}{dt} = -\frac{1}{D_I} \underbrace{[\sum_{m=1}^{N_f} (\vec{F}_c - \vec{F}_v)_m \Delta S_m) - (\vec{Q} D)_I]}_{R_I} = -\frac{1}{D_I} \vec{R}_I \tag{2.44}$$

where N_f is the number of faces the cell has and ΔS_m is the area of face "m". The terms $(\vec{F}_c)_m, (\vec{F}_v)_m$ represent the convective and viscous fluxes through face m.

2.3.1 Reconstruction of variables

In order to calculate the fluxes appearing in the right hand side of (2.44), the values of all flow variables at the face centers are needed. This information is absent, since all flow variables are defined at the cell centers. Passing the flow information from the cell centers to the faces is carried out by means of *variable reconstruction*.

Consider two cells *I,J* being in contact over face *f*. Variable reconstruction on *f* can be defined either starting from cell *I* or cell *J*. For compressible solvers it is assumed that across the face the flow experiences a jump defined by the left *L* and right *R* states. The L/R specification depends on the normal to *f* which directs from L to R. These states are used because the interpolation of variables on a specific face is done twice; once for the left side and once for the right side of the face. Afterwards, the flux on the face is computed.

PLR

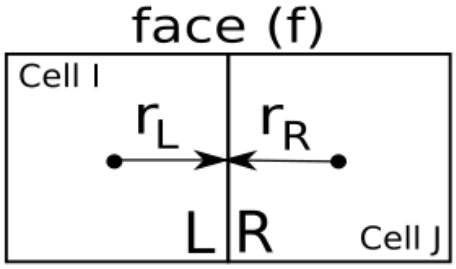

Figure 2.1: *Two cell stencil for the reconstruction of variables on a face (f) using the PLR scheme.*

PLR is a 2^{nd} order accurate scheme which utilizes Venkatakrishnan's limiter [52]. The utilized stencil consists of two cells (one cell in both L and R directions), as shown in fig. 2.1. The assumption that the solution is partially and linearly distributed in the finite volume is made. Left and right states are computed as follows:

$$\vec{W}_L = \vec{W}_I + \Psi_I(\nabla\vec{W}_I \cdot \vec{r}_L) \tag{2.45}$$

$$\vec{W}_R = \vec{W}_J - \Psi_J(\nabla\vec{W}_J \cdot \vec{r}_R) \tag{2.46}$$

where $\vec{W}$ is the primitive variables vector:

$$\vec{W} = \begin{pmatrix} \rho \\ u \\ v \\ w \\ E \end{pmatrix} \tag{2.47}$$

and $\vec{r_L}, \vec{r_R}$ is the corresponding distance of each cell center from the shared cell face between these two cells.

An important factor in the described scheme is the computation of $\nabla(\vec{W}_I)$ in (2.45),(2.46). The derivative computation utilizes the Green-Gauss approximation, thus:

$$\nabla\vec{W} \approx \frac{1}{\Omega}\int_{\partial\Omega} \vec{W}\vec{n}dS \tag{2.48}$$

In cell centered schemes, (2.48) is discretized as follows:

$$\nabla\vec{W}_I \approx \frac{1}{\Omega}\sum_{J=1}^{N_f} \frac{1}{2}(\vec{W}_I + \vec{W}_J)\vec{n}_{IJ}\Delta S_{IJ} \tag{2.49}$$

Ψ is the limiter function that prevents variables from reaching extreme values in regions with discontinuities. Venkatakrishnan's limiter [52] is a limiter applied to ∇U. The implementation is as follows:

$$\Psi_i = min_j \begin{cases} \frac{1}{\Delta_2}\left[\frac{\Delta^2_{1,max}+\epsilon^2)\Delta_2+2\Delta^2_2\Delta_{1,max}}{\Delta^2_{1,max}+2\Delta^2_2+\Delta_{1,max}\Delta_2+\epsilon^2}\right] & \Delta_2 > 0 \\ \frac{1}{\Delta_2}\left[\frac{\Delta^2_{1,min}+\epsilon^2)\Delta_2+2\Delta^2_2\Delta_{1,min}}{\Delta^2_{1,min}+2\Delta^2_2+\Delta_{1,min}\Delta_2+\epsilon^2}\right] & \Delta_2 < 0 \\ 1 & \Delta_2 = 0 \end{cases} \tag{2.50}$$

where

$$\Delta_{1,max} = U_{max} - U_i \tag{2.51}$$

$$\Delta_{1,min} = U_{min} - U_i \tag{2.52}$$

The purpose of the parameter ϵ^2 is to define limiter strictness. If it has zero value the limiter is very strict whereas for large values of the parameter the limiter reaches values close to unity and eventually does not have a significant effect on variable values. Parameter ϵ is practically proportional to mesh length scale:

$$\epsilon^2 = (K\Delta h)^3 \tag{2.53}$$

where K is a free parameter. Small values of K make the limiter strict rendering the PLR first order, while $K = \infty$ leads to an unlimited scheme. Typically the value of $K = 5$ is used.

MUSCL

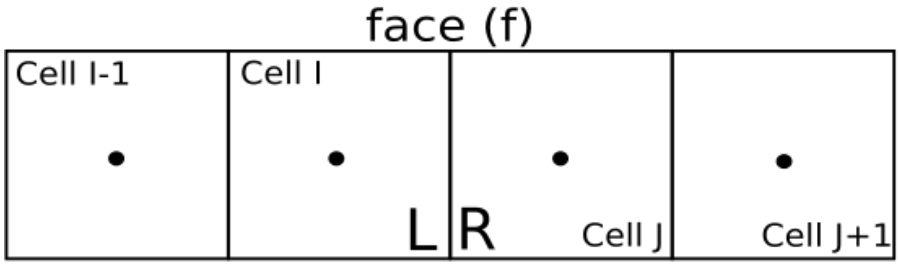

Figure 2.2: *Four cell stencil for the reconstruction of variables on a face (f) using the MUSCL and QUICK schemes. In contrast to the PLR scheme, MUSCL and QUICK schemes do not utilize distance vectors.*

The MUSCL scheme was first introduced by B. van Leer in [53]. Starting from the scheme of Godunov [54], the piecewise constant approximation is replaced by reconstructed states, which are derived from cell-averaged states from the previous timestep. For every face, slope limited, reconstructed left and right states are obtained and used to calculate fluxes at the cell boundaries. MUSCL takes into account the second order derivative whereas the third order derivative is ignored, thus the scheme is considered 3$^{\text{rd}}$ order accurate.

For the equations presented below, the following subscript notation is adopted (see fig. 2.2):

- The 1$^{\text{st}}$ Left cell is noted with "I"
- The 2$^{\text{nd}}$ Left cell is noted with "I-1"
- The 1$^{\text{st}}$ Right cell is noted with "J"
- The 2$^{\text{nd}}$ Right cell is noted with "J+1"

The left and right states are computed as follows:

$$\vec{W}_L = \vec{W}_I + \frac{1}{4}((1-\kappa)(\vec{W}_I - \vec{W}_{I-1})\phi(r_{I-1}) + (1+\kappa)(\vec{W}_J - \vec{W}_I)\phi(r_I)) \tag{2.54}$$

$$\vec{W}_R = \vec{W}_J + \frac{1}{4}((1-\kappa)(\vec{W}_{J+1} - \vec{W}_J)\phi(r_J) + (1+\kappa)(\vec{W}_J - \vec{W}_I)\phi(r_{J+1})) \tag{2.55}$$

where $\kappa = 1/3$.

In contrast to the PLR scheme, r_I is not a distance vector. It is instead calculated as:

$$r_I = \frac{\vec{W}_I - \vec{W}_{I-1}}{\vec{W}_J - \vec{W}_I} \tag{2.56}$$

If the denominator is lower than 0, $r_I = 1$. Finally, $\phi(r)$ is the limiter function which can either be the superbee limiter [55] or the limiter of van Albada [56].

The superbee limiter reads:

$$\phi(r_I) = max(0, min(2r_I, 1), min(r_I, 2)) \tag{2.57}$$

whereas that of van Albada reads:

$$\phi(r_I) = \frac{r_I^2 + r_I}{r_I^2 + 1} \tag{2.58}$$

QUICK

QUICK is a higher-order differencing scheme that considers a three-point upstream weighted quadratic interpolation for the cell face values. The scheme was first introduced by B. P. Leonard in 1979 [57]. A quadratic function passing through two bracketing or surrounding nodes and one node in the upstream side is used in order to find the cell face value. In central differencing schemes and second order upwind schemes the first order derivative is included whereas the second order derivative is ignored. QUICK takes the second order derivative into account, but ignores the third order derivative and thus is considered 3^{rd} order accurate.

For the equations presented below, the following subscript notation is adopted (see fig. 2.2):

- The 1^{st} Left cell is noted with "I"
- The 2^{nd} Left cell is noted with "I-1"
- The 1^{st} Right cell is noted with "J"
- The 2^{nd} Right cell is noted with "J+1"

The implemented algorithm is based on [58] and is as follows:

Left state:

If $|\vec{W}_J - \vec{W}_{I-1}| \leq 10^{-8}$, then

$$\vec{W}_L = \frac{1}{2}(\vec{W}_I + \vec{W}_J) - \frac{1}{8}(\vec{W}_J - 2\vec{W}_I + \vec{W}_{I-1}) \tag{2.59}$$

Else if $|\vec{W}_J - 2\vec{W}_I + \vec{W}_{I-1}| \leq 0.3|\vec{W}_J - \vec{W}_{I-1}|$, then

$$\vec{W}_L = \frac{1}{2}(\vec{W}_I + \vec{W}_J) - \frac{1}{8}(\vec{W}_J - 2\vec{W}_I + \vec{W}_{I-1}) \tag{2.60}$$

Else

$$\vec{W}_{Invd} = \frac{\vec{W}_I - \vec{W}_{I-1}}{\vec{W}_J - \vec{W}_{I-1}} \tag{2.61}$$

$$\begin{aligned}
&\text{If} \quad \vec{W}_{Invd} \geq 1.5 \text{ or } \vec{W}_{Invd} \leq -1 \text{ or } 0.35 \leq \vec{W}_{Invd} \leq 0.65 \\
&\vec{W}_{face} = 0.75 + 0.75(\vec{W}_{Invd} - 0.5), \\
&\text{else if} \quad -1 < \vec{W}_{Invd} \leq 0, \\
&\vec{W}_{face} = 0.375\vec{W}_{Invd} \\
&\text{else if} \quad 0 < \vec{W}_{Invd} \leq 0.35 \text{ or } 0.65 < \vec{W}_{Invd} \leq 1, \\
&\vec{W}_{face} = \frac{\sqrt{\vec{W}_{Invd}(1 - \vec{W}_{Invd})^3} - \vec{W}_{Invd}^{\,2}}{1 - 2\vec{W}_{Invd}} \\
&\text{else if} \quad 1 < \vec{W}_{Invd} \leq 1.5, \\
&\vec{W}_{face} = \vec{W}_{Invd}
\end{aligned} \tag{2.62}$$

$$\vec{W}_L = \vec{W}_{I-1} + (\vec{W}_J - \vec{W}_{I-1})\vec{W}_{face} \tag{2.63}$$

Right state:

If $|\vec{W}_J - \vec{W}_{J+1}| \leq 10^{-8}$, then

$$\vec{W}_R = \frac{1}{2}(\vec{W}_J + \vec{W}_I) - \frac{1}{8}(\vec{W}_I - 2\vec{W}_J + \vec{W}_{J+1}) \tag{2.64}$$

Else if $|\vec{W}_I - 2\vec{W}_J + \vec{W}_{J+1}| \leq 0.3|\vec{W}_I - \vec{W}_{J+1}|$, then

$$\vec{W}_R = \frac{1}{2}(\vec{W}_J + \vec{W}_I) - \frac{1}{8}(\vec{W}_I - 2\vec{W}_J + \vec{W}_{J+1}) \tag{2.65}$$

Else

$$\vec{W}_{Jnvd} = \frac{\vec{W}_J - \vec{W}_{J+1}}{\vec{W}_I - \vec{W}_{J+1}} \tag{2.66}$$

$$\begin{aligned}
&\text{If} \quad \vec{W}_{Jnvd} \geq 1.5 \text{ or } \vec{W}_{Jnvd} \leq -1 \text{ or } 0.35 \leq \vec{W}_{Jnvd} \leq 0.65, \\
&\vec{W}_{face} = 0.75 + 0.75(\vec{W}_{Jnvd} - 0.5) \\
&\text{else if} \quad -1 < \vec{W}_{Jnvd} \leq 0, \\
&\vec{W}_{face} = 0.375\vec{W}_{Jnvd} \\
&\text{else if} \quad 0 < \vec{W}_{Jnvd} \leq 0.35 \text{ or } 0.65 < \vec{W}_{Jnvd} \leq 1 \\
&\vec{W}_{face} = \frac{\sqrt{\vec{W}_{Jnvd}(1 - \vec{W}_{Jnvd})^3} - \vec{W}_{Jnvd}^{\,2}}{1 - 2\vec{W}_{Jnvd}} \\
&\text{else if} \quad 1 < \vec{W}_{Jnvd} \leq 1.5 \\
&\vec{W}_{face} = \vec{W}_{Jnvd}
\end{aligned} \tag{2.67}$$

$$\vec{W}_R = \vec{W}_{J+1} + (\vec{W}_I - \vec{W}_{J+1})\vec{W}_{face} \tag{2.68}$$

2.3.2 Convective Fluxes

The discretization of the convective fluxes can be based on central, flux-vector or flux-difference schemes. Central schemes calculate the convective fluxes across faces as the arithmetic average of the values obtained at the two sides of the face plus an artificial dissipation term added to enhance stability [59]. Flux-vector schemes are based on *upwinding* which respects the direction of propagation of waves [60][61]. Finally, flux-difference schemes calculate convective fluxes at cell faces by solving the Riemann problem for the Left and Right states defined on the face [62].

The present work uses Roe's approximate Riemann solver [62], which is a flux-difference scheme. Roe's scheme consists of constructing the convective flux as a sum of wave contributions:

$$(\vec{F}_c)_{I+\frac{1}{2}} = \frac{1}{2}[\vec{F}_c(\vec{V}_R) + \vec{F}_c(\vec{V}_L) - |A_{Roe}|_{I+\frac{1}{2}}(\vec{V}_R - \vec{V}_L)] \tag{2.69}$$

where the Left and Right states $(\vec{V}_L, \vec{V}_R)$ are calculated using one of the available numerical schemes. The Roe matrix A_{Roe} has the same form as the convective flux Jacobian but instead of formally averaged values, the following Roe-averaged variables are used:

$$\begin{aligned}
\tilde{\rho} &= \sqrt{\rho_L \rho_R} \\
\tilde{u} &= \frac{u_L\sqrt{\rho_L} + u_R\sqrt{\rho_R}}{\sqrt{\rho_L} + \sqrt{\rho_R}} \\
\tilde{v} &= \frac{v_L\sqrt{\rho_L} + v_R\sqrt{\rho_R}}{\sqrt{\rho_L} + \sqrt{\rho_R}} \\
\tilde{w} &= \frac{w_L\sqrt{\rho_L} + w_R\sqrt{\rho_R}}{\sqrt{\rho_L} + \sqrt{\rho_R}} \\
\tilde{H} &= \frac{H_L\sqrt{\rho_L} + H_R\sqrt{\rho_R}}{\sqrt{\rho_L} + \sqrt{\rho_R}} \\
\tilde{c} &= \sqrt{(\gamma - 1)(\tilde{H} - \tilde{q}^2/2)} \\
\tilde{q} &= \tilde{u}^2 + \tilde{v}^2 + \tilde{w}^2
\end{aligned}$$

In (2.69), $|A_{Roe}|$ is constructed using the absolute values of the eigenvalues and the the right eigenvector matrix R:

$$|A_{Roe}| = R^{-1}|\Lambda|R \tag{2.70}$$

In case the preconditioned system of equation is used, the eigenvalues and the eigenvectors of the preconditioned system must be used $(\Lambda_\Gamma, R_\Gamma)$. Thus, according to [63], $|A_{Roe}|$ is changed to:

$$
\begin{aligned}
|A_{\Gamma Roe}| &= |\Gamma^{-1}\Gamma A_{Roe}| \\
&\simeq \Gamma^{-1}|\Gamma A_{Roe}| \\
&\simeq \Gamma^{-1}R_{\Gamma}^{-1}|\Lambda_{\Gamma}|R_{\Gamma}
\end{aligned} \tag{2.71}
$$

2.3.3 Viscous Fluxes

For the calculation of Viscous Fluxes, variable values and space derivatives are needed. For the face in between cells I and J, variable values are obtained from simple averaging:

$$
\vec{V}_{IJ} = \frac{1}{2}\left(\vec{V}_I + \vec{V}_J\right) \tag{2.72}
$$

while for the gradients, the Green-Gauss formula is applied using the face averaged values $\vec{V}_{IJ}$ as defined in (2.72) but supplemented with a directional derivative[64]:

$$
\nabla\vec{V}_{IJ} = \overline{\nabla\vec{V}_{IJ}} - \left[\overline{\nabla\vec{V}_{IJ}}\cdot\vec{t_{IJ}} - \left(\frac{\partial\vec{V}}{\partial l}\right)_{IJ}\right]\cdot\vec{t_{IJ}} \tag{2.73}
$$

where

$$
\overline{\nabla\vec{V}_{IJ}} = \frac{1}{2}\left(\nabla\vec{V}_I + \nabla\vec{V}_J\right) \tag{2.74}
$$

is the mean gradient,

$$
\left(\frac{\partial\vec{V}}{\partial l}\right)_{IJ} \approx \frac{\vec{V}_J - \vec{V}_I}{l_{IJ}} \tag{2.75}
$$

and l_{IJ} is the distance between cell centers I and J and $\vec{t_{IJ}}$ is the unit vector pointing from cell center I to cell center J.

2.4 Temporal discretization

For the temporal discretization the method of lines is used. This means that temporal and spatial discretization are done separately leading for every control volume to the following equation:

$$
\frac{d\left(D_I\vec{U}_I\right)}{dt} = -R_I \tag{2.76}
$$

In comparison to (2.43) the form of equation (2.76) is more general in the sense that the control volume can vary with time.

Temporal discretization can be either explicit or implicit. Explicit methods use the $\vec{U}^n$ known solution and march in time using the corresponding residual $\vec{R}^n$ to obtain solution at $(t+\Delta t)$. On the other hand the implicit schemes use $R(\vec{U}^{n+1}) = \vec{R}^{n+1}$ to obtain the new solution and are favored because they allow larger time-steps. Since $\vec{R}^{n+1}$ is unknown, the following linear approximation is used:

$$
\vec{R}^{n+1} \approx \vec{R}^n + \left(\frac{\partial\vec{R}}{\partial\vec{U}}\right)_n \cdot \Delta\vec{U}^n, \quad \Delta\vec{U}^n = \vec{U}^{n+1} - \vec{U}^n \tag{2.77}
$$

In MaPFlow a finite difference scheme is used for the time derivative [65]:

$$
\frac{1}{\Delta t}\left[\phi_{n+1}\left(D\vec{U}\right)^{n+1} + \phi_n\left(D\vec{U}\right)^{n} + \phi_{n-1}\left(D\vec{U}\right)^{n-1} + \phi_{n-2}\left(D\vec{U}\right)^{n-2} + \dots\right] = -R^{n+1} \tag{2.78}
$$

Depending on the choice of ϕ_n the corresponding backwards difference formulae (BDF) of the temporal scheme is defined. $BDF2OPT$, refers to a class of optimized, second-order, backward difference methods with an error constant half as large as the conventional 2^{nd} order scheme [66].

Table 2.1: *Backwards Difference Schemes*

order	ϕ_{n+1}	ϕ_n	ϕ_{n-1}	ϕ_{n-1}
1^{st}	1	-1	0	0
2^{nd}	3/2	-2	1/2	0
3^{rd}	11/6	-3	3/2	$-1/3$
$BDF2OPT$	$3/2-\phi_{n-2}$	$-2+3\phi_{n-2}$	$1/2-3\phi_{n-2}$	$-0.58/3$

2.4.1 Steady State Computations

Even when steady state simulations are considered a pseudo-unsteady technique is followed. For steady state simulations 1^{st} order scheme is chosen to march the solution in pseudo-time until convergence is reached. At 1^{st} order, after linearizing R^{n+1}, (2.78) becomes:

$$\frac{\left(D_I \Delta \vec{U}_I^n\right)}{\Delta t_I} = \vec{R}_I^n + \left(\frac{\partial \vec{R}}{\partial \vec{U}}\right)_I \Delta \vec{U}_I^n \tag{2.79}$$

By rearranging the terms the final system of discrete equations is obtained in which the system matrix defines the *implicit operator* of the scheme:

$$\underbrace{\left[\frac{(D)_I}{\Delta t_I} + \left(\frac{\partial \vec{R}}{\partial \vec{U}}\right)_I\right]}_{\text{Implicit Operator}} \Delta \vec{U}_I^n = -\vec{R}_I^n \tag{2.80}$$

Local Time Stepping

In order to facilitate convergence, the Local Time Step technique is used [67]. The time step for steady state calculation can be defined using the spectral radii of each cell. For every cell, a different time step is defined by:

$$\Delta t = CFL \frac{D_I}{\left(\hat{\Lambda}_c + C\hat{\Lambda}_v\right)_I} \tag{2.81}$$

where $\hat{\Lambda}_c$, $\hat{\Lambda}_v$ is the sum of convective and viscous eigenvalues over all cell faces. The convective spectral radii is defined by:

$$(\hat{\Lambda}_c)_I = \sum_{J=1}^{N_f} (|\vec{u}_{IJ} \cdot \vec{n}_{IJ}| + c_i j) \Delta S_{IJ} \tag{2.82}$$

and the viscous spectral radii by:

$$(\hat{\Lambda}_v)_I = \frac{1}{D_I} \sum_{J=1}^{N_f} [max(\frac{3}{3\rho_{IJ}}, \frac{\gamma_{IJ}}{\rho_{IJ}})(\frac{\mu_L}{Pr_L} + \frac{\mu_T}{Pr_T})_{IJ} (\Delta S_{IJ})^2] \tag{2.83}$$

2.4.2 Time True Computations

When making Time True computations, temporal discretization is crucial because any remaining numerical error will propagate in the flow as a disturbance. In order to minimize temporal errors higher order schemes should be used in conjunction with the Dual Time-Step technique [68].

Dual Time-Stepping

The Dual Step approach adds an extra time-like derivative in the transport equation that refers to a different "time variable" τ, called "pseudo-time". The conservative variables in the pseudo-time problem are denoted by $U^\star$, because they don't satisfy the original unsteady problem until convergence is reached

Using this approach the unsteady problem is transformed into a steady one. In every true time-step the following problem is solved in the pseudo-time (τ) :

$$\frac{\partial (D^{n+1} \vec{U}^\star)}{\partial \tau} + \vec{R}^\star = 0 \tag{2.84}$$

Setting,

$$\vec{R}^{\star} = \frac{\partial(D\vec{U}^{\star})}{\partial t} + R(\vec{U}^{\star}) \tag{2.85}$$

the following final form is obtained:

$$\frac{\partial(D^{n+1}\vec{U}^{\star})}{\partial \tau} + \frac{\partial(D\vec{U}^{\star})}{\partial t} = -R(\vec{U}^{\star}) \tag{2.86}$$

When (2.84) converges, $R^{\star} = 0, \vec{U}^{\star} = \vec{U}$ which satisfies the original unsteady problem.

The discretized form of (2.86) can be written as:

$$\frac{D^{n+1}\Delta U^{\star k}}{\Delta \tau} + \frac{1}{\Delta t}\left[\phi_{n+1}\left(D\vec{U}^{\star}\right)^{n+1} + \phi_n\left(D\vec{U}\right)^{n} + \phi_{n-1}\left(D\vec{U}\right)^{n-1}\right] = -R^{k+1} \tag{2.87}$$

or

$$\frac{D^{n+1}\Delta U^{\star k}}{\Delta \tau} = -R^{\star k+1} \tag{2.88}$$

with

$$\Delta U^{\star k} = U^{\star k+1} - U^{\star k} \tag{2.89}$$

and

$$R^{\star k+1} = R^{k+1} - \frac{1}{\Delta t}\left[\phi_{n+1}\left(D\vec{U}^{\star}\right)^{n+1} + \phi_n\left(D\vec{U}\right)^{n} + \phi_{n-1}\left(D\vec{U}\right)^{n-1}\right] \tag{2.90}$$

where k denotes the steady state problem sub-iteration.

In order to apply an Implicit Scheme in the Dual Time-Step procedure we must linearize the unsteady residual $R^{\star k+1}$:

$$\vec{R}^{\star k+1} \approx \vec{R}^{\star k} + \left(\frac{\partial \vec{R}}{\partial \vec{U}^{\star}}\right)_k \cdot \Delta\vec{U}^{\star k} \tag{2.91}$$

or

$$\begin{aligned}\vec{R}^{\star k+1} \approx \vec{R}^{k} - \frac{1}{\Delta t}\left[\phi_{n+1}\left(D\vec{U}^{\star}\right)^{n+1} + \phi_n\left(D\vec{U}\right)^{n} + \phi_{n-1}\left(D\vec{U}\right)^{n-1}\right] \\ + \frac{\partial \vec{R}}{\partial \vec{U}^{\star}}\Delta\vec{U}^{\star} - \phi_{n+1}\frac{D^{n+1}}{\Delta t}\Delta\vec{U}^{\star}\end{aligned} \tag{2.92}$$

The correction $\Delta U^{\star}$ refers to the steady problem defined in pseudo-time. Thus, when the steady problem converges, $\Delta U^{\star} = 0$. However, this does not correspond to $U^{n+1} - U^{n} = 0$ but to $U^{k+1,n+1} - U^{k,n+1} = 0$. The ϕ coefficients change according to the desired time discretization scheme (see Table 2.1).

Substituting in (2.88) the final form is obtained:

$$\left[\frac{D^{n+1}}{\Delta \tau} + \phi_{n+1}\frac{D^{n+1}}{\Delta t} + \frac{\partial \vec{R}}{\partial \vec{U}^{\star}}\right]\Delta U^{\star k} = -R^{k} - Q^{k}_{dual} \tag{2.93}$$

where the dual step unsteady source-like terms Q^{k}_{dual} are given by:

$$Q^{k}_{dual} = \frac{1}{\Delta t}\left[\phi_{n+1}\left(D\vec{U}^{\star}\right)^{n+1} + \phi_n\left(D\vec{U}\right)^{n} + \phi_{n-1}\left(D\vec{U}\right)^{n-1}\right] \tag{2.94}$$

It is noted here that the pseudo time step $\Delta\tau$ is defined as in the Steady state computations using local timestepping (2.81).

2.5 Boundary conditions

In external aerodynamics the following boundary conditions are needed:

- Far-field Boundaries
- Solid wall Boundaries
- Symmetry Boundaries
- Periodic Boundaries

Before analyzing each one of the boundary condition types, it is important to discuss the concept of dummy cells. Dummy cells are additional virtual cells that extend the computational domain. Their purpose is to provide assistance in calculating the flow variables at the computational domain boundaries. Far-field and solid wall conditions are defined exactly at the boundary face while the other two are applied at the center of the dummy cell.

2.5.1 Far-field Boundaries

In the far-field, it is important to comply with the hyperbolic character of the problem as expressed when formulated in characteristic variables. The information provided is related to the sign of the eigenvalues of the flow state at the far-field boundary and the associated Riemann invariants. Both must be respected and therefore the far-field boundary conditions must be accordingly defined. The approach followed is based on the characteristics of the 1D Euler equations along the normal direction to the boundary [44], $u = \vec{V} \cdot \vec{n}$. The sign of each of the three eigenvalue u, $u + c$, $u - c$, defines the direction of propagation while along the corresponding characteristic the associated Riemann invariants R, $R+$, $R-$ (see fig. 2.3).

$$\begin{aligned} R^{\pm} &= u \pm \frac{2c}{\gamma - 1} \\ R &= s \end{aligned} \tag{2.95}$$

remain constant.

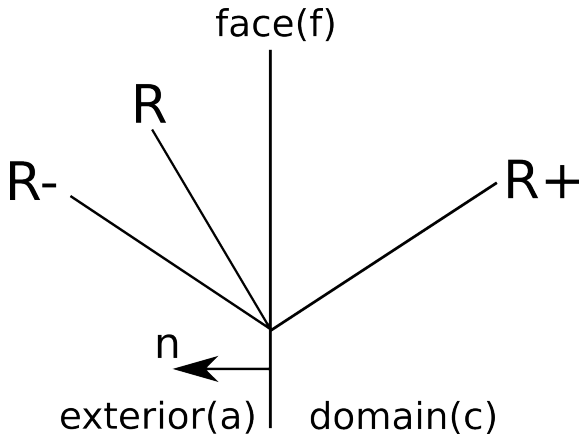

Figure 2.3: *The case of a subsonic inlet face. Note that on an inlet face and the normal defined to point outwards, the normal to the boundary velocity component $u = \vec{V} \cdot \vec{n} < 0$. This means that in reality the flow information associated to $R, R-$ is provided by the state defined in (a).*

Thus on an inflow face (and similarly for an outflow face), using the invariants:

$$\begin{aligned} &\text{from } R^{+} && u_f + \frac{2c_f}{\gamma - 1} = u_c + \frac{2c_c}{\gamma - 1} \\ &\text{from } R^{-} && u_f - \frac{2c_f}{\gamma - 1} = u_a - \frac{2c_a}{\gamma - 1} \\ &\text{isentropic assumption} && s_f = s_a \end{aligned} \tag{2.96}$$

Although the flow variables at boundary faces can be obtained as linear combinations of these invariants, in

the present formulation, the characteristic equations are used instead:

$$\begin{aligned} d\rho - \frac{1}{c^2}dp = 0 \qquad & \text{along} \qquad \lambda_1 = u \\ du + \frac{1}{\rho c}dp = 0 \qquad & \text{along} \qquad \lambda_2 = u + c \\ du - \frac{1}{\rho c}dp = 0 \qquad & \text{along} \qquad \lambda_3 = u - c \end{aligned} \tag{2.97}$$

Supersonic Inlet-Outlet

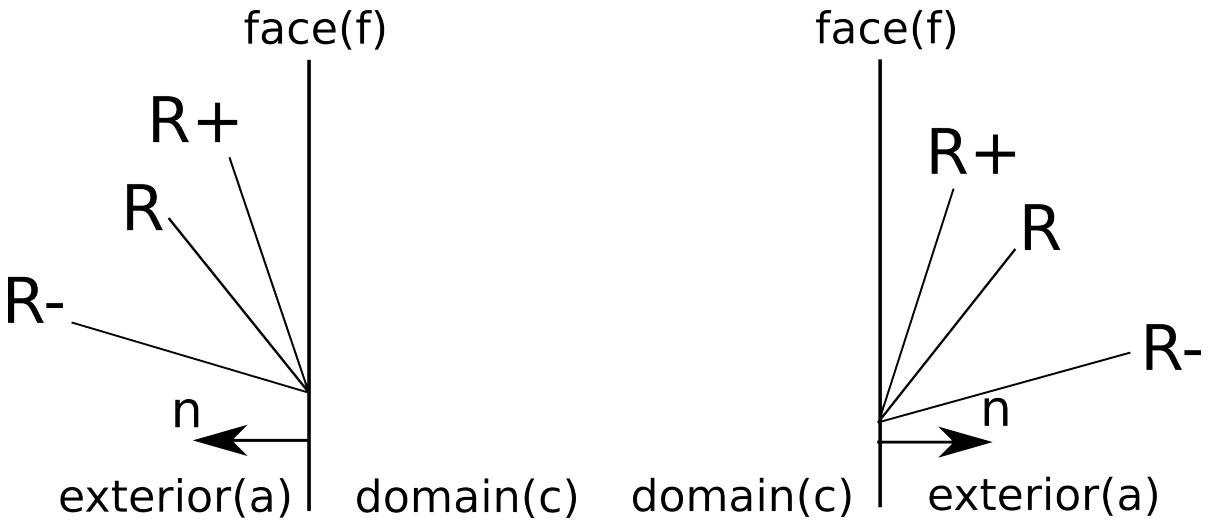

(a) *Supersonic Inlet* **(b)** *Supersonic Outlet*

Figure 2.4: *Riemann Invariants on a far-field supersonic boundary*

In the supersonic case all eigenvalues are positive since $V > c$. This means that in the case of inflow, all flow information is propagating from outside into the domain (fig. 2.4) and therefore all flow variables must be given as input:

$$\vec{V}_{inlet} = \vec{V}_{\infty} \tag{2.98}$$

On the contrary in the case of outflow all flow information propagates from inside of the domain:

$$\vec{V}_{outlet} = \vec{V}_{domain} \tag{2.99}$$

Subsonic inlet-outlet

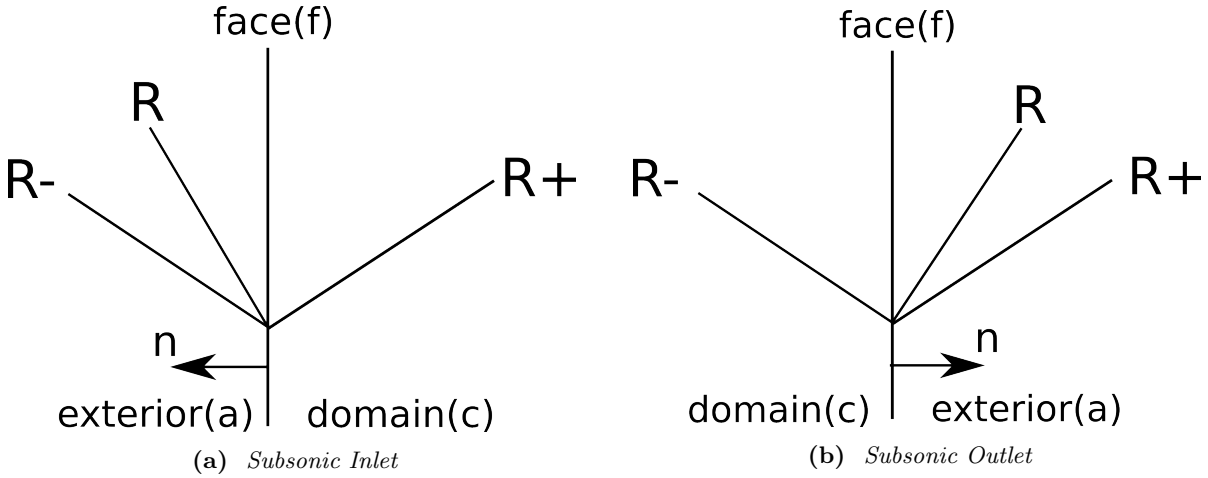

(a) *Subsonic Inlet* **(b)** *Subsonic Outlet*

Figure 2.5: *Riemann Invariants on a far-field subsonic boundary*

For subsonic inflow and along the normal to the boundary, the two characteristics propagate information from outside of the domain while the third propagates flow information from inside of the domain (fig. 2.5). The situation reverses in case of subsonic outflow where two characteristics propagate information from inside the domain while the third propagates information from outside into the flow domain. Note that the three Riemann invariants, associated with the eigenvalues, are defined with respect to the normal direction; hence for the subsonic inlet with the normal vector pointing outwards $u - c < 0$, $u < 0$, $u + c > 0$, while for the subsonic outlet $u - c < 0$, $u > 0$, $u + c > 0$.

Based on (2.97), with the normal pointing outwards of the inlet face:

$$\begin{aligned}
\frac{p_f}{\rho_f^\gamma} &= \frac{p_a}{\rho_a^\gamma} \qquad \text{along} \qquad \lambda_1 = u, (R) \\
p_f - p_c + \frac{1}{\rho_a c_a}\left(u_f - u_c\right) &= 0 \qquad \text{along} \qquad \lambda_2 = u + c, (R+) \\
p_f - p_a - \frac{1}{\rho_a c_a}\left(u_f - u_a\right) &= 0 \qquad \text{along} \qquad \lambda_3 = u - c, (R-)
\end{aligned} \tag{2.100}$$

By combining R^+ and R^- pressure and velocity at the boundary are determined. Density can be retrieved from the isentropic relation. As reference state at the inlet, that at the exterior of the domain is used. Similarly, under the assumption that the normal direction is pointing outside of the domain, at the outlet boundary,

$$\begin{aligned}
\frac{p_f}{\rho_f^\gamma} &= \frac{p_c}{\rho_c^\gamma} \qquad \text{along} \qquad \lambda_1 = u, (R) \\
p_f - p_c + \frac{1}{\rho_c c_c}\left(u_f - u_c\right) &= 0 \qquad \text{along} \qquad \lambda_2 = u + c, (R+) \\
p_f - p_a - \frac{1}{\rho_c c_c}\left(u_f - u_a\right) &= 0 \qquad \text{along} \qquad \lambda_3 = u - c, (R-)
\end{aligned} \tag{2.101}$$

in which the reference state is defined from inside of the computational domain.

Preconditioned characteristic equations

As already discussed in Low Mach Preconditioning (Section 2.2.3) , the eigenvalues and eigenvectors of the system change (2.26). Hence, it is expected that the characteristic equations change too. When Eriksson's Preconditioning Matrix is used, like in the present case, the 1-D characteristic equations take the form [69]:

$$\begin{aligned}
d\rho - \frac{1}{c^2}dp = 0 \qquad &\text{along} \qquad \lambda_1 = u \\
du + \frac{c' - \alpha_m u}{\rho\alpha c^2}dp = 0 \qquad &\text{along} \qquad \lambda_2 = u' + c' \\
du - \frac{c' + \alpha_m u}{\rho\alpha c^2}dp = 0 \qquad &\text{along} \qquad \lambda_3 = u' - c'
\end{aligned} \tag{2.102}$$

with,

$$\begin{aligned}
\alpha_m &= \frac{(1-\alpha)}{2} \\
u' &= \frac{1}{2}\left(1+\alpha\right)u \\
c' &= \frac{1}{2}\sqrt{\left[\left(1-\alpha\right)u\right]^2 + 4\alpha c^2}
\end{aligned} \tag{2.103}$$

As in the un-preconditioned case, the characteristic equations are combined to obtain $\rho, \vec{u}, p$ at the boundary face,

$$\begin{aligned}
\rho_f &= \rho_o\left(\frac{p_b}{p_o}\right)^\gamma \\
V_{nf} &= V_{nc} + \left(\frac{1}{\rho c'}\right)\left(\frac{p_c - p_a}{2}\right) - \left(1 - \frac{\alpha_m V_{no}}{c'}\right)\left(\frac{V_{nc} - V_{na}}{2}\right) \\
p_f &= p_a + \left(1 - \frac{\alpha_m V_{no}}{c'}\right)\left(\frac{p_c - p_a}{2}\right) + \left(\frac{\rho\alpha c^2}{c'}\right)\left(\frac{V_{nc} - V_{na}}{2}\right) \\
u_f &= u_o + \left(V_{nf} - V_{no}\right)\cdot n_x \\
v_f &= v_o + \left(V_{nf} - V_{no}\right)\cdot n_y \\
w_f &= w_o + \left(V_{nf} - V_{no}\right)\cdot n_z
\end{aligned} \tag{2.104}$$

where

$$V_{n(\cdot)} = u_{(\cdot)} \cdot n_x + v_{(\cdot)} \cdot n_y + w_{(\cdot)} \cdot n_z \tag{2.105}$$

The reference state, here denoted by subscript o, is decided by the isentropic wave, λ_1. At a subsonic inlet face it corresponds to the outer flow data whereas at a subsonic outlet face the values from inside of the computational domain are used.

2.5.2 Wall Boundary Conditions

Inviscid Wall

When the fluid is assumed inviscid on solid boundaries,

$$(\vec{u} - \vec{u}_g) \cdot \vec{n} = 0 \tag{2.106}$$

where $\vec{u}_g$ denotes the mesh velocity. Density and pressure are set equal to their values at the cell center next to the wall,

$$p_w = p_I,\ \rho_w = \rho_I \tag{2.107}$$

Viscous Wall

In the general case, the fluid is viscous and the no slip wall condition is applied,

$$\vec{u} = \vec{u}_g \tag{2.108}$$

Density and pressure are treated as in the inviscid case. Regardless of the assumptions made for the fluid, the convective fluxes take the form,

$$\vec{F}_{cwall} = \begin{pmatrix} 0 \\ n_x p_w \\ n_y p_w \\ n_z p_w \\ p_w V_g \end{pmatrix} \tag{2.109}$$

where

$$V_g = \vec{u}_g \cdot \vec{n} \tag{2.110}$$

2.5.3 Symmetry and Periodic Boundary Conditions

Symmetry

When the flow is symmetric with respect to a plane, the simulation can only concern half of the flow domain. Over the symmetry plane, the condition imposed resembles to that applied to an Inviscid Wall. In both cases there is no flux across the boundary. However, in symmetry conditions gradients normal to the boundary must also vanish [64]. So,

$$\begin{aligned} \vec{u} \cdot \vec{n} &= 0, \qquad \text{zero flux} \\ \nabla \vec{U} \cdot \vec{n} &= 0, \qquad \text{zero normal gradients} \end{aligned} \tag{2.111}$$

Periodic Flows

If the flow is periodic, the simulation is conducted on one single period. In such cases, parts of the outer boundary of the mesh will correspond to the periodic surfaces on which explicit boundary data are not available. Closure of the problem is done by the Periodic boundary conditions that basically transfer the flow variables from one periodic surface to the next one. Periodicity can be either translational (e.g. as in the case of a wing equipped with an array of vortex generators) or rotational (e.g. as in the case of multi-bladed rotors) depending on the motion required for collapsing a periodic surface to its associate. The implementation is based on ghost cells [64].

Let A, B denote the two associated periodic surfaces (fig. 2.6). For every cell in contact with A, it's corresponding ghost cell is associated to a cell in contact with B. Scalar quantities are transferred from B to the ghost cells of A as they are, while vector (and tensor) variables follow the motion required for collapsing A on B. The motion is defined as a transformation matrix R_A, and so,

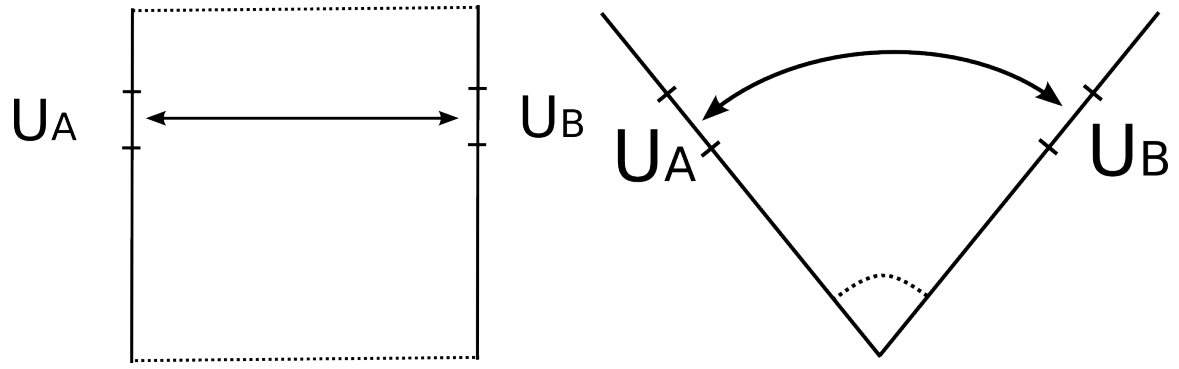

(a) *Translational Periodicity* **(b)** *Rotational Periodicity*

Figure 2.6: *Periodic Boundary Conditions*

$$\begin{aligned} U_A &= U_B \\ \vec{U}_A &= R_A \vec{U}_B \end{aligned} \tag{2.112}$$

In translational periodicity $R_A = I$ while in rotational periodicity R_A is the corresponding rotation matrix.

2.6 Turbulence modeling

In order to account for turbulence modeling, flow variables are split in their mean:

$$\overline{u_i} = \lim_{T\to\infty} \frac{1}{T} \int_t^{t+T} u_i dt \tag{2.113}$$

and fluctuating parts u_i':

$$u_i = \overline{u}_i + u_i' \tag{2.114}$$

with

$$\overline{u_i'} = 0 \tag{2.115}$$

$$\overline{u_i' u_j'} \neq 0 \tag{2.116}$$

The above is known as Reynold's time averaging and is suitable for statistically stationary turbulence. In compressible flows due to the fluctuation of density, the Favre (Mass) Averaging is applied:

$$\widetilde{u_i} = \frac{1}{\overline{\rho}} \lim_{T\to\infty} \frac{1}{T} \int_t^{t+T} \rho u_i dt \tag{2.117}$$

where

$$u_i = \widetilde{u_i} + u_i'' \tag{2.118}$$

with

$$\widetilde{\rho u_i} = \overline{\rho} \tilde{u_i} \tag{2.119}$$

$$\overline{\rho u''} = 0 \tag{2.120}$$

$$\overline{u_i''} \neq 0 \tag{2.121}$$

Favre's averaging is similar to Reynold's averaging but not identical. Again, $\widetilde{u_i''} = 0$ and $\widetilde{u_i'' u_j''} \neq 0$. Application of Favre's averaging to the governing equations leads to a considerably more complex system. Thus, Reynold's averaging is applied to density and pressure while Favre's averaging is applied to all other variables [64]. Dropping the bar and the tilde sign for the averaged variables:

$$
\begin{aligned}
\frac{\partial \rho}{\partial t} + \frac{\partial \rho u_i}{\partial x_i} &= 0 \\
\frac{\partial \rho u_i}{\partial t} + \frac{\partial \rho u_i u_j}{\partial x_j} &= -\frac{\partial p}{\partial t} + \frac{\partial}{\partial x_j}\left(\tau_{ij} - \rho\widetilde{u_i'' u_j''}\right) \\
\frac{\partial \rho E}{\partial t} + \frac{\partial \rho u_j H}{\partial x_j} &= \frac{\partial}{\partial x_j}\left(k\frac{\partial T}{\partial x_j} - \rho\widetilde{u_j'' h''} + \widetilde{\tau_{ij} u_i''} - \rho\widetilde{u_j'' K}\right) \\
&\quad + \frac{\partial}{\partial x_j}\left[u_i\left(\tau_{ij} - \rho\widetilde{u_i'' u_j''}\right)\right]
\end{aligned}
\tag{2.122}
$$

where $\rho K = 1/2\rho\widetilde{u_i'' u_i''}$ denotes the Turbulent Kinetic Energy.

The above system defines the compressible Reynolds-averaged Navier-Stokes equations or the Favre-averaged Navier-Stokes equations. By introducing the Favre-Averaged Reynolds-stress tensor as:

$$
\tau_{ij}^F = -\bar{\rho}\widetilde{u_i'' u_j''} \tag{2.123}
$$

and by neglecting temperature variations, molecular diffusion of K and turbulent transport, the equations (2.122) become:

$$
\begin{aligned}
\frac{\partial \rho}{\partial t} + \frac{\partial \rho u_i}{\partial x_i} &= 0 \\
\frac{\partial \rho u_i}{\partial t} + \frac{\partial \rho u_i u_j}{\partial x_j} &= -\frac{\partial p}{\partial t} + \frac{\partial}{\partial x_j}\left(\tau_{ij} + \tau_{ij}^F\right) \\
\frac{\partial \rho E}{\partial t} + \frac{\partial \rho u_j H}{\partial x_j} &= \frac{\partial}{\partial x_j}\left[u_i\left(\tau_{ij} + \tau_{ij}^F\right)\right]
\end{aligned}
\tag{2.124}
$$

Eddy-Viscosity Hypothesis

The turbulence models implemented in MaPFlow are first order closures based on the Boussinesq approximation for the Reynold's stresses:

$$
\tau_{ij}^F = 2\mu_T\left(S_{ij} - \frac{1}{3}\frac{\partial u_k}{\partial x_k}\right) - \frac{2}{3}K\delta_{ij} \tag{2.125}
$$

where:

$$
S_{ij} = \frac{1}{2}\left(\frac{\partial u_i}{\partial x_j} + \frac{\partial u_j}{\partial x_i}\right) \tag{2.126}
$$

and μ_T denotes the turbulent molecular viscosity. Depending on the specific turbulence model, turbulent kinetic energy is either used or neglected in the state equation,

$$
p = (\gamma - 1)\left[\rho E - \rho\frac{u^2 + v^2 + w^2}{2} - \rho K\right] \tag{2.127}
$$

2.6.1 Spalart-Allmaras (S-A) Turbulence Model

The Spalart-Allmaras model [70] solves the following transport equation for $\tilde{\nu}$:

$$
\mu_T = \rho\tilde{\nu} f_{v1} \tag{2.128}
$$

$$
\begin{aligned}
\frac{\partial \rho\tilde{\nu}}{\partial t} + \frac{\partial}{\partial x_j}(\rho\tilde{\nu}u_j) &= \rho C_{b1}\left[1 - f_{t2}\right]\tilde{S}\tilde{\nu} - \rho\left[C_{w1} f_w - \frac{C_{b1}}{\kappa^2} f_{t2}\right]\left(\frac{\tilde{\nu}}{d_w}\right)^2 + \\
&\quad \frac{\rho}{\sigma}\left[\frac{\partial}{\partial x_j}\left((\nu + \tilde{\nu})\frac{\partial \tilde{\nu}}{\partial x_j}\right) + C_{b2}\frac{\partial \tilde{\nu}}{\partial x_i}\frac{\partial \tilde{\nu}}{\partial x_i}\right]
\end{aligned}
\tag{2.129}
$$

where

$$
\tilde{S} = \Omega + \frac{\tilde{\nu}}{\kappa^2 d_w^2} f_{v2} \tag{2.130}
$$

$$
\begin{aligned}
\Omega &= \sqrt{2W_{ij}W_{ij}} \\
W_{ij} &= \frac{1}{2}\left(\frac{\partial u_j}{\partial x_i} - \frac{\partial u_i}{\partial x_j}\right)
\end{aligned}
\tag{2.131}
$$

In (2.129) d_w is defined as the distance from the cell center to the nearest wall and

$$\chi = \frac{\tilde{\nu}}{\nu} \tag{2.132}$$

$$f_{v1} = \frac{\chi^3}{\chi^3 + C_{v1}} \tag{2.133}$$

$$f_{v2} = 1 - \frac{\chi}{1 + \chi f_{v1}} \tag{2.134}$$

$$g = r + c_{w2}(r^6 - r) \tag{2.135}$$

$$r = min\left[\frac{\tilde{\nu}}{\tilde{S}\kappa^2 d_w^2}, 10\right] \tag{2.136}$$

$$f_w = g\left[\frac{1 + c_{w3}^6}{g^6 + c_w 3}^6\right]\frac{1}{6} \tag{2.137}$$

$$f_{t2} = c_{t3}\exp(-c_{t4}\chi^2) \tag{2.138}$$

with constants

$$\begin{aligned} C_{b1} &= 0.1355 \\ \sigma &= 2/3 \\ C_{b2} &= 0.622 \\ k &= 0.41 \\ C_{w2} &= 0.3 \\ C_{w3} &= 2 \\ C_{v1} &= 7.1 \\ C_{t3} &= 1.2 \\ C_{t4} &= 0.5 \\ C_{w1} &= \frac{Cb1}{\kappa^2} + \frac{1 + C_{b2}}{\sigma} \end{aligned} \tag{2.139}$$

In order to avoid numerical problems, the production term $\tilde{S}$ must be kept positive. Thus, $\tilde{S} = max(\tilde{S}, 10^-20)$. In case the equation tends to yield a negative solution for $\tilde{\nu}$ then it is recommended to set $\tilde{\nu}$ equal to a small positive number.

Boundary Conditions

The boundary conditions as suggested in [70] are:

$$\tilde{\nu}_{wall} = 0 \tag{2.140}$$

$$\tilde{\nu}_{\infty} = [3 - 5]\,\nu_{\infty} \tag{2.141}$$

In cases where transition from laminar to turbulent flow is considered, the boundary conditions become:

$$\tilde{\nu}_{wall} = 0 \tag{2.142}$$

$$\tilde{\nu}_{\infty} = 0.01\nu_{\infty} \tag{2.143}$$

2.6.2 Menter $k - \omega$ Shear Stress Transport (SST) Turbulence Model

Menter's Shear Stress Transport (SST) turbulence model [71] is a modification of Wilcox's two equation Eddy-Viscosity model [72] defined for the turbulence kinetic energy k and the specific dissipation rate ω. The transport equations of k and ω are given below:

$$\frac{\partial \rho k}{\partial t} + \frac{\partial}{\partial x_j}(\rho k u_j) = P - \beta^\star \rho \omega k + \frac{\partial}{\partial x_j}\left[(\mu + \sigma_k \mu_T)\frac{\partial k}{\partial x_j}\right] \tag{2.144}$$

$$\frac{\partial \rho \omega}{\partial t} + \frac{\partial}{\partial x_j}(\rho \omega u_j) = \frac{\gamma}{\nu_T}P - \beta^\star \rho \omega^2 + \frac{\partial}{\partial x_j}\left[(\mu + \sigma_\omega \mu_T)\frac{\partial k}{\partial x_j}\right] + 2(1 - F_1)\frac{\rho \sigma_{\omega 2}}{\omega}\frac{\partial k}{\partial x_j}\frac{\partial \omega}{\partial x_j} \tag{2.145}$$

where:

$$P = \tau_{ij} \frac{\partial u_i}{\partial x_j} \tag{2.146}$$

$$\tau_{ij} = \mu_T \left(2S_i - \frac{2}{3} \frac{\partial u_k}{\partial x_k} \right) - \frac{2}{3} \rho k \delta_{ij} \tag{2.147}$$

S_{ij} is the stress tensor given by (2.126) and $\nu_T = \mu_T / \rho$. Eddy viscosity μ_T is given by:

$$\mu_T = \frac{\rho \alpha_1 k}{max(\alpha_1 \omega, \Omega F_2)} \tag{2.148}$$

with Ω being the vorticity magnitude as in (2.131).

The constants for Menter's SST turbulence model are a blend of inner (1) and outer (2) constants defined by the following weighted expression:

$$\phi = F_1 \phi_1 + (1 - F_1) \phi_2 \tag{2.149}$$

with F_1 being defined by:

$$F_1 = tanh(\arg_1^4) \tag{2.150}$$

$$\arg_1 = min \left[max \left(\frac{\sqrt{k}}{\beta^\star \omega d} \frac{500\nu}{d_w^2 \omega} \right), \frac{4\rho\sigma_{\omega 2} k}{CD_{K\omega} d_w^2} \right] \tag{2.151}$$

$$CD_{k\omega} = max \left(2\rho\sigma_{\omega 2} \frac{1}{\omega} \frac{\partial k}{\partial x_j} \frac{\partial \omega}{\partial x_j}, 10^{-20} \right) \tag{2.152}$$

$$F_2 = tanh(\arg_2) \tag{2.153}$$

$$\arg_2 = max \left(2 \frac{\sqrt{k}}{\beta^\star \omega d_w} \frac{500\nu}{d_w^2 \omega} \right) \tag{2.154}$$

In the above equations, d_w is the distance from the cell center to the viscous wall boundary.

The inner constants (those denoted with subscript 1) are:

$$\begin{aligned} \gamma_1 &= \frac{\beta_1}{\beta^\star} - \frac{\sigma_{\omega 1} \kappa^2}{\sqrt{\beta^\star}} \\ \sigma_{k1} &= 0.85 \\ \sigma_{\omega 1} &= 0.5 \\ \beta_1 &= 0.075 \\ \beta^\star &= 0.09 \\ \kappa &= 0.41 \\ \alpha_1 &= 0.31 \end{aligned} \tag{2.155}$$

The outer constants (those with subscript 2) are:

$$\begin{aligned} \gamma_2 &= \frac{\beta_2}{\beta^\star} - \frac{\sigma_{\omega 2} \kappa^2}{\sqrt{\beta^\star}} \\ \sigma_{k2} &= 1.0 \\ \sigma_{\omega 2} &= 0.856 \\ \beta_2 &= 0.0828 \end{aligned} \tag{2.156}$$

In [73], a limiter on the production term in the K equation is recommended. Hence, the production term in the K-equation is replaced by:

$$P = min(P, 20\beta^\star \rho k \omega) \tag{2.157}$$

Boundary Conditions

The boundary conditions as defined in [71] are:

$$\frac{U_\infty}{L} < \omega_\infty < 10\frac{U_\infty}{L} \tag{2.158}$$

$$\frac{10^{-5}U_\infty^2}{Re_L} < k_\infty < \frac{10^{-1}U_\infty^2}{Re_L} \tag{2.159}$$

$$\omega_{wall} = \frac{6\nu}{\beta_1 d_1^2} \tag{2.160}$$

$$k_{wall} = 0 \tag{2.161}$$

where L is the approximate length of the computational domain and d_1 the distance to the next point off the wall.

2.6.3 Remarks on the formulation of turbulence equations

Even though both models were presented in their differential form, their integral form is actually used. The transport equation for a generic turbulence model variable U_T, takes the form,

$$\int_D \frac{\partial U_T}{\partial t} dD + \int_D \frac{\partial}{\partial x_j}\left(\rho u_j U_T\right) dD - \int_D \rho \frac{\partial}{\partial x_j}\left[\ldots \frac{\partial U_T}{\partial x_j}\right] dD = \int_D \rho(S_{Prod} + S_{Destr}) dD \tag{2.162}$$

which by means of the Green Gauss formula is transformed into:

$$\int_D \frac{\partial U_T}{\partial t} dD + \oint_{\partial D}\left(\rho u_j U_T\right)\vec{n} dS - \oint_{\partial D} \rho(\ldots)\frac{\partial U_T}{\partial x_j}\vec{n} dS = \int_D \rho(S_{Prod} + S_{Destr}) dD \tag{2.163}$$

where

$$F_{Tc} = \left(\rho u_j U_T\right)\vec{n} \tag{2.164}$$

$$F_{Tv} = \rho(\ldots)\frac{\partial U_T}{\partial x_j}\vec{n} \tag{2.165}$$

denote the convective and viscous fluxes respectively and S_{Prod}, S_{Destr} the Production and Destruction source terms.

From (2.163) the following differential form is obtained,

$$\frac{D\,U_T}{Dt} = S_{Prod} + Diff - S_{Destr} \tag{2.166}$$

$$\frac{DU_T}{Dt} = \frac{\partial U_T}{\partial t} + u_j\frac{\partial U_T}{\partial x_j} = \frac{\partial U_T}{\partial t} + \frac{\partial}{\partial x_j}\left(u_j U_T\right) - U_T\frac{\partial u_j}{\partial x_j} \tag{2.167}$$

$$Diff = \frac{\partial}{\partial x_j}\left[\ldots \frac{\partial(U_T)}{\partial x_j}\right] \tag{2.168}$$

For incompressible flows, $\partial u_j/\partial x_j = 0$ and thus:

$$\frac{\partial U_T}{\partial t} + u_j\frac{\partial U_T}{\partial x_j} = \frac{\partial U_T}{\partial t} + \frac{\partial}{\partial x_j}\left(u_j U_T\right) \tag{2.169}$$

However, when the compressible equations are solved $\partial u_j/\partial x_j \neq 0$. In order to bring (2.167) in conservative form, the continuity equation is used,

$$\frac{\partial U_T}{\partial t} + u_j\frac{\partial U_T}{\partial x_j} + U_T\left(\frac{\partial \rho}{\partial t} + \frac{\partial}{\partial x_j}(\rho u_j)\right) = \frac{1}{\rho}\frac{\partial}{\partial t}\left(\rho U_T\right) + \frac{1}{\rho}\frac{\partial}{\partial x_j}\left(\rho u_j U_T\right) \tag{2.170}$$

leading to the final conservative form of the turbulence model equation:

$$\frac{\partial}{\partial t}\left(\rho U_T\right) + \frac{\partial}{\partial x_j}\left(\rho u_j U_T\right) - \rho\frac{\partial}{\partial x_j}\left[\ldots \frac{\partial U_T}{\partial x_j}\right] = \rho\cdot\left(S_{Prod} - S_{Destr}\right) \tag{2.171}$$

2.6.4 Discretization

Convective terms

For the convective term first order up-winding is applied:

$$\rho u_j n_j U_T = max(\rho_L V_{Ln} U_{TL}, 0) + min(\rho_R V_{Rn} U_{TR}, 0) \tag{2.172}$$

When the PLR scheme is used, boundness and monotonicity are not guaranteed [52]. The left and right states are thus taken as the values at the cell centers I, J, which corresponds to a first order approximation, and V is the corresponding contravariant velocity.

$$U_L = U_I \tag{2.173}$$
$$U_R = U_J \tag{2.174}$$
$$V_{(\cdot)n} = \vec{u}_{(\cdot)} \cdot \vec{n} \tag{2.175}$$

For higher order schemes (MUSCL and QUICK), the left and right states are calculated in the same way as for the primary variables.

Diffusion terms

The discretization of the diffusion terms consists of first order central differencing. The value of the diffusion terms at a face is taken as an arithmetic mean of the values at the center of the cells sharing the face. The gradient that appears on that term is calculated in the same manner as the gradients of flow variables that contribute to the governing equation diffusion terms (2.73).

Finally the discretization of the temporal and source terms is done in the same manner as for the governing equations.

2.7 Solution of the System of Equations

The final form of the discrete equations corresponds to a linear system

$$AX = B \tag{2.176}$$

of large dimension. The above system can be either solved directly or iteratively. Direct solvers are accurate but have demanding memory requirements and are not easily parallelised. On the contrary, iterative solvers might need many iterations to converge but are suitable for parallel coding and have limited memory requirements. Therefore in the present work, an iterative solver was chosen. Following the work of [74], the Jacobi iterative solver was implemented.

Noting that all but one terms in the discrete form of the equations for cell I,

$$\left[\frac{(D)_I}{\Delta t_I} + \left(\frac{\partial \vec{R}}{\partial \vec{U}}\right)_I\right] \Delta \vec{U}_I^n = -\vec{R}_I^n \tag{2.177}$$

refer to the cell in consideration, the following splitting

$$D_I \Delta \vec{U}_I^n + O_I \sum \Delta \vec{U}_J^n = -\vec{R}_I^n \tag{2.178}$$

is introduced. In (2.178), the first term is block diagonal and is linked to cell I, while the second contains the off diagonal contributions in (2.177) that are linked to $\left(\frac{\partial \vec{R}}{\partial \vec{U}}\right)_I$. This term involves the cells that surround I.

Jacobi iterative solver

A solution to (2.178) can be achieved using the Jacobi method:

$$D_I \Delta \vec{U}_I^{n,k+1} = -\vec{R}_I^n - O_I \sum \Delta \vec{U}_J^{n,k} \tag{2.179}$$

where k is the Jacobi iterations index.

Gauss-Seidel iterative solver

As an alternative, the Gauss-Seidel method can be used. It is similar to Jacobi solver, except the fact that the off diagonal terms are calculated using the current update for $\vec{U}$,

$$D_I \Delta \vec{U}_I^{n,k+1} = -\vec{R}_I^n - O_I \sum \Delta \vec{U}_L^{n,k+1} - O_I \sum \Delta \vec{U}_J^{n,k} \tag{2.180}$$

where U_L concerns the cell values that have been updated in $k+1$ iteration.

The performance of the Gauss-Seidel method strongly depends on the type of the matrix A in (2.176). If A is banded, the matrix can be split in an Upper and Lower part and thus Gauss-Seidel becomes:

$$D_I \Delta \vec{U}_I^{n,k+1} = -\vec{R}_I^n - O_I \sum \Delta \vec{U}_L^{n,k+1} - O_I \sum \Delta \vec{U}_R^{n,k} \tag{2.181}$$

However if the sparsity of A is substantial, the Gauss-Seidel solver has the same convergence properties as the Jacobi method [75].

In case the mesh is structured, the matrix is indeed banded and the Gauss-Seidel solver will behave well. On the contrary, if an unstructured mesh is used, because the band width of the matrix depends on the cell numbering, good performance is directly linked to proper renumbering. In this respect the Reverse Cuthill-Mckee (RCM) reordering scheme [75] substantially reduces the band-width and therefore the Gauss-Seidel methods outperforms the Jacobi solver.

It is important to note here that in a parallel environment even if Gauss-Seidel iterative solver is used the update ΔU_J^n must remain in the k iteration if U_J is a multi-block ghost cell. The reason behind this constraint is to ensure that the solution will be continuous across the blocks at all times.

2.8 Mesh Deformation

Often the mesh must deform, as in the case of a deformable trailing edge flap [76] or fluid-structure interaction. In such cases, on one hand the mesh deformation must ensure that the mesh lines do not overlap and that the change of the cell volume is taken into account.

For mesh deformation, the work by Zhao [77] was followed. The idea in Zhao's scheme is to propagate the displacements of the solid boundaries into the mesh without changing the far-field boundary while keeping the same mesh topology. This is carried out at nodal level as follows:

$$d\vec{r}(node) = f(node) d\vec{r}(node_{wall}) \tag{2.182}$$

where $\vec{dr}$ is the displacement of the any mesh node, $\vec{dr}(node_{wall})$ is the displacement of a node on the solid boundary and f is the propagation function. For a two-dimensional problem:

$$f(x) = \frac{ly^2(x)}{lx^2(x) + ly^2(y)} \tag{2.183}$$

$$lx(x) = \frac{1 - \exp(-d(x)/d_{max})}{(e-1)/e}$$

$$ly(x) = \frac{1 - \exp(1 - d(x)/d_{max})}{(e-1)/e} \tag{2.184}$$

where $d(x)$, is the distance of the node to the nearest solid node and d_{max} is the maximum distance of all nodes from the solid boundary.

Mesh deformation will render the cell volume $D(t)$ time dependent. Thomas and Lombard [78] proposed the so called Geometric Conservation Law (GCL)

$$\frac{d}{dt} \int_{D(t)} dD = \oint_{\partial D(t)} \vec{V}_g \cdot \vec{n} dS \tag{2.185}$$

The principle of GCL is that a uniform flow solution must remain unchanged regardless of the mesh motion.

Various numerical implementations of the GCL are found in the literature (e.g [79]). In the present work the implementation in [80] is adopted, which consists of adding a source term to the original equations. Starting from the integral form of the equations and assuming volume averaged approximation,

$$\frac{d}{dt}(\vec{U} D) + R = 0 \tag{2.186}$$

it follows that

$$\frac{d\vec{U}}{dt} D + \frac{dD}{dt} \vec{U} + R = 0 \tag{2.187}$$

So by introducing (2.185),

$$\frac{d\vec{U}}{dt}D + R = -\vec{U}\oint_{\partial D(t)} \vec{V}_g \cdot \vec{n} dS \tag{2.188}$$

and applying (2.78), the following discrete formulation is obtained,

$$\frac{1}{\Delta t}\left[\phi_{n+1}\vec{U}^{n+1} + \phi_n\vec{U}^n + \phi_{n-1}\vec{U}^{n-1} + \phi_{n-2}\vec{U}^{n-2} + \dots\right] \cdot D^{n+1} = -R^{n+1} - \vec{U}\oint_{\partial D(t)} \vec{V}_g \cdot \vec{n} dS \tag{2.189}$$

It is noted that for rigid body motions $\oint_{\partial D(t)} \vec{V}_g \cdot \vec{n} dS \approx 0$.

2.9 Discussion

In this Chapter, a detailed overview of the employed computational solver has been presented. However, besides the utilized difference schemes for the discretized equations, the boundary conditions, and the employed turbulence models, there are also other numerical parameters that can have a significant effect on the produced results.

Regarding transitional simulations, mesh generation and mesh resolution dependence are discussed in Chapter 5, Section 5.2. These types of simulations utilize RANS turbulence models. Reaching a mesh independent solution is therefore possible. On the contrary, mesh resolution dependence was not assessed explicitly in the case of LES and DES. Both these methods are not expected to yield a truly mesh independent solution. With continuing mesh refinement, a higher amount of small scales will be resolved and not modeled. The strategy is thus to use the finer mesh allowed by one's computational resources.

Similarly, the effect of the employed physical timestep used in time true computations for transitional flows is discussed in Chapter 5, Section 5.3. For LES and DES simulations, timestep dependence analysis was not carried out due to limited computational resources. Timestep values noted in the literature were used instead.

In regards to difference scheme, the bulk of the simulations presented in this thesis utilized the 2^{nd} order PLR scheme for the reconstruction of variables. For simulations at low to moderate angles of attack, it was found that the numerical scheme had a minor effect on the predicted aerodynamic performance. Since the higher order schemes are harder to converge sufficiently, thus increasing the overall computational cost, they were only used in supplementary simulations for selected cases with DES at higher angles of attack with massive flow separation. For a brief view on the effect of the numerical scheme, the reader is referred to Appendix A.

Moreover, computational results can vary due to the usage, or absence thereof, of numerical limiters. As stated previously, MaPFlow has the option for Venkatakrishnan's limiter for the PLR scheme, and superbee and Van Leer's limiters for the MUSCL scheme (Section 2.3). Simulations at lower Mach numbers ($Ma_\infty < 0.29$) using the PLR scheme were carried out without the use of numerical limiters, in contrast to simulations on transonic regimes. The decision to not include limiters in low Mach simulations was an important step, as the inclusion of limiters significantly affected the final results of the simulations, preventing the solution from reaching a mesh independent solution. For a brief view on the effect of the numerical limiter, the reader is referred to Appendix B. However, further analysis and assessment of the behavior of numerical limiters is beyond the scope of this work.

This page intentionally left blank

Chapter 3

Transition modeling

3.1 Introduction

Throughout the years, many empirical transition models have been developed which most often correlate transition location prediction to boundary layer development. A simple model for transition prediction is that of Michel [81], which uses an empirical correlation between the momentum thickness Reynolds number Re_θ and the Reynolds number based on local length Re_x in order to trigger transition. This model has been used for many airfoil types [82][83] and is able to give decent results. However, it does not account for surface roughness or freestream turbulence. Another commonly used model is that of Eppler [84], which was employed for the design of many NREL S-series wind turbine airfoils [6][7]. This empirical method incorporates a roughness factor in order to predict transition. Another popular transition criterion is that of Abu-Ghannam and Shaw [85], which addresses natural as well as bypass transition. All these criteria are local in the sense that for each wall station, boundary layer parameters are compared to critical values in order to determine whether the flow has transitioned to turbulence.

A similarly popular empirical transition method is that of Granville [24][86] which uses experimental correlations to predict the neutral stability point and after that calculates the difference between the local momentum thickness Reynolds number and the neutral stability point momentum thickness Reynolds number. This difference is then compared to a critical value in order to trigger transition. The downside of this method is that it also does not account for surface roughness and freestream turbulence. A similar approach is the Arnal-Habiballah-Delcourt (AHD) criterion [87] which incorporates freestream turbulence levels to predict transition and in addition can be used for highly compressible flows, up to Mach 4 [88]. These two methods are non-local because they require upstream boundary layer knowledge in order to define the transition onset location. Therefore, the flow state cannot be determined using only the parameters of a single boundary layer station.

A different approach in transition prediction is through the use of stability theory. The Orr-Sommerfeld equations describe when the linearized modes in parallel shear flows will amplify and will result in turbulence breakdown. The downside of this approach is that transition is treated as a purely linear phenomenon, an assumption that is not entirely correct as nonlinear effects can create large destabilizing transients that may result in turbulence. A commonly used method is the e^N method of Smith et al [89] and Van-Ingen [90], which both correlate the amplitude ratio of the largest mode to the location of transition. The e^N method also requires upstream boundary layer information, similarly to the Granville and AHD empirical models.

The inherent need for boundary layer calculation when using conventional transition criteria does not comply with the local nature of the Navier-Stokes equations. Unfortunately, the transported variables ρ,u,v,w and P do not translate to boundary layer properties. Consequently, some type of boundary layer calculation approach must be implemented in order to apply empirical transition criteria. For local transition models, boundary layer parameters can be calculated via an integration in the normal direction at every wall station. The process of calculating boundary layer parameters directly from flow data in corresponding cells will be referred to as *Direct CFD Boundary Layer*.

However, Direct CFD Boundary Layer integration will add computational effort that can be quite significant. Contemporary computational solvers aim at parallel execution, thus utilizing domain decomposition for computationally demanding problems. In such cases, parts of the boundary layer map may be assigned to different computational blocks, which makes the process impossible to fully execute in parallel. Subsequently, boundary layer integration will require additional communication overhead and will impose barriers on the solution of the Navier-Stokes equations, essentially behaving like an in-situ post process that halts the simulation.

Instead of using the Direct CFD Boundary Layer approach, boundary layer parameters can be calculated via integral methods like the approximate Polhausen method or by solving boundary layer momentum and

kinetic energy equations at the wall surface. These methods also suffer from the fact that they cannot be fully parallelized, because their integral nature requires their solution algorithm to start from the stagnation point and march downstream. However, since only wall elements are considered, the computation is significantly faster than that of the Direct CFD Boundary Layer method.

In addition, non-local transition models (like AHD or e^N method) require boundary layer history information. This means that streamlines on the wall surface must also be calculated. This problem essentially does not exist in a two-dimensional simulation, where every body has a single stagnation point and the upper and lower boundary layers can only march towards the trailing on a single direction. However, in three dimensional simulations the computation of streamlines can be quite complex. Three-dimensional geometries often do not have a single stagnation point, but rather a stagnation line. The direction in which the boundary layer moves towards would need to be calculated at every iteration, raising the required computational effort. The computation of streamlines is essential for integral boundary layer solutions when facing three-dimensional problems. Even though at first glance the Direct CFD Boundary Layer does not need the computation of streamlines, due to the fact that boundary layer parameters at a given station can be computed only using flow data in the current normal direction, unfortunately this is valid only when local transition criteria are used. Non-local models will require the computation of streamlines, even in cases where the latter is not necessary for boundary layer definition.

In order to avoid the shortcoming of boundary layer integration and streamline calculation, while maintaining the parallelization of modern CFD solvers, researchers tried to develop frameworks that enable the use of boundary layer transition criteria in transport equation form. Transport equations are utilized by the Navier-Stokes equations and by turbulence models, and they are fully compatible with parallel execution. The main advantage of transport equations is that only local flow data are used in every computational cell. The challenge in transition modeling is to correlate transition onset prediction to local flow data. If this principle is satisfied, then a model is fully suitable for modern CFD solvers without the need for additional boundary layer or streamline interfaces. This step is really important in order to implement transition prediction capabilities in complex geometries.

The first model in this direction was the $\gamma - Re_\theta$ transition model, developed by F.Menter and R.Langtry [91][92][93], which solves two transport equations for the intermittency γ and the transition onset momentum thickness Reynolds number $Re_{\theta t}$. The $\gamma - Re_\theta$ model was revised by F. Menter [94] to only solve one equation for the intermittency, while including some additional modifications that make the use of correlations Galilean invariant. This is referred to as the γ transition model. A recently developed model is the Amplification Factor Transport (AFT) model, developed by C.Coder [95][96][97]. This model is based on a transport equation for the amplification factor, following the principles of the approximate e^N envelope method described by M.Drela [98]. An additional intermittency transport equation is solved, similar to the ones used by the $\gamma - Re_\theta$ and γ models. Newer versions of the model satisfied Galilean invariance. Because the aforementioned transition models do not attempt to model the physics of transition (unlike turbulence models), but instead utilize transition correlations, they are referred to as *correlation transition models*.

A different family of transition models is those that attempt to model the physics, which are called *physics based transition models*. The most notable example is the Laminar Kinetic Energy model (k-k_l-ω model) by Walters et al [99]. This model uses a transport equation for the laminar fluctuation energy which is then linked to the underlying turbulence model through the use of sink and source terms. This way, the laminar kinetic energy can be transferred into the turbulent kinetic energy equation and thus initiate the transition process. However, since the pre-transitional phase can be very different between various transition scenarios (natural, bypass, crossflow), it is quite challenging to tackle all the transition scenarios within a single physics based transition model. Moreover, this model is not as popular as the γ-Re_θ model, having been implemented only in a few solvers. For this reason, assessment of this model was not deemed as a priority and thus it was not implemented in MaPFlow.

In this Chapter, the transition models implemented in MaPFlow are presented. Boundary layer transition implementation is discussed in Section 3.2. Three different approaches to calculate boundary layer parameters are described in Section 3.2.1. The available empirical transition criteria for use within the boundary layer transition framework are presented in Section 3.2.2, whereas the e^N method is described in Section 3.2.3. The strategy that couples the boundary layer transition model and the CFD solver is discussed in Section 3.2.4, whereas Section 3.2.5 and Section 3.2.6 list the detailed interaction of boundary layer transition with the SST and SA turbulence models. Section 3.2.7 gives some important remarks regarding the implementation of the boundary layer transition module whereas Section 3.2.8 lists the steps of the boundary layer transition algorithm. The formulation of the γ-Re_θ, γ, and AFT transition models, as well as their interaction with the available turbulence models, are presented in Section 3.3, Section 3.4, and Section 3.5 respectively.

3.2 Boundary layer transition modeling

In this section the boundary layer transition approach will be discussed. Boundary layer transition prediction consists of two distinct parts:

a. boundary layer calculation

b. application of a transition criterion

Most transition criteria that have been developed for aerodynamic simulations correlate transition onset with boundary layer development. Boundary layer definition is not a straightforward task because the boundary layer edge is not well defined within a computational flow domain. As discussed in Section 5.1, there are two different approaches regarding boundary layer definition and calculation in the context of a Navier-Stokes solver. The first one calculates boundary layer parameters directly from the corresponding flow elements (Direct CFD Boundary Layer - internal method). The second one solves integral boundary layer equations on the wall surface. One option is utilizing the approximate method of Polhausen. A second option is solving the integral momentum and kinetic energy equations. Once the boundary layer parameters are defined, an empirical transition criterion is applied in order to determine whether the flow has transitioned to turbulence.

3.2.1 Boundary layer calculation in a Navier-Stokes solver

Direct integration from the CFD flow data

Boundary layer parameters can be calculated by integration on the normal to the wall direction. Starting from each wall station, the boundary layer thickness δ can be defined as the distance from the wall of the cell that has local velocity parallel to the viscous wall which corresponds to $0.99 \cdot U_e$, where U_e can be obtained by the compressible Bernoulli equation:

$$\frac{U_e}{U_\infty}(s) = \sqrt{1 + \frac{1 - \left(1 + \left[\frac{\tilde{\gamma}}{2} M_\infty^2\right] c_p(s)\right)^{\frac{\tilde{\gamma}-1}{\tilde{\gamma}}}}{\frac{\tilde{\gamma}-1}{2} M_\infty^2}} \tag{3.1}$$

In (3.1), $c_p(s)$ is the local pressure coefficient at the curvilinear distance s from the stagnation point on either side of the airfoil:

$$c_p(s) = \frac{p(s) - p_\infty}{\frac{1}{2}\rho U_\infty^2} \tag{3.2}$$

and $\tilde{\gamma} = 1.4$ is the isentropic constant.

The pressure $p(s)$ on the wall is derived directly from the Navier-Stokes solver. Once the boundary layer thickness is determined, the remaining boundary layer parameters can be calculated using their corresponding integrals for compressible flow:

$$\delta^* = \int_0^\delta \left(1 - \frac{\rho(y)u(y)}{\rho_e U_e}\right) dy \tag{3.3}$$

$$\theta = \int_0^\delta \frac{\rho(y)u(y)}{\rho_e U_e} \left(1 - \frac{u(y)}{U_e}\right) dy \tag{3.4}$$

$$H = \frac{\delta^*}{\theta} \tag{3.5}$$

where ρ_e is the density at the boundary layer edge.

A different approach in defining the boundary layer thickness which does not a priori require U_e is to identify δ as the distance of the cell in the normal direction from the airfoil where the vorticity changes sign. This approach is safer because local velocity in a Navier-Stokes simulation may not reach the $0.99 \cdot U_e$ level when trying to locate the boundary layer edge. Stations too close to the stagnation point should be excluded, as in this region the boundary layer thickness definition criteria (U_e percentage or vorticity sign change) are not expected to work well. In this thesis, stations with local C_p greater than 95% of the stagnation value were excluded. This convention can be safely implemented because disturbances are always damped in this region. For higher angles of attack where the flow is expected to overturn the physical leading edge, additional streamwise refinement is required due to the increased curvature of the airfoil contour.

Implementing this approach on an unstructured solver adds some extra difficulties regarding the normal to the airfoil direction which, unlike in structured solvers, is not readily defined. However, this can be managed by a search algorithm that builds the boundary layer map via element connectivity. Since this search algorithm will only be called once at the start of the simulation, implementation of the approach on structured and unstructured solvers is not expected to differ in regards to computational cost.

Approximate method of Polhausen

An approximation of the boundary layer can be achieved by applying the integral method of Polhausen, as described in [24], which solves a single momentum equation for the boundary layer. Using the definitions of the boundary layer thickness δ and its momentum thickness θ, the Polhausen method introduces the three characteristic parameters:

$$\Lambda = \frac{\rho\delta^2}{\mu}\frac{dU_e}{ds} \tag{3.6}$$

$$K_p = \frac{\rho\theta^2}{\mu}\frac{dU_e}{ds} \tag{3.7}$$

$$Z_p = \frac{\rho\theta^2}{\mu} \tag{3.8}$$

which are related as follows:

$$K_p(\Lambda) = Z_p\frac{dU_e}{ds} = \left(\frac{37}{315} - \frac{\Lambda}{945} - \frac{\Lambda^2}{9072}\right)^2 \Lambda \tag{3.9}$$

Then, the calculation of the laminar boundary layer is based on the solution of the differential equation for Z_p:

$$\frac{dZ_p}{ds} = \frac{F_p(K_p)}{U_e} \tag{3.10}$$

where

$$F_p(K_p) = F_p(\Lambda) = 2\left[\frac{37}{315} - \frac{\Lambda}{945} - \frac{\Lambda^2}{9072}\right]\left[2 - \frac{116}{315}\Lambda + \left(\frac{2}{945} + \frac{1}{120}\right)\Lambda^2 + \frac{2\Lambda^3}{9072}\right] \tag{3.11}$$

The implemented method follows the *Schlichting* [24] proposal to define Z_p through the simplified explicit formula of Walz:

$$Z_p(s) = \frac{0.47}{U_e^6}\int_{s=0}^{s} U_e^5 ds \tag{3.12}$$

After calculating Z_p, the parameter K_p is found numerically from the first part of (3.9), while Λ is determined by solving the second part. The boundary layer parameters δ and θ are then obtained directly from (3.6). The shape factor H is also a function of the main parameter Λ :

$$H = \frac{\frac{3}{10} - \frac{\Lambda}{120}}{\frac{37}{315} - \frac{\Lambda}{945} - \frac{\Lambda^2}{9072}} = H(\Lambda) \tag{3.13}$$

The Polhausen solution for the boundary layer is valid up to the onset of laminar separation. This happens at $H \approx 3.8$ for the laminar boundary layer velocity profiles, although laminar separation appears for even lower shape factor values in Navier-Stokes solvers. If laminar separation occurs and transition has not yet been predicted then the transition location is set to the laminar separation point, as the method cannot reliably solve the boundary layer inside the bubble.

Boundary layer momentum and kinetic energy equations

This method has been succesfully used by Drela and Giles [98] in a viscous-inviscid interaction solver. Implementation in a Navier-Stokes solver has been carried out by Johansen et al [83]. The model uses a two equation integral model based on dissipation closure.

The first equation is the von Karman integral momentum equation, as follows:

$$\frac{d\theta}{ds} + (2+H)\frac{\theta}{U_e}\frac{dU_e}{ds} = \frac{C_f}{2} \tag{3.14}$$

where C_f is the skin friction coefficient.

The second equation is the kinetic energy equation and is given by:

$$\theta \frac{dH^*}{ds} + H^*(1-H)\frac{\theta}{U_e}\frac{dU_e}{ds} = 2C_D - H^*\frac{C_f}{2} \tag{3.15}$$

where H^* is the kinetic energy shape parameter and C_D is the dissipation coefficient.

For laminar flows, the two first order differential equations are solved using the following closure relationships obtained from the Falkner-Skan family [100] for H^*, C_f and C_D respectively:

$$H^* = \begin{cases} 1.515 + 0.076\frac{(4-H)^2}{H}, & H < 4 \\ 1.515 + 0.040\frac{(H-4)^2}{H}, & H > 4 \end{cases} \tag{3.16}$$

$$Re_\theta \frac{C_f}{2} = -0.067 + 0.01977\frac{(7.4-H)^2}{(H-1)} \tag{3.17}$$

$$Re_\theta \frac{2C_D}{H^*} = \begin{cases} 0.207 + 0.00205(4-H)^{5.5}, & H < 4 \\ 0.207 - 0.003\frac{(H-4)^2}{(1+0.02(H-4)^2)}, & H > 4 \end{cases} \tag{3.18}$$

Using (3.1), (3.14) and (3.15) can be solved directly using a Newton-Raphson method. From the stagnation point and up to the point of laminar separation, the direct approach is employed and the equations are solved with U_e as input and with respect to θ and H. When approaching separation, which takes place at $H \approx 3.8$, the direct solution approach becomes ill-conditioned due to the fact that a single C_f value corresponds to two different velocities: one positive and one negative. To overcome this difficulty, the equations are solved inversely. By taking C_f from the Navier-Stokes solver, $H_{inverse}$ is computed using (3.17) and the equations are solved with respect to θ and U_e.

Direct approach

The boundary layer equations are discretized using a 2$^{\text{nd}}$ order central difference scheme [83]. With U_e being directly calculated by the solver, the boundary layer parameters θ and H are computed by solving (3.14) and (3.15) directly. The discretized equations for the direct solution take the form:

$$f_1 = \frac{\theta_i - \theta_{i-1}}{s_i - s_{i-1}} + \left(2 + \frac{H_i - H_{i-1}}{2}\right)\frac{\theta_i + \theta_{i-1}}{U_{e_i} + U_{e_{i-1}}}\frac{U_{e_i} - U_{e_{i-1}}}{s_i - s_{i-1}} - \frac{C_f}{2}|_{i-\frac{1}{2}} = 0 \tag{3.19}$$

$$f_2 = \frac{\theta_i + \theta_{i-1}}{2}\frac{dH^*}{dH}\frac{H_i - H_{i-1}}{s_i - s_{i-1}} + H^*|_{i-\frac{1}{2}}\left(1 - \frac{H_i + H_{i-1}}{2}\right)\frac{\theta_i + \theta_{i-1}}{U_{e_i} + U_{e_{i-1}}}\frac{U_{e_i} - U_{e_{i-1}}}{s_i - s_{i-1}}$$
$$- 2C_D|_{i-\frac{1}{2}} + H^*|_{i-\frac{1}{2}}\frac{C_f}{2}|_{i-\frac{1}{2}} = 0 \tag{3.20}$$

where H^*, $\frac{C_f}{2}$ and $2C_D$ are given from (3.16)-(3.18).

The chain rule used for the discretization of H^* is as follows:

$$\frac{\partial H^*}{\partial s} = \frac{\partial H^*}{\partial H}\frac{\partial H}{\partial s} \tag{3.21}$$

where

$$\frac{\partial H^*}{\partial H} = \begin{cases} 0.076\left(1 - \frac{16}{\left(\frac{H_i + H_{i-1}}{2}\right)^2}\right), & H < 4 \\ 0.040\left(1 - \frac{16}{\left(\frac{H_i + H_{i-1}}{2}\right)^2}\right), & H > 4 \end{cases} \tag{3.22}$$

The Newton-Raphson equivalent of the system of equations with respect to θ and H takes the form:

$$\begin{bmatrix} \frac{\partial f_1}{\partial \theta_i} & \frac{\partial f_1}{\partial H_i} \\ \frac{\partial f_2}{\partial \theta_i} & \frac{\partial f_2}{\partial H_i} \end{bmatrix} \begin{bmatrix} \delta\theta_i \\ \delta H_i \end{bmatrix} = - \begin{bmatrix} f1 \\ f2 \end{bmatrix} \tag{3.23}$$

where

$$\frac{\partial f_1}{\partial \theta_i} = \frac{1}{s_i - s_{i-1}} + \left(2 + \frac{H_i + H_{i-1}}{2}\right) \frac{U_{e_i} - U_{e_{i-1}}}{U_{e_i} + U_{e_{i-1}}} \frac{1}{s_i - s_{i-1}} - \frac{\partial \frac{C_f}{2}}{\partial \theta_i} \tag{3.24}$$

$$\frac{\partial f_1}{\partial H_i} = \frac{1}{2} \frac{\theta_i - \theta i - 1}{U_{e_i} + U_{e_{i-1}}} \frac{U_{e_i} - U_{e_{i-1}}}{s_i - s_{i-1}} - \frac{\partial \frac{C_f}{2}}{\partial H_i} \tag{3.25}$$

$$\begin{aligned} \frac{\partial f_2}{\partial \theta_i} = & \frac{1}{2} \frac{\partial H^*}{\partial H} \frac{H_i - H_{i-1}}{s_i - s_{i-1}} \\ & + H^*|_{i-\frac{1}{2}} \left(1 - \frac{H_i + H_{i+1}}{2}\right) \frac{U_{e_i} - U_{e_{i-1}}}{U_{e_i} + U_{e_{i-1}}} \frac{1}{s_i - s_{i-1}} \\ & - \frac{\partial 2 C_D}{\partial \theta_i} + H^*|_{i-\frac{1}{2}} \frac{\partial \frac{C_f}{2}}{\partial \theta_i} \end{aligned} \tag{3.26}$$

$$\begin{aligned} \frac{\partial f_2}{\partial H_i} = & \frac{\theta_i + \theta_{i-1}}{2} \left(\frac{dH^*}{dH} - 0.076 \cdot 16 \cdot 2 \frac{1}{\left(\frac{H_i + H_{i-1}}{2}\right)^3} \frac{H_i - H_{i-1}}{s_i - s_{i-1}} \right) \\ & + \frac{\theta_i - \theta_{i-1}}{U_{e_i} + U_{e_{i-1}}} \frac{U_{e_i} - U_{e_{i-1}}}{s_i - s_{i-1}} \left(-\frac{H^*}{2}|_{i-\frac{1}{2}} + \frac{\partial H^*}{\partial H} \left(1 - \frac{H_i + H_{i-1}}{2}\right) \right) \\ & - \frac{\partial 2 C_D}{\partial H_i} + \frac{\partial H^*}{\partial H} \frac{C_f}{2} + H^*|_{i-\frac{1}{2}} \frac{\partial \frac{C_f}{2}}{\partial H_i} \end{aligned} \tag{3.27}$$

The derivatives of $\frac{C_f}{2}$ and C_D are derived directly from (3.17)-(3.18). The initial solution for θ to start the iterative process is given by the approximate Walz formula (3.12) for the momentum thickness.

Inverse approach

When the boundary layer approaches separation, the equations are solved inversely with respect to θ and U_e. The skin friction C_f is obtained from the Navier-Stokes solution and is used in (3.17) to calculate an inverse shape factor, $H_{inverse}$. Using (3.19) and (3.20), the following matrix for the inverse problem is obtained:

$$\begin{bmatrix} \frac{\partial f_1}{\partial \theta_i} & \frac{\partial f_1}{\partial U_{e_i}} \\ \frac{\partial f_2}{\partial \theta_i} & \frac{\partial f_2}{\partial U_{e_i}} \end{bmatrix} \begin{bmatrix} \delta \theta_i \\ \delta U_{e_i} \end{bmatrix} = - \begin{bmatrix} f1 \\ f2 \end{bmatrix} \tag{3.28}$$

where

$$\frac{\partial f_1}{\partial \theta_i} = \frac{1}{s_i - s_{i-1}} + \left(2 + \frac{H_i + H_{i-1}}{2}\right) \frac{U_{e_i} - U_{e_{i-1}}}{U_{e_i} + U_{e_{i-1}}} \frac{1}{s_i - s_{i-1}} \tag{3.29}$$

$$\frac{\partial f_1}{\partial U_{e_i}} = \left(2 + \frac{H_i + H_{i-1}}{2}\right) \frac{\theta_i + \theta_{i-1}}{s_i - s_{i-1}} \frac{2 U_{e_{i-1}}}{(U_{e_i} + U_{e_{i-1}})^2} \tag{3.30}$$

$$\begin{aligned} \frac{\partial f_2}{\partial \theta_i} = & \frac{1}{2} \frac{\partial H^*}{\partial H} \frac{H_i - H_{i-1}}{s_i - s_{i-1}} \\ & + H^*|_{i-\frac{1}{2}} \left(1 - \frac{H_i + H_{i+1}}{2}\right) \frac{U_{e_i} - U_{e_{i-1}}}{U_{e_i} + U_{e_{i-1}}} \frac{1}{s_i - s_{i-1}} - \frac{\partial 2 C_D}{\partial \theta_i} \end{aligned} \tag{3.31}$$

$$\frac{\partial f_2}{\partial U_{e_i}} = \frac{\theta_i + \theta_{i-1}}{s_i - s_{i-1}} H^*|_{i-\frac{1}{2}} \left(1 - \frac{H_i + H_{i+1}}{2}\right) \frac{2 U_{e_{i-1}}}{(U_{e_i} + U_{e_{i-1}})^2} - \frac{\partial 2 C_D}{\partial U_{e_i}} \tag{3.32}$$

The derivatives of $\frac{C_f}{2}$ and C_D are again computed using (3.17) and (3.18).

3.2.2 Transition criteria

This section contains the available empirical transition criteria that can be used in the context of boundary layer transition. The prediction accuracy of the criteria is assessed separately in Section 5.4.2.

Michel

A simple, local transition prediction model is the empirical criterion by Michel [81], which has been proven to yield satisfactory results for many airfoil flows [101]. The Michel criterion is based on experimental data taken over flat plate flow with almost zero pressure gradient and correlates local values of momentum thickness to transition onset. It simply states that transition takes place where

$$Re_{\theta,tr} = 1.174 \left(1 + \frac{22400}{Re_{x,tr}}\right) Re_{x,tr}^{0.46} \tag{3.33}$$

At first glance it seems that the model does not include pressure gradient effects. However, the effect of the pressure gradient is included in Re_θ.

Granville/Schlichting

According to Schlichting [24], the transition zone is defined as the intermittent area between the point of instability (i) and the point of transition to turbulence (tr). He assumed that instability appears when the Reynolds number based on the displacement thickness δ^* reaches an empirical critical value $Re_{\delta^*,crit}$, which is related to the local Polhausen parameter $\Lambda(s)$:

$$Re_{\delta^*} = \frac{U_e \cdot \delta^*}{\nu} \geq Re_{\delta^*,crit}(\Lambda)(= Re_{\delta^*,crit}(s)) \tag{3.34}$$

$$\Lambda(s) = \frac{\rho\delta^2}{\mu}\frac{dU_e}{ds}(s) \tag{3.35}$$

Values of Re_{δ^*} with respect to Λ are given in Table 3.1.

Table 3.1: *Critical Re_{δ^*} with respect to Λ*

Λ	-5.769	-2.538	-0.821	2.231	3.538	4.923	6.025	6.897	8.460
$Re_{\delta^*,crit}$	100	200	400	2500	5000	8000	10000	11000	11830

The location of the transition point is identified as the point where the difference between the local Re_θ number and the one at the instability point exceeds an empirical critical value. According to the experimental data of Graville [102] regarding boundary layers under pressure gradients, this critical value is a function of the mean value of the parameter $\bar{K}_p$ between the transition and instability points:

$$\delta Re_{\theta,crit} = \left(\frac{U_e\theta}{\nu}\right)_{tr} - \left(\frac{U_e\theta}{\nu}\right)_{i} = \delta Re_{\theta,crit}(\bar{K}_p) \tag{3.36}$$

with

$$\bar{K}_p = \frac{1}{s_{tr} - s_i}\int_{s_i}^{s_{tr}} K_p(s)ds \tag{3.37}$$

$$K_p = \frac{\rho\theta^2}{\mu}\frac{dU}{ds} \tag{3.38}$$

Values of this function are given in Table 3.2.

Table 3.2: *Critical Re_θ difference with respect to $\bar{K}_p$*

$\bar{K}_p$	0.0242	0.0212	0.0145	0.0104	0.0056	0.0	-0.01	-0.02	-0.03
$\delta Re_{\theta,crit}$	1990	1790	1390	1190	993	820	598	499	455

Arnal-Habiballah-Delcourt (AHD)

The AHD criterion [87] is based on systematic stability calculations and was derived from N-factor stability curves computed for attached self-similar Falkner-Skan velocity profiles. The curves are expressed as:

$$N = N(Re_\theta - Re_{\theta,crit}, K_p) \tag{3.39}$$

with $Re_{\theta,crit}$ being the critical momentum thickness Reynolds number where the first instabilities start to grow. The criterion is based on the averaged Polhausen parameter K_p, similarly to the Schlichting-Granville criterion:

$$\bar{K_p} = \frac{1}{s_{tr} - s_i} \int_{s_i}^{s_{tr}} K_p(s) ds \tag{3.40}$$

$$K_p = \frac{\rho\theta^2}{\mu} \frac{dU}{ds} \tag{3.41}$$

with the criterion itself being:

$$Re_{\theta,tr} - Re_{\theta,crit} = -206 \cdot exp(25.7\bar{K_p})[ln(16.8Tu) - 2.77\bar{K_p}] \tag{3.42}$$

In (3.42), local Tu is used in its percent form. The criterion is activated after detecting a critical location which is set where:

$$Re_\theta \geq Re_{\theta,crit} = exp(\frac{52}{H} - 14.8) \tag{3.43}$$

This formulation was developed for incompressible flow. However, the AHD criterion has been extended to flows up to Mach 4 [88]. In that case, (3.42) and (3.43) become:

$$Re_{\theta,tr} - Re_{\theta,crit} = -A \cdot exp(B\bar{K_p})[ln(CTu) - D\bar{K_p}] \tag{3.44}$$

$$Re_\theta \geq Re_{\theta,crit} = exp(\frac{E}{H} - F) \tag{3.45}$$

where parameters A to F are functions of the boundary layer edge Mach number M_e:

$$\begin{aligned}
A &= 98.64M_e^3 - 356.44M_e^2 + 117.13M_e - 236.69 \\
B &= -13.04M_e^4 + 38.5M_e^3 - 30.07M_e^2 + 10.89M_e + 22.7 \\
C &= 0.21M_e^3 + 4.79M_e^2 - 1.76M_e + 22.56 \\
D &= -3.48M_e^4 + 6.26M_e^3 - 3.45M_e^2 + 0.23M_e + 12 \\
E &= 0.6711M_e^3 - 0.7379M_e^2 + 0.167M_e + 51.904 \\
F &= 0.3016M_e^5 - 0.7061M_e^4 + 0.3232M_e^3 + 0.0083M_e^2 - 0.1745M_e + 14.6
\end{aligned} \tag{3.46}$$

3.2.3 e^N method

The e^N method for transition prediction is based on linear stability analysis using the Orr-Sommerfeld equations to determine the growth of spatially developing TS waves. The method places transition onset where the amplitude of the most unstable frequency exceeds the initial unstable amplitude by the factor e^N. The critical value for N (N_{crit}) is set by the user, with values typically ranging from 8 to 10, with $N_{crit} = 9$ usually used to simulate natural transition, however N_{crit} can also be related to the freestream turbulence intensity Tu by the formula proposed by Mack (taken from [103]):

$$N_{crit} = -8.43 - 2.4 \cdot ln(Tu) \tag{3.47}$$

Approximate envelope approach

This approach was first implemented in the viscous-inviscid analysis tool ISES [98] by Drela et al. Using the Falkner-Skan velocity profile family, the Orr-Sommerfeld equation was solved for the spatial amplification rates of a wide range of shape factors and unstable frequencies. The envelopes of the integrated rates were approximated by straight lines as follows:

$$\tilde{N} = \frac{d\tilde{N}}{dRe_\theta}(H)[Re_\theta - Re_{\theta_0}(H)] \tag{3.48}$$

where the slope $d\tilde{N}/dRe_\theta$ and the critical Reynolds number Re_{θ_0} are approximated by the following empirical formulas:

$$\frac{d\tilde{N}}{dRe_\theta} = 0.01[2.4H - 3.7 + 2.5tanh(1.5H - 4.65)]^2 + 0.25]^{1/2} \tag{3.49}$$

$$log_{10}Re_{\theta_0} = \left(\frac{1.415}{H-1} - 0.489\right) tanh\left(\frac{20}{H-1} - 12.9\right) + \frac{3.295}{H-1} + 0.44 \tag{3.50}$$

When similar flows are considered, H is constant and Re_θ is uniquely related to the streamwise coordinate s. Thus, (3.48) gives the amplification factor $\tilde{N}$ as a function of s. For nonsimilar flows, the amplification factor is calculated by integrating the local amplification factor downstream from the point of instability. The integration with respect to Re_θ is expressed as follows:

$$\tilde{N} = \int_{Re_{\theta_0}}^{Re_\theta} \frac{d\tilde{n}}{dRe_\theta} dRe_\theta \tag{3.51}$$

However, (3.51) is not suitable for determining transition in separation bubbles since Re_θ hardly varies in the laminar portion of a typical bubble and thus (3.51) implies that very little amplification will occur inside the separation bubble, which is not realistic. A better approach is to integrate the amplification factor in the spatial direction s.

The spatial amplification factor with respect to s is determined as follows:

$$\frac{d\tilde{N}}{ds} = \frac{d\tilde{N}}{dRe_\theta}\frac{dRe_\theta}{ds} = \frac{d\tilde{N}}{dRe_\theta}\frac{1}{2}\left(\frac{s}{U_e}\frac{dU_e}{ds} + 1\right)\frac{\rho_e U_e \theta^2}{\mu_e s}\frac{1}{\theta} \tag{3.52}$$

By using the Falkner-Skan velocity profile family, the following empirical relations were derived:

$$\frac{\rho_e U_e \theta^2}{\mu_e s} \equiv l(H) = \frac{6.54H - 14.07}{H^2} \tag{3.53}$$

$$\frac{s}{U_e}\frac{dU_e}{ds} \equiv m(H) = \left(0.058\frac{(H-4)^2}{H-1} - 0.068\right)\frac{1}{l(H)} \tag{3.54}$$

The amplification factor with respect to s is thus a function of H and θ:

$$\frac{d\tilde{N}}{ds}(H,\theta) = \frac{d\tilde{N}}{dRe_\theta}(H)\frac{m(H)+1}{2}l(H)\frac{1}{\theta} \tag{3.55}$$

and the explicit expression for $\tilde{n}$ becomes:

$$\tilde{N}(s) = \int_{s_0}^{s} \frac{d\tilde{N}}{ds} ds \tag{3.56}$$

where s_0 is the point where $Re_\theta = Re_{\theta_0}$.

Orr-Sommerfeld stability database approach

A different approach in tracking TS waves was presented by H. Stock and E. Degenhart [104] who suggested building a database within which instability data can be evaluated. The main idea is that a discrete set of results to the Orr-Sommerfeld equations is representative for all possible laminar velocity profiles and for all relevant disturbance frequencies. For various values of the reduced perturbation frequency f, the N-factor can be extracted from every frequency as:

$$N(H, Re_\theta, f) = -\int_{s_0}^{s_{tr}} \alpha_i ds \tag{3.57}$$

where s_0 is the point where the tracked wave enters the unstable zone, which occurs when the imaginary part of the amplitude -α_i, the spatial amplification rate- becomes negative and s_{tr} is the point where the local integrated N-factor exceeds the preset critical value. Tracking this amplification rate for a wide range of frequencies results in a number of N curves, the envelope of which forms a N_{max} curve which can be used to determine the point of transition. In the implemented version of the method, the Orr-Sommerfield database from the XFOIL code [3] is used. By utilizing the database, α_i in (3.57) can be evaluated as a function of the boundary layer parameters H and Re_θ along with the normalized circular frequency ω:

$$\alpha_i = \alpha_i(H, Re_\theta, \omega) \tag{3.58}$$

$$\omega = \frac{2\pi f \theta}{U_e} \tag{3.59}$$

3.2.4 Activating turbulence - Transition location prescription

In regards to turbulence in the context of aerodynamic simulations, the region of interest is close to the solid surface. The presence of turbulence in the freestream (far from the solid surface) does not affect the overall aerodynamic results. This leads to defining the flow as turbulent everywhere, while containing the laminar region close to the airfoil.

The reason for defining the region as turbulent everywhere except for the "small" laminar region close to the solid surface is for practical reasons. Defining the laminar region everywhere would pose difficulties in appropriately defining the turbulent region, especially for multi-element airfoils or multiple body configurations. Additionally, since in most applications the inflow turbulent quantities correspond to turbulent viscosity orders of magnitude smaller than the laminar viscosity and in the absence of turbulence production in the farfield region, the aforementioned definition of the laminar region should not introduce numerical errors. Finally, in cases where inflow turbulence is considered, the confinement of the laminar flow in the near wall region enables the convection of the inflow turbulence properties.

For boundary layer transition simulations, the laminar/transitional/turbulent region identification is first carried out on the solid surface by calculating the boundary layer parameters and then applying a transition criterion, as discussed in Section 3.2.1 and Section 3.2.2. This identification needs to be further extended beyond the solid surface along the normal to the wall direction, in order to define the laminar region in the computational domain. A zone of width $d_{laminar}$ is defined, where $d_{laminar}$ represents the maximum distance from the nearest wall surface that a flow field point can be treated as laminar in the simulation. Beyond this maximum distance, all points are treated as turbulent. The value of this maximum distance can either be set by the user of computed by the solver based on the local laminar boundary layer thickness. In either case, $d_{laminar}$ is subject to two limitations:

a. The local value of the limiting distance must be greater than the local laminar boundary layer thickness, $d_{laminar} > max(\delta_{i=1,N_{wall}})$, with N_{wall} being the total number of airfoil points

b. In case of multi-element configurations, the laminar regions of downstream elements must be small enough to not influence the turbulent regions of upstream elements and by that prevent loss of information in turbulent wakes

When the Direct boundary layer approach is considered (Section 3.2.1), the boundary layer thickness is directly calculated. For the Polhausen method (Section 3.2.1), the boundary layer thickness is estimated via (3.6). However, when solving the two integral equations for the boundary layer (Section 3.2.1), boundary layer thickness is not explicitly calculated. This can be managed by augmenting the solution with (3.6) and (3.9). With known θ from (3.14), Z_p is also known and by means of (3.6) K_p and Λ can be calculated. Λ gives an approximation of the local laminar boundary layer thickness δ. The maximum local boundary layer thickness is used to calculate the extent of the laminar region around the airfoil:

$$d_{laminar} = a \cdot \delta \tag{3.60}$$

with $1 < a < 1.5$ being a safety factor that increases the laminar region in case the approximation underpredicts the laminar boundary layer thickness. It was found that as long as $d_{laminar}$ is greater than the local boundary thickness, the predicted aerodynamic results remain the same. Example of a laminar region and a boundary layer vector close-up on the upper transition location are shown in fig. 3.1 with the extent of the laminar region shown in blue.

Turbulence production is handled with the help of an additional intermittency variable γ_{BL}, which interacts with the turbulence models. The variable γ_{BL} is defined in the following way:

a. For every mesh cell, the distance to the wall and the closest wall element are both known by the solver.

b. If the cell is located further than the maximum local boundary layer thickness, a turbulent flag is assigned to it. This corresponds to $\gamma_{BL} = 1$.

c. If the cell is located closer than the maximum local boundary layer thickness, it takes the laminar/turbulent flag of the corresponding closest wall element. If it is a laminar wall element, $\gamma_{BL} = 0$, whereas for a turbulent wall element $\gamma_{BL} = 1$.

It should be noted here that for the results presented in this thesis "point transition" was assumed. This means that upstream from the transition location all points are treated as laminar ($\gamma_{BL} = 0$), whereas downstream from the transition location all stations are treated as turbulent ($\gamma_{BL} = 1$). However, in transitional flows there are intermediate regions where the flow is not fully laminar but has not yet fully transitioned to turbulence. This corresponds to $0 < \gamma_{BL} < 1$. The length of this intermediate region can be estimated via a transition length model like that of Chen et al [105] of that of Narasimha [106]. The absence of transition length will slightly raise predicted drag levels. However, since the predicted intermittent regions are usually of low length, differences in overall aerodynamic performance will be insignificant.

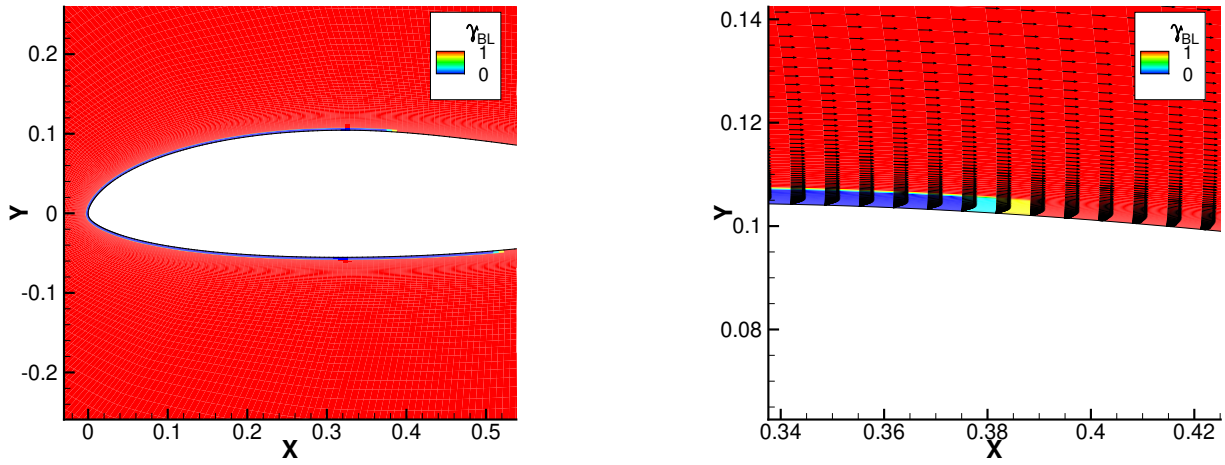

(a) *Laminar region* **(b)** *Upper boundary layer close-up*

Figure 3.1: *Example of the laminar region around the NLF(1)-0416 airfoil at* $Re = 4\ x\ 10^6$, $Ma_\infty = 0.1$, $Tu_\infty = 0.05\%$

3.2.5 Interaction with the k-ω SST turbulence model

The boundary layer transition routine interacts with the SST turbulence model (Section 2.6.2) by modifying the source and destruction term of (2.144) as follows:

$$\tilde{P}_k = \gamma_{BL} P_k \tag{3.61}$$

$$\tilde{D}_k = min\left(max\left(\gamma_{BL}, 0.1\right), 1.0\right) D_k \tag{3.62}$$

where P_k and D_k are the original production and destruction terms of the SST model. This approach was adopted based on the original formulation for the interaction of the intermittency variable used in the γ-Re_θ model and the SST production terms (see Langtry et al [91]).

3.2.6 Interaction with the Spalart-Allmaras turbulence model

The boundary layer transition model interacts with the Spalart-Allmaras turbulence model (Section 2.6.1) by modifying the f_{t2} function in (2.138):

$$f_{t2} = c_{t3}[1 - \gamma_{BL}] \tag{3.63}$$

The function f_{t2} has a limited basin of attraction to laminar flow. Excessive values of freestream modified viscosity ratio may overwhelm the function [70], thus for simulations with free transition the freestream modified viscosity ratio is limited as:

$$\frac{\tilde{\nu}_\infty}{\nu_\infty} \leq 0.1 \tag{3.64}$$

3.2.7 Remarks on the implementation of boundary layer transition modeling

Wall face sorting

The wall faces are sorted using face connectivity at the start of the simulation. This only needs to be done once and works for both static and moving/deformable meshes, since face indexes do not change during the

simulation.

For two-dimensional configurations, the connectivity criterion between two wall faces is one shared node. Normal vectors to the faces are used in order to ensure that the faces are sorted in clockwise order. For three-dimensional configurations, the chordwise, normal and spanwise directions also need to be given as input. The final sorting is carried out in two-dimensional sections. Starting from a random face, the faces that form a two-dimensional section in clockwise order are located. Thus, the connectivity criterion is two shared nodes in the chordwise direction. The sorting then moves to the next spanwise section, by utilizing the connectivity criterion of two shared nodes in the spanwise direction.

In both two and three-dimensional cases, the sorted faces are then re-indexed. The first face on the lower side starting from the trailing edge is always the first face (index= 1), while the rest are indexed accordingly assuming clockwise order.

For the definition of the leading and trailing edges, the following algorithm is employed:

a. For every wall station in a two-dimensional section, calculate distance from all other stations.

b. Locate the maximum distance between two wall stations. These two stations define the biggest chord and will be used to approximate the leading and trailing edges.

c. Between these two stations, set leading and trailing edge according to the flow direction. The employed convention is that the leading edge is the one located upstream.

Flow initialization

When using the Polhausen method or the two integral boundary layer equations for boundary layer calculation (see Section 3.2.1), the flow around the airfoil can be initialized as either turbulent or laminar. This is possible because the C_p contour is used as input. Laminar and turbulent C_p levels may differ, however the transition method can utilize both leading to slightly different transition locations. However, when Direct CFD boundary layer integration is considered the flow around the airfoil must be initialized as laminar because the turbulent boundary layer, which will be calculated in case of turbulent flow, cannot be used to predict transition. For laminar flow, the initial transition locations are set far downstream (close to the trailing edge).

Laminar separation check

At the initial phase of the simulation, the wall faces are checked for laminar separation ($C_f < 0$ in the laminar region). This process starts at a prescribed number of solver iterations. In MaPFlow, this number was set to 500 iterations, during which the flow on the wall surface has most likely started to develop. Nevertheless, this number can be set to any value. However, laminar separation is not expected to develop during the very early transient phase of the simulation, thus checking for laminar separation at lower stages of the simulation is most likely redundant.

If laminar separation is detected, the separation point is used as an approximation of the transition location. The laminar separation location is underrelaxed as:

$$\tilde{x}_{sep}^{u,l}(iter^k) = x_{sep}^{u,l}(iter^k) + a \cdot (x_{sep}^{u,l}(iter^k) - x_{sep}^{u,l}(iter^{k-1})) \tag{3.65}$$

with $0 < a < 0.5$.

Under relaxing prevents the laminar separation from being placed too far upstream in during the converging phase. After the initial check at 500 iterations, the check is repeated every 100 iterations. There is no need to repeat the search at every iteration, since in that case the flow will not have changed drastically. If laminar separation is detected, it is again underrelaxed. The Navier-Stokes equations are iterated until the lift coefficient has reached an almost constant value. From then on, the boundary layer module is called.

Wall face repaneling in the case of integral boundary layer methods

At the initial call of the boundary layer transition module, the wall geometry is repaneled to a specified number of surface panels. Based on what was presented in Section 3.2.1 for the integral methods, the curvilinear distance ds between two airfoil stations is mostly present on the denominator of fractions. Very fine meshes will result in very low ds values that may lead to convergence problems during the iterative boundary layer solution. This step was therefore necessary in order to ensure that the boundary layer transition module can converge even on very fine meshes. It should be noted that the *Direct CFD boundary layer* approach does not require repaneling.

The default number of panels is 140. The paneling routine starts from the wall points of the Navier-Stokes simulation, which serve as the starting buffer geometry. It first searches for sharp edges in the buffer geometry, which indicate the presence of blunt trailing edges. These are excluded from paneling. Since the flow on sharp edges will separate, there is no need for boundary calculation beyond those points. The routine then applies a

b-spline curve on the remaining buffer points, forming the panel geometry. More panels are placed close to the stagnation point, since at that region the velocity gradients are higher.

Calling the boundary layer module

The boundary layer transition module is called every 500 iterations. The module utilizes either the initial Navier-Stokes geometry (in the case of *Direct CFD boundary layer*) or the repaneled geometry (in the case of integral methods).

When integral boundary layer methods are considered, input flow quantities on the buffer geometry are interpolated on the panel geometry (C_p, C_f, ρ, μ_L, boundary layer edge velocity U_e calculated via (3.1), and their corresponding gradients, all derived from the Navier-Stokes simulation).

The boundary layer solution marches from the stagnation point towards the trailing edge on both sides. For each station, after calculating the boundary layer parameters, the chosen transition criterion is examined. When the criterion is met, the boundary layer transition module stops. The predicted transition locations $x_{tr}^{u,l}(iter^k)$ are underrelaxed in the same manner as the laminar separation ones:

$$\tilde{x}_{tr}^{u,l}(iter^k) = x_{tr}^{u,l}(iter^k) + a \cdot (x_{tr}^{u,l}(iter^k) - x_{tr}^{u,l}(iter^{k-1})) \tag{3.66}$$

with $0 < a < 0.5$.

Underrelaxation damps the transition point shift and prevents too abrupt changes that may possibly hold the transition location from converging. At the last iteration, $a = 0$.

Checking for transition convergence

The boundary layer transition module is checked for convergence as follows:

$$\Delta\tilde{x}_{tr}^{u,l} = |\tilde{x}_{tr}^{u,l}(cyc^k) - \tilde{x}_{tr}^{u,l}(cyc^{k-1})| < \epsilon \tag{3.67}$$

$$\epsilon = c \cdot chord \tag{3.68}$$

with c being a percentage of the local chord (usually $1e^{-5} < c < 1e^{-3}$). If the convergence criterion is met for both sides, the iterations for the transition locations are stopped.

3.2.8 Boundary layer transition modeling algorithm

The boundary layer transition module algorithm consists of the following steps:

1. **Sort wall faces.**
2. **Set initial flow conditions and start the simulation.**
3. **After a prescribed number of iterations, start checking for laminar separation on the wall surface.**
4. **Underrelax laminar separation locations and set as a transition location approximation.**
5. **Flag laminar/turbulent wall stations (0 or 1, respectively) and define γ_{BL}, based on what was discussed in Section 3.2.4.**
6. **Continue the simulation until a converged solution has been obtained, repeating steps 3-5 at a fixed step of iterations.**
7. **If the solution has converged, continue; else go to step 6.**
8. **In case of integral boundary layer methods, repanel wall geometry.**
9. **Call the boundary layer module to solve the boundary layer and apply the transition criterion.**
10. **Underrelax transition locations.**
11. **Flag laminar/turbulent wall stations (0 or 1, respectively) and define γ_{BL}, based on what was discussed in Section 3.2.4.**
12. **Check module for convergence.**
13. **If convergence is reached, stop calling the transition module; else go to step 9.**

3.3 γ-Re_θ transition model

The first version of the model implemented in MaPFlow is the one of Langtry and Menter, originally presented in [91], and then further modified in [107][92][93][108]. The main idea behind the model is that the vorticity Reynolds number, concept first presented by Van Driest and Blumer [109], can be used to provide a link between the transition onset momentum thickness Reynolds number $Re_{\theta t}$ obtained from an empirical correlation and the local boundary layer quantities. This assumption helps the model avoid the need for explicit boundary layer integration in order to predict transition. This idea was first presented by Menter [110].

The vorticity or strain-rate Reynolds number used in the model is defined as:

$$Re_\nu = \frac{\rho d_w^2}{\mu}\left|\frac{\partial u}{\partial y}\right| = \frac{\rho d_w^2}{\mu} S \tag{3.69}$$

where d_w is the distance from the nearest wall and S the strain rate magnitude. (3.69) suggests that Re_ν can be computed at every cell because it depends on density, viscosity, wall distance, and shear-strain rate.

A scaled profile of the vorticity Reynolds number is shown in fig. 3.2 (reproduced from Langtry [92]) for a Blasius laminar boundary layer. The profile is scaled in order to have a maximum of one inside the boundary layer. This is achieved by dividing the Blasius velocity profile by the corresponding momentum thickness Reynolds number and a constant of 2.193. This essentially means that the maximum of the profile is proportional to the momentum thickness Reynolds number and can be related to the transition correlations via the formula:

$$Re_\theta = \frac{max(Re_\nu)}{2.193} \tag{3.70}$$

Based on this observation, a general, locally defined framework can be built, which can incorporate correlation-based transition models in a Navier-Stokes simulation.

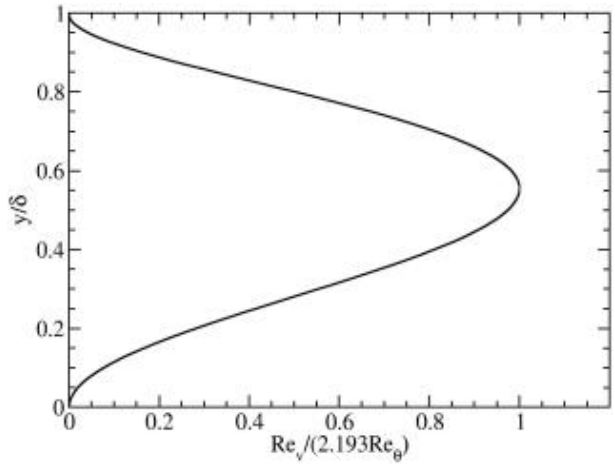

Figure 3.2: *Scaled vorticity Reynolds number Re_v profile in a blasius boundary layer*

The γ-Re_θ model is based on a transport equation for the intermittency γ, which can be used to trigger transition locally. In addition to γ, a second transport equation is solved for the transition onset momentum-thickness Reynolds number $\tilde{Re}_{\theta t}$. This is required to capture the non-local influence of the turbulence intensity. The second transport equation is an essential part of the model as it ties the empirical correlation to the onset criteria in the intermittency equation. The correlation used by the authors is a modified version of the Abu-Ghannam and Shaw correlation [85], although the model can utilize any locally defined correlation.

3.3.1 Transport equation for the intermittency (γ)

The transport equation for the intermittency γ reads:

$$\frac{\partial(\rho\gamma)}{\partial t} + \frac{(\rho U_j \gamma)}{\partial x_j} = P_\gamma - E_\gamma + \frac{\partial}{\partial x_j}\left[\left(\mu + \frac{\mu_t}{\sigma_f}\right)\frac{\partial \gamma}{\partial x_j}\right] \tag{3.71}$$

with the source term defined as:

$$P_\gamma = F_{length}\left[\gamma F_{onset}\right]^{0.5} c_{\alpha 1}\rho S\left(1 - c_{e1}\gamma\right) \tag{3.72}$$

where S is the strain-rate magnitude. F_{length} is an empirical correlation that controls the length of the transition region, and F_{onset} controls the transition onset location. Both are dimensionless functions that are used to

control the intermittency equation in the boundary layer. The destruction/relaminarization source is defined as follows:

$$E_\gamma = c_{\alpha 2}\rho\Omega\gamma F_{turb}\left(c_{e2}\gamma - 1\right) \tag{3.73}$$

where Ω is the vorticity magnitude.

The transition onset is controlled by the following functions:

$$\begin{aligned}
F_{onset} &= max\left(F_{onset2} - F_{onset3}, 0\right) && (3.74)\\
F_{onset3} &= max\left(1 - \left(\frac{R_T}{2.5}\right)^3, 0\right)\\
F_{onset2} &= min\left(max\left(F_{onset1}, F_{onset1}^4\right), 2.0\right)\\
F_{onset1} &= \frac{Re_v}{2.193 \cdot Re_{\theta c}}\\
F_{turb} &= e^{-(R_T/4)^4} && (3.75)\\
Re_\nu &= \frac{\rho d_w^2}{\mu} S && (3.76)\\
R_T &= \frac{\rho k}{\mu\omega} && (3.77)\\
Re_{\theta c} &= f(\tilde{Re}_{\theta t}) && (3.78)\\
F_{length} &= f(\tilde{Re}_{\theta t}) && (3.79)
\end{aligned}$$

The constants for the intermittency transport equation are

$$\begin{aligned}
c_{e1} &= 1.0\\
c_{\alpha 1} &= 2.0\\
c_{e2} &= 50\\
c_{\alpha 2} &= 0.06\\
\sigma_f &= 1.0
\end{aligned} \tag{3.80}$$

A modified γ is also calculated in order to predict separation induced transition:

$$\begin{aligned}
\gamma_{sep} &= min\left(s_1 max\left[0, \left(\frac{Re_v}{3.235 Re_{\theta c}}\right) - 1\right] F_{reattach}, 2\right) F_{\theta t} && (3.81)\\
F_{reattach} &= e^{-\left(\frac{R_T}{20}\right)^4}\\
s_1 &= 2
\end{aligned}$$

The effective value for γ used in the interaction with turbulence models (see Section 3.3.7 and Section 3.3.8) is the maximum of the one calculated via (3.71) and the one calculated via (3.81):

$$\gamma_{eff} = max\left(\gamma, \gamma_{sep}\right) \tag{3.82}$$

In (3.78) and (3.79), $\tilde{Re}_{\theta t}$ is transition onset momentum thickness Reynolds number obtained from the second transport equation for the γ-Re_θ model, which is presented in the following section. $Re_{\theta c}$ and F_{length} are calculated from correlations discussed in Section 3.3.3.

3.3.2 Transport equation for the transition onset momentum thickness Reynolds number ($\tilde{Re}_{\theta t}$)

The transport equation for the transition momentum-thickness Reynolds number $\tilde{Re}_{\theta t}$ reads:

$$\frac{\partial\left(\rho\tilde{Re}_{\theta t}\right)}{\partial t} + \frac{\partial\left(\rho U_j \tilde{Re}_{\theta t}\right)}{\partial x_j} = P_{\theta t} + \frac{\partial}{\partial x_j}\left[\sigma_{\theta t}\left(\mu + \mu_t\right)\frac{\partial \tilde{Re}_{\theta t}}{\partial x_j}\right] \tag{3.83}$$

Outside the boundary layer, the source term $P_{\theta t}$ is designed to force the transported scalar $\tilde{R}e_{\theta t}$ to match the local value of $Re_{\theta t}$ calculated from an empirical correlation. The source term is defined as follows:

$$P_{\theta t} = c_{\theta t}\frac{\rho}{t}\left(Re_{\theta t} - \tilde{R}e_{\theta t}\right)(1.0 - F_{\theta t}) \tag{3.84}$$

$$t = \frac{500\mu}{\rho U^2} \tag{3.85}$$

where t is a time scale, which is present for dimensional reasons. The blending function $F_{\theta t}$ is used to turn off the source term in the boundary layer and allow the transported scalar $\tilde{R}e_{\theta t}$ to diffuse in from the freestream. $F_{\theta t}$ is equal to zero in the freestream and one in the boundary layer. The $F_{\theta t}$ blending function is defined as follows:

$$\begin{aligned}
F_{\theta t} &= min\left(max\left(F_{wake}\cdot e^{-\left(\frac{-y}{\delta}\right)^4}, 1.0 - \left(\frac{\gamma - \frac{1}{c_{e2}}}{1.0 - \frac{1}{c_{e2}}}\right)^2\right), 1.0\right) \\
\theta_{BL} &= \frac{\tilde{R}e_{\theta t}\mu}{\rho U} \\
\delta_{BL} &= \frac{15}{2}\theta_{BL} \\
\delta &= \frac{50\Omega d_w}{U}\cdot\delta_{BL} \\
Re_\omega &= \frac{\rho\omega d_w^2}{\mu} \\
F_{wake} &= e^{-\left(\frac{Re_\omega}{1E+5}\right)^2}
\end{aligned} \tag{3.86}$$

The F_{wake} function ensures that the blending function is not active in the wake regions downstream of solid boundaries. The model constants for the $\tilde{R}e_{\theta t}$ transport equation are:

$$\begin{aligned}
c_{\theta t} &= 0.03 \\
\sigma_{\theta t} &= 2.0
\end{aligned} \tag{3.87}$$

The empirical correlations for $Re_{\theta t}$ present in (3.84) are discussed in Section 3.3.4.

3.3.3 Empirical correlations for $Re_{\theta c}$ and F_{length}

In (3.74), $Re_{\theta c}$ is the critical Reynolds number where the intermittency first starts to increase in the boundary layer. This occurs upstream of the transition Reynolds number $\tilde{R}e_{\theta t}$, and the difference between the two is obtained from an empirical correlation. F_{length} is a function that controls the length of the transitional region. The available correlations in MaPFlow arep presented below. The accuracy of the correlations is discussed separately in Section 5.5.2.

Langtry

Langtry et al [92] proposed the following correlations for F_{length} and $Re_{\theta c}$:

$$F_{length} = \begin{cases} [398.189\cdot 10^{-1} + (-119.270\cdot 10^{-4})\tilde{R}e_{\theta t} + (-132.567\cdot 10^{-6})\tilde{R}e_{\theta t}^2], & \tilde{R}e_{\theta t} < 400 \\ [263.404 + (-123.939\cdot 10^{-2})\tilde{R}e_{\theta t} + (194.548\cdot 10^{-5})\tilde{R}e_{\theta t}^2 + (-101.695\cdot 10^{-8})\tilde{R}e_{\theta t}^3], & 400 \le \tilde{R}e_{\theta t} < 596 \\ [0.5 - (\tilde{R}e_{\theta t} - 596.0)\cdot 3.0\cdot 10^{-4}], & 596 \le \tilde{R}e_{\theta t}1200 \\ [0.3188], & 1200 \le \tilde{R}e_{\theta t} \end{cases}$$

$$Re_{\theta c} = \begin{cases} [\tilde{R}e_{\theta t} - (396.035\cdot 10^{-2} + (-120.656\cdot 10^{-4})\tilde{R}e_{\theta t} + (868.230\cdot 10^{-6})\tilde{R}e_{\theta t}^2 \\ +(-696.506\cdot 10^{-9})\tilde{R}e_{\theta t}^3 + (174.105\cdot 10^{-12})\tilde{R}e_{\theta t}^4), & \tilde{R}e_{\theta t} \le 1870 \\ [\tilde{R}e_{\theta t} - (593.11 + (\tilde{R}e_{\theta t} - 1870.0)\cdot 0.482)], & \tilde{R}e_{\theta t} > 1870 \end{cases} \tag{3.88}$$

In addition, Langtry et al [91][92] suggest the following modification to F_{length}:

$$
\begin{aligned}
F_{length} &= F_{length}(1 - F_{sublayer} + 40.0 \cdot F_{sublayer}) \\
F_{sublayer} &= e^{-\frac{R\omega}{0,4}^2} \\
R_\omega &= \frac{\rho d_w^2 \omega}{500\mu}
\end{aligned}
\tag{3.89}
$$

This modification was suggested because the $\tilde{Re}_{\theta t}$ scalar may decrease to very small values in the boundary layer shortly after transition. Because F_{length} is based on $\tilde{Re}_{\theta t}$ values, this can result in a local increase in the source term for the intermittency equation, which in turn can increase the skin friction significantly. This behavior is unphysical and seems to happen due to a sharp increase of the y^+ in the viscous sublayer where intermittency decreases to its minimum value as a result of its destruction term. This effect can be eliminated by forcing F_{length} to always take its maximum value (in this case 40.0) in the viscous sublayer.

Suluksna

The correlations of Suluksna et al [111] are as follows:

$$
\begin{aligned}
F_{length} &= min((0.1e^{-0.22Re_{\theta t}+12} + 0.45), 300) \\
Re_{\theta c} &= min(max((-(0.025Re_{\theta t})^2 + 1.47Re_{\theta t} - 120), 125), Re_{\theta t})
\end{aligned}
\tag{3.90}
$$

Malan

The correlations of Malan et al [112] are as follows:

$$
\begin{aligned}
F_{length} &= min((e^{7.168-0.01173Re_{\theta t}} + 0.5), 300) \\
Re_{\theta c} &= min((0.615Re_{\theta t} + 61, 5), Re_{\theta t})
\end{aligned}
\tag{3.91}
$$

3.3.4 Empirical correlations for $Re_{\theta t}$

The empirical correlation for $Re_{\theta t}$ is based on the following parameters:

$$
\lambda_\theta = \frac{\rho\theta^2}{\mu}\frac{dU}{ds} \tag{3.92}
$$

$$
Tu = 100\frac{\sqrt{2k/3}}{U} \tag{3.93}
$$

The parameter λ_θ should not be confused with the Polhausen K_p parameter (3.9). The latter is used in the context of boundary layers whereas the former is calculated everywhere in the flowfield. The adopted notation for λ_θ was chosen as it follows the formulation of the model presented in [91][92].

In (3.92), dU/ds is the velocity gradient along the streamwise direction and can be computed by taking the derivative of the velocity U in the x, y, and z directions and then summing the contribution of these derivatives along the streamwise flow direction:

$$
U = \left(u^2 + v^2 + w^2\right)^{\frac{1}{2}} \tag{3.94}
$$

$$
\begin{aligned}
\frac{dU}{dx} &= \frac{1}{2}\left(u^2 + v^2 + w^2\right)^{-\frac{1}{2}} \cdot \left[2u\frac{du}{dx} + 2v\frac{dv}{dx} + 2w\frac{dw}{dx}\right] \\
\frac{dU}{dy} &= \frac{1}{2}\left(u^2 + v^2 + w^2\right)^{-\frac{1}{2}} \cdot \left[2u\frac{du}{dy} + 2v\frac{dv}{dy} + 2w\frac{dw}{dy}\right] \\
\frac{dU}{dz} &= \frac{1}{2}\left(u^2 + v^2 + w^2\right)^{-\frac{1}{2}} \cdot \left[2u\frac{du}{dz} + 2v\frac{dv}{dz} + 2w\frac{dw}{dz}\right]
\end{aligned}
\tag{3.95}
$$

$$
\frac{dU}{ds} = \left[(u/U)\frac{dU}{dx} + (v/U)\frac{dU}{dy} + (w/U)\frac{dU}{dz}\right] \tag{3.96}
$$

The use of the streamline direction is not Galilean invariant. However, this deficiency is inherent to all correlation-based models, as their main variable, the turbulence intensity, is already based on the local freestream

velocity and does therefore violate Galilean invariance. This is not problematic, as the correlations are defined with respect to a wall boundary layer and all velocities are therefore relative to the wall. Nevertheless, multiple moving walls in one domain will likely require additional information.

The available transition onset correlation are presented below. The accuracy of the correlations is discussed separately in Section 5.5.2.

Langtry

The empirical correlation is presented in [93]. For pressure gradient flows, the correlation predictions are similar to the correlation of Abu-Ghannam and Shaw [85]. The empirical correlation is defined as follows:

$$Re_{\theta t} = \begin{cases} [1173.51 - 589.428Tu + \frac{0.2196}{u^2}]F(\lambda_\theta), & Tu \leq 1.3 \\ 331.50[Tu - 0.5658]^{-0.671}F(\lambda_\theta), & Tu > 1.3 \end{cases} \tag{3.97}$$

$$F(\lambda_\theta) = \begin{cases} 1 - [-12.986\lambda_\theta - 123.66\lambda_\theta^2 - 405.689\lambda_\theta^3]e^{-\left[\frac{Tu}{1.5}\right]^{1.5}}, & \lambda_\theta \leq 0 \\ 1 + 0.275\left[1 - e^{[-35.0F\lambda_\theta]}\right]e^{\left[\frac{-Tu}{0,5}\right]}, & \lambda_\theta > 0 \end{cases} \tag{3.98}$$

Abu-Ghannam and Shaw

The correlation of Abu-Ghannam and Shaw is presented in [85]. Transition takes place when:

$$Re_{\theta t} = 163 + e^{(F(\lambda_\theta) - \frac{F(\lambda_\theta)}{6.91}Tu)} \tag{3.99}$$

$$F(\lambda_\theta) = \begin{cases} 6.91 + 12.75\lambda_\theta + 63.64\lambda_\theta^2, & \lambda_\theta \leq 0 \\ 6.91 + 2.48\lambda_\theta - 12.27\lambda_\theta^2, & \lambda_\theta > 0 \end{cases} \tag{3.100}$$

Variable limiting

For numerical robustness, the acceleration parameter, the turbulence intensity and the transition onset momentum thickness Reynolds number are limited as follows:

$$\begin{aligned} -0.1 \leq \lambda_\theta \leq 0.1 \\ Tu \geq 0.027 \\ Re_{\theta t} \geq 20 \end{aligned} \tag{3.101}$$

According to [93] and [92], a minimum turbulence intensity of 0.027% results in a transition momentum-thickness Reynolds number of 1450, which is the largest experimentally observed flat-plate transition Reynolds number based on the Sinclair and Wells [113] data. For cases where larger transition Reynolds number are believed to occur (e.g., aircraft in flight), the authors suggest that this limiter may need to be adjusted downwards. The empirical correlation is used only in the source term of the transport equation for the transition onset momentum-thickness Reynolds number (3.83). An iterative process must be utilized in order to solve (3.97) and (3.98) (or (3.99) and (3.100)), because the momentum thickness θ_t is present in the left-hand side of the $Re_{\theta t}$ equation and also in the right-hand side of the F_{length} equation in the pressure gradient parameter λ_θ.

3.3.5 Predicting crossflow transition

The original version of the γ-Re_θ model is geared towards the prediction of two-dimensional transition mechanisms. Such mechanisms are transition due to Tollmien-Schlichting waves, laminar separation induced transition or bypass transition. However, for simulations of external flows on three dimensional configurations, a major transition mechanism is transition due to crossflow instability. For low freestream turbulence environments, stationary crossflow instability is the main transition mechanism present on swept wings. As turbulence levels become higher, traveling crossflow modes become more important and eventually dominate the crossflow mechanism.

In recent years, many publications have proposed various models that aim towards the implementation of crossflow transition capabilities in the γ-Re_θ transition model. Examples are the works of Medida et al [114], who developed a semi-local empirical crossflow model based on experimental data, and of Grabe et al [115], who incorporated the well known Arnal C1 crossflow transition criterion [87] into the γ-Re_θ framework. However, both approaches required a priori knowledge of the topology. In addition, the models were suitable for wing-like configurations and not for arbitrarily shaped geometries. Choi et al [116][117] also evaluated the C1 criterion

locally by creating a database of solutions to the Falkner-Skan-Cooke velocity profiles [118]. Even though they were able to get promising results, the use of a database in the framework of a locally defined model is not always desirable.

The first crossflow transition model implemented in MaPFlow is due to Langtry et al [119], who proposed a new model for stationary crossflow that accounts for surface roughness. The crossflow model is based on the local streamwise vorticity, also known as helicity. The second is due to Grabe et al [13], who proposed two different crossflow transition models. The first one (named *Crossflow C1 -CFC1-*), was based on the C1 criterion [87] and was semi-local. The second one (named *Crossflow helicity -CFHE-*), which is the one implemented in MaPFlow, is also based on the local helicity. Both model formulations are presented below.

Langtry crossflow model

The crossflow model was first presented in [119]. The streamwise helicity is defined as follows:

$$\vec{U} = \left(\frac{u}{\sqrt{(u^2)+(v)^2+(w)^2}}, \frac{v}{\sqrt{(u^2)+(v)^2+(w)^2}}, \frac{w}{\sqrt{(u^2)+(v)^2+(w)^2}} \right) \tag{3.102}$$

$$\vec{\Omega} = \left(\frac{\partial w}{\partial y} - \frac{\partial v}{\partial z}, \frac{\partial u}{\partial z} - \frac{\partial w}{\partial x}, \frac{\partial v}{\partial x} - \frac{\partial u}{\partial y} \right) \tag{3.103}$$

$$He_{streamwise} = |\vec{U} \cdot \vec{\Omega}| \tag{3.104}$$

$He_{streamwise}$ is non-dimensionalized into a measure of the crossflow strength, similar to the pressure gradient parameter (3.92) that is used in empirical transition correlations. The non-dimensional crossflow strength is defined as follows:

$$H_{crossflow} = \frac{d_w He_{streamwise}}{U} \tag{3.105}$$

Langtry [119] notes that the use of the velocity U in (3.105) is not Galilean invariant. However, this practice is deemed as acceptable due to the fact that the turbulence intensity in (3.93) is also not Galilean invariant. $H_{crossflow}$ is constant near the wall, peaks in the middle of the boundary layer and goes to 0 at the edge of the boundary layer.

The empirical correlation for crossflow transition was built based on experimental data on the NLF(2)-0415 swept airfoil by Radeztsky et al [120] and on a 6:1 prolate spheroid [121] and is defined as follows:

$$Re_{SCF} = \frac{\theta_t \rho \left(\frac{U}{0.82}\right)}{\mu} = -35.088 ln\left(\frac{h}{\theta_t}\right) + 319.51 + f(+\Delta H_{crossflow}) - f(-\Delta H_{crossflow}) \tag{3.106}$$

where h is the surface roughness.

The correlation is a logarithmic fit to the NLF experiment with a shift up $f(+\Delta H_{crossflow})$ or down $f(-\Delta H_{crossflow})$ depending on the local crossflow strength. The velocity magnitude U on the left hand side is divided by 0.82 to account for the approximate difference between freestream velocity and the local velocity in the boundary layer where vorticity Reynolds number is maximum and transition starts.

The crossflow strength shift terms are defined as follows:

$$\Delta H_{crossflow} = H_{crossflow}\left(1.0 + min\left[1.0\frac{\mu_t}{\mu}, 0.4\right]\right) \tag{3.107}$$

The additional eddy viscosity ratio present on the right hand side of (3.107) counteracts the decrease of the $H_{crossflow}$ term that may be caused by the change in velocity profile when transition starts. When crossflow strengths are different than the NLF experiment, the shift up the logarithmic fit is defined as:

$$\begin{aligned} +\Delta H_{crossflow} &= max(0.1066 - \Delta H_{crossflow}, 0) \\ f(+\Delta H_{crossflow}) &= 6200(+\Delta H_{crossflow}) + 50000(+\Delta H_{crossflow})^2 \end{aligned} \tag{3.108}$$

whereas for strengths greater than the NLF experiment the shift down is defined as:

$$\begin{aligned} -\Delta H_{crossflow} &= max(-1.0(0.1066 - \Delta H_{crossflow}), 0) \\ f(-\Delta H_{crossflow}) &= 75 tanh\left(\frac{-\Delta H_{crossflow}}{0.0125}\right) \end{aligned} \tag{3.109}$$

The interaction with the baseline γ-Re_θ model is achieved with the inclusion of a new stationary crossflow sink term D_{SCF} in the transport equation for $\tilde{Re}_\theta$ (3.83) as follows:

$$\frac{\partial\left(\rho\tilde{Re}_{\theta t}\right)}{\partial t}+\frac{\partial\left(\rho U_j\tilde{Re}_{\theta t}\right)}{\partial x_j}=P_{\theta t}+D_{SCF}+\frac{\partial}{\partial x_j}\left[\sigma_{\theta t}\left(\mu+\mu_t\right)\frac{\partial\tilde{Re}_{\theta t}}{\partial x_j}\right] \tag{3.110}$$

$$D_{SCF}=c_{\theta t}\frac{\rho}{t}c_{crossflow}min(Re_{SCF}-\tilde{Re}_{\theta t},0.0)(F_{\theta t2}) \tag{3.111}$$

$$F_{\theta t2}=min\left(F_{wake}e^{-(\frac{d_w}{\delta})^4},1.0\right) \tag{3.112}$$

$$c_{crossflow}=0.6 \tag{3.113}$$

The $F_{\theta t2}$ term is used to confine the crossflow sink term so that it is only active inside the laminar boundary layer. The D_{SCF} term is also active only when the stationary crossflow correlation Re_{SCF} drops below the transported value $\tilde{Re}_{\theta t}$. When two-dimensional flowfields are considered, D_{SCF} is zero and the original form of the γ-Re_θ model is recovered.

Crossflow helicity (CFHE) crossflow model

The crossflow model was first presented in [13]. The helicity Reynolds number, which is a local quantity, is defined as:

$$Re_{He}=\frac{\rho d_w^2}{\mu}\frac{He_{streamwise}}{U} \tag{3.114}$$

where He is given from (3.104). It is again noted that the explicit use of the helicity is not Galilean invariant.

For the new proposed crossflow criterion the authors define a helicity Reynolds number at transition onset, $Re^+_{He,t}$, which is a function of the streamwise shape factor H_{12}. This is carried out in order to account for the influence of the pressure gradient on the transition location. The critical crosswise Reynolds number ration is thus:

$$\frac{Re_{He,max}}{Re^+_{He,t}}=1 \tag{3.115}$$

The superscript + is used to note crossflow quantities. Through calibration against experimental data of infinite swept wing flows and of a 6:1 prolate spheroid, the following criterion is proposed:

$$Re^+_{He,t}=max(-456.83H^++1332.7,150.0)) \tag{3.116}$$

The shape factor H^+ is approximated by a pressure gradient parameter similar to (3.92). It is not possible to use the same equation because the helicity Reynolds number has its maximum at a different wall-normal position than the vorticity Reynolds number (3.69). A new parameter λ^+_θ is defined by using a length scale θ^+ which represents the momentum thickness at the point where the helicity Reynolds number reaches its maximum in the boundary layer:

$$\lambda^+_\theta=\frac{\rho\theta^+}{\mu}\frac{d|\vec{u}_e|}{d\vec{s}} \tag{3.117}$$

where

$$\theta^+=\frac{1}{c_{He,max}}\frac{2}{15}d_w \tag{3.118}$$

$$c_{He,max}=0.6944$$

The velocity at the boundary-layer edge $|\vec{u}_e|$ is calculated via:

$$|\vec{u}_e|=\sqrt{u^2_\infty+\frac{2\tilde{\gamma}}{\tilde{\gamma}-1}\left[1-\left(\frac{p}{\rho_\infty}\right)^{1-\frac{1}{\tilde{\gamma}}}\right]\frac{p_\infty}{\rho_\infty}} \tag{3.119}$$

where $\tilde{\gamma}=1.4$ is the isentropic constant.

The gradient $d|\vec{u}_e|/d\vec{s}$ is calculated via:

$$
\begin{aligned}
\frac{d|\vec{u}_e|}{d\vec{s}} &= \frac{u}{|\vec{u}|}\frac{d|\vec{u}_e|}{dx} + \frac{v}{|\vec{u}|}\frac{d|\vec{u}_e|}{dy} + \frac{w}{|\vec{u}|}\frac{d|\vec{u}_e|}{dz} \\
\frac{d|\vec{u}_e|}{dx} &= -\frac{1}{|\vec{u}_e|\rho_\infty}\left(\frac{p}{p_\infty}\right)^{\frac{1}{\bar{\gamma}}}\frac{dp}{dx} \\
\frac{d|\vec{u}_e|}{dx} &= -\frac{1}{|\vec{u}_e|\rho_\infty}\left(\frac{p}{p_\infty}\right)^{\frac{1}{\bar{\gamma}}}\frac{dp}{dx} \\
\frac{d|\vec{u}_e|}{dx} &= -\frac{1}{|\vec{u}_e|\rho_\infty}\left(\frac{p}{p_\infty}\right)^{\frac{1}{\bar{\gamma}}}\frac{dp}{dx}
\end{aligned}
\tag{3.120}
$$

The shape factor H^+ is computed using the correlation of Cliquet [122]:

$$
H^+ = 4.02923 - \sqrt{-8838.4\lambda_\theta^{+4} + 1105.1\lambda_\theta^{+3} - 67.962\lambda_\theta^{+2} + 17.754\lambda_\theta^{+} + 2.0593} \tag{3.121}
$$

The interaction with the baseline γ-Re_θ model is achieved with the addition of a crossflow term in the production of γ (3.72):

$$
P_\gamma = \left(F_{length}\left[\gamma F_{onset}\right]^{0.5} + F_{length,cf}\left[\gamma F_{onset,cf}\right]^{0.5}\right) c_{\alpha 1}\rho S\left(1 - c_{e1}\gamma\right) \tag{3.122}
$$

where:

$$
\begin{aligned}
F_{onset,cf} &= max\left(F_{onset2,cf} - F_{onset3,cf}, 0\right) \\
F_{onset3,cf} &= max\left(1 - \left(\frac{R_T}{2.0}\right)^3, 0\right) \\
F_{onset2,cf} &= min\left(max\left(F_{onset1,cf}, F_{onset1,cf}^4\right), 2.0\right) \\
F_{onset1,cf} &= \frac{Re_{He}}{c \cdot Re_{He,t}^+} \\
c &= 0.7
\end{aligned}
\tag{3.123}
$$

3.3.6 Boundary conditions

The boundary condition for γ at a wall is zero normal flux, while for an inlet γ is equal to 1.0 . An inlet γ equal to 1.0 is necessary to preserve the original turbulence model's freestream turbulence decay rate. The boundary condition for $\tilde{R}e_{\theta t}$ at a wall is zero flux. The boundary condition for $\tilde{R}e_{\theta t}$ at an inlet should be calculated from the empirical correlations based on the inlet turbulence intensity.

3.3.7 Interaction with the k-ω SST turbulence model

The γ-Re_θ model interacts with the SST turbulence model (Section 2.6.2) by modifying the source and destruction terms of the k-equation (2.144 as follows (also discussed in Section 3.2.5 for boundary layer transition):

$$
\tilde{P}_k = \gamma_{eff} P_k \tag{3.124}
$$

$$
\tilde{D}_k = min\left(max\left(\gamma_{eff}, 0.1\right), 1.0\right) D_k \tag{3.125}
$$

where P_k and D_k are the original production and destruction terms for the SST model and γ_{eff} is the effective intermittency calculated via (3.82).

In addition, the F_1 function of the SST model is modified as:

$$
\begin{aligned}
F_1 &= max\left(F_{1orig}, F_3\right) \\
F_3 &= e^{-\left(\frac{R_{d_w}}{120}\right)^8} \\
R_{d_w} &= \frac{\rho d_w \sqrt{k}}{\mu}
\end{aligned}
\tag{3.126}
$$

where F_{1orig} is the baseline SST blending function given from (2.150).

The production term in the ω equation is not modified. To capture the laminar and transitional boundary layers correctly, the mesh must have a y^+ of approximately 1 at the first point off the wall. If y^+ is too large (i.e., greater than 5), then the transition onset location moves upstream as y^+ increases.

3.3.8 Interaction with the Spalart-Allmaras turbulence model

The γ-Re_θ model interacts with the Spalart-Allmaras turbulence model (Section 2.6.1) by modifying the f_{t2} function (2.138) used by the employed transport equation for the modified viscosity ratio (2.129) as follows (also discussed in Section 3.2.6):

$$f_{t2} = c_{t3}[1 - \gamma] \tag{3.127}$$

However, additional modifications are necessary because the original formulation for the $\gamma - Re_\theta$ model uses the local turbulent kinetic energy k and dissipation ω which are directly available in the SST model but not in the Spalart-Allmaras model. The adopted formulation is based on the work by Medida et al [123] and Crivellini et al [124]. The viscosity ratio R_T and the $F_{\theta t}$ blending function are calculated as:

$$R_T = \frac{\nu_t}{\nu} \tag{3.128}$$

$$F_{\theta t} = min\left(max\left(exp-\left(\frac{U^2}{375\Omega\nu\tilde{Re}_{\theta t}}\right)^4, 1.0 - \left(\frac{\gamma - \frac{1}{c_{e2}}}{1.0 - \frac{1}{c_{e2}}}\right)^2\right), 1.0\right) \tag{3.129}$$

In addition, the $\gamma - Re_\theta$ model utilizes the local turbulence intensity for the empirical correlations that trigger transition. When using the Spalart-Allmaras turbulence model, local turbulence intensity is not directly calculated. In order to apply the transition model, the freestream value for the turbulence intensity is used in the whole domain. With this value, the pressure gradient parameter is calculated in the same way as the SST model and the correlations return the critical $Re_{\theta t}$ number.

$$Tu_{local} = Tu_\infty \tag{3.130}$$

The freestream modified eddy viscosity is again limited as (Section 3.2.6):

$$\frac{\tilde{\nu}_\infty}{\nu_\infty} \leq 0.1 \tag{3.131}$$

3.4 γ transition model

The implemented version is that of Menter [94] who proposed a revised version of the γ-Re_θ model. According to the author, the main objective of the revision was to reduce the overall complexity of the model by including only one transport equation for γ and provide meaningful calibration coefficients that can be altered by the end user to match specific applications, while also achieving a Galilean invariant formulation. The model is again driven by the concept that the vorticity Reynolds number is tied to the transition onset momentum thickness Reynolds number (Section 3.3).

3.4.1 Transport equation for the intermittency (γ)

The transport equation for the intermittency γ is the same as the one used by the γ-Re_θ model:

$$\frac{\partial(\rho\gamma)}{\partial t} + \frac{(\rho U_j \gamma)}{\partial x_j} = P_\gamma - E_\gamma + \frac{\partial}{\partial x_j}\left[\left(\mu + \frac{\mu_t}{\sigma_f}\right)\frac{\partial \gamma}{\partial x_j}\right] \tag{3.132}$$

However, the intermittency source term has been simplified as:

$$P_\gamma = F_{length}\rho S\gamma\left(1-\gamma\right)F_{onset} \tag{3.133}$$

where S is the strain rate magnitude. Due to the F_{onset} function, the source term is designed to be equal to zero in the laminar boundary layer upstream of transition and is activated once the local transition onset criteria are met. In addition, F_{length} was previously a function while now is a constant value. The destruction/relaminarization term is the same as the one used in the γ-Re_θ model:

$$E_\gamma = c_{a2}\rho\Omega\gamma F_{turb}\left(c_{e2}\gamma - 1\right) \tag{3.134}$$

where Ω is the magnitude of the absolute vorticity rate.

The formulation of the F_{onset} function, which is used to trigger the intermittency production, is similar to the one used in the γ-Re_θ model. However, in the γ model the critical momentum thickness Reynolds number $Re_{\theta c}$ is not computed from a transport equation but algebraically, using local flow variables. Thus, transition onset is controlled by the following functions:

$$F_{onset} = max\left(F_{onset2} - F_{onset3}, 0\right) \tag{3.135}$$

$$F_{onset3} = max\left(1 - \left(\frac{R_T}{3.5}\right)^3, 0\right) \tag{3.136}$$

$$F_{onset2} = min\left(F_{onset1}, 2.0\right) \tag{3.137}$$

$$F_{onset1} = \frac{Re_v}{2.2 \cdot Re_{\theta c}} \tag{3.138}$$

$$F_{turb} = e^{-(R_T/2)^4} \tag{3.139}$$

$$Re_v = \frac{\rho d_w^2 S}{\mu} \tag{3.140}$$

$$R_T = \frac{\rho k}{\mu\omega} \tag{3.141}$$

$$Re_{\theta c} = f(Tu_L, \lambda_{\theta L}) \tag{3.142}$$

The model constants are:

$$\begin{aligned} F_{length} &= 100 \\ c_{e2} &= 50 \\ c_{a2} &= 0.06 \\ \sigma_f &= 1.0 \end{aligned} \tag{3.143}$$

In (3.142), $\tilde{Re}_{\theta c}$ is calculated from an empirical correlation. Similarly to what was discussed for the γ-Re_θ model in Section 3.3, any local transition correlation for $Re_{\theta c}$ can be used. The effect of the employed transition correlations is discussed in Section 5.5.2. The new empirical correlation proposed by Menter in [94] is presented below.

3.4.2 New empirical correlation for $Re_{\theta c}$

The subscript L used for the Tu and λ_θ values in the transition correlation (3.142) essentially notes that both of these quantities are now approximated locally, in contrast to the original γ-Re_θ model. This removes the need for an additional transport equation for Re_θ and renders the formulation Galilean invariant. These two arguments are calibrated so that $Re_{\theta c}$ has the correct values in a region between the middle and the edge of the boundary layer, where the γ model triggers transition. The local form for turbulence intensity (Tu_L) reads:

$$Tu_L = min\left(100\frac{\sqrt{2k/3}}{\omega d_w}, 100\right) \tag{3.144}$$

where d_w is the distance from the wall and the combination ωd_w provides a velocity scale inside the boundary layer that replaces the freestream velocity U used in the γ-Re_θ model:

$$U \sim S d_w \sim \omega d_w$$

This formulation ensures that in the middle of the boundary layer, Tu_L approximately equals the freestream Tu value. The pressure gradient parameter used in empirical correlations is defined as follows:

$$\lambda_\theta = -\frac{\theta^2}{\mu}\frac{1}{U}\frac{dP}{ds} = \frac{\rho\theta^2}{\mu}\frac{dU}{ds} \tag{3.145}$$

where dU/ds is the velocity gradient in the streamwise direction. For a flat plate, one can write:

$$\lambda_\theta = \frac{\rho\theta^2}{\mu}\frac{dU}{dx} = -\frac{\rho\theta^2}{\mu}\frac{dV}{dy} \tag{3.146}$$

where V and y are the wall-normal velocity and coordinate in the freestream. In the general case:

$$\frac{dV}{dy} \equiv \nabla(\vec{n}\cdot\vec{V})\cdot\vec{n} \tag{3.147}$$

In order to provide a local approximation of λ_θ, the momentum thickness θ is replaced by the wall distance d_w. As already noted, transition triggering starts at the middle of the boundary layer. At that location, $d_w = \delta/2 \sim \theta$ (δ is the boundary layer thickness). Menter [94] calibrated (3.147) against the Falkner-Skan family of velocity profiles in order to ensure that in the middle of the boundary layer, $\lambda_\theta \approx \lambda_{\theta L}$. The final formula for $\lambda_{\theta L}$ reads:

$$\lambda_{\theta L} = -7.57\cdot 10^{-3}\frac{dV}{dy}\frac{d_w^2}{\nu} + 0.0128 \tag{3.148}$$

For numerical robustness, $\lambda_{\theta L}$ is again limited such that:

$$\lambda_{\theta L} = min(max(\lambda_{\theta L}, -1.0), 1.0) \tag{3.149}$$

The constant 0.0128 accounts for the fact that in the middle of the boundary layer the velocity gradient dV/dy is not zero even for zero pressure gradient flows, due to the growth of the boundary layer. The basic transition correlation was recalibrated and simplified. The new correlation reads:

$$Re_{\theta c}(Tu_L, \lambda_L) = C_{TU1} + C_{TU2}exp(-C_{TU3}Tu_L F_{PG}(\lambda_{\theta L})) \tag{3.150}$$

$$C_{TU1} = 100.0 \qquad C_{TU2} = 1000.0 \qquad C_{TU3} = 1.0$$

For zero pressure gradient flows, the form of (3.150) is similar to the Abu-Ghannam and Shaw correlation. The constants in (3.151) are model parameters that can be changed by the user. C_{TU1} defines the minimal value of $Re_{\theta c}$, whereas the sum of $C_{TU1} + C_{TU2}$ defines its maximal value. C_{TU3} controls how fast $Re_{\theta c}$ decreases with increasing turbulence intensity Tu.

The function $F_{PG}(\lambda_{\theta L})$ is an empirical function which modifies the correlation for non-zero pressure gradient flows. The function was calibrated using the Falkner-Skan profiles. The resulting formula for $F_{PG}(\lambda_{\theta L})$ reads:

$$F_{PG}(\lambda_\theta L) = \begin{cases} min(1 + C_{PG1}\lambda_{\theta L}, C_{PG1}^{lim}), & \lambda_{\theta L} \geq 0 \\ min(1 + C_{PG2}\lambda_{\theta L} + C_{PG3}\cdot min[\lambda_{\theta L} + 0.0681, 0], C_{PG2}^{lim}), & \lambda_{\theta L} < 0 \end{cases} \tag{3.151}$$

$$C_{PG1} = 14.68 \qquad C_{PG2} = -7.34 \qquad C_{PG3} = 0.0 \tag{3.152}$$

$$C_{PG1}^{lim} = 1.5 \qquad C_{PG2}^{lim} = 3.0 \tag{3.153}$$

A limiter is then applied to F_{PG} in order to avoid negative values:

$$F_{PG} = max(F_{PG}, 0) \tag{3.154}$$

The constants in (3.152) are model parameters. C_{PG1} controls the value of the critical $Re_{\theta c}$ number in areas with favorable pressure gradient, whereas C_{PG2} controls in areas with adverse pressure gradient. C_{PG3} becomes active in regions with separation. The constants in (3.153) define the limits of the F_{PG} function and typically do not require adjustments.

In addition, the implemented γ model also includes a modification to the constant 2.2 present in the denominator of (3.135). This modification was proposed by Colonia et al [125] and essentially substitutes the constant with a logarithmic fitting formula that accounts for different Reynolds numbers. The modification changes (3.135) as follows:

$$F_{onset1} = \frac{Re_v}{C_{onset} \cdot Re_{\theta c}} \tag{3.155}$$

where

$$C_{onset1} = min(4.84, max(2.2, 1.388ln(Re \cdot 10^{-6}) + 0.705)) \tag{3.156}$$

The motivation behind the modification was that with increasing Re the original formulation of the model predicted transition too early. With the proposed modification, the parameter in (3.135) can vary between the original value of 2.2 up to the value of 4.84, essentially delaying the predicted onset of transition. In addition, according to [125] the constants C_{TU1} and C_{TU2} present in Menter's transition correlation (3.150) were also modified as:

$$C_{TU1} = 163.0 \qquad C_{TU2} = 1002.25 \tag{3.157}$$

3.4.3 Boundary conditions

The boundary condition for γ at a wall is again zero normal flux, while at the inlet it is equal to 1.

3.4.4 Interaction with the k-ω SST turbulence model

The γ model interacts with the SST turbulence model in the same way as the γ-Re_θ model (Section 3.3.7):

$$\tilde{P}_k = \gamma_{eff} P_k \tag{3.158}$$

$$\tilde{D}_k = min\left(max\left(\gamma_{eff}, 0.1\right), 1.0\right) D_k \tag{3.159}$$

where P_k and D_k are the original production and destruction terms for the SST model. Since no additional γ_{sep} is calculated by the γ transition model, the effective value for γ is the one calculated via (3.132):

$$\gamma_{eff} = \gamma \tag{3.160}$$

The F_1 function of the SST model is modified as:

$$\begin{aligned} F_1 &= max\left(F_{1orig}, F_3\right) \\ F_3 &= e^{-\left(\frac{R_{d_w}}{120}\right)^8} \\ R_{d_w} &= \frac{\rho d_w \sqrt{k}}{\mu} \end{aligned} \tag{3.161}$$

where F_{1orig} is the baseline SST blending function given from (2.150).

3.4.5 Interaction with the Spalart-Allmaras turbulence model

The γ model interacts with the Spalart-Allmaras turbulence model in the same way as the γ-Re_θ model (Section 3.3.8), by modifying the f_{t2} function as:

$$f_{t2} = c_{t3}[1 - \gamma] \tag{3.162}$$

Since k and ω are not available, (3.141) is different:

$$R_T = \frac{\nu_t}{\nu} \tag{3.163}$$

Similarly, local Tu is not directly calculated, thus:

$$Tu_{local} = Tu_\infty \tag{3.164}$$

The freestream modified eddy viscosity is again limited as (Section 3.2.6):

$$\frac{\tilde{\nu}_\infty}{\nu_\infty} \leq 0.1 \tag{3.165}$$

3.5 Amplification Factor Transport transition model

The Amplification Factor Transport (AFT) model was first published by C.Coder and M.Maughmer in [95], and further modified in [126][127][128]. The employed transition prediction approach is the approximate e^N envelope method of Drela et al (Section 3.2.3) modified to fit the transport equation framework.

3.5.1 Transport equation for the amplification factor ($\tilde{N}$)

The first publication of the model utilized a single equation for the amplification factor as follows:

$$\frac{\partial(\rho\tilde{N})}{\partial t} + \frac{\partial(\rho u_j\tilde{N})}{\partial x_j} = \rho\Omega F_{crit}F_{growth}\frac{d\tilde{N}}{dRe_\theta} + \frac{\partial}{\partial x_j}\left[\frac{1}{\sigma_n}(\mu+\mu_t)\frac{\partial\tilde{N}}{\partial x_j}\right] \tag{3.166}$$

where Ω is the vorticity magnitude.

The source term of (3.166) is a rewritten form of the integrand from (3.48) and is an expression of the streamwise growth of the T-S instabilities. The F_{crit} function is used to determine if the local boundary layer is capable of containing unstable modes and is defined as:

$$F_{crit} = \begin{cases} 0, & Re_v < Re_{v,0} \\ 1, & Re_v \geq Re_{v,0} \end{cases} \tag{3.167}$$

with

$$Re_{v,0} = k_y Re_{\theta,0} \tag{3.168}$$

$$k_y = (0.246175H^2 - 0.141831H + 0.008886) \tag{3.169}$$

$$Re_v = \frac{\rho S d^2}{\mu+\mu_t} \tag{3.170}$$

The function k_y is based on the Falkner-Skan profiles and describes the proportionality of the two Reynolds numbers Re_v and Re_θ, where H_L is maximum in the profile. The stability characteristics are taken from the approximate envelope method:

$$log_{10}(Re_{\theta,0}) = 0.7tanh\left(\frac{14}{H-1} - 9.24\right) + \frac{2.492}{(H-1)^0.43} + 0.62 \tag{3.171}$$

$$\frac{d\tilde{N}}{dRe_\theta} = 0.028(H-1) - 0.0345exp\left[-\left(\frac{3.87}{H-1} - 2.52\right)\right] \tag{3.172}$$

The function F_{growth} in (3.166) is a combination of correlations describing the shape factor dependency of the local boundary layer growth rate in the streamwise direction:

$$F_{growth} = D(H)[1+m(H)]\frac{l(H)}{2} \tag{3.173}$$

where

$$l(H) = \frac{6.54H - 14.07}{H^2} \tag{3.174}$$

$$m(H) = \left(0.058\frac{(H-4)^2}{H-1} - 0.068\right)\frac{1}{l(H)} \tag{3.175}$$

are the same as (3.53) and (3.54) and

$$D(H) = \frac{H}{0.5482H - 0.5185} \tag{3.176}$$

is a correlation that relates the local flow velocity and wall vicinity effects to the local vorticity along the locus of maximum H_L for the Falkner-Skan profiles.

The source term thus depends on the local boundary layer shape factor H. However, the shape factor H used by M.Drela et al [98] cannot be exactly defined within a Navier-Stokes simulation by using only local flow

data. The authors of the model utilize a formula which estimates the H factor using a local pressure gradient parameter H_L. The version implemented in this work follows the formulation presented by Coder at al in [96]:

$$H_L = \frac{d_w^2}{\mu}[\nabla(\rho\vec{u}\cdot\vec{n}_{wall})\cdot\vec{n}_{wall}] \tag{3.177}$$

In (3.177), $\vec{n}_{wall}$ represents the wall-normal unit vector. This formulation renders the model Galilean invariant. H_L, which is essentially the wall-normal gradient of wall-normal momentum, relates to the boundary layer shape factor H as:

$$H = 0.376960 + \sqrt{\frac{H_L + 2.453432}{0.6531181}} \tag{3.178}$$

For numerical robustness, H_L is limited such that $-0.25 \leq H_L \leq 200$, which corresponds to $2.21 \leq H \leq 17.98$. (3.178) is used everywhere in the flow field despite being developed for a small region of H_L. Lower values of H_L correspond to favorable pressure gradients, which have slower growing amplification factors.

3.5.2 Transport equation for the intermittency (γ)

Moreover, the implemented version of the model also uses an additional transport equation for the intermittency γ, similar to the one used by the $\gamma - Re_\theta$ and γ transition models (Section 3.3 and Section 3.4):

$$\frac{\partial(\rho\gamma)}{\partial t} + \frac{(\rho U_j\gamma)}{\partial x_j} = P_\gamma - E_\gamma + \frac{\partial}{\partial x_j}\left[\left(\mu + \frac{\mu_t}{\sigma_f}\right)\frac{\partial\gamma}{\partial x_j}\right] \tag{3.179}$$

with source and destruction terms:

$$P_{\gamma 1} = F_{length}c_{\alpha 1}\rho S\left[\gamma F_{onset}\right]^{0.5}(1 - c_{e1}\gamma) \tag{3.180}$$
$$E_{\gamma 1} = c_{\alpha 2}\rho\Omega\gamma F_{turb}(c_{e2}\gamma - 1) \tag{3.181}$$

The blending F functions are also similar:

$$F_{onset} = max[F_{onset,2} - F_{onset,3}, 0] \tag{3.182}$$
$$F_{onset3} = max\left[1 - \left(\frac{\mu_t}{3.5\mu}\right), 0\right] \tag{3.183}$$
$$F_{onset2} = min(F_{onset,1}, 2) \tag{3.184}$$
$$F_{onset1} = \tilde{N}/N_{crit} \tag{3.185}$$
$$F_{turb} = exp\left[-\left(\frac{\mu_t}{2\mu}\right)^4\right] \tag{3.186}$$

Transition occurs then the transported amplification factor $\tilde{n}$ reaches N_{crit}. N_{crit} can be calculated by Mack's relation (3.47). The constants for the intermittency equation are given by Menter:

$$\begin{aligned} c_{e1} &= 1.0 \\ c_{\alpha 1} &= 2.0 \\ c_{e2} &= 50 \\ c_{\alpha 2} &= 0.06 \\ \sigma_f &= 1.0 \end{aligned} \tag{3.187}$$

while F_{length} is set to 100, similar to the γ model.

3.5.3 Boundary conditions

The boundary condition for both the amplification factor and the intermittency transport equations at a solid wall is zero normal flux, while in the freestream $\tilde{N}_\infty = 0$ and $\gamma_\infty = 1$.

3.5.4 Interaction with the k-ω SST turbulence model

The AFT model interacts with the SST turbulence model in the same way as the γ-Re_θ and γ models (Section 3.3.7, Section 3.4.4):

$$\tilde{P}_k = \gamma_{eff} P_k \tag{3.188}$$

$$\tilde{D}_k = min\left(max\left(\gamma_{eff}, 0.1\right), 1.0\right) D_k \tag{3.189}$$

where P_k and D_k are the original production and destruction terms for the SST model. Since no additional γ_{sep} is calculated by the AFT transition model, the effective value for γ is the one calculated via (3.179):

$$\gamma_{eff} = \gamma \tag{3.190}$$

The F_1 function of the SST model is modified as:

$$\begin{aligned} F_1 &= max\left(F_{1orig}, F_3\right) \\ F_3 &= e^{-\left(\frac{R_{d_w}}{120}\right)^8} \\ R_{d_w} &= \frac{\rho d_w \sqrt{k}}{\mu} \end{aligned} \tag{3.191}$$

where F_{1orig} is the baseline SST blending function given from (2.150).

3.5.5 Interaction with the Spalart-Allmaras turbulence model

The AFT model interacts with the Spalart-Allmaras turbulence model in the same way as the γ-Re_θ and γ models (see section 3.3.8, section 3.4.5):

$$f_{t2} = c_{t3}[1 - \gamma] \tag{3.192}$$

The viscosity ratio is again calculated as:

$$R_T = \frac{\nu_t}{\nu} \tag{3.193}$$

The freestream modified eddy viscosity is again limited as (Section 3.2.6):

$$\frac{\tilde{\nu}_\infty}{\nu_\infty} \leq 0.1 \tag{3.194}$$

This page intentionally left blank

Chapter 4

High fidelity turbulence modeling

4.1 Introduction

As far as aerodynamic simulations are considered, computational solvers most often utilize some type of model for turbulence closure. Throughout the years, both algebraic and transport equation turbulence models have been used, however in recent the focus has shifted towards the latter. Examples of transport equation models are the Spalart-Allmaras model (Section 2.6.1) and the k-ω SST model (Section 2.6.2), which is a modified version of the Wilcox two equation model [129]. Other notable turbulence models are the two equation k-ϵ model [130], which is often used for atmospheric flow simulations, and the algebraic Baldwin-Lomax model [131].

These are referred to as Reynolds-Averaged Navier-Stokes (RANS) turbulence models because they employ Reynolds-Averaging for the modeling of turbulence. Therefore, they are primarily geared towards predicting the averaged effect of turbulence in the context of a Navier-Stokes simulation. In that sense, the averaged effect of the Reynolds stresses on the flow is completely modeled, bypassing the need to resolve the eddies of any scale in the computational mesh. This decreases the required computational resources significantly. For two-dimensional flow and attached boundary layers, RANS models are able to give very accurate predictions when compared to experimental data. This is backed up by results available from the turbulence modeling resource of NASA [132], where results for different solvers using various available turbulence models indicate that attached flows are predicted with great accuracy at least up to the point of stall. Other examples include the works of Seyfert et al [133] and Johansen et al [83], who considered turbulent and transitional flows, showing that 2D simulations with RANS models work well in the linear region where either no stall or mild stall are present.

However, the same does not hold true for highly unsteady, separated flows. Utilization of time or ensemble averaging, which is carried out by RANS models, hinders the development of instantaneous, three dimensional turbulent structures. This is also discussed in the works of Strelets [31] and Xu et al [32], who use 3D Unsteady RANS (URANS) to simulate the flow past airfoils at angles up to 90°. Both works show that 3D URANS supresses the development of 3D turbulent structures and severely overpredicts lift and drag in the deep stall region.

The use of Direct Numerical Simulation (DNS), where all turbulent scales are resolved, can in theory eliminate the need for turbulence modeling. However, this requires very fine meshes and very low physical timesteps, bringing the cost for DNS to unacceptable levels for most industrial applications. The mesh requirements of DNS are discussed in Choi et al [29], where DNS for turbulent boundary layer on a flat plate is shown to have mesh point requirement that scales with Reynolds number as:

$$N_{DNS} \sim Re_{L_x}^{37/14} \tag{4.1}$$

Therefore, DNS is used only for research purposes at very low Reynolds numbers. Most often it serves as a *numerical experiment*, in the sense that due to its accuracy it can aid in the understanding of physics which in turn can be useful for the development and calibration of turbulence models.

Large Eddy Simulation (LES) was initially proposed as a DNS/RANS hybrid. Contrary to the RANS approach, LES resolves the large scales (eddies) of the turbulent flows directly, leaving only the small scales (sub-grid scales, SGS) to be modeled. This is achieved by applying a spatial filter in the governing equations, separating the eddies into large and sub-grid components. Due to the fact that the smaller scales are the most expensive to fully resolve, the cost of LES is significantly lower than the cost of DNS. LES was proposed as early as 1960 by J. Smagorinsky [134]. If mesh resolution is fine enough, LES can provide more accurate results than RANS because large eddies carry most of the turbulent energy and are thus responsible for most of the momentum transfer and turbulent mixing. The effect of the large eddies is captured in full with LES, whereas it is only modeled with RANS.

In the work of Choi et al [29], the mesh point requirements for LES are also discussed. The cost for wall resolved LES for a flat plat turbulent boundary layer is show as:

$$N_{LES,wr} \sim Re_{L_x}^{13/7} \tag{4.2}$$

whereas for wall modeled LES is shown as:

$$N_{LES,wm} \sim Re_{L_x} \tag{4.3}$$

It is evident that the cost of LES is significantly lower than that of DNS, especially when wall modeling is used. In that sense, LES can be used to simulate flows with Reynolds numbers at least one order of magnitude higher than DNS.

Even though the cost of LES is significantly lower than that of DNS, it remains high for everyday applications at moderate to high Reynolds numbers. This is primarily due to the mesh requirements for the solution of boundary layers. As stated previously, this cost can be alleviated via use of wall models. However, wall models are not suitable for the prediction of separated boundary layers.

This led to the development of hybrid techniques that try to combine the best aspects of RANS and LES methodologies within a single strategy. This idea was first presented by P. Spalart [135], as a modification to the Spalart-Allmaras turbulence model. P. Spalart also introduced the term *Detached Eddy Simulation* (DES) in the same paper. The modification enables boundary layer and separation regions to be treated in a RANS-like manner, whereas downstream of separation the turbulence model behaves like a Smagorinsky-SGS model and large eddies are fully resolved and not modeled. The RANS equations are well suited for attached boundary layers and can produce decent results with relatively coarse meshes. For separated regions and free shear layers, where the RANS predictions are not expected to have sufficient accuracy, the turbulence model switches to the LES mode.

DES can be used with any turbulence model that has an appropriately defined length scale. Besides the Spalart-Allmaras model, other candidates are the SST k-ω and the k-ϵ models. Compared to classical LES methods, DES requires less computational effort due to the lower costs of the RANS approach inside the boundary layer region, while also offering some of the advantages of an LES method in separated regions and wakes. The initial version of DES [135], called DES97, has since evolved to the Delayed DES (DDES) concept, initially presented by Menter et al in [136], and the Improved Delayed DES (IDDES) concept, initially presented by Spalart et al in [137], which addressed some of the deficiencies of the DES97 approach.

In addition, some simulations require the presence of turbulent inflow. In such cases, the freestream velocity is not constant but, rather, varies around a mean value. The values for the variations are created using a synthetic turbulence generator. Simulations with turbulent inflow usually LES in order to fully capture the effect of the unsteady velocity fluctuations. On the contrary, turbulent inflow is rarely used in conjuction with RANS methods, in which the averaging of turbulent structures will most likely eliminate their time-dependent character.

In this Chapter, the LES and DES strategies implemented in MaPFlow are presented. LES is discussed in Section 4.2. The filtered governing equations are presented in Section 4.2.1, whereas the process of filtering is discussed in Section 4.2.2. Subgrid-scale modeling is discussed in Section 4.2.3. Detached eddy simulation is discussed in Section 4.3. Section 4.3.1 presents the initial DES idea, as presented by Spalart in [135], followed by the DDES and IDDES concepts for both Spalart-Allmaras and k-ω SST models in Section 4.3.2. Finally, turbulent inflow implementation is presented in Section 4.4.

4.2 Large Eddy Simulation

4.2.1 Filtered equations

The governing equations are the Navier-Stokes equations, presented in Section 2.2. However, since in LES only large eddies are resolved directly, a low-pass spatial filter is applied to the equations in order to formulate the 3D unsteady system for large eddies. This is called explicit filtering. By applying a filter, the velocity components and the energy are decomposed as:

$$u = \tilde{u} + u' \tag{4.4}$$

where $\tilde{u}$ is the filtered and u' the sub-filter component. In fig. 4.1, the difference between the filtered velocity $\tilde{u}$ and the instantaneous velocity u is shown.

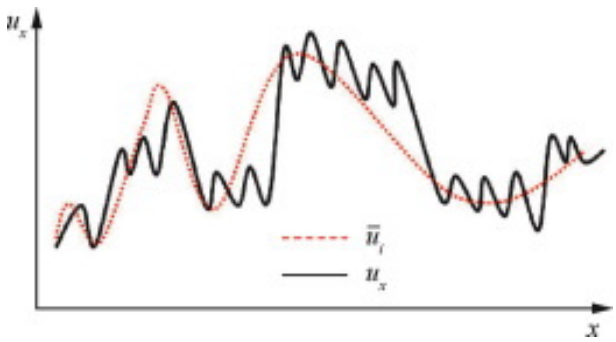

Figure 4.1: *Difference between filtered and instantaneous velocity (reproduced from [1])*

For the governing equations of compressible flow, each equation is filtered. Starting with the conservation of mass, we get:

$$\frac{\partial \bar{\rho}}{\partial t} + \frac{\partial \overline{u_i \rho}}{\partial x_i} = 0 \tag{4.5}$$

In (4.5), an additional sub-filter term ($\overline{u_i \rho}$) is present. Having to model the sub-filter scales of the mass conservation equation is generally not desirable. In order to overcome this, Favre filtering is employed, which is a density-weighted filtering operation. For an arbitrary quantity g, Favre filtering is defined as:

$$\tilde{g} = \frac{\overline{\rho g}}{\bar{\rho}} \tag{4.6}$$

which becomes the normal filtering operation in the limit of incompressibility. The filtered conservation of mass thus becomes:

$$\frac{\partial \bar{\rho}}{\partial t} + \frac{\partial \bar{\rho} \tilde{u}_i}{\partial x_i} = 0 \tag{4.7}$$

Applying the Favre filtering concept to the momentum equation, one gets:

$$\frac{\partial \bar{\rho} \tilde{u}_i}{\partial t} + \frac{\partial (\bar{\rho} \tilde{u}_j \tilde{u}_i)}{\partial x_j} + \frac{\partial \bar{p}}{\partial x_i} - \frac{\partial \tilde{\sigma_{ij}}}{\partial x_j} = -\frac{\partial \bar{\rho} \tau^r_{ij}}{\partial x_j} + \frac{\partial}{\partial x_j}(\overline{\sigma}_{ij} - \tilde{\sigma}_{ij}) \tag{4.8}$$

where σ_{ij} is the shear stress tensor. For a Newtonian fluid, σ_{ij} is given by:

$$\sigma_{ij} = 2\mu(T) S_{ij} - \frac{2}{3}\mu(T)\delta_{ij} S_{kk} \tag{4.9}$$

The term $\frac{\partial}{\partial x_j}(\overline{\sigma_{ij}} - \tilde{\sigma_{ij}})$ in (4.8) represents a sub-filter viscous contribution from evaluating the viscosity $\mu(T)$ using the Favre-filtered temperature $\tilde{T}$. The subgrid stress tensor is given by:

$$\tau^r_{ij} = \bar{\rho}(\widetilde{u_i \cdot u_j} - \tilde{u_i}\tilde{u_j}) \tag{4.10}$$

The filtered energy field is [64]:

$$\frac{\partial \bar{\rho} \tilde{e}}{\partial t} + \frac{(\partial (\bar{\rho} \tilde{u_j} \tilde{e}))}{\partial x_j} + \frac{\partial \tilde{q}}{\partial x_j} + \bar{p}\tilde{S_{kk}} - \tilde{\sigma_{ij}}\tilde{S_{ij}} = -A - B - C + D \tag{4.11}$$

where

$$A = \frac{\partial}{\partial x_j}[\bar{\rho}(\tilde{u_j e} - \tilde{u_j}\tilde{e})]$$

- divergence of subgrid-scale heat flux

$$B = \frac{\partial}{\partial x_j}[\bar{q}_j - \tilde{q_j}]$$

- divergence of subgrid scale heat diffusion

$$C = [\overline{pS_{kk}} - \bar{p}\tilde{S_{kk}}]$$

- subgrid scale pressure dilatation

$$D = [\overline{\sigma_{ij}S_{ij}} - \tilde{\sigma_{ij}}\tilde{S_i}j]$$

- subgrid scale viscous dissipation

and

$$\begin{aligned}
\overline{\sigma_i j} &= \overline{2\mu S_i j} + \overline{\left(\mu_B - \frac{2\mu}{3}\right)\delta_i j S_k k} \\
\tilde{\sigma_i j} &= 2\tilde{\mu}\tilde{S_i}j + \left(\tilde{\mu_B} - \frac{2\tilde{\mu}}{3}\right)\delta_i j \tilde{S_k} k \\
\tilde{S_i}j &= \frac{1}{2}\left(\frac{\tilde{u_i}}{\partial x_j}\frac{\partial u_j}{\partial x_i}\right) \\
\bar{q}_j &= -k\frac{\overline{\partial T}}{\partial x_j} \\
\tilde{q_j} &= -\tilde{k}\frac{\partial \tilde{T}}{\partial x_j}
\end{aligned} \tag{4.12}$$

In (4.7)-(4.12), μ, μ_B and k stand for molecular viscosity, bulk viscosity and thermal conductivity, respectively, whereas $\tilde{\mu}$, $\tilde{\mu_b}$ and $\tilde{k}$ are the respective values at the filtered temperature $\tilde{T}$.

The right hand side of (4.7),(4.8) and (4.11) contains terms which have to be modeled. In the momentum equation, the subgrid stress tensor (4.10) is approximated with the use of subgrid scale models, but the second term ($\overline{\sigma}_{ij} - \tilde{\sigma}_{ij}$) is usually neglected. In the filtered energy equation, term A can be expressed through the subgrid stress tensor, term B can be neglected and terms C and D can be modeled [64].

4.2.2 Filter implementation

The filtering operation in LES can be either implicit or explicit. In explicit filtering, an LES filter is applied to the discretized Navier-Stokes equations. LES filters have a well-defined filter shape and they reduce truncation errors. Examples of LES filters include the tophat, cut-off and Gaussian filters [64]. When using the finite volume method, integration is carried out over control volumes. This is in practice equivalent to a convolution with a top-hat filter. Therefore, there does not exist a need to apply additional explicit filtering to the instantaneous equations. The use of control volumes as filter is called implicit filtering.

However, it is worth noting that with implicit filtering truly mesh independent results cannot be obtained, because by refining the mesh the solver will solve more of the sub-grid scales. Eventually, with continuing mesh refinement, a DNS simulation will be reached. On the other hand, explicit filtering requires a finer mesh than implicit filtering, and the computational cost increases with $(\Delta x)^4$.

4.2.3 Subgrid-scale modeling

Subgrid-scale modeling refers to the important small-scale physical processes which occur at length scales that cannot be adequately resolved by the computational mesh. In LES, subgrid-scale modeling is used to represent the effects of unresolved small-scale turbulent structures (eddies, vortices) in the Navier-Stokes equations which govern the solution of the large-scale motions. The SGS stress is a symmetric tensor, invariant to Galilean transformation, and, as a proper tensor quantity, it must transform from one frame to another that may be rotated in appropriate fashion.

When compared to the large scales, the SGS scales are more isotropic and homogenous in nature. This makes SGS modeling simpler than RANS modeling, which tries to captures all turbulent scales within a single framework. Various subgrid-scale models have been developed throughout the years and the research is still ongoing. Different subgrid-scale models are compared in the work of Lenormand et al [138].

Eddy-Viscosity models

The majority of the SGS models are based on the eddy-viscosity concept. These models are able to represent the global dissipative effects of the small scales. However, they are unable to reproduce the local details of the energy exchange between large and small scales. Traditionally, the effect of SGS motions upon resolved scales are modeled in analogy with molecular degrees of freedom in e.g. kinetic theory of gases, in which the momentum fluxes are linearly dependent on the rate of strain of the large scales. This leads to the following eddy-viscosity closure:

$$\tau_{ij}^{ev} = -2\nu_{sgs}\bar{S_{ij}} \tag{4.13}$$

where ν_{sgs} is the kinematic eddy viscosity. This approach complies with Galilean invariance, symmetry, and transformations from one frame to another. Like turbulence models, the units of the eddy viscosity are velocity times a characteristic length-scale, or kinetic energy density multiplied by a time-scale.

Smagorinsky model

The best known eddy-viscosity SGS model is that of Smagorinsky [134], which was published in 1963. In this model, the subgrid scale eddy viscosity is expressed as a characteristic length scale Δ times a velocity scale $|\bar{S}|$, representing a Galilean invariant estimation of velocity derivatives over length-scales of order Δ. The model itself can be written as:

$$\tau_{ij}^{smag} = -2(C_s\Delta)^2|\bar{S}| \tag{4.14}$$

where $|\bar{S}| = (2\bar{S_{ij}}\bar{S_{ij}})^{1/2}$ is the magnitude of the strain-rate tensor and C_s is the Smagorinsky constant. The theoretical value found by Lilly [139] is $C_s = 0.18$. However, the value of the constant is largely dependent on the type of flow. The filter width Δ in (4.14) is chosen to be the average mesh cell size, hence $\Delta = (\Delta x_1 \Delta x_2 \Delta x_3)^{1/3}$. Other common filter widths are twice the average width size $\Delta = 2(\Delta x_1 \Delta x_2 \Delta x_3)^{1/3}$ or the maximum dimension of the mesh cell $\Delta = max(\Delta x_1, \Delta x_2, \Delta x_3)$.

Small scales exhibit reduced growth near solid walls. In order to account for this, the Smagorinsky eddy viscosity ν_{smag} is adjusted according to Van Driest damping as follows:

$$\nu_{smag} = \left[C_s\Delta(1 - e^{-y^+/25})\right]^2 |\bar{S}| \tag{4.15}$$

where y^+ is the dimensionless wall distance.

There are also versions of the Smagorinsky model in which the value for C_s is dynamic in space and time. These are called *dynamic subgrid scale models*. The most popular dynamic model is that of Germano et al [140]. However, dynamic models are not considered in this thesis.

4.3 Detached Eddy Simulation

4.3.1 Original Detached Eddy Simulation (DES97)

The transport equation solved by the Spalart-Allmaras model (Section 4.3.2) is repeated here:

$$\frac{\partial \rho\tilde{\nu}}{\partial t} + \frac{\partial}{\partial x_j}(\rho\tilde{\nu}u_j) = \rho C_{b1}\left[1 - f_{t2}\right]\tilde{S}\tilde{\nu} - \rho\left[C_{w1}f_w - \frac{C_{b1}}{\kappa^2}f_{t2}\right]\left(\frac{\tilde{\nu}}{d_w}\right)^2 + \frac{\rho}{\sigma}\left[\frac{\partial}{\partial x_j}\left((\nu + \tilde{\nu})\frac{\partial\tilde{\nu}}{\partial x_j}\right) + C_{b2}\frac{\partial\tilde{\nu}}{\partial x_i}\frac{\partial\tilde{\nu}}{\partial x_i}\right] \tag{4.16}$$

The initial modification proposed in [135] replaced the wall distance d_w in (4.16) with a modified distance function $\tilde{d}$ defined as:

$$\tilde{d} = min\left[d_w, C_{DES}\Delta\right] \tag{4.17}$$

In (4.17) C_{DES} is constant in the order of 1. $C_{DES} = 0.65$ is used most often. Δ is a local mesh length scale, similar to the one used in LES subgrid-scale models (Section 4.2.3):

$$\Delta = (\Delta x \Delta y \Delta z)^{1/3} \tag{4.18}$$

or

$$\Delta = max(\Delta x, \Delta y, \Delta z) \tag{4.19}$$

Both length scales can be used. DES simulations most often use (4.19). However, selection of Δ is a separate, discussion raising issue [41]. The modification to the original turbulence model may seem simple, however it drastically changes the model behavior. In regions with fine enough mesh resolution, the model behaves like Smagorinsky-LES one with a wall model. Inside boundary layers or when approaching separation, the model switches to the original form, behaving like a RANS turbulence model. Even though the modification presented here refers to the Spalart-Allmaras model, the DES approach can be implemented in any turbulence model that has an appropriately defined length scale.

Early development of DES is noted in Spalart et al. [141][142], where results from separated flow around the NACA0012 airfoil as well as from channel flow are presented in an effort to assess the computational cost and the feasibility of the DES strategy. The "classic" problem of flow past a circular cylinder was tackled using DES by Travin et al [36]. Both laminar and turbulent separation cases were considered, with Reynolds numbers ranging from 50000 for the laminar separation case up to 3 x 10^6 for the turbulent separation case. Deviations from the experimental data were noted. It was also found that simulations with unsteady RANS were much less accurate than DES for the laminar separation case, but the two were similar for the turbulent separation case.

In the work of M. Strelets [31], massively separated flow around the NACA0012 airfoil at very high angles of attack was simulated and compared to experiments, using DES versions of both the Spalart-Allmaras and k-ω SST turbulence models. The comparison was favorable, especially in very high angles of attack where the unsteady RANS solution deviated from the experiments significantly. Breuer et al [41] considered the flow past an inclined flat plate using unsteady RANS, DES and LES. The initial results showed that the unsteady RANS approach failed to predict the unsteady characteristics of the separated flow, whereas DES results were closer to LES. However, some deviations between DES and LES were noted, even when using the same computational mesh. A revised version of the Spalart-Allmaras for the DES strategy was also suggested, which was able to give results closer to LES. Johansen et al [143] performed DES around the parked NREL phase VI blade rotor at fixed angle of attack. DES results show more three-dimensional flow structures when compared to conventional two-equation RANS. However, no significant improvement was shown in the global blade characteristics. The DES approach has also been combined with transport equation transition models for transitional flows. An example is the work of Srensen et al [144], who combined the original DES version of the SST k-ω model proposed in [31] with the γ-Re_θ correlation transition model (see Section 3.3). Flow around the circular cylinder and the DU-96-W-351 airfoil was considered. Results using the transition model were shown to improve the results of the standard, fully turbulent DES simulation.

4.3.2 Delayed Detached Eddy Simulation

The original DES formulation discussed in Section 4.3.1 was found to contain some inconsistencies in the quality of the produced results. In [136], two main concerns with the original DES formulation were discussed. The first was how quickly the unsteady turbulent structures develop after the model has switched from the RANS to the LES mode. This is important in the prediction of separated shear layers, because the delayed onset of resolved

turbulent structures would lead to underprediction of turbulent stresses due to reduced unresolved turbulence levels by the DES formulation. The second was the robustness of the switching mechanism employed by the original DES formulation. In order to prevent the activation of the DES limiter in attached boundary layers, a lower limit on the local surface mesh resolution is typically enforced. If this condition is violated, the consistency of the RANS model is severely compromised. In most cases, this results in Grid Induced Separation (GIS).

Moreover, Spalart et al [137] note that GIS begins when the mesh spacing parallel to the wall becomes less than the boundary-layer thickness δ. This may occur due to either mesh refinement or boundary layer thickening. In both scenarios, mesh spacing is fine enough for the DES length scale to follow the LES branch (4.17), lowering the eddy viscosity below the RANS level. However, resolved Reynolds stresses deriving from velocity fluctuations, which Spalart et al note as "LES content", have not replaced the modeled Reynolds stresses. Pure LES content derived from the velocity fluctuations may be lacking because the resolution is not fine enough to fully support it, or because its generation is hindered by the presence of instabilities. The reduced eddy viscosity will, thus, not be counteracted by any sizable resolved stress. The depleted stresses reduce skin friction, which can lead to premature separation. Spalart et al [137] referred to this behavior as modeled-stress depletion (MSD).

The new DES version was named *Delayed Detached Eddy Simulation* (DDES), because it addresses this concern by delaying the onset of artificial separation caused by local mesh refinement.

Spalart-Allmaras Delayed Detached Eddy Simulation

In [137], the DDES version of the Spalart-Allmaras model is presented. The original parameter r for the model (Section 2.6.1) reads:

$$r = min\left[\frac{\tilde{\nu}}{\tilde{S}\kappa^2 d_w^2}, 10\right] \tag{4.20}$$

The modified parameter r_d is defined as:

$$r_d \equiv \frac{\nu_t + \nu}{\sqrt{u_{i,j}u_{i,j}}\kappa^2 d_w^2} \tag{4.21}$$

where subscript d stands for "delayed". When compared to the original DES model, the length scale now depends not only on the local mesh spacing, but also on the flow solution.

In (4.21), ν_t is the eddy viscosity, ν the kinematic viscosity, κ the Von Karman constant and d the distance to the wall. Similar to the original version of the Spalart-Allmaras model, r equals 1 in the logarithmic layer and drops to 0 towards the boundary layer edge. The addition of ν in the numerator helps in ensuring that r_d does not reach 0 even in regions with $y^+ \leq 10$. When using the Spalart-Allmaras model, $\tilde{\nu}$ can be used instead of $\nu_t + \nu$. The value r_d from (4.21) is used to calculate the function f_d as follows:

$$f_d \equiv 1 - tanh([8r_d^3]) \tag{4.22}$$

The function f_d is designed to be 1 in LES regions, where $r_d \ll 1$, and 0 elsewhere. Using $tanh$ also makes the function insensitive to r_d exceeding 1 in very near-wall regions. The values 8 and 3 for the constants in (4.22) were calculated in [137] by matching DDES and RANS results for flat plate boundary layer simulations.

The function f_d is used in the modified length scale:

$$\tilde{d} \equiv d_w - f_d \cdot max(0, d_w - C_{DES}\Delta) \tag{4.23}$$

Setting f_d equal to 0 returns the RANS mode ($\tilde{d} = d_w$), while setting it equal to 1 returns the original DES formulation $\tilde{d} = min(d_w, C_{DES}\Delta)$.

Spalart-Allmaras Improved Delayed Detached Eddy Simulation

In [145], a newer strategy which combines delayed detached-eddy simulation (DDES) with an improved RANS-LES hybrid model aimed at wall modelling in LES (WMLES) was presented. The modification aims at providing a different response based on whether the simulation does or does not contain inflow turbulent content. The new version was named Improved Detached Eddy Simulation (IDDES).

In cases with turbulent inflow, the model behaves like a Wall Modelled LES and most of the turbulent content is resolved except near the wall. Empirical improvements to the model were added in order to provide an increase in the resolved turbulence activity in near-wall regions. This step was crucial in addressing the issue of "log layer mismatch" which was present in earlier DES and other Wall Modeled LES methods. Simulations with DES or Wall Modeled LES produced two logarithmic layers: the inner log-layer, which is calculated by the RANS mode of the model, and the outer log-layer, which is calculated by the LES mode of the model, which is functioning well when the local mesh sizes are smaller than the local distance to the wall. These two log-layers

turned out unmatched , resulting in underpredicted friction coefficients. The primary addition to remedy this behavior was a different definition for the subgrid length-scale which depends not only on the mesh spacing, but also takes the distance to the wall into account. For the case without inflow turbulent content, IDDES performs as DDES, and thus returns a pure RANS solution for attached flows and a DES-like solution for massively separated ones. The two branches are combined using a blending function.

In [145], simulations showed that the Spalart-Allmaras IDDES performs well in all modes that it was designed for. Channel flow in a wide Reynolds-number range and flow over a hydrofoil with trailing-edge separation, which are Wall Modeled LES test cases, an airfoil in deep stall, which is a natural DES case, and a backward-facing step flow, which utilizes both branches of the model in different flow regions, all produced satisfactory results.

New length scale

The IDDES model definition for the local length scale Δ reads:

$$\Delta = min[max(C_w d_w, C_w h_{max}, h_{wn}), h_{max}] \tag{4.24}$$

where C_w is an empirical constant, h_{wn} is the mesh step in the wall normal direction and $h_{max} = max(\Delta x, \Delta y, \Delta z)$. For C_w, the value of 0.15 was chosen.

DDES branch

Replacing distance notation d with length notation l, (4.23) can be rewritten as:

$$l_{DDES} = l_{RANS} - f_d max(0, l_{RANS} - l_{LES}) \tag{4.25}$$

where for the Spalart-Allmaras model, $l_{RANS} = d_w$. The blending function f_d is again given by:

$$f_d \equiv 1 - tanh([8r_d^3]) \tag{4.26}$$

Moreover, the definition for r_d is similar to the one for the DDES model:

$$r_d \equiv \frac{\nu_t + \nu}{max(\sqrt{u_{i,j}u_{i,j}}, 10^{-10})\kappa^2 d_w^2} \tag{4.27}$$

The LES length scale l_{LES} in (4.25) reads:

$$l_{LES} = C_{DES}\Psi\Delta \tag{4.28}$$

where C_{DES} is the empirical DES constant used in all DES models and Δ is the length scale calculated via (4.24).

Ψ is a low Reynolds number correction defined as:

$$\Psi = min\left[10^2, \frac{1 - \frac{c_{b1}}{c_{w1}\kappa^2 f_w^*}[f_{t2} + (1 - f_{t2})f_{v2}]}{f_{v1} max(10^{-10}, 1 - f_{t2})}\right] \tag{4.29}$$

Only f_w^* is different than the baseline Spalart-Allmaras model:

$$f_w^* = 0.424 \tag{4.30}$$

The rest of the definitions remain the same and are repeated for completeness:

$$\mu_T = \rho\tilde{\nu} f_{v1} \tag{4.31}$$

$$f_{v1} = \frac{x^3}{x^3 + C_{v1}^3} \tag{4.32}$$

$$x = \frac{\tilde{\nu}}{\nu} \tag{4.33}$$

$$\tilde{S} = \Omega + \frac{\tilde{\nu}}{\kappa^2 d_w^2} f_{v2} \tag{4.34}$$

$$f_{v2} = 1 - \frac{x}{1 + x f_{v1}} \tag{4.35}$$

$$\Omega = \sqrt{2\Omega_{ij}\Omega_{ij}} \tag{4.36}$$

$$\mu_T = \rho\tilde{\nu} f_{v1} \tag{4.37}$$

$$f_w = g\frac{1 + C_{w3}^6}{g^6 + C_{w3}^6}^{1/6} \tag{4.38}$$

$$g = r + C_{w2}(r^6 - r) \tag{4.39}$$

$$r = min\left[\frac{\tilde{\nu}}{\tilde{S}\kappa^2 d_w^2}, 10\right] \tag{4.40}$$

$$f_{t2} = C_{t3} exp(-C_{t4} x^2) \tag{4.41}$$

WMLES branch

RANS and LES approaches are coupled by introducing the following blended RANS-LES length scale:

$$l_{WMLES} = f_B(1 + f_e) l_{RANS} + (1 - f_B) l_{LES} \tag{4.42}$$

where similar to the DDES branch, l_{RANS} and l_{LES} are the RANS and LES length scales, respectively. The empirical blending function f_B is calculated using the d_w/h_{max} ratio as:

$$f_B = min(2exp(-9\alpha^2), 1.0) \tag{4.43}$$

where

$$\alpha = 0.25 - \frac{d_w}{h_{max}} \tag{4.44}$$

The values for the function f_B vary from 0 to 1. When $f_B = 1$ the model is on the RANS mode, whereas when $f_B = 0$ the model is on the LES mode. The function enables the model to switch rapidly from RANS to LES mode within the range of wall distance $0.5h_{max} < d_w < h_{max}$.

The second empirical blending function in (4.42), the elevating function f_e, helps preventing excessive reduction of the RANS Reynolds stresses in the interaction of RANS and LES regions. The presence of f_e helps address the log-layer mismatch discussed in previous paragraphs. The function itself reads:

$$f_e = max((f_{e1} - 1), 0)\Psi f_{e2} \tag{4.45}$$

where

$$f_{e1} = \begin{cases} 2 \cdot exp(-11.09 \cdot \alpha^2), & \alpha \geq 0 \\ 2 \cdot exp(-9.0 \cdot \alpha^2), & \alpha < 0 \end{cases} \tag{4.46}$$

$$f_{e2} = 1.0 - max(f_t, f_l) \tag{4.47}$$

$$f_t = tanh\left((C_t^2 \cdot r_{dt})^3\right) \tag{4.48}$$

$$f_l = tanh\left((C_l^2 \cdot r_{dl})^1 0\right) \tag{4.49}$$

$$r_{dl} = \frac{\nu}{\kappa^2 d_w^2 \sqrt{0.5(S^2 + \Omega^2)}} \tag{4.50}$$

$$r_{dt} = \frac{\nu_t}{\kappa^2 d_w^2 \sqrt{0.5(S^2 + \Omega^2)}} \tag{4.51}$$

Constants c_t and c_l depend on the background RANS turbulence model and should be adjusted so that function f_{e2} is virtually zero when either r_{dt} or r_{dl} is close to 1.0.

Blending the DDES and WMLES branches

The DDES length scale in (4.25) and the WMLES scale in (4.42) do not blend directly in a way that the proper mode will be automatically selected. The blending is however possible via the use of a modified version of (4.25):

$$\tilde{l}_{DDES} = \tilde{f}_d l_{RANS} + (1 - \tilde{f}_d l_{LES}) \tag{4.52}$$

where $\tilde{f_d}$ is defined by

$$\tilde{f_d} = max((1 - f_{dt}), f_B) \tag{4.53}$$

with

$$f_{dt} = 1 - tanh[(8r_{dt})^3] \tag{4.54}$$

By utilizing (4.52), the required IDDES length scale which combines the DDES and WMLES branches can be implemented as:

$$l_{hyb} = \tilde{f_d}(1 + f_e)l_{RANS} + (1 - \tilde{f_d})l_{LES} \tag{4.55}$$

As noted in [145], f_e in (4.45) should become insignificant (i.e close to 0) in cases when the mesh is sufficient for a wall-resolved LES or when the IDDES model given by (4.55) performs as the background RANS model. For simulations with inflow turbulence, $r_{dt} \ll 1$. This returns f_{dt} close to 1.0 and thus $\tilde{f_d}$ is equal to f_B. The length scale in (4.55) reduces to $l_{hyb} = l_{WMLES}$. In the absence of turbulent inflow, f_e is zero and (4.55) reduces to $l_{hyb} = \tilde{l}_{DDES}$.

SST k-ω Delayed Detached Eddy Simulation

Initial modifications to the SST-DES model were presented by Menter et al in [136]. However, the SST-DDES version implemented in MaPFlow is that presented in Gritskevich et al [146]. As stated previously, the primary concern with the initial DES formulation was the unwanted switch to LES mode close to the wall which led to Grid Induced Separation. The shielding function initially developed in [137] was considered generic enough to be used in most RANS turbulence models. However, in [146] it is shown that the shielding function is essentially calibrated for the Spalart-Allmaras model and requires different calibration to be used with the SST model.

The governing equations for the SST-DDES model are the same k and ω equations used in the original SST model (Section 2.6.2), which are repeated here:

$$\frac{\partial(\rho k)}{\partial t} + \frac{\partial(\rho u_j k)}{\partial x_j} = P_k - D_k + \frac{\partial}{\partial x_j}[(\mu + \sigma_\kappa \mu_t)\frac{\partial k}{\partial x_j}] \tag{4.56}$$

$$\frac{\partial(\rho \omega)}{\partial t} + \frac{\partial(\rho u_j \omega)}{\partial x_j} = \frac{\gamma}{\mu_t}P_k - D_\omega + \frac{\partial}{\partial x_j}[(\mu + \sigma_\omega \mu_t)\frac{\partial \omega}{\partial x_j}] + 2(1 - F_1)\frac{\rho\sigma_{\omega 2}}{\omega}\frac{\partial k}{\partial x_j}\frac{\partial \omega}{\partial x_j} \tag{4.57}$$

P_k and D_k are both modified in the DDES version, whereas D_ω is not:

$$P_k = min(\mu_t S^2, 10 \cdot C_\mu \rho k \omega) \tag{4.58}$$

$$D_k = \rho\sqrt{k^3}/l_{DDES} \tag{4.59}$$

$$D_\omega = \beta^* \rho \omega^2 \tag{4.60}$$

The original definition for the turbulent molecular viscosity reads:

$$\mu_t = \frac{\rho \alpha_1 k}{max(\alpha_1 \omega, \Omega F_2)} \tag{4.61}$$

However, the newer definition for μ_t presented in [147] can also be used:

$$\mu_t = \frac{\rho \alpha_1 k}{max(\alpha_1 \omega, S F_2)} \tag{4.62}$$

Blending functions and other parameters are the same as those used in the original SST model:

$$F_1 = tanh(arg_1^4) \tag{4.63}$$

$$arg_1 = min\left(max\left(\frac{\sqrt{k}}{\beta\omega d}, \frac{500\nu}{d^2\omega}\right), \frac{4\rho\sigma_{\omega 2}k}{CD_{k\omega}d^2}\right) \tag{4.64}$$

$$CD_{k\omega} = max(2\rho\sigma_{\omega 2}\frac{1}{\omega}\frac{\partial k}{\partial x_j}\frac{\partial \omega}{\partial x_j}, 10^{-20}) \tag{4.65}$$

$$F_2 = tanh2(arg_2^2) \tag{4.66}$$

$$arg_2 = max\left(2\frac{\sqrt{k}}{\beta\omega d}, \frac{500\nu}{d^2\omega}\right) \tag{4.67}$$

The length scale l_{DDES} in (4.59) reads:

$$l_{DDES} = l_{RANS} - f_d max(0, l_{RANS} - l_{LES}) \tag{4.68}$$
$$l_{LES} = C_{DES}\Delta \tag{4.69}$$
$$l_{RANS} = \frac{\sqrt{k}}{C_\mu \omega} \tag{4.70}$$
$$C_{DES} = C_{DES_1} \cdot F_1 + C_{DES_2} \cdot (1 - F_1) \tag{4.71}$$
$$\tag{4.72}$$

In (4.69), Δ is the mesh length scale. This is most often chosen as the maximum edge length of the cell (Section 4.3.1). The empiric blending function f_d in (4.68) is computed with the use of the following relations:

$$f_d = 1 - tanh\left[(C_{d_1} r_d)^{C_{d_2}}\right] \tag{4.73}$$

$$r_d = \frac{\nu_t + \nu}{\kappa^2 d_w^2 \sqrt{0.5 \cdot (S^2 + \Omega^2)}} \tag{4.74}$$

where S is the magnitude of the strain rate tensor and Ω is the magnitude of the vorticity tensor.

The constants are defined as follows:

$$\gamma_1 = \frac{\beta_1}{\beta^*} - \frac{\sigma_{\omega 1}\kappa^2}{\sqrt{\beta^*}} \tag{4.75}$$
$$\gamma_2 = \frac{\beta_2}{\beta^*} - \frac{\sigma_{\omega 2}\kappa^2}{\sqrt{\beta^*}} \tag{4.76}$$
$$\sigma_{\kappa 1} = 0.85$$
$$\sigma_{\omega 1} = 0.5$$
$$\sigma_{\kappa 2} = 1.00$$
$$\sigma_{\omega 2} = 0.856$$
$$\beta_1 = 0.075$$
$$\beta_2 = 0.0828$$
$$\alpha_1 = 0.31$$
$$\alpha_2 = 0.44$$
$$\beta^* = 0.09$$
$$\kappa = 0.41$$
$$C_\mu = 0.09$$
$$C_{DES_1} = 0.78$$
$$C_{DES_2} = 0.61$$
$$C_{d_1} = 20$$
$$C_{d_2} = 3$$

Constants without index are a blend of an inner (1) and outer (2) constant, defined by:

$$\varphi = F_1\varphi_1 + (1 - F_1)\varphi_2 \tag{4.77}$$

where ϕ_1 represents constant 1 and ϕ_2 represents constant 2.

SST k-ω Improved Delayed Detached Eddy Simulation

In addition to the calibration for the DDES approach for the SST model, in [146] a newer version is also presented which improves the near-wall capabilities of the DDES modification, named Improved Delayed Detached Eddy Simulation (IDDES).

The governing equations of the SST IDDES are presented in Section 4.3.2, with l_{DDES} in (4.59) being replaced by l_{IDDES}:

$$l_{IDDES} = \tilde{f}_d \cdot (1 + f_e) \cdot l_{RANS} + (1 - \tilde{f}_d) \cdot l_{LES} \tag{4.78}$$

$$l_{LES} = C_{DES}\Delta \tag{4.79}$$

$$l_{RANS} = \frac{\sqrt{k}}{C_\mu \omega} \tag{4.80}$$

$$C_{DES} = C_{DES_1} \cdot F_1 + C_{DES_2} \cdot (1 - F_1) \tag{4.81}$$

However, the definition for the length scale Δ is different than the one used in the SST-DDES model. Let $h_{max} = max(\Delta x, \Delta y, \Delta z)$. One then gets Δ for the IDDES model by:

$$\Delta = min\left[C_w max[d_w, h_{max}], h_{max}\right] \tag{4.82}$$

The empiric blending functions $\tilde{f}_d$ and f_e in (4.78) are computed with the use of the following relations:

$$\begin{aligned}
r_{dt} &= \frac{\nu_t + \nu}{\kappa^2 d_w^2 \sqrt{0.5 \cdot (S^2 + \Omega^2)}} \\
r_{dl} &= \frac{\nu}{\kappa^2 d_w^2 \sqrt{0.5 (S^2 + \Omega^2)}} \\
\alpha &= 0.25 - d_w / h_{max} \\
f_b &= min[2exp(-9\alpha^2), 1.0] \\
f_{dt} &= 1 - tanh\left[(C_{dt1} \cdot r_{dt})^{C_{dt2}}\right] \\
\tilde{f}_d &= max[(1 - f_{dt}), f_b] \\
f_t &= tanh\left((C_t^2 \cdot r_{dt})^3\right) \\
f_l &= tanh\left((C_l^2 \cdot r_{dl})^1 0\right) \\
f_{e1} &= \begin{cases} 2 \cdot exp(-11.09 \cdot \alpha^2), & \alpha \geq 0 \\ 2 \cdot exp(-9.0 \cdot \alpha^2), & \alpha < 0 \end{cases} \\
f_{e2} &= 1.0 - max(f_t, f_l) \\
f_e &= f_{e2} max[(f_{e1} - 1.0), 0.0]
\end{aligned} \tag{4.83}$$

Alternatively, a simplified version of IDDES can be utilized. In that case, f_e in (4.78) is set to zero, and thus the length scale l_{IDDES} becomes:

$$l_{IDDES} = \tilde{f}_d \cdot l_{RANS} + (1 - \tilde{f}_d) \cdot l_{LES} \tag{4.84}$$

The additional constants for the SST-IDDES model are:

$$\begin{gathered}
C_w = 0.15 \\
C_{dt_1} = 20 \\
C_{dt_2} = 3 \\
C_l = 5 \\
C_t = 1.87
\end{gathered}$$

4.4 Turbulent inflow

In order to generate inflow turbulence, the generator of J. Mann [148] is used. The inputs to the generator are the characteristics of the velocity field:

a. Γ: Parameter of the sheared spectral tensor

b. L: Length scale of the spectral velocity tensor

c. $\alpha\epsilon^{2/3}$: Product of the Kolmogorov constant (α) and the dissipation of turbulent kinetic energy (ϵ)

along with the spacings (Δx, Δy, Δz) and the number of points in each direction.

The output of the generator is a 3D box that contains the velocity fluctuations. Example of a box that was created using $\Delta x = \Delta y = \Delta z = 4m$ and 512, 128 and 128 elements in the x, y, and z directions respectively is shown in fig. 4.2, whereas examples of velocity fluctuation and vorticity contours are shown in fig. 4.3.

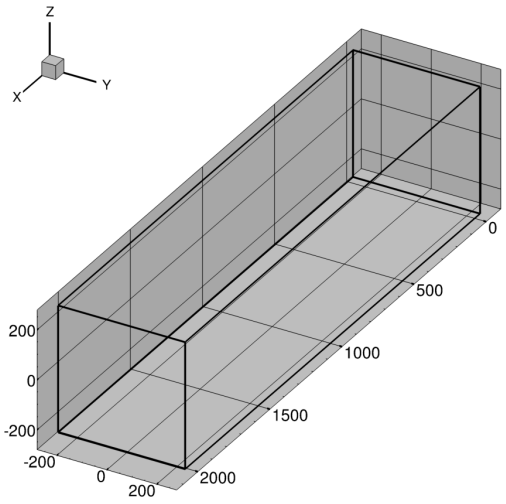

Figure 4.2: *Mann box with 512, 128 and 128 points in the x, y, and z axis and with* $\Delta x = \Delta y = \Delta z = 4m$

The most commonly adopted approach when applying pre-generated turbulent fluctuations in a computational domain is to superimpose the fluctuating velocities to the mean velocities at the inlet boundary. This approach requires that the resolution of the computational mesh on the upstream part be fine enough to resolve the turbulence all the way to the region of interest. However, since the region of interest is most often required to be located far away from the inlet in order to avoid boundary effects, this leads to a large number of mesh cells for the upstream region in order to preserve turbulence. This can raise the computational cost of a simulation significantly. Alternatively, the turbulent fluctuations can be imposed in the interior of the computational domain in a cross section located close to the region of interest. This saves computational resources and leads to less distorted turbulence impacting the region of interest. This approach was used by Gilling [33] for the simulation of turbulent flows over airfoils and by Troldborg et al in [38][39][40] for the simulation of atmospheric flows.

The effect of the velocity variances on the main equations is carried out via use of source terms. According to momentum theory, the force per unit volume required to accelerate the fluid from U to $U + U'$, where U and U' are vectors containing the three components of the mean and fluctuating velocity is [40]:

$$f_p = \frac{\rho U'}{\Delta n}\left(U_n + \frac{1}{2}U'_n\right) \tag{4.85}$$

In (4.85), U_n and U'_n are the magnitude of the mean and fluctuating velocity which are perpendicular to the turbulence plane. In [38] and [40], where actuator methods were considered, Δn is taken to be the mesh spacing normal to the actuator.

The source terms are not only applied on the turbulence plane locations. They are instead smeared in the direction normal to the turbulence plane using a one-dimensional Gaussian approach as:

$$\begin{aligned} f_e &= f_p * \eta_\epsilon \\ \eta_\epsilon(n) &= \frac{1}{\epsilon\sqrt{\pi}} exp\left[-\left(\frac{n - n_d}{\epsilon}\right)^2\right] \end{aligned} \tag{4.86}$$

where ϵ is a parameter that adjusts the concentration of the regularized load and $n - n_d$ is the normal distance from a mesh point to the turbulence plane. Besides adding the source terms to the momentum equations, the work of the source terms is also added to the energy equation as:

$$f_w = (f_{e,x}U + f_{e,y}V + f_{e,z}W) * \eta_\epsilon \tag{4.87}$$

where $f_{e,x}$, $f_{e,y}$ and $f_{e,z}$ are the momentum equation source terms for the three axis, calculated via (4.85) and (4.86)

Implementation in MaPFlow assumes that the Mann Box moves with velocity U_∞ (defined by the simulation) on the x-axis. The Mann Box is used in conjuction with the computational mesh. This means that the y and z axis represent the yz space, whereas the x axis represents time. Let i, j and k be the indexes for the x, y and z axis of the Mann Box. If Δt is the physical timestep, we then get:

$$t_{mann}(x) = (i-1)\Delta t \tag{4.88}$$

which is the discreet physical time t corresponding to each Mann Box i position.

Therefore, a random time t in the simulation is located between two i positions of the Mann Box. Similarly, each element of the computational mesh lies between two y planes and two z planes (j and k positions). In order to calculate the variance for each cell of the computational domain, the Mann Box values are interpolated in space and time. The implemented algorithm for a point P is as follows:

- Based on the y and z coordinates of the element P, the previous and next j and k planes of the Mann Box are located. Let j_p and j_n be the previous and next y planes and k_p and k_n the previous and next z planes.
- Based on the current physical time t, the previous and next x planes of the Mann Box are located. Let i_p and i_n be the previous and next x planes.
- A bilinear interpolation in space is carried out separately on i_p and i_n, using the j_p, j_n, k_p and k_n planes. This results in two variance values, one for i_p and one for i_n which correspond to $t_p = (i_p - 1)\Delta t$ and $t_n = (i_n - 1)\Delta t$.
- The variance value for time t is derived by using linear interpolation between t_p and t_n.

The resulting variances for the each mesh cell are used in (4.85), (4.86) and (4.87) in order to calculate the source terms for the momentum and energy equations.

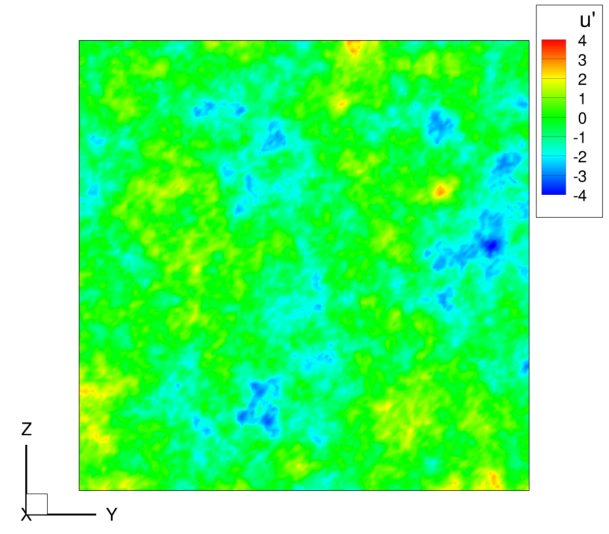

(a) u'

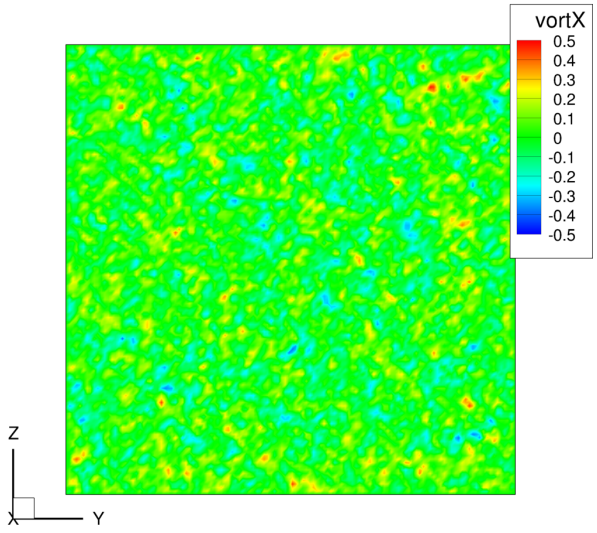

(b) *Vorticity on the x-axis*

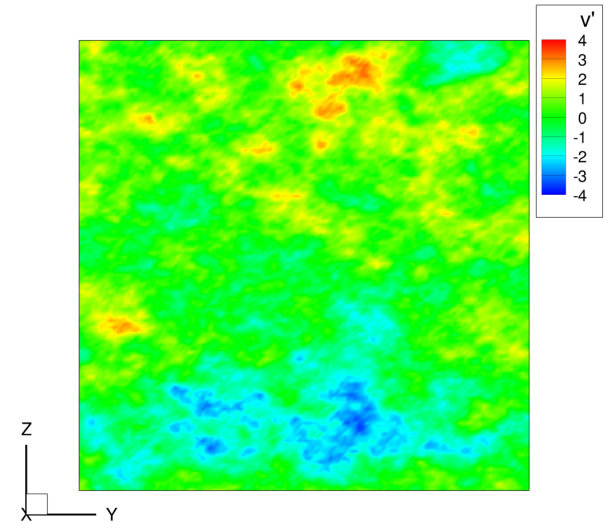

(c) v'

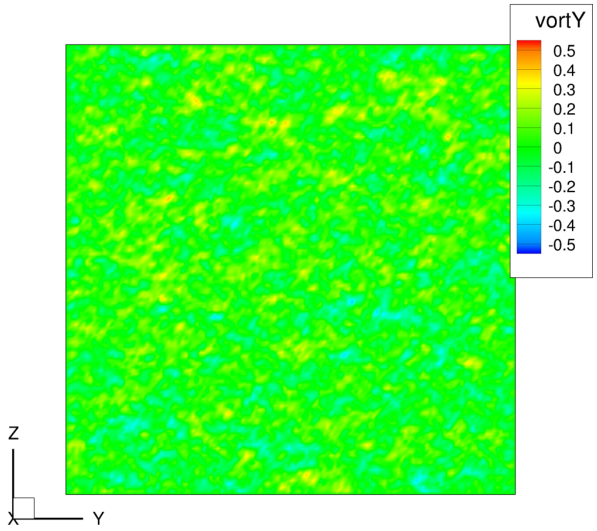

(d) *Vorticity on the y-axis*

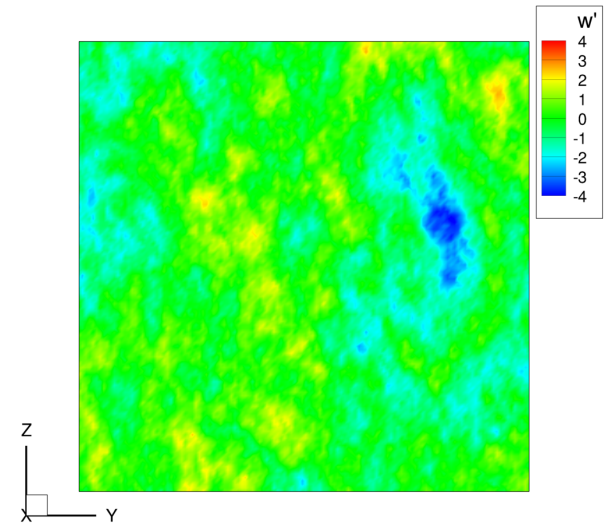

(e) w'

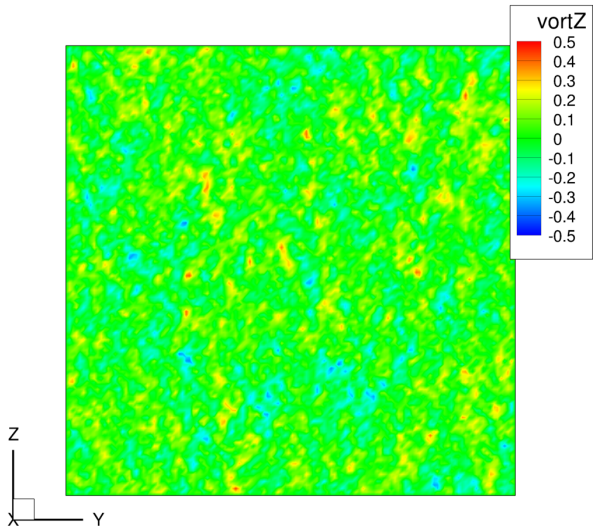

(f) *Vorticity on the z-axis*

Figure 4.3: *Contours of u', $'v'$, w' and vorticity on the three axes on a random x-slice of the Mann Box.*

This page intentionally left blank

Chapter 5

Transition modeling verification and validation

5.1 Introduction

In this Chapter, a comparative verification and validation of the transition models is made. The choice of the computational mesh is discussed in Section 5.2, whereas Section 5.3 contains the timestep dependence analysis for unsteady simulations. In Section 5.4, the various aspects of the boundary layer transition model are analyzed. Section 5.4.1 compares the different approaches for boundary layer calculation, as presented in Section 3.2.1, whereas in Section 5.4.2 the empirical criteria for transition prediction discussed in Section 3.2.2 are assessed. Similarly, in Section 5.5 the various aspects regarding the performance of transport equation transition models are discussed. For these models, correct definition of inflow turbulence parameters is crucial. Due to the local nature of the transport equations, it is important for the turbulence quantities in the wall region (i.e. airfoil/rotor blade) to have the appropriate levels. Defining suitable inflow values and counteracting turbulent decay imposed by the computational mesh are both equally important. The effect of these parameters is discussed in Section 5.5.1. Specifically for the γ-Re_θ and γ transition models, different local transition correlations are available. The effect of these correlations is assessed in Section 5.5.2. Finally, 2D airfoil cases are presented in Section 5.6, whereas 3D cases are presented in Section 5.7.

5.2 Computational mesh generation and resolution dependence

5.2.1 2D geometries

For two-dimensional simulations, O-type meshes were utilized. The domain inlet was set to at least 1000 chords away from the airfoil, in order to minimize farfield influence on viscous walls, while the first layer was set to values that guaranteed $y^+ \leq 1$ at all times. In the normal to the wall direction the cells were distributed using geometric expansion, with ratio always being less than 1.1.

It is useful to assess how mesh resolution affects the final solution of the solver. It was decided to present this part of the study only for one airfoil. However, the conclusions derived from this analysis can also be used for other 2D airfoil configurations. For this part of the analysis, a structured approach was adopted for mesh generation, even though the solver treats the mesh as unstructured. This was decided because the structured approach is more straightforward in regards to how the resolutions translate to the contour of the airfoil and the farfield, thus being more suitable for the first part of the mesh resolution analysis.

The NLF(1)-0416 airfoil is considered, at $Re = 4$ x 10^6, $Ma_\infty = 0.1$, $Tu_\infty = 0.15\%$, which corresponds to $N_{crit} = 7$ via (3.47). Example of a mesh is shown in fig. 5.1. This is a classic airfoil case for transition modeling validation on airfoils. Experimental aerodynamic loads as well as transition locations are available [4], thus forming a complete reference point. This airfoil is also proposed as a standard validation case for CFD laminar-turbulent transition modeling in the work of Coder [149], where many configurations that are of particular interest with regards to transition modeling are suggested. However, for this part of the analysis the focus is on mesh resolution convergence and not on prediction accuracy against experimental data. The analysis is performed on three angles: $\alpha = -6°$, $0°$, and $6°$.

The k-ω SST turbulence model is used, although similar results are expected when using the Spalart-Allmaras turbulence model. Regarding transition modeling, the original formulations for the γ-Re_θ and AFT transition models are used, presented in Section 3.3, and Section 3.5, respectively. Results for the γ model are omitted, since the model utilizes the same framework as the γ-Re_θ model and therefore exhibits similar behavior. Boundary layer transition modeling is tested using the e^N database method presented in Section 3.2.3, paired with the Falkner-Skan velocity profiles for boundary layer calculation, presented in Section 3.2.1. The reasoning behind the choice of boundary layer method is discussed in Section 5.4.1. For the AFT model and the e^N method, N_{crit} was set to 7 using Mack's formula (3.47).

The simulations utilized ambient turbulence terms to counteract turbulent decay, in addition to using the Kato-Launder production limiter for the SST model [150]. The details of turbulent parameter specification are discussed in Section 5.5.1. Ambient values were set to $Tu_{amb} = 0.15\%$ and $\omega_{amb} = 50\frac{U_\infty}{c}$, which corresponds to $(\mu_t/\mu)_{amb} = 0.27$. It should be noted that the usage of ambient turbulence terms does not affect the final outcome of the mesh resolution analysis. Similar results are expected when modified inlet turbulence values are used or when no particular handling of turbulence is adopted, besides the use of a standard turbulence model.

The employed mesh resolutions are presented in Table 5.1. The extra fine mesh was created first. In the normal direction, 256 elements were placed up to 0.1 chords away from the wall, 128 were placed in the region between 0.1 and 10 chords, and 128 were placed in the region between 10 and 1000 chords. After creating the extra fine mesh, each coarser level was created by removing every 2^{nd}, 4^{th}, and 8^{th} node in both dimensions. For the considered test case, the extra fine mesh had $y^+(1) < 0.1$ whereas the fine mesh had $y^+(1) < 0.2$. For the transport equation transition models, the solver needs to be able to accurately solve the thin laminar boundary layer [94]. Ensuring proper y^+ values is thus crucial. However, the meshes utilized should not yield excessively low y^+ values, as the simulation will not sufficiently converge.

The results from the analysis are presented in Table 5.2. Each row lists the deviations in lift and drag coefficients with respect to the results of the extra fine mesh. The results of the fine mesh have deviations of 2% or less. The medium mesh is able to produce adequate results for $\alpha = 0°$. However, for the other angles of attack the discrepancies are higher due to errors induced by insufficient mesh resolution.

For the second part of the mesh dependence analysis, a hybrid mesh was generated based on the baseline structured mesh. Up to 0.1 chords away from the airfoil, the two meshes had the same number of wrap around and normal elements. This was achieved by keeping this near wall region structured-like. The rest of the domain was unstructured, using quad elements. This approach is more suitable for multi-element configurations. Trying to use a structured approach in such cases can severely deteriorate the quality of the mesh, especially for geometries where two bodies overlap on one of the axes (for example main element-flap configurations with small or negative flap overhang). Hybrid meshes can have independent structured-like boundary layer regions around each of the elements, while filling the rest of the domain with unstructured quads. An example of the hybrid mesh for the NLF(1)-0416 airfoil is shown in fig. 5.2, whereas fig. 5.3 shows the mesh used for the NLR-7301 airfoil with flap. The results from the structured and hybrid meshes for the NLF(1)-0416 are shown in Table 5.3, with the hybrid mesh having approximately 110 thousand elements. It is evident that the results are almost identical and thus both structured and unstructured approaches can be used. Using unstructured meshes with less elements produced results that deviated from those using the baseline structured mesh. This led to the

choice of the 110 thousand mesh as the hybrid baseline, which when compared to the 130 thousand element structured mesh can be up to 15% faster for the same flow case.

Based on these observations, the 512 x 256 mesh with the guidelines discussed in this section will be used for single element configurations, whereas multi-element meshes will be created based on the hybrid mesh guidelines. It should be noted that for airfoil cases where a wide range of Re numbers is considered, the first layer spacing of the employed mesh should be adjusted accordingly between different Re. Ensuring that $y^+ < 1$ for moderate Re flows does not guarantee that the same will hold true for higher Re. However, excessive refinement close to the wall should be avoided due to the fact that lower Re cases may reach regions where $y^+ << 1$, which could lead to convergence problems.

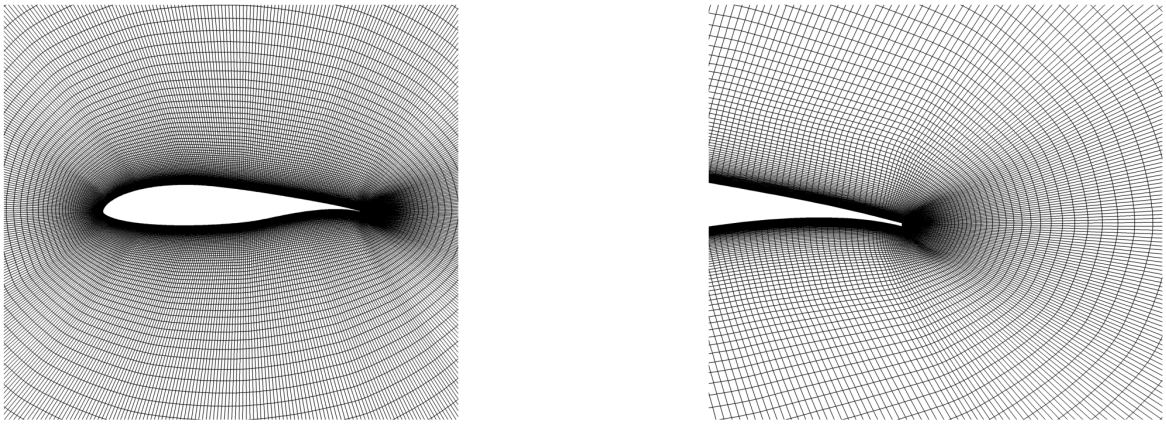

(a) *Partial view* **(b)** *Trailing edge detail*

Figure 5.1: *NLF(1)-0416, 130 thousand element structured mesh*

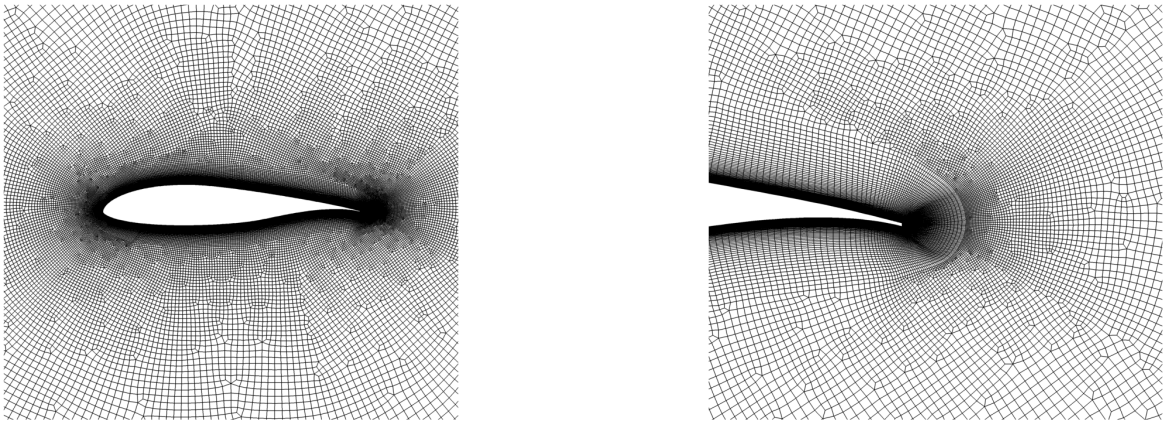

(a) *Partial view* **(b)** *Trailing edge detail*

Figure 5.2: *NLF(1)-0416, 110 thousand element hybrid mesh*

5.2.2 3D geometries

Regarding 3D simulations, the meshes for wing-like geometries were created from the corresponding 2D meshes by extrusion in the spanwise direction. For wind turbine blades the meshes were created from scratch, as they cannot be extruded from a 2D geometry. For multi-bladed rotors, only one of the blades was simulated using periodic boundary conditions. The domain extent was set to at least 50 rotor diameters away from the viscous walls. First layer spacing was again set to values that guaranteed $y^+ < 1$. Mesh examples for the NREL Phase

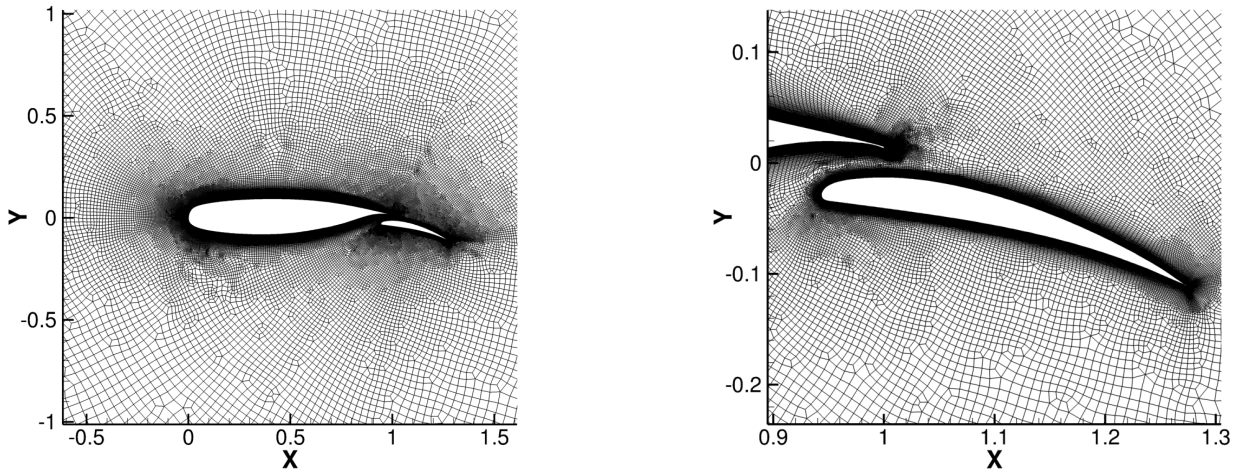

(a) *Partial view* **(b)** *Flap detail*

Figure 5.3: *NLR-7301, 150 thousand element hybrid mesh*

Table 5.1: *Resolutions for the 2D structured mesh dependence study*

Mesh Level	Wrap-around elements	Normal elements	Total elements
Coarse	128	64	8192
Medium	256	128	32768
Fine	512	256	131072
Extra Fine	1024	512	524288

VI Rotor are shown in fig. 5.4. This particular wind turbine has two rotating blades so the computational mesh is build around one blade with 180 degrees rotational periodicity. Other wind turbine meshes were created using a similar strategy. Openly available meshes were also used in some cases.

It is again useful to assess how mesh resolution affects the final solution of the solver. The NREL Phase VI Rotor is chosen as the test case for this analysis. The employed resolutions are listed in Table 5.4. Unfortunately, an even finer mesh than the fine mesh listed on this table would contain 32 million elements, which is prohibitively expensive in regards to required computational time. The flow conditions were $U_{wind} = 7m/s$, $Ma_\infty = 0.11$, $\nu_\infty = 1.56$ x 10^{-5}, $Tu_\infty = 0.07\%$, which corresponds to $N_{crit} = 9$. The rotational speed was set to 72 RPM. Ambient turbulence terms were again used, similar to what was used for the 2D mesh dependence analysis. For this simulation, $Tu_{amb} = 0.07\%$, $\omega_{amb} = 50\frac{U_\infty}{c}$, with c being equal to 5 m which is the rotor radius. The rationale behind the ambient terms is explained in detail in Section 5.5.1.

Pressure coefficients are compared to experimental data in fig. 5.5-5.9. Clearly, the fine mesh outperforms both the medium and coarse meshes, which exhibit significant deviations from the experiments and the fine mesh, especially for $r/R = 0.63$ and 0.80. On the contrary, results using the fine mesh are adequately close to the experiments at all spanwise positions. For all Wind Turbine rotor blades presented in this thesis, the fine mesh resolution is used.

Table 5.2: *Deviations in lift and drag coefficients for varying mesh resolution with respect to the results of the extra fine mesh (see Table 5.1). NLF(1)-0416 airfoil at $Re = 4\ x\ 10^6$, $Ma_\infty = 0.1$, $\alpha = -6$, 0, and 6°. Ambient turbulence source terms used. $Tu_{amb} = 0.15\%$, $\omega_{amb} = 50\frac{U_\infty}{c}$.*

Mesh Level	C_l, $\alpha = -6°$	C_d, $\alpha = -6°$	C_l, $\alpha = 0°$	C_d, $\alpha = 0°$	C_l, $\alpha = 6°$	C_d, $\alpha = 6°$
Coarse	6.70%	22.54%	1.09%	3.13%	0.17%	10.20%
Medium	0.73%	0.98%	0.71%	1.04%	0.51%	0.28%
Fine	0.19%	0.98%	0.32%	0.01%	0.19%	0.11%

(a) *Fully turbulent*

Mesh Level	C_l, $\alpha = -6°$	C_d, $\alpha = -6°$	C_l, $\alpha = 0°$	C_d, $\alpha = 0°$	C_l, $\alpha = 6°$	C_d, $\alpha = 6°$
Coarse	6.76%	27.58%	0.60%	10.15%	0.20%	16.29%
Medium	0.61%	2.30%	0.55%	0.01%	0.34%	0.85%
Fine	0.57%	1.15%	0.35%	0.01%	0.01%	0.30%

(b) e^N *method with Orr-Sommerfeld database*

Mesh Level	C_l, $\alpha = -6°$	C_d, $\alpha = -6°$	C_l, $\alpha = 0°$	C_d, $\alpha = 0°$	C_l, $\alpha = 6°$	C_d, $\alpha = 6°$
Coarse	0.30%	25.35%	1.35%	1.78%	1.78%	41.62%
Medium	0.86%	1.41%	0.78%	1.78%	1.21%	21.18%
Fine	0.56%	1.41%	0.19%	0.01%	0.10%	0.68%

(c) γ-Re_θ *transition model*

Mesh Level	C_l, $\alpha = -6°$	C_d, $\alpha = -6°$	C_l, $\alpha = 0°$	C_d, $\alpha = 0°$	C_l, $\alpha = 6°$	C_d, $\alpha = 6°$
Coarse	4.45%	22.41%	0.95%	8.77%	2.5%	35.01%
Medium	0.53%	2.30%	0.51%	1.75%	1.44%	15.40%
Fine	0.28%	0.01%	0.16%	1.75%	0.41%	1.21%

(d) *AFT transition model*

Table 5.3: *Deviations in lift and drag coefficients using the structured and hybrid fine meshes with respect to the results of the extra fine mesh. NLF(1)-0416 airfoil at $Re = 4\ x\ 10^6$, $Ma_\infty = 0.1$, $\alpha = -6$, 0, and 6°. Ambient turbulence source terms used. $Tu_{amb} = 0.15\%$, $\omega_{amb} = 50\frac{U_\infty}{c}$. The structured fine mesh has 512 wrap-around and 256 normal elements, resulting in approximately 130 thousand elements (see Table 5.1). The hybrid fine mesh has 512 wrap-around elements, 128 prismatic elements in the region up to 0.1 chords away from the wall, and the rest of the outer region unstructured, resulting in approximately 110 thousand elements.*

Mesh Level	C_l, $\alpha = -6°$	C_d, $\alpha = -6°$	C_l, $\alpha = 0°$	C_d, $\alpha = 0°$	C_l, $\alpha = 6°$	C_d, $\alpha = 6°$
Structured, 130k elements	0.19%	0.98%	0.32%	0.01%	0.19%	0.11%
Hybrid, 110k elements	0.27%	0.01%	0.31%	0.01%	0.25%	0.16%

Table 5.4: *Resolutions for the 3D structured mesh dependence study*

Mesh Level	**Blade Wrap-around**	**Blade Spanwise**	**Blade Normal**	**Tip x-axis**	**Tip y-axis**	**Tip z-axis**	**Total**
Coarse	64	32	32	16	32	16	73728
Medium	128	64	64	32	64	32	589824
Fine	256	128	128	64	128	64	4718592

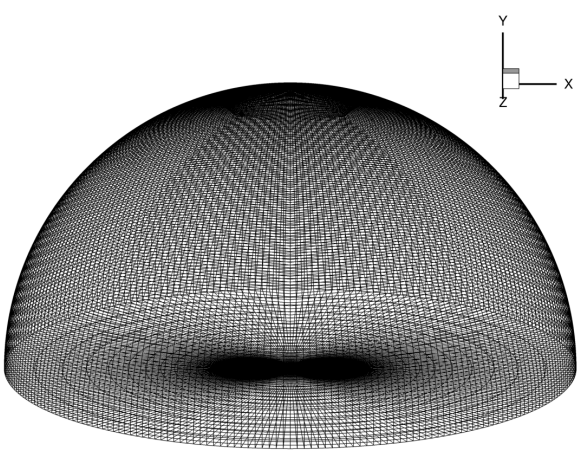

(a) *3D computational domain*

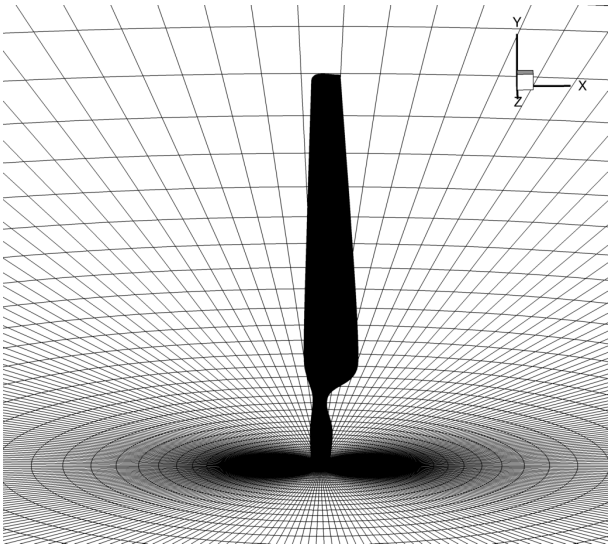

(b) *Blade close-up*

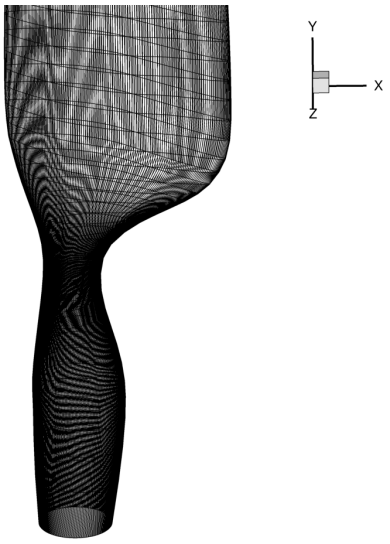

(c) *Root close-up*

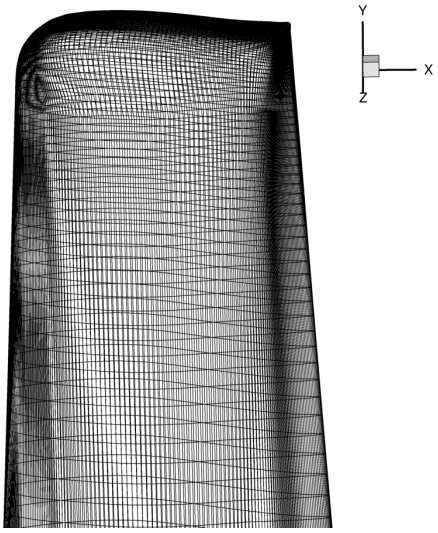

(d) *Tip close-up*

Figure 5.4: *NREL Phase VI Rotor, 256(wrap-around) x 128(normal) x 128(spanwise) element mesh*

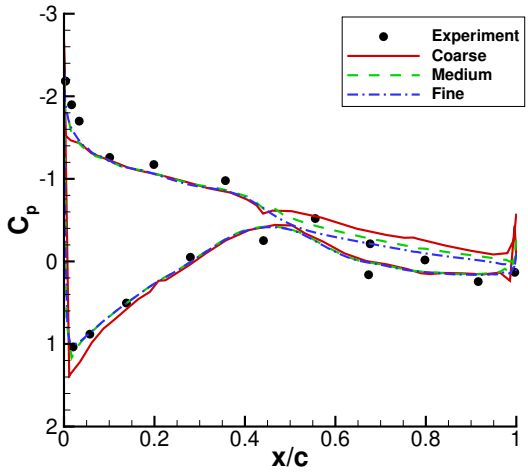

(a) *Fully turbulent*

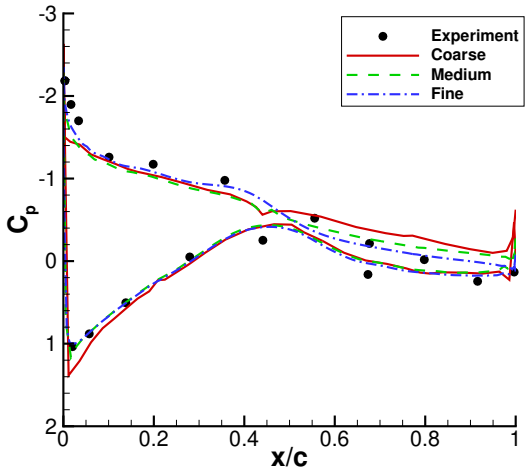

(b) *Boundary layer transition,* e^N

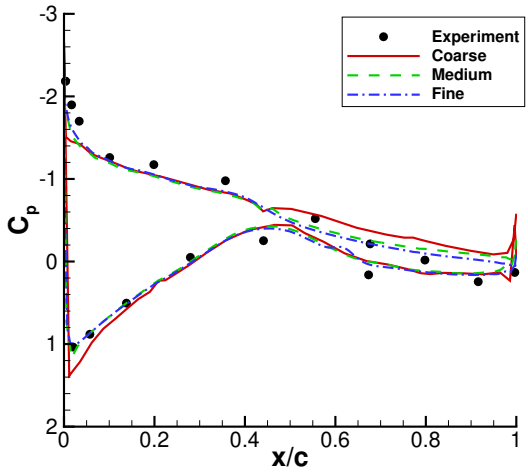

(c) γ-Re_θ

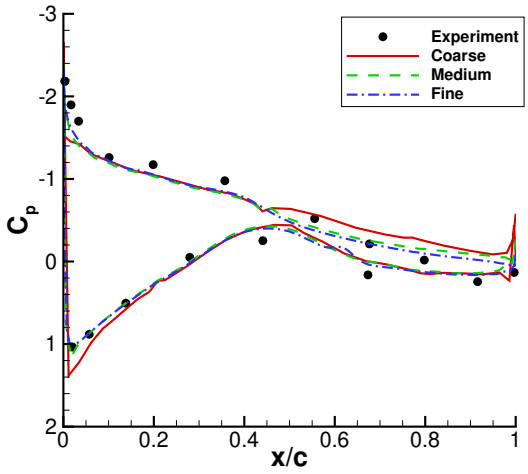

(d) γ

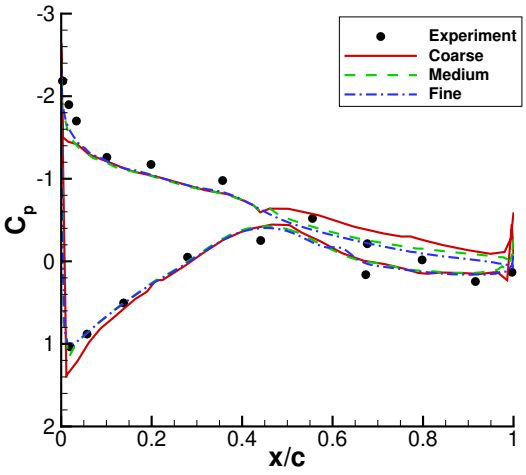

(e) *AFT*

Figure 5.5: *Effect of mesh resolution. NREL Phase VI rotor,* $U_{wind} = 7m/s$, $Ma_\infty = 0.11$, $Tu_{amb} = 0.07\%$, $\omega_{amb} = 50\frac{U_{wind}}{radius}$, $\nu_\infty = 1.56\ x\ 10^{-5}$, $\omega = 75\ rpm$. *Pressure coefficient at* $r/R = 0.3$. *Comparison with experimental data [2].*

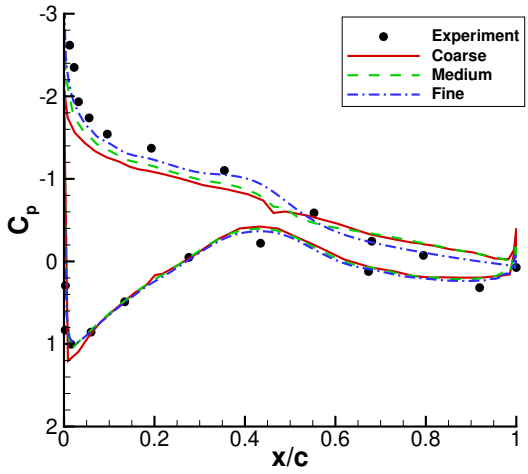

(a) *Fully turbulent*

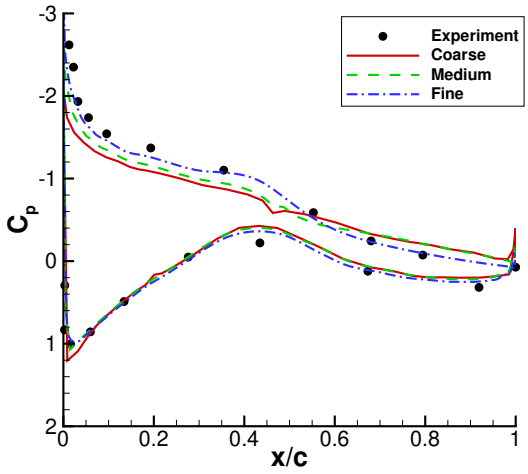

(b) *Boundary layer transition,* e^N

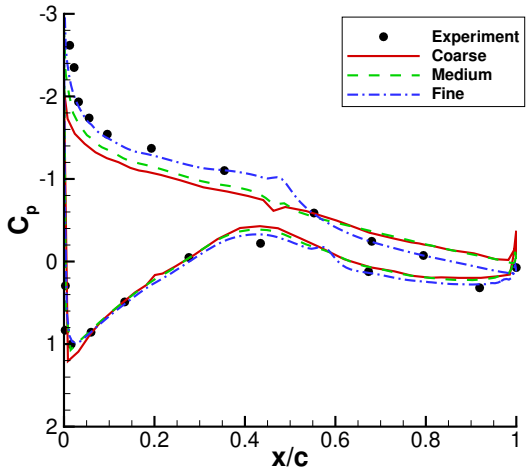

(c) γ-Re_θ

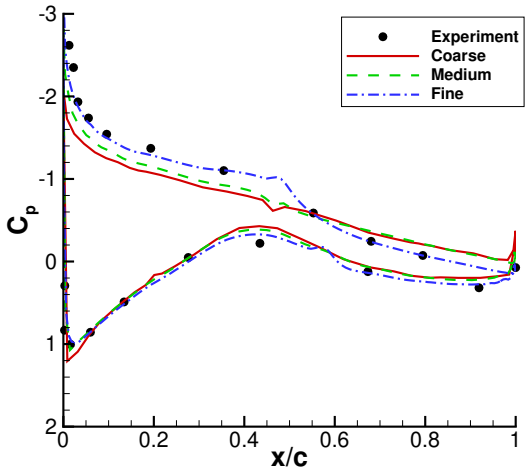

(d) γ

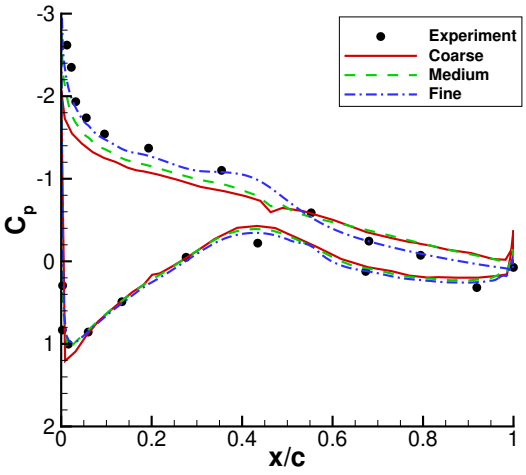

(e) *AFT*

Figure 5.6: *Effect of mesh resolution. NREL Phase VI rotor,* $U_{wind} = 7m/s$, $Ma_\infty = 0.11$, $Tu_{amb} = 0.07\%$, $\omega_{amb} = 50\frac{U_{wind}}{radius}$, $\nu_\infty = 1.56\ x\ 10^{-5}$, $\omega = 75\ rpm$. *Pressure coefficient at* $r/R = 0.47$. *Comparison with experimental data [2].*

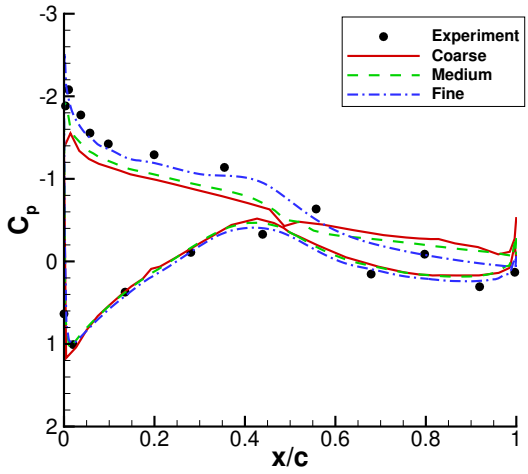

(a) *Fully turbulent*

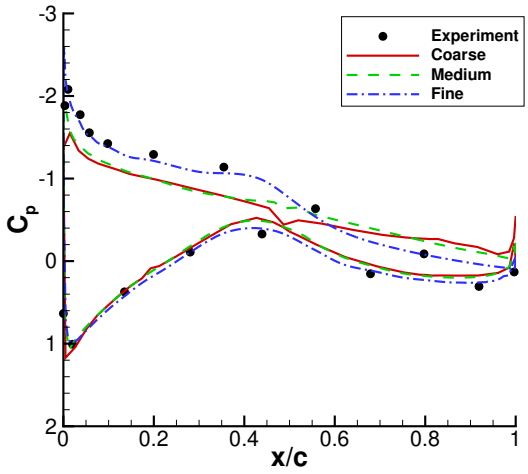

(b) *Boundary layer transition,* e^N

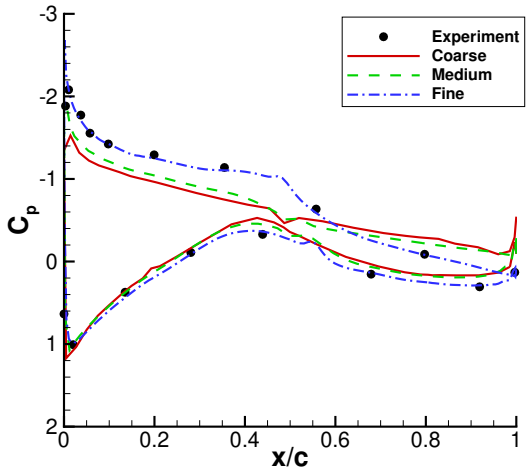

(c) γ-Re_θ

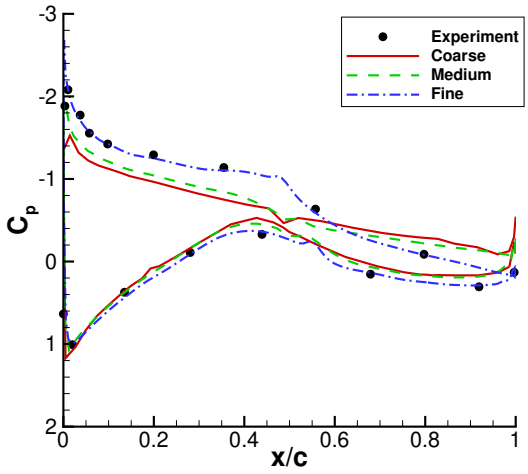

(d) γ

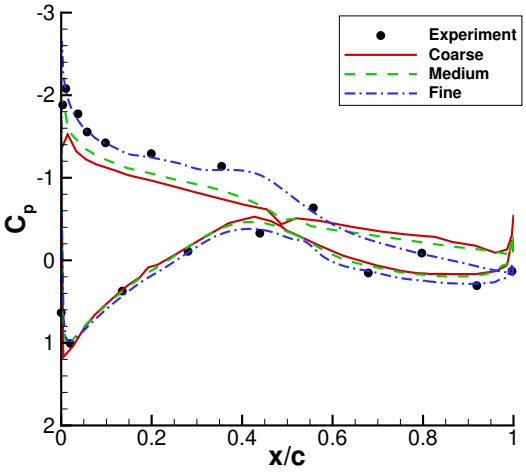

(e) *AFT*

Figure 5.7: *Effect of mesh resolution. NREL Phase VI rotor,* $U_{wind} = 7m/s$, $Ma_\infty = 0.11$, $Tu_{amb} = 0.07\%$, $\omega_{amb} = 50\frac{U_{wind}}{radius}$, $\nu_\infty = 1.56\ x\ 10^{-5}$, $\omega = 75\ rpm$. *Pressure coefficient at* $r/R = 0.63$. *Comparison with experimental data [2].*

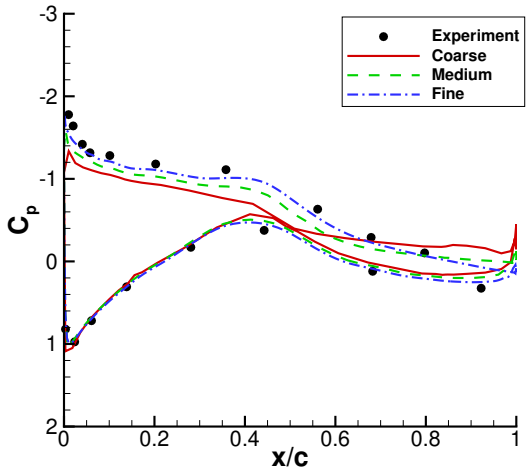

(a) *Fully turbulent*

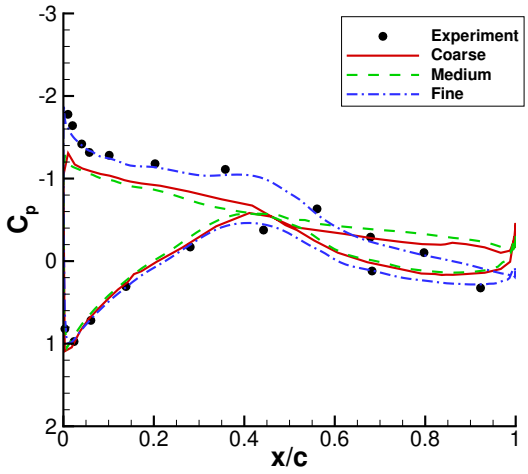

(b) *Boundary layer transition,* e^N

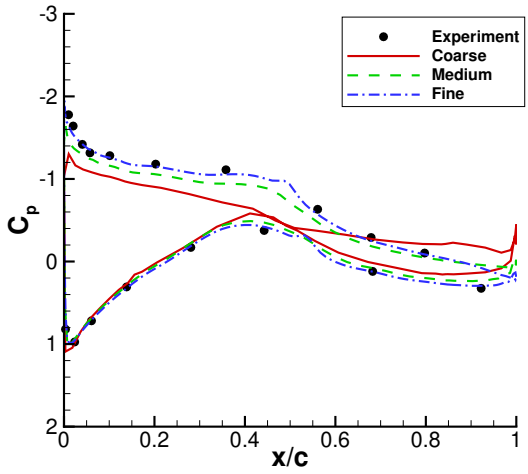

(c) γ-Re_θ

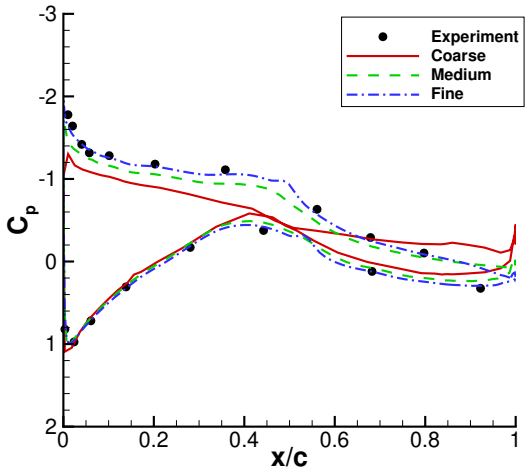

(d) γ

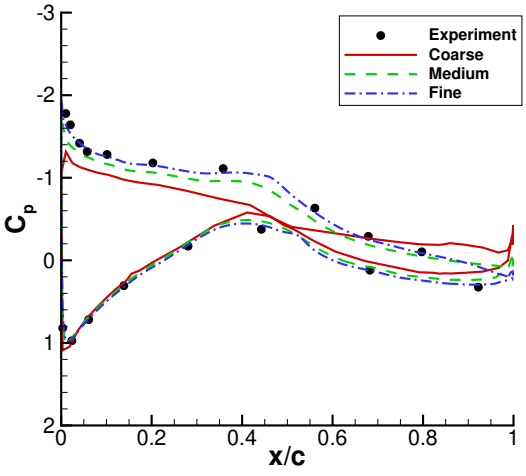

(e) *AFT*

Figure 5.8: *Effect of mesh resolution. NREL Phase VI rotor,* $U_{wind} = 7m/s$, $Ma_\infty = 0.11$, $Tu_{amb} = 0.07\%$, $\omega_{amb} = 50\frac{U_{wind}}{radius}$, $\nu_\infty = 1.56\ x\ 10^{-5}$, $\omega = 75\ rpm$. *Pressure coefficient at* $r/R = 0.80$. *Comparison with experimental data [2].*

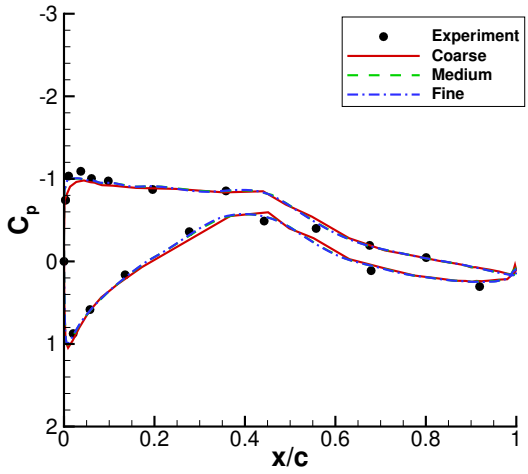

(a) *Fully turbulent*

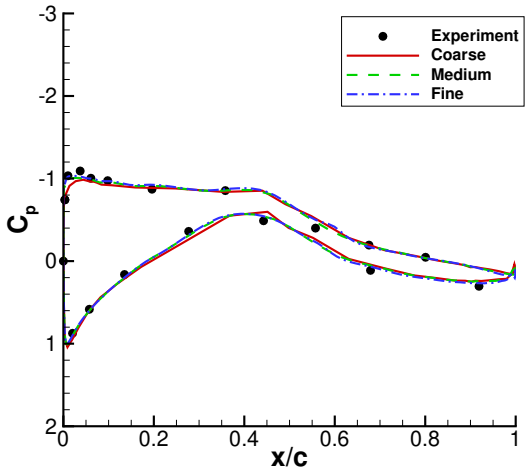

(b) *Boundary layer transition,* e^N

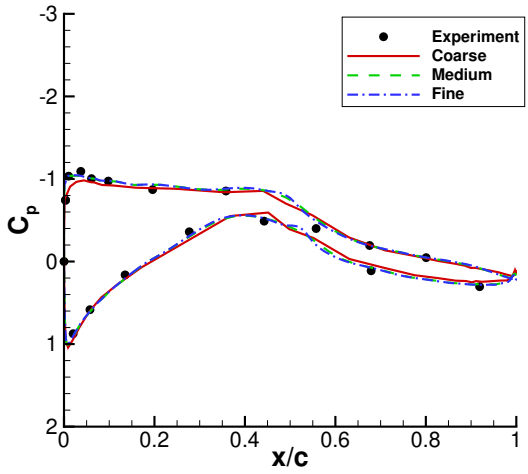

(c) γ-Re_θ

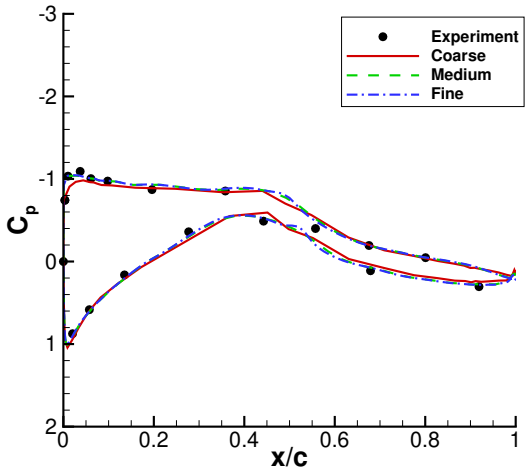

(d) γ

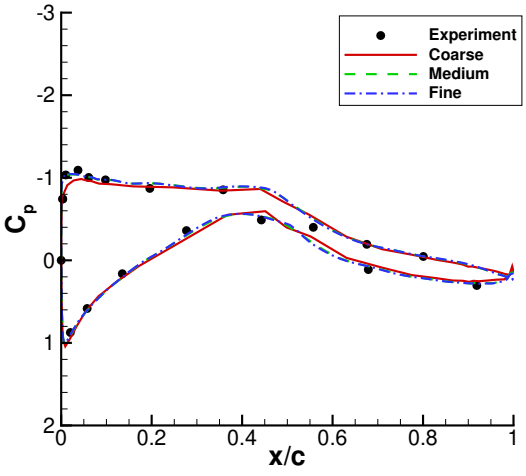

(e) *AFT*

Figure 5.9: *Effect of mesh resolution. NREL Phase VI rotor,* $U_{wind} = 7m/s$, $Ma_\infty = 0.11$, $Tu_{amb} = 0.07\%$, $\omega_{amb} = 50\frac{U_{wind}}{radius}$, $\nu_\infty = 1.56\ x\ 10^{-5}$, $\omega = 75\ rpm$. *Pressure coefficient at* $r/R = 0.95$. *Comparison with experimental data [2].*

5.3 Timestep dependence

For unsteady calculations, it is useful to assess the influence of the employed physical timestep. The NLF(1)-0416 airfoil at $Re = 4$ x 10^6, $Ma = 0.1$ and $Tu_\infty = 0.15\%$ is considered. Angle of attack was set to 15°. This angle is located in the post stall region and thus oscillations are expected. The simulations were run in free transition using the γ-Re_θ model. This was chosen because fully turbulent simulations are more amenable to a timestep dependence analysis due to the absence of transition locations that can influence the final results. In the context of transitional simulations, transition locations should also converge with decreasing timestep in order to provide timestep independent results.

Results are presented in fig. 5.10. It is evident that different timestep values may produce oscillations and may also alter the mean value of the results. For timesteps of 0.002 and 0.001 nondimensional units, the results are similar in mean value and barely show any oscillations. For transitional unsteady computations in this thesis, the timestep of 0.002 nondimensional units will be used.

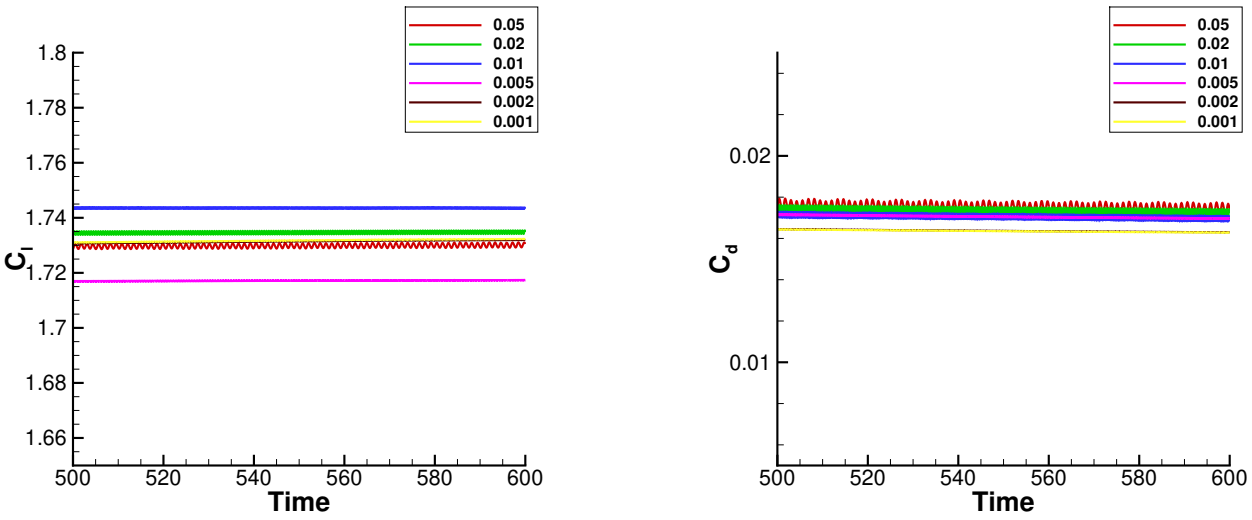

(a) C_l **(b)** C_d

Figure 5.10: *Timestep dependence analysis. NLF(1)-0416 airfoil at* $Re = 4\ x\ 10^6$, $M = 0.1$, $Tu_{amb} = 0.15\%$, $\omega_{amb} = 50\frac{U_\infty}{c}$, $\alpha = 15°$. *Transitional simulations using the* γ-Re_θ *model.*

5.4 Boundary layer transition model aspects

5.4.1 Evaluating the available boundary layer calculation approaches

In this section, boundary layer results from the approaches discussed in Section 3.2.1 are compared. The investigation is carried out for the DU-00-W212 airfoil at Re = 15 x 10^6, Ma = 0.08, Tu_∞ = 0.3346% ($N_{crit} = 5.25$) and an angle of attack of 4°. When extracting the boundary layer characteristics from the CFD solution, mesh resolution within the boundary layer is crucial. The baseline mesh follows the guidelines presented in Section 5.2. Variants of the baseline mesh were generated, with increasing number of cells in a region close to the wall (50,75 and 100 cells in the normal direction). In order to ensure that the boundary layer will be contained in the refined area, the width of this region was taken to be 0.01 length units. However the height of the first cell as well as the number of cells outside of this region remained constant ($h = 5 \cdot 10^{-6}$ chords, yielding $y^+ < 1$). It is evident that the integral boundary layer approach (using either the Polhausen method or the two boundary layer equations with the Falkner-Skan profiles) do not require additional boundary layer refinement, since they only utilize the C_p distribution. Nevertheless, all methods were tested using all created meshes. The purpose of this comparison is to highlight differences in boundary layer prediction up to an a priori prescribed transition point. In the simulations, transition locations were fixed at the locations predicted using XFOIL [3] for the same flow conditions.

Boundary layer results from the Direct CFD boundary layer solution (noted as *RANS BL*), the Polhausen one-parameter profile, and the Falkner-Skan two-parameter profiles are compared to reference XFOIL results in fig. 5.11. The distributions of H and Re_θ are considered. Only the lower side is shown along which the differences are more pronounced compared to those over the upper side. As expected, since mesh resolution within the boundary layer does not affect the surface pressure distribution, results from the Polhausen and Falkner-Skan profiles remain the same for all mesh resolutions, as shown in fig. 5.11a. On the contrary, fig. 5.11b shows that the results that are obtained directly from the CFD data depend on the mesh resolution. In fact, the comparison indicates that a significantly finer boundary layer region than the baseline is required in order to achieve sufficient mesh convergence. Having poor resolution leads to overall lower H levels. However, the converged results obtained from the CFD data closely resemble those from XFOIL and those based on the Falkner-Skan profiles. In contrast to the CFD data and Falkner-Skan approaches, use of the Polhausen profile has a slightly different trend, exhibiting an overall lower H level at all mesh resolutions and an earlier rise at $x/c = 0.3$. In a free transition scenario, using the Polhausen method would possibly lead to upstream transition prediction with respect to the Falkner-Skan and CFD data predictions for the same transition criterion.

While the above confirms that the necessary information can be obtained directly from the CFD solution, convergence of said solution is a critical issue. In fig. 5.12a-5.12b, the convergence of the pressure and H distributions during a simulation is shown by cross-plotting the difference of the current iteration from the final solution, which in this case was obtained at 20000 steady-state iterations. Since the pressure converges fast, transition predictions based on the solution of the boundary layer equations will converge equally fast. On the contrary, use of direct integration requires all cells in the boundary layer regions to also converge, thus increasing the overall computational cost.

As a result of the above analysis, the option of using the Falkner-Skan boundary layer solution will be primarily used for boundary layer calculation. This choice does not eliminate the possibility of using direct integration in other applications. One such application is transition prediction in transonic airfoils. The profiles used in the boundary layer equation approaches are developed for incompressible flow. In order to calculate the boundary layer characteristics in transonic flows, CFD data are needed. However, it is important to have sufficient mesh resolution and monitor convergence.

5.4.2 Evaluating available transition criteria

In this section, the empirical transition criteria described in Section 3.2.2 are compared in the context of boundary layer transition. Based on what was discussed in Section 5.4.1, the Falkner-Skan profiles are used for boundary layer calculation. Once more the NLF(1)-0416 at Re = 4 x 10^6, $Ma_\infty = 0.1$, Tu_∞ = 0.15% ($N_{crit} = 7$) is chosen because transition locations are available from the experiment [4]. The mesh chosen is the baseline one, as described in Section 5.2. Ambient turbulence terms are employed (Section 5.5.1), even though they do not have a significant effect in boundary layer transition simulations. The main purpose of these source terms is to counteract turbulent decay in the freestream, ensuring that adequate turbulence levels reach the airfoil. However, this only affects boundary layer cells and has little effect on the final pressure coefficient, which is the main parameter required for boundary layer calculation. Nevertheless, primarily for consistency reasons, it was decided to include the ambient terms.

The results are presented in fig. 5.13. The Granville and Michel criteria seem to predict transition downstream for higher angles of attack, which is not the case when using the variants of the e^N method or the AHD criterion. On the other hand, the former criteria are able to give a very accurate prediction at $\alpha = 0°$, in contrast to the

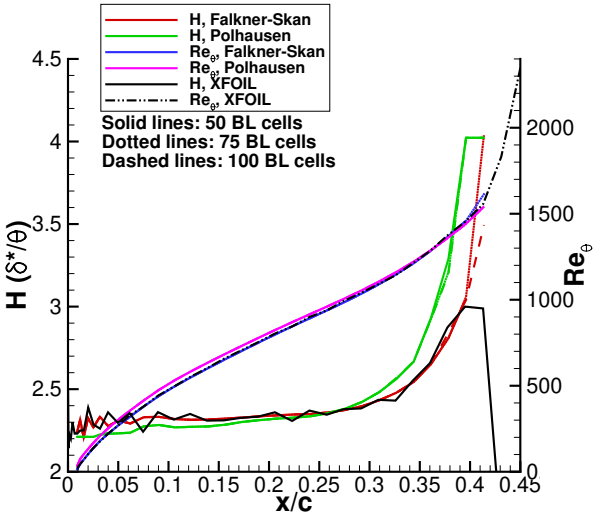

(a) *Results obtained by solving the boundary layer equations*

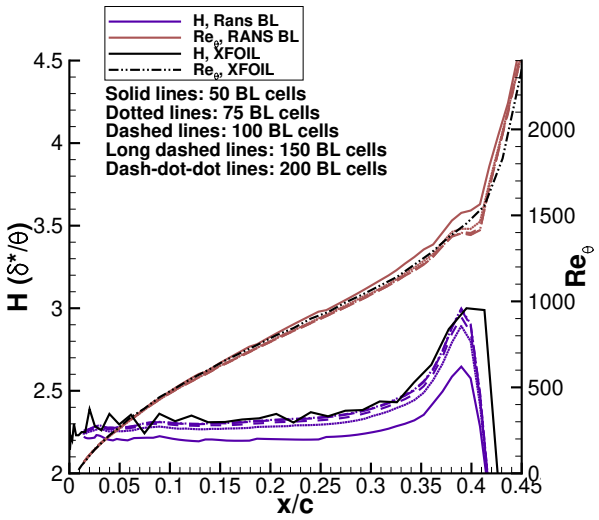

(b) *Results obtained by integrating the CFD flow data*

Figure 5.11: *H and Re_θ distributions on the lower side of DU-00-W212 airfoil at $Re = 15\ x\ 10^6$, $M = 0.08$, $Tu_\infty = 0.3346\%$, $\alpha = 4°$, using different mesh resolutions inside the boundary layer. Comparison with results using XFOIL [3].*

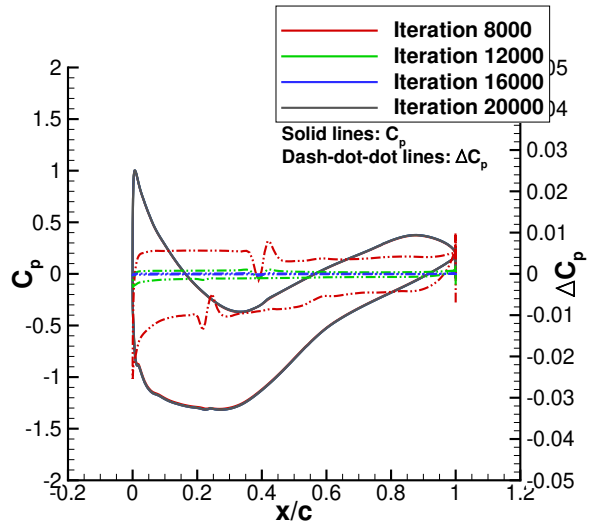

(a) *C_p convergence.*

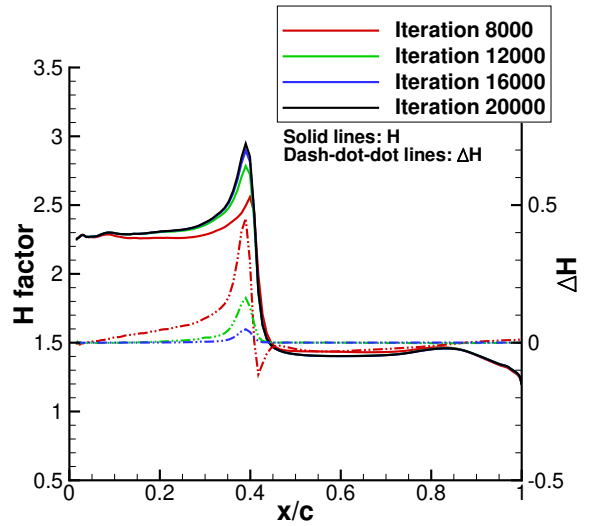

(b) *H factor convergence*

Figure 5.12: *C_p and H factor convergence rate, CFD flow boundary layer. Comparison between the final and earlier iterations of the solver on the DU-00-W212 airfoil at $Re = 15\ x\ 10^6$, $M = 0.08$, $Tu_\infty = 0.3346\%$, $\alpha = 4°$. C_p converges faster than the H factor and thus boundary layer equations, which are based on C_p, will converge faster than the direct integration of the CFD flow data.*

AHD criterion and the approximate envelope e^N method. However, the main downside of the Granville and Michel criteria is that they do not take the freestream turbulence intensity into account and therefore their use is limited to flows with very low turbulence levels.

Based on these observations, the e^N method is chosen as the default criterion for boundary layer transition simulations. Out of the envelope and database approaches, the latter was more consistent in predicting the transition locations for the examined case. Therefore, transitional simulations with the e^N method will utilize the database approach. However, when transonic and supersonic transition predictions are considered the AHD criterion should be used, since the e^N method is calibrated only for incompressible flows.

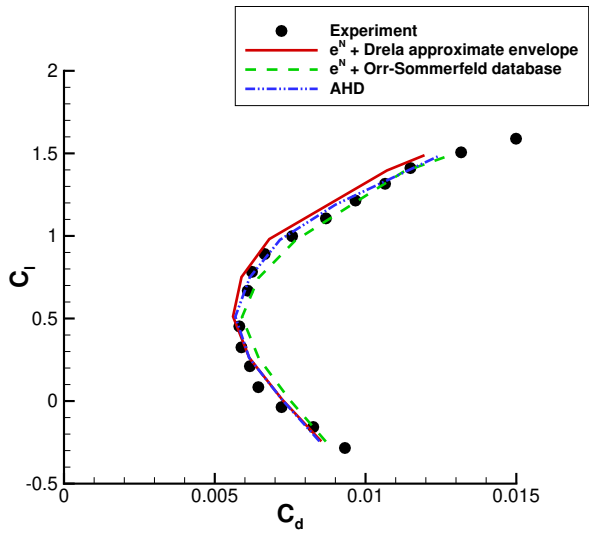

(a) *e^N method using both envelope and database approaches and AHD criterion, C_l-C_d polar*

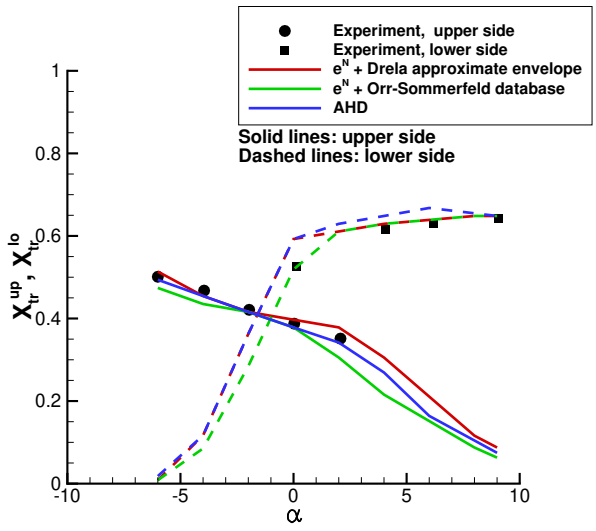

(b) *e^N method using both envelope and database approaches and AHD criterion, transition locations*

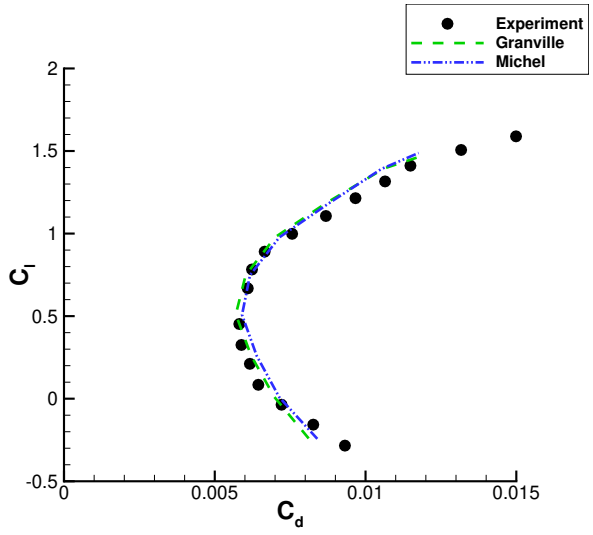

(c) *Granville and Michel criteria, C_l-C_d polar*

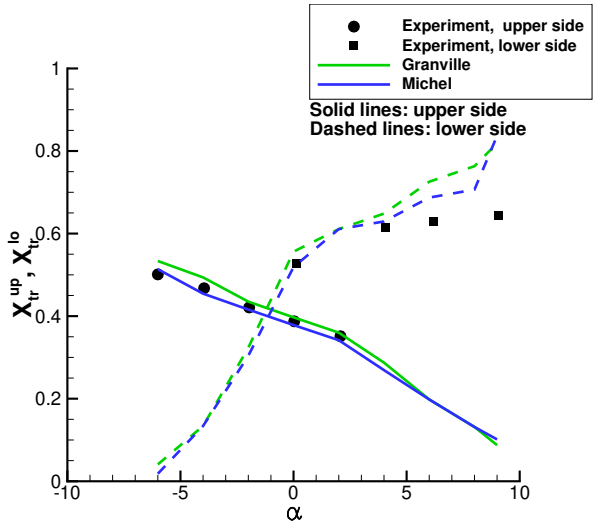

(d) *Granville and Michel criteria, transition locations*

Figure 5.13: *Effect of different boundary layer transition criteria. Free transition simulations for the NLF(1)-0416 airfoil, $Re = 4\ x\ 10^6$, $Ma_\infty = 0.1$, $Tu_\infty = 0.15\%$. Comparison with experimental data [4].*

5.5 Transport equation transition model aspects

5.5.1 Inflow turbulence specification

For the γ-Re_θ and γ models it is crucial to specify appropriate inflow conditions to ensure that Tu near the wall region is at the desired level. Turbulent parameters naturally decay in the computational domain and thus only specifying inlet turbulence is not sufficient.

One approach is to specify turbulent parameters at the inlet in a way that ensures that the desired Tu levels near the wall region are reached. As noted in [92], in order to account for turbulent decay the inlet viscosity ratio ($(\mu_t/\mu)_{inlet}$) should be increased. For given inlet turbulence intensity (Tu_{inlet}), this essentially decreases the turbulent dissipation (ω). Doing so can ensure that the inlet value for Tu will not decay when traveling towards the wall region. The inlet parameters can be calculated via the following turbulent decay equation also given in [92]:

$$Tu_{target} = \sqrt{Tu_{inlet}^2 \left(1 + \frac{3 \cdot \rho \cdot U \cdot dist \cdot \beta \cdot Tu_{inlet}^2}{2 \cdot \mu \cdot \left(\frac{\mu_t}{\mu}\right)_{inlet}}\right)^{-\beta^*/\beta}} \tag{5.1}$$

where $dist$ is the distance from the inlet to the region of interest (i.e. airfoil), Tu_{target} is the target turbulence intensity at the region of interest and $\beta = 0.09$, $\beta^* = 0.0828$.

Using (5.1) and specifying Tu_{target}, Tu_{inlet} can be calculated as a function of the inlet viscosity ratio. However, higher values of Tu_{target} will require increasing inlet viscosity ratios. For instance, if $Tu_{target} = 1\%$ is to be achieved at a distance of 50 chords from the domain inlet (which is typical for CFD computational meshes), the resulting inlet viscosity ratio will exceed the value of 10 ($(\mu_t/\mu)_{inlet} \geq 10$). Using high viscosity ratios alters the freestream Reynolds number, so this option should be avoided. In cases where $(\mu_t/\mu)_{inlet} = 10$ is not enough to calculate the desired Tu_{target} based on a specified value for Tu_{inlet}, then the latter is also increased.

A different approach than setting higher viscosity ratio and turbulence intensity at the inlet is to add production terms in the $k-\omega$ SST turbulence model. These terms are used to ensure that the ambient values of k and ω are sustained throughout the domain (this modification is known as $k-\omega$ SST SUST) [151]. The additional production terms are calculated as follows:

$$P_{k,amb} = \beta^* \omega_{amb} k_{amb} \tag{5.2}$$

$$P_{\omega,amb} = \beta \omega_{amb}^2 \tag{5.3}$$

where

$$k_{amb} = \frac{3}{2} Tu_\infty^2 U_\infty^2 \tag{5.4}$$

$$\omega_{amb} = \frac{\rho k_{amb}}{\mu \left[\frac{\mu_t}{\mu}\right]_\infty} \tag{5.5}$$

In this thesis, ambient values for k were calculated using the turbulence intensity noted in the corresponding experiment. Ambient values for ω were set in such a way that the solver has as small ambient viscosity ratio as possible. Since $\mu_t = k/\omega$, lower viscosity ratio for given laminar μ results in higher ω.

Additionally, as denoted in [152], there is overproduction of k in the stagnation region when using the baseline SST model. The second transport equation of the γ-Re_θ model (3.83) transfers the transition onset momentum thickness number. The source term for the equation is switched off inside the boundary layer and thus the Reynolds number values just outside the boundary layer are left to naturally diffuse in. Higher values of k in the stagnation region will lead to lower Re_θ values which will in turn act as a sink for the source term of the transport equation. This will bring the transition location upstream. To mitigate this artifact the Kato-Launder limiter can be employed [150]:

$$P_k = \mu_t S \Omega \tag{5.6}$$

It is here noted that even though the γ model does not solve the second transport equation, it however calculates Re_θ values for each cell in order to trigger transition. Using the k production limiter is, thus, also important for the γ model.

The last modification follows Menter's work [94]. An additional production term P_k^{lim} is introduced in the k-equation in order to ensure proper generation of k at transition locations for really low Tu levels. The need

for this term stems from the observation that for very low values of freestream turbulence, the baseline SST k-ω model requires a relatively long running length to produce turbulence inside the boundary layer, even when correctly triggered by the transition model. This additional term is designed to be turned off when the transition process is completed and the boundary layer has reached its fully turbulent state. The P_k^{lim} term is calculated as follows:

$$P_k^{lim} = 5C_k \cdot max(\gamma - 0.2, 0) \cdot (1-\gamma) F_{on}^{lim} \cdot max(3C_{sep}\mu - \mu_t, 0) \cdot S \cdot \Omega \tag{5.7}$$

$$F_{on}^{lim} = min\left[max\left(\frac{Re_v}{2.2 \cdot Re_{\theta c}^{lim}} - 1, 0\right), 3\right] \tag{5.8}$$

$$Re_{\theta c}^{lim} = 1100 \tag{5.9}$$

$$C_k = 1.0, \qquad C_{sep} = 1.0 \tag{5.10}$$

In order to investigate the effect of the Kato-Launder limiter on k production, the DU-00-W212 airfoil is considered, with flow conditions Re = 3 x 10^6, $Ma_\infty = 0.075$, $Tu_\infty = 0.0864\%$. The computational mesh followed the guidelines discussed in Section 5.2. However, the domain extent was set to 50 chords instead of 1000. The latter value for the domain extent requires too high inlet turbulence and viscosity ratio values due to the increased distance from the inlet to the wall region, therefore it is not suitable for this part of the analysis. For 50 chords domain extent, the values $Tu_{inlet} = 0.864\%$ and $(\mu_t/\mu)_{inlet} = 10$ (corresponding to $\omega \approx 34\frac{U_\infty}{c}$) are used, which were calculated via (5.1). Results presented in fig. 5.14a show that without the limiter, laminar bucket corners appear at lower C_l values in the positive C_l region and in higher C_l values in the negative C_l region. This is explained by the results in fig. 5.14b, where it is shown that transition at $C_l = 1$ ($\alpha = 6°$) on the suction side is predicted too early. This occurs because in the un-limited case, over-production of k (and thus of Tu), lowers the value of $Re_{\theta t}$ which is calculated by the transition correlation ((3.97) in this case). Lower values of $Re_{\theta t}$ essentially act as a sink in the equation of $\tilde{Re}_{\theta t}$, leading to earlier transition onset [152]. Contour plots in fig. 5.15 correspond to predictions without/with the limiter at $C_l = 1$ ($\alpha = 6°$). Tu levels are significantly lower when the limiter is not used.

The effects of the inflow conditions and of the source terms are discussed next. The DU-00-W212 airfoil with same flow conditions is again considered. The simulations with adjusted inflow conditions had $Tu_{inlet} = 0.864\%$ and $(\mu_t/\mu)_{inlet} = 10$ ($\omega \approx 34\frac{U_\infty}{c}$). The simulations with ambient source terms are noted with the subscript *amb*. For these simulations, the ambient dissipation was set as $\omega_{amb} = 5$, 50 and $100\frac{U_\infty}{c}$ and the ambient turbulence intensity as $Tu_{amb} = Tu_\infty = 0.0864\%$, corresponding to $(\mu_t/\mu)_{amb} = 0.74$, 0.074 and 0.037 respectively. It is noted that when source terms are used, the ambient values for k and ω are also set as inlet values in the domain. In fig. 5.16, the results indicate that the two approaches are close when $\omega_{amb} = 5\frac{U_\infty}{c}$. When $\omega_{amb} = 50$ or $100\frac{U_\infty}{c}$, the resulting freestream turbulent viscosity is lower and thus the drag level within the laminar bucket decreases. In spite of that, the corners of the bucket are predicted at the same angle, as they are only affected by turbulence intensity. If the measured turbulence intensity is to be used as inlet condition, then the best option is to add ambient source terms in the turbulence equations. For ω_{amb}, the intermediate value $50\frac{U_\infty}{c}$ is selected, which yields lower freestream turbulent viscosity as compared to that obtained with $5\frac{U_\infty}{c}$. This value for ω_{amb} is also low enough for the solver to converge deeply. High dissipation values will also keep the viscosity ratio low, which will not add extra turbulent viscosity inside the turbulent boundary layer at increasing Reynolds numbers, keeping overall drag values lower. This point is also discussed in [151], where it is shown that ω_{amb} values up to $100\frac{U_\infty}{c}$ are considered safe. The range of ω_{amb} is, thus, not too narrow. Above this upper ω_{amb} value, the simulation may not converge, especially at higher Reynolds numbers.

For the purpose of this work, simulations will utilize the ambient term approach. In each case, k_{amb} will be calculated from the given freestream turbulence intensity measured in the experiment, whereas ω_{amb} will be always set to $50\frac{U_\infty}{c}$.

5.5.2 Evaluating available correlations for $Re_{\theta c}$, F_{length}, and $Re_{\theta t}$

Similar to what was discussed in Section 5.4.2, it is also useful to assess the performance of the various empirical correlations available for use with the two correlation transition models (γ-Re_θ and γ). The test case is again the NLF(1)-0416 airfoil at Re = 4 x 10^6, $Ma_\infty = 0.1$, for which transition locations have been measured. Freestream turbulence intensity is set to $Tu_\infty = 0.15\%$, as suggested by G. Coder in [149]. Experimental data are taken from [4]. Ambient turbulent source terms were used, based on what was discussed in Section 5.5.1: $Tu_{amb} = 0.15\%$, $\omega_{amb} = 50\frac{u_\infty}{c}$.

The available correlations for $Re_{\theta t}$ are those of Langtry (3.97), of Abu-Ghannam and Shaw (3.99) and of Menter (3.150). From these three, the former two have been widely used with the γ-Re_θ model, whereas the latter is relatively new and was mainly developed in an effort to make the γ model more amenable to fine-tuning. The γ-Re_θ model was only tested using the correlations of Langtry and of Abu-Ghannam and Shaw, whereas the γ model was tested with all three correlations. For this part of the analysis, the γ-Re_θ model utilized

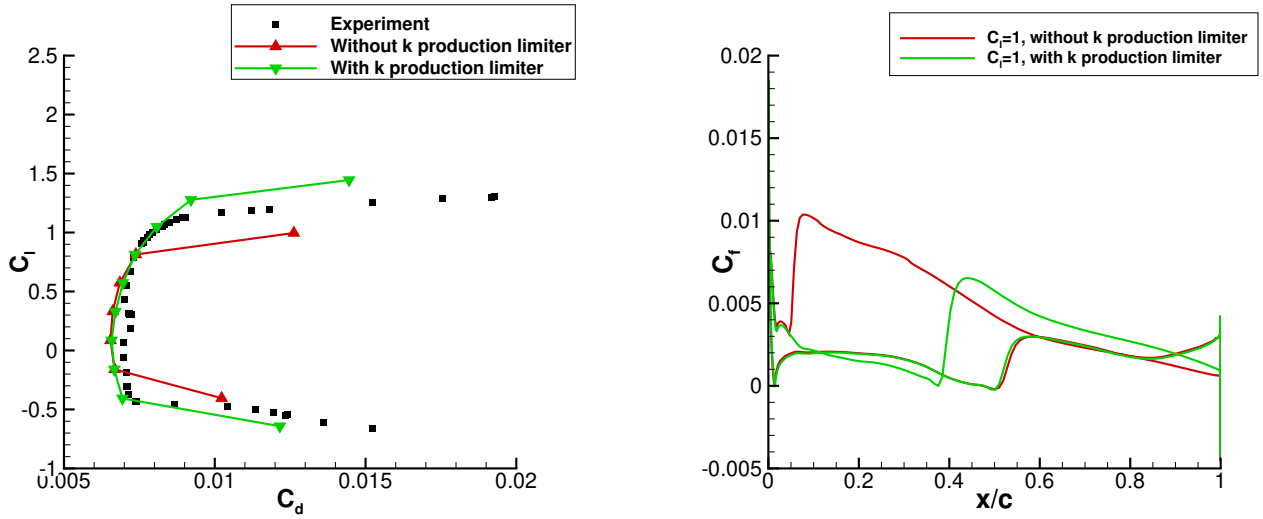

(a) C_l-C_d *polar* **(b)** C_f

Figure 5.14: *Effect of turbulent kinetic energy production limiter on γ-Re_θ results. Free transition simulations for the DU-00-W212 airfoil, $Re = 3\ x\ 10^6$, $Ma_\infty = 0.075$, $Tu_{inlet} = 0.864\%$, $(\mu_t/\mu)_{inlet} = 10$. No ambient turbulence production terms. Comparison with experimental data [5].*

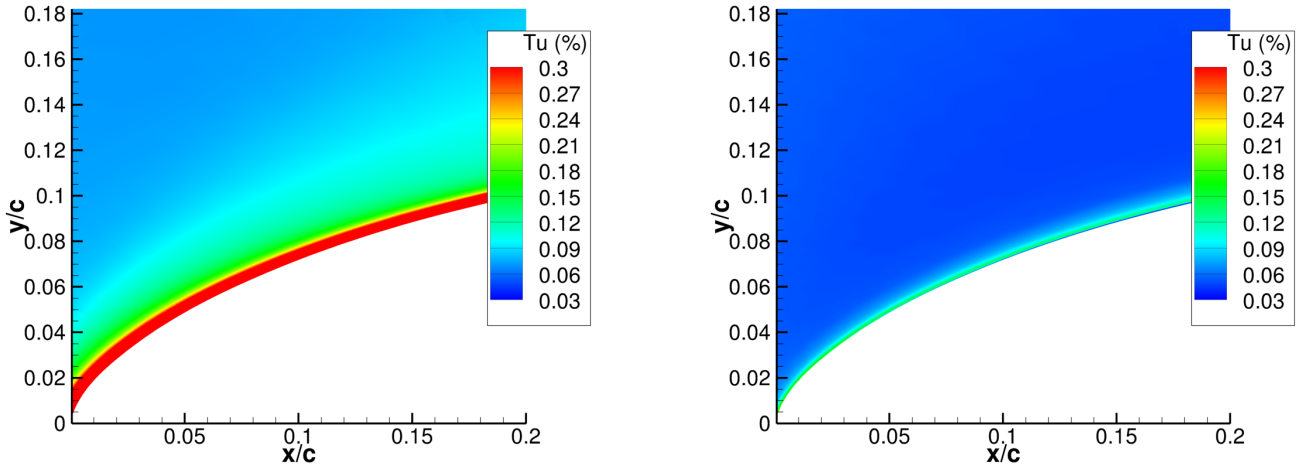

(a) *Without k production limiter* **(b)** *With k production limiter*

Figure 5.15: *Effect of turbulent kinetic energy production limiter on γ-Re_θ results. Free transition simulations for the DU-00-W212 airfoil, $Re = 3\ x\ 10^6$, $Ma_\infty = 0.075$, $Tu_{inlet} = 0.864\%$, $(\mu_t/\mu)_{inlet} = 10$, $C_l = 1$ $(\alpha = 6^\circ)$. No ambient turbulence production terms. Tu along the upper side in the region close to the leading edge.*

the original correlations for $Re_{\theta c}$ (3.88) and for F_{length} (3.98). For the γ model, F_{length} was set to 100.0, as suggested in the original formulation of the model [94]. It should be noted that the γ model does not use the critical momentum thickness Reynolds number but replaces it with the transition onset momentum thickness Reynolds number in (3.135), in contrast to what is used in (3.74) for the γ-Re_θ model. $Re_{\theta c}$ is the momentum thickness Reynolds number where the intermittency first starts to increase in the boundary layer, and is always lower than $Re_{\theta t}$, which is the momentum thickness Reynolds where transition starts to take place.

The results are presented in fig. 5.17. C_l-C_d polars and transition locations are considered. As shown in fig. 5.17a-5.17b, the γ-Re_θ model gives fairly accurate predictions using both Langtry and Abu-Ghannam and Shaw correlations. The correlation of Abu-Ghannam and Shaw predicts transition slightly upstream, with the most notable difference being the lower side transition at $\alpha = -2°$. The overall upstream transition locations also explain the C_l-C_d polar behavior, with the Abu-Ghannam and Shaw correlation predicting slightly higher drag levels inside the laminar bucket. The γ model is also adequately close to the experimental data when using either the correlation of Langtry or that of Abu-Ghannam and Shaw, as shown in fig. 5.17c-5.17d, whereas the correlation of Menter does not give as accurate results. Overall, the γ model predicts transition upstream from the experiment, which is the opposite from what is observed in the predictions of the γ-Re_θ model. Apart from the overall upstream transition locations, the most notable difference between the two models is the lower side transition location shift towards the leading edge with decreasing α. For the γ-Re_θ model this occurs at $\alpha = -2^o$ whereas for the γ model it starts at $\alpha = 2^o$. This difference is crucial, as it alters the location of the laminar bucket corner on the C_l-C_d curve. Nevertheless, this initial comparison shows that both models can give decent results using two different correlations. The fact that the γ model predicts transition upstream than the γ-Re_θ model can be justified. By substituting $Re_{\theta c}$ with $Re_{\theta t}$ in (3.135), the γ model essentially utilizes a higher Re number in order to trigger transition. The fact that $Re_{\theta c}$ is always lower than $Re_{\theta t}$ [91] brings transition upstream for the γ model. In this work, the Abu-Ghannam and Shaw correlation for $Re_{\theta t}$ will be utilized for both γ-Re_θ and γ models.

The effect of different correlations for $Re_{\theta c}$ is discussed next. Those are the correlations of Langtry (3.88), of Suluksna et al (3.90) and of Malan et al (3.91). The results presented in fig. 5.18 use the Abu-Ghannam and Shaw correlation for $Re_{\theta t}$. Both the correlations of Suluksna and Malan are closer to the experimental data when compared to the correlation of Langtry. Transition locations are predicted upstream, which results in slightly higher drag levels inside the laminar drag bucket. The most pronounced difference is at $\alpha = -2°$, where the correlations of Suluksna and Malan both predict significantly upstream transition location on the lower side of the airfoil. However, this behavior indicates better performance only partially, as there are not experimental data for the transition location on the lower side at that angle of attack. Nevertheless, given the fact that at $\alpha = 0°$ the transition point starts shifting towards the leading edge, it is valid to assume that the lower side transition location for $\alpha = -2°$ will be located somewhere between $x/c = 0.4$ and 0.5. The original correlation of Langtry predicts transition at $x/c \approx 0.56$, which is downstream than the one measured at $\alpha = 0°$ ($x/c \approx 0.53$). Overall, the results do not deviate significantly. Therefore, it is safe to use any of the available correlations. For this work, the correlation of Malan will be used.

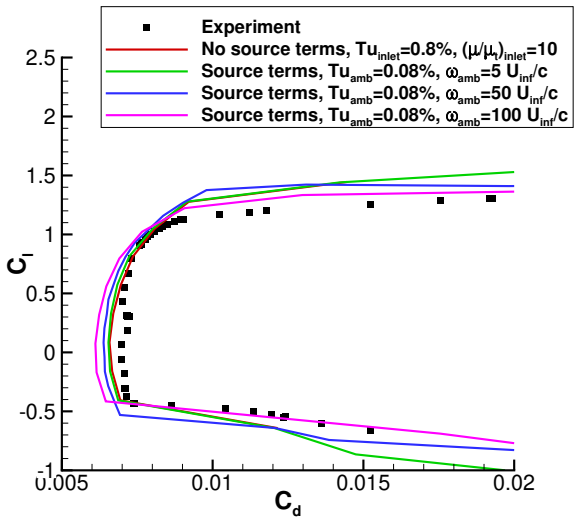

Figure 5.16: *Inflow conditions and ambient source term effect on γ-Re_θ results. Free transition simulations for the DU-00-W212 airfoil, $Re = 3\ x\ 10^6$, $Ma_\infty = 0.075$. Parameters discussed in Section 5.5.1. Comparison with experimental data [5]. C_l vs C_d polar.*

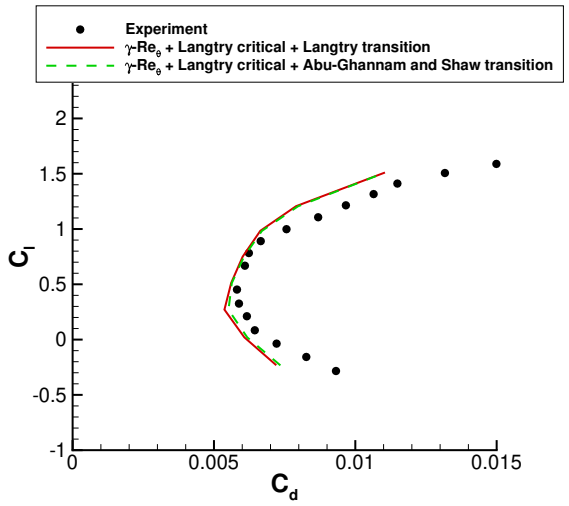

(a) *γ-Re_θ model, C_l-C_d polar*

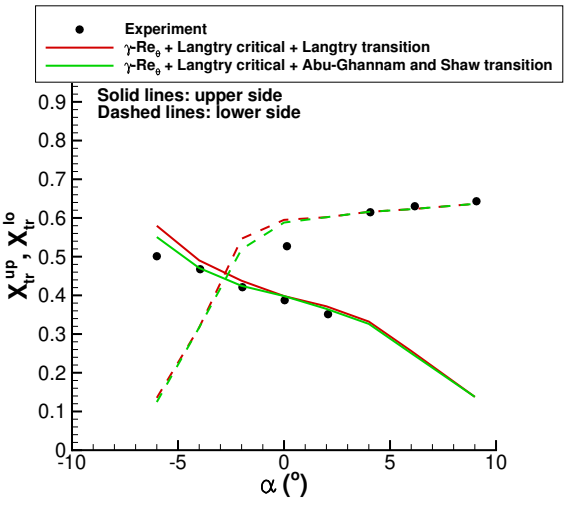

(b) *γ-Re_θ model, transition locations*

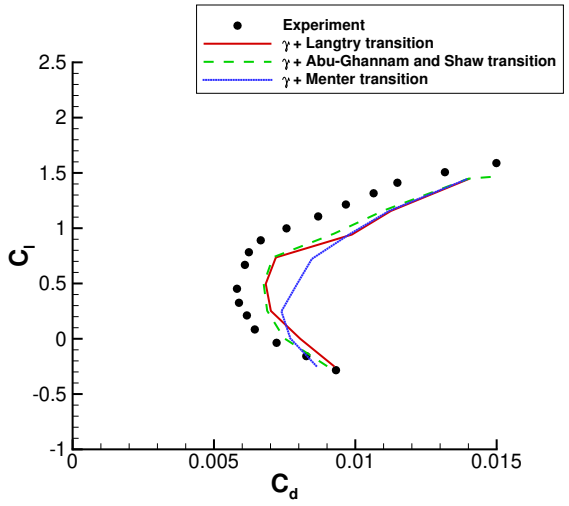

(c) *γ model, C_l-C_d polar*

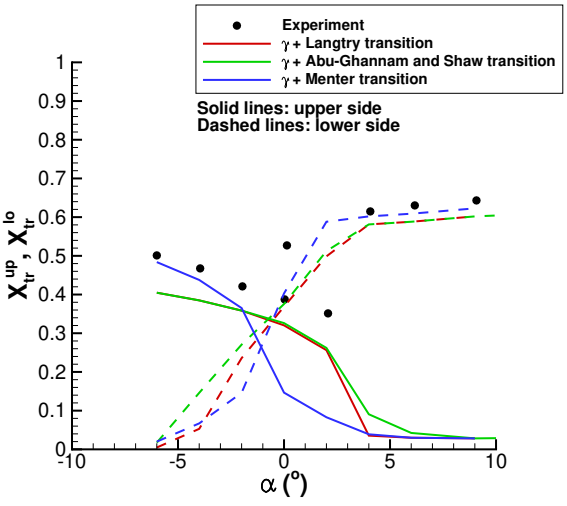

(d) *γ model, transition locations*

Figure 5.17: *Effect of different empirical correlations for $Re_{\theta t}$. Free transition simulations for the NLF(1)-0416 airfoil, $Re = 4\ x\ 10^6$, $Ma_\infty = 0.1$, $Tu_{amb} = 0.15\%$, $\omega_{amb} = 50\frac{u_\infty}{c}$. Comparison with experimental data [4].*

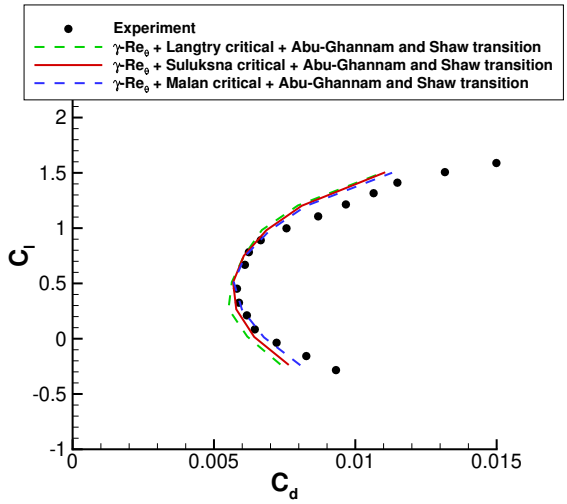

(a) *γ-Re_θ model, C_l-C_d polar*

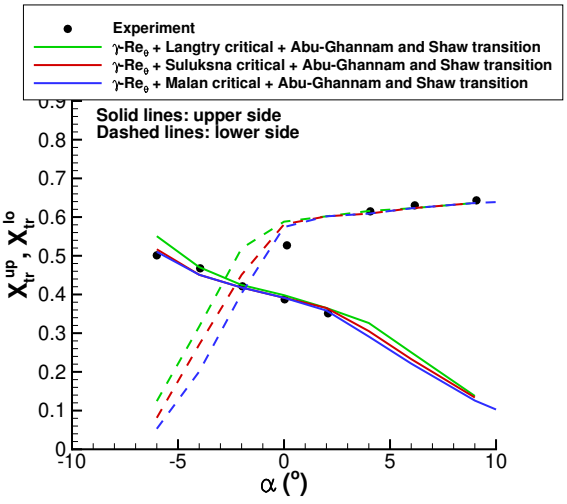

(b) *γ-Re_θ model, transition locations*

Figure 5.18: *Effect of different empirical correlations for $Re_{\theta c}$ and F_{length}. Free transition simulations for the NLF(1)-0416 airfoil, $Re = 4\ x\ 10^6$, $Ma_\infty = 0.1$, $Tu_{amb} = 0.15\%$, $\omega_{amb} = 50\frac{u_\infty}{c}$. Comparison with experimental data [4].*

5.6 Two-dimensional test cases

This section presents the results from two dimensional simulations. Based on what was discussed in Section 5.4.1, boundary layer calculation utilizes the two integral equations paired with the Falkner-Skan velocity profile closures. For boundary layer transition prediction, according to what was presented in Section 5.4.2, the e^N method with the Orr-Sommerfeld database is used. For all simulations, ambient turbulent production terms are introduced based on the results presented in Section 5.5.1. From what was discussed in Section 5.5.2, both γ-Re_θ and γ models use the correlation of Abu-Ghannam and Shaw for $Re_{\theta t}$, and the γ-Re_θ model uses the correlations of Malan for $Re_{\theta c}$ and F_{length}.

5.6.1 NLF(1)-0416 airfoil at $Re = 4$ x 10^6

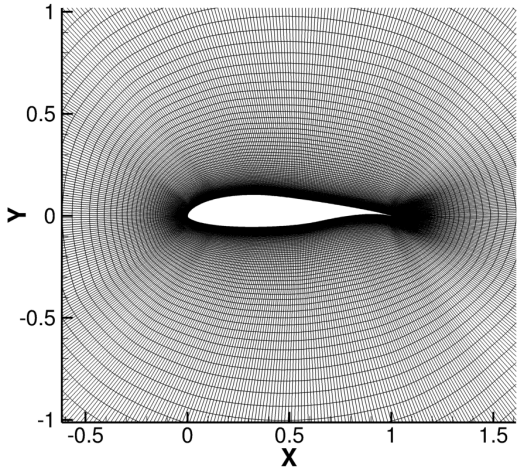

Figure 5.19: *NLF(1)-0416 airfoil mesh*

The laminar airfoil NLF(1)-0416 was experimentally investigated in the low-speed NASA Langley Low-Turbulence Pressure Tunnel LTPT [4] at $Re = 4$ x 10^6 and $Ma_\infty = 0.1$ with $Tu_\infty = 0.15\%$ giving $N_c = 7.17$. Ambient turbulent production terms were: $Tu_{amb} = 0.15\%$, $\omega_{amb} = 50\frac{U_\infty}{c}$.

In fig. 5.20 predictions are compared to measurements over the range $[-6°, 12°]$. The γ model deviates from the experimental results slightly more than all the other models, since it predicts all transition locations upstream. The other three approaches yield similar results. For the lower side, best agreement is obtained with the e^N method. Specifically at $\alpha = 0°$, the γ-Re_θ and AFT models predict transition slightly downstream. Apart from this specific angle, the AFT model and the e^N method are very close. This is expected, as the AFT model is also based on the e^N method. For the upper side, the γ-Re_θ model is closer to the experimental transition locations, whereas results from the e^N method and the AFT model are located slightly upstream.

Apart from the γ model, all transition models predict aerodynamic loads with good accuracy. Since this particular airfoil is characterized by laminar flow, strong low-drag laminar bucket corners do not appear and the transition location shift with increasing α exhibits a relatively linear trend. However, for higher α values some differences in the predicted transition locations on the upper side are noted. Beyond $\alpha = 2°$, the discrepancies between the results from the γ-Re_θ model and from the e^N method and the AFT model increase. The e^N method and the AFT model move faster towards the leading edge of the airfoil. This explains the differences in predicted C_d as C_l increases. Lacking experimental measurements on the upper side beyond $\alpha = 2°$, it is not possible to verify which model gives better predictions in regards to transition locations. Nevertheless, the C_l-C_d polar shows that the γ-Re_θ model is in better agreement with the experiment at higher C_l values, which suggests that it also predicts transition locations with sufficient accuracy. On the contrary, both the e^N method and the AFT model predict increased C_d and lower C_l, which are caused by upstream transition locations.

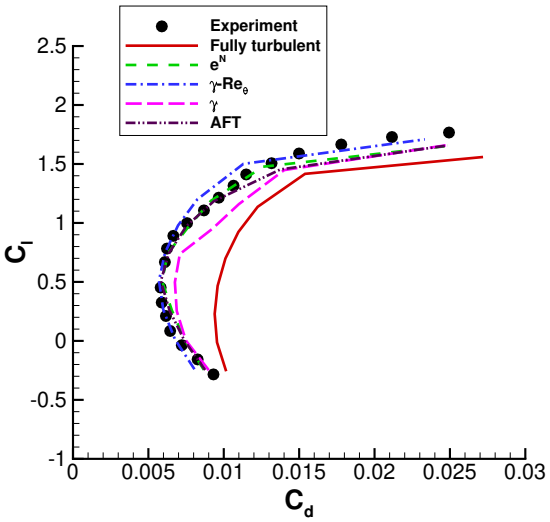

(a) C_l *vs* C_d

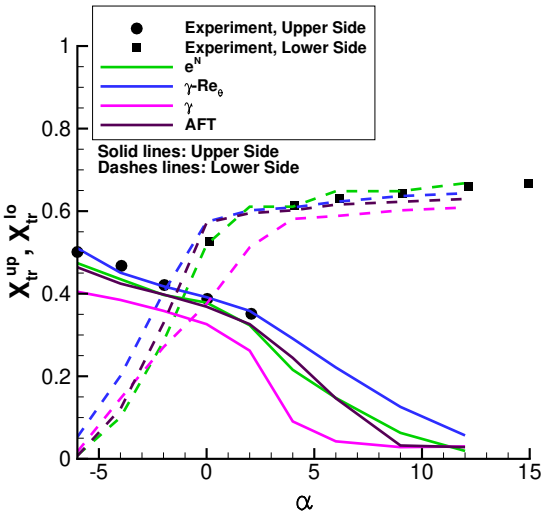

(b) *Transition locations*

Figure 5.20: *Free transition simulations for the NLF(1)-0416 airfoil at* $Re = 4\ x\ 10^6$, $Ma_\infty = 0.1$, $Tu_{amb} = 0.15\%$, $\omega_{amb} = 50\frac{U_\infty}{c}$. *Comparison with experimental data [4].*

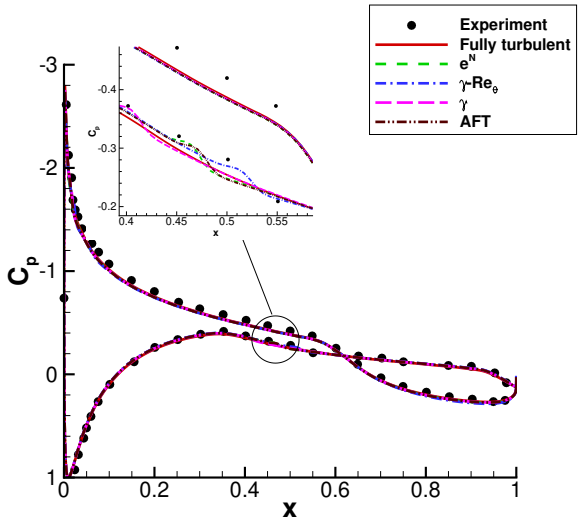

(c) C_p, $\alpha = -6^\circ$ *(*$C_l = -0.26$*)*

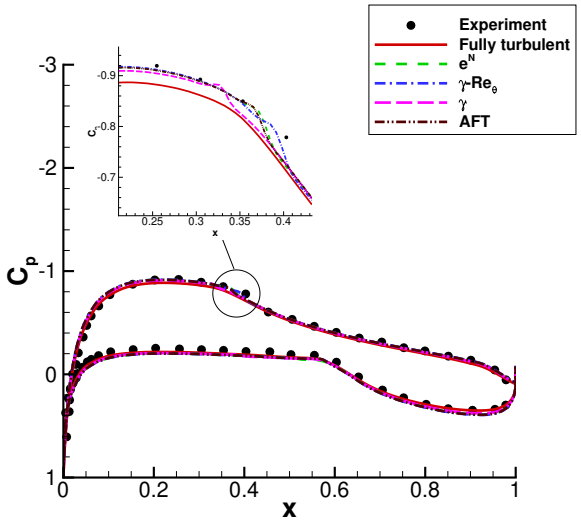

(d) C_p, $\alpha = 0^\circ$ *(*$C_l = 0.47$*)*

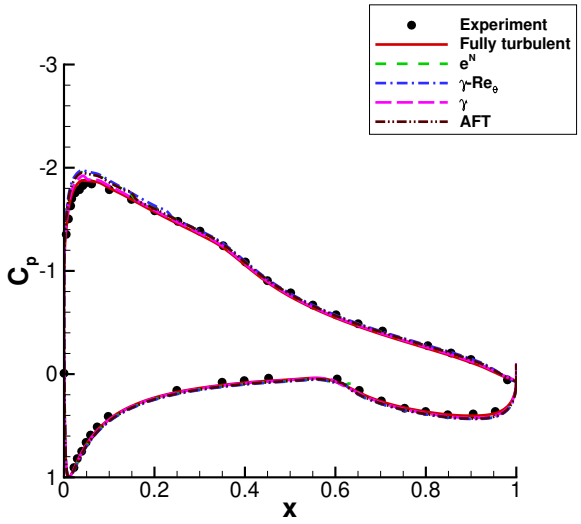

(e) C_p, $\alpha = 6^\circ$ *(*$C_l = 1.14$*)*

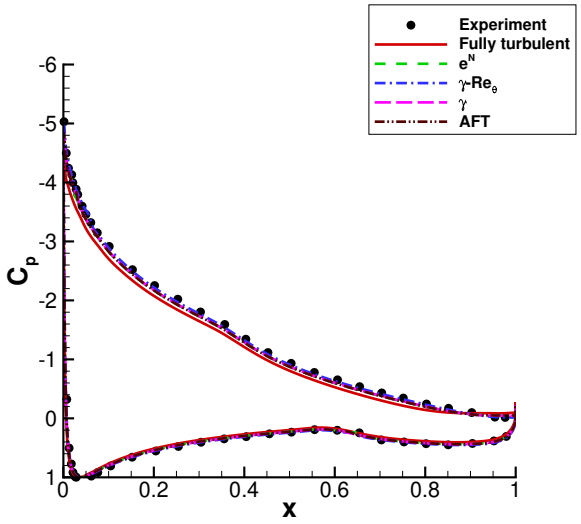

(f) C_p, $\alpha = 12^\circ$ *(*$C_l = 1.56$*)*

Figure 5.20: *(concluded)*

5.6.2 S809 airfoil at $Re = 2$ x 10^6

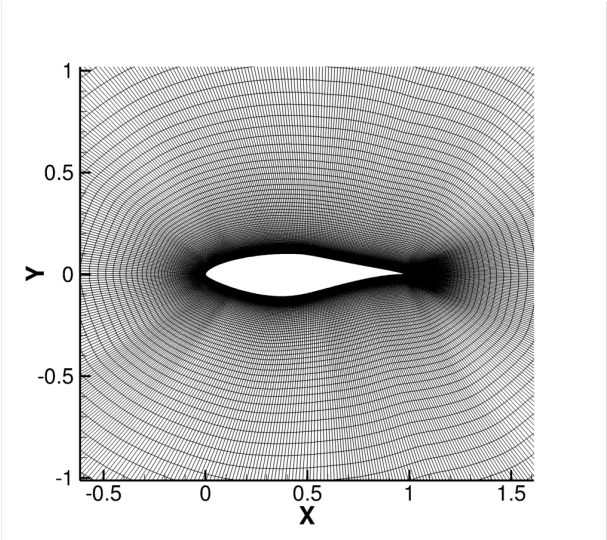

Figure 5.21: *S809 airfoil mesh*

This S-series airfoil is used in the NREL wind turbine and has behavior that is dominated by effects of transition. The back half of the upper surface is designed to have a "transition ramp", an extended region of gentle pressure recovery which encourages smooth transition from laminar to turbulent flow [153]. In contrast to the NLF(1)-0416 airfoil discussed in Section 5.6.1, the S809 airfoil exhibits a very pronounced laminar bucket with sharp upper and lower corners, due to the fact that the laminar bubbles essentially prevent the transition location from changing position for a wide range of angles of attack. The airfoil was measured by D.Somers [6] at $Re = 2$ x 10^6, $Ma_\infty = 0.1$ and $Tu_\infty < 0.05\%$. The ambient turbulent production terms were: $Tu_{amb} = 0.05\%$, $\omega_{amb} = 50\frac{U_\infty}{c}$.

Computational results for this airfoil for the region between $-10°$ and $10°$ are presented in fig. 5.22. The drag bucket (fig. 5.22a) is adequately predicted by all transition models, although a slightly lower level than the experiment is observed. Simulations do not predict stall inside the examined range; experimental stall appears at $C_l = 1$ ($\alpha = 8°$). This behavior is common and is attributed to the turbulence model, which predicts stall at higher angles especially in two dimensional simulations. When comparing transition locations (fig. 5.22b), the predictions are close to the experimental measurements on both sides of the airfoil. Both γ-Re_θ and AFT models predict slightly upstream transition, whereas the γ model predicts transition even more upstream. At positive angles, the e^N method predicts the laminar bucket corner at $\alpha = 6°$, which is also the angle observed in the experiments, whereas the γ-Re_θ and AFT models exhibit a delay of $1°$. At negative angles, the e^N method predicts the laminar bucket corner at $\alpha = -4°$, which is earlier than the experiment by $2°$, whereas the γ-Re_θ and AFT models again exhibit a delay of $1°$ when compared to the experimental laminar bucket which appears at $\alpha = -6°$. On the contrary, the γ model predicts the bucket corners at $\alpha = 5°$ and $-3°$ for positive and negative angles, respectively. The location of laminar bucket corner for negative angles using the γ model agrees with the experiment.

C_p contours for various angles are also compared. For the case of $1°$ ($C_l = 0.29$, fig. 5.22f), all models are very close to the experimental data, with the e^N method capturing the laminar bubbles with greater accuracy. For the cases of $6°$ ($C_l = 0.89$, fig. 5.22g) and $8°$ ($C_l = 1.05$, fig. 5.22h), all transition models give very good results of the C_p levels near the suction peak. For the case of $-5°$ ($C_l = -0.44$, fig. 5.22e), the e^N method predicts lower side transition close to the leading edge (fig. 5.22b). This leads to trailing edge separation on the lower side; C_p levels close to the trailing edge are similar to those of the fully turbulent simulation, which also exhibits trailing edge separation. Similarly, for the case of $-6°$ ($C_l = -0.55$, fig. 5.22d) both e^N method and γ model predict lower side transition close to the leading edge, leading to trailing edge separation, in contrast to the results of the γ-Re_θ and AFT models. Lastly, for $-8°$ ($C_l = -0.62$, fig. 5.22c) all transition models predict the same lower side transition location. However, all simulations fail to predict the onset of separation that is present on the experiments, leading to different C_p levels on the suction (lower) side. The differences in separation prediction could be attributed to the turbulence model.

An interesting observation is the behavior of the transition models in the vicinity of laminar bucket corners. C_f contours for $\alpha = 6°$ and $\alpha = -6°$ ($C_l = 0.89$ and -0.55) are compared in fig. 5.22i-5.22j. At $\alpha = 6°$, no leading edge separation bubble is observed and the predicted C_f contours have similar trends, even though the models do not predict transition at the same position. However, this does not occur at $\alpha = -6°$. Both γ-Re_θ and AFT models exhibit leading edge laminar separation bubbles, whereas the transition locations are

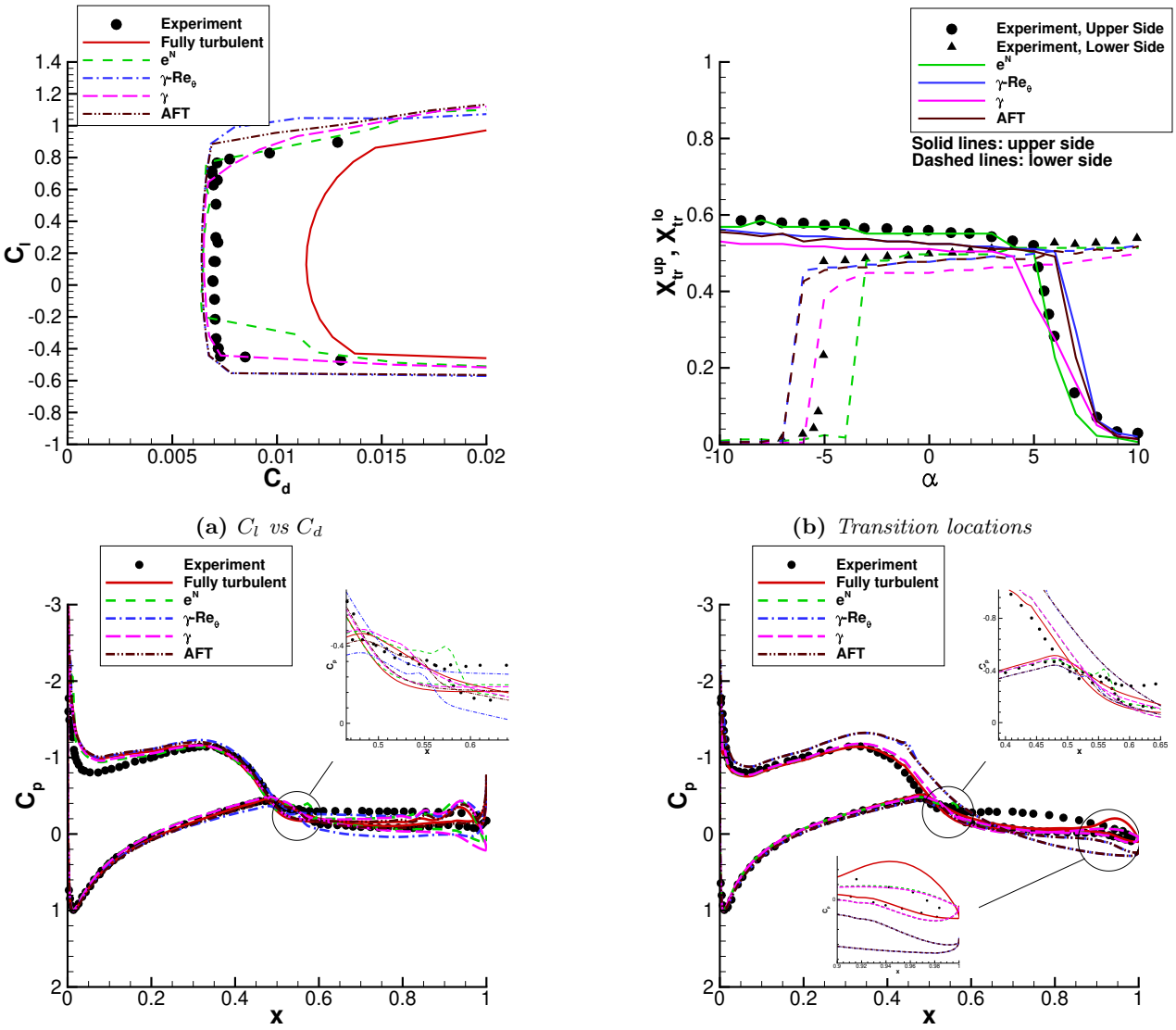

(a) C_l *vs* C_d

(b) *Transition locations*

(c) C_p, $\alpha = -8°$ *(*$C_l = -0.62$*)*

(d) C_p, $\alpha = -6°$ *(*$C_l = -0.55$*)*

Figure 5.22: *Free-transition simulations for the S809 airfoil at* $Re = 2\ x\ 10^6$, $Ma_\infty = 0.1$, $Tu_{amb} = 0.05\%$, $\omega_{amb} = 50\frac{U_\infty}{c}$. *Comparison with experimental data [6] and results using XFOIL [3].*

still located close to the middle of the chord. On the contrary, the transition location from the e^N method has already moved close to the leading edge. In order to have a more concise understanding of this deviation between the transition models, the predicted shape factor H and critical amplification factor N for $\alpha = -6°$ using the e^N method are plotted in fig. 5.22k-5.22l, accompanied by results using XFOIL [3]. The implemented e^N method yields very similar results to those taken from XFOIL and predicts transition locations at almost identical positions. However, it is clear that both boundary layers are separated. Separation occurs at $H \approx 3.9$ in boundary layer solvers, whereas in Navier-Stokes simulations separation can occur at even lower values of H. Moreover, at $H = 7.4$ the boundary layer can be assumed to be well separated [83]. Both XFOIL and MaPFlow predict H values higher than 7.4. In these scenarios, N-factor grows rapidly and thus transition is predicted close to the leading edge. On the other hand, the results using γ-Re_θ and AFT models show laminar bubbles that are contained close to the leading edge. In fig. 5.22m, the z-axis vorticity from the AFT model is shown along with streamtraces. Even though two small laminar bubbles are present, they do not cause separation induced transition, as shown in the intermittency contour in fig. 5.22n. Inside the bubbles, γ is clearly greater than 1, suggesting turbulent flow. However, these values of γ are not diffused downstream in the boundary layer and thus transition locations are not affected.

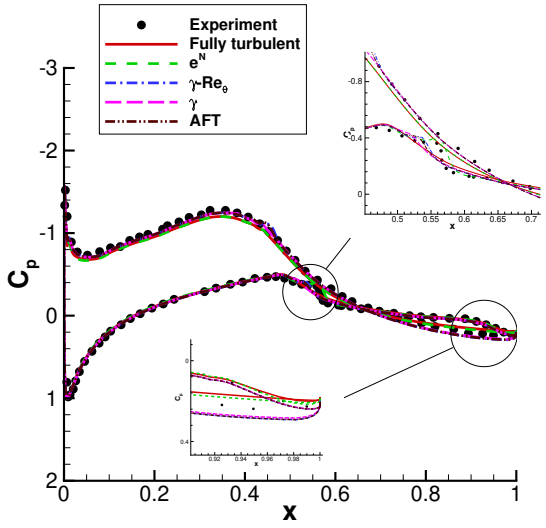

(e) C_p, $\alpha = -5^\circ$ *($C_l = -0.44$)*

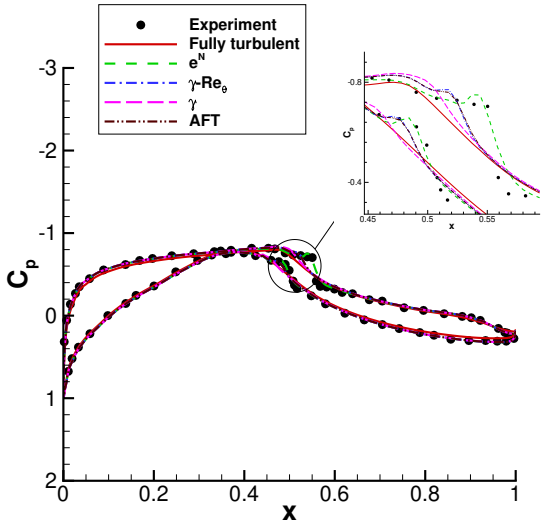

(f) C_p, $\alpha = 1^\circ$ *($C_l = 0.29$)*

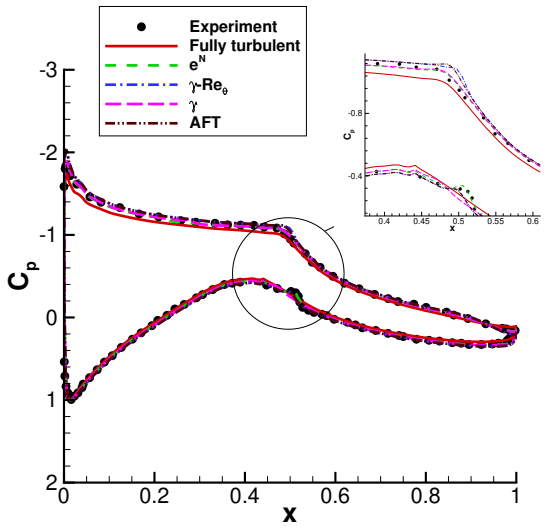

(g) C_p, $\alpha = 6^\circ$ *($C_l = 0.89$)*

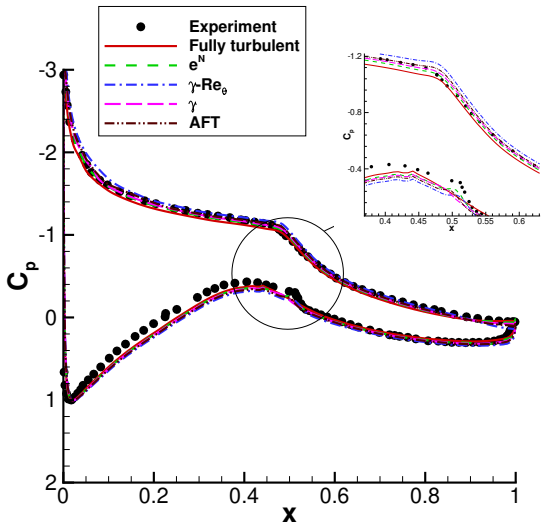

(h) C_p, $\alpha = 8^\circ$ *($C_l = 1.04$)*

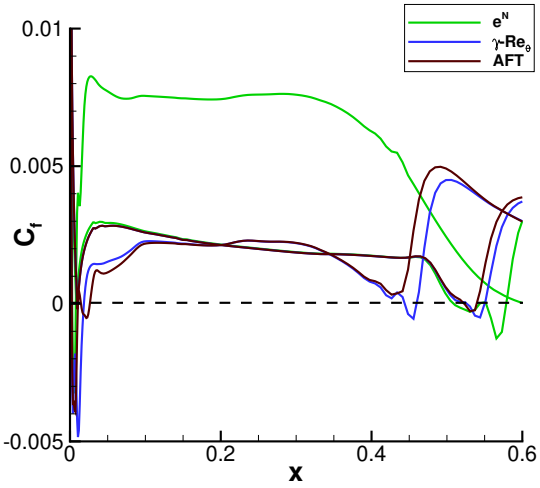

(i) C_f, $\alpha = -6^\circ$ *($C_l = -0.55$)*

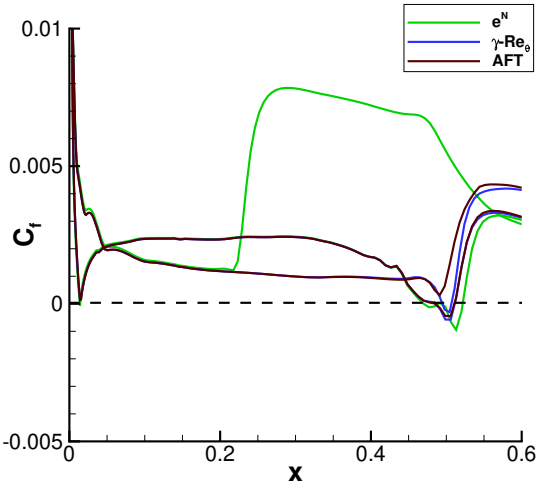

(j) C_f, $\alpha = 6^\circ$ *($C_l = 0.89$)*

Figure 5.22: *(continued)*

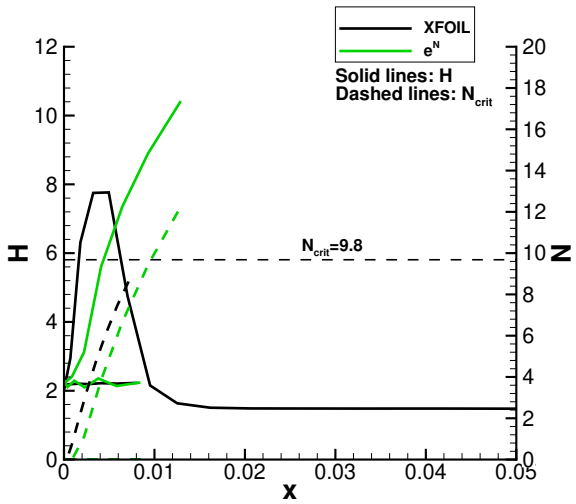

(k) *Shape factor H and critical amplification ratio N_{crit}, $\alpha = -6^\circ$ ($C_l = -0.55$), lower side*

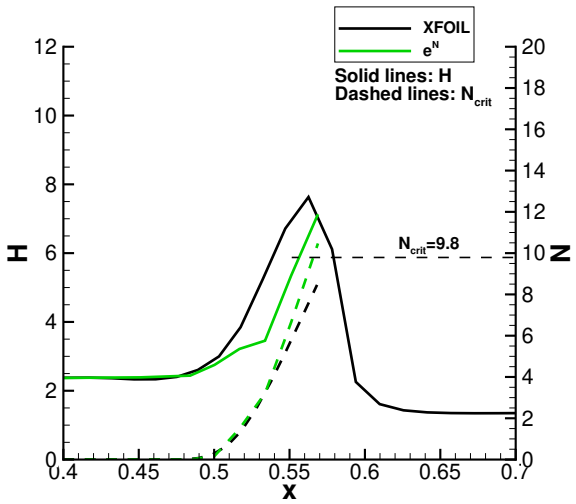

(l) *Shape factor H and critical amplification ratio N_{crit}, $\alpha = -6^\circ$ ($C_l = -0.55$), upper side*

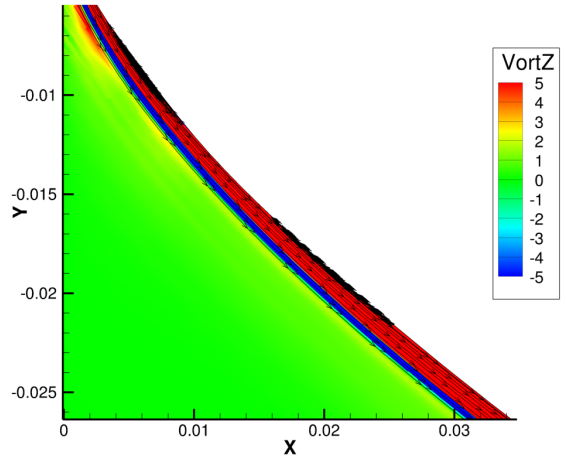

(m) *Laminar separation bubbles, $\alpha = -6^\circ$ ($C_l = -0.55$), lower side, AFT transition model*

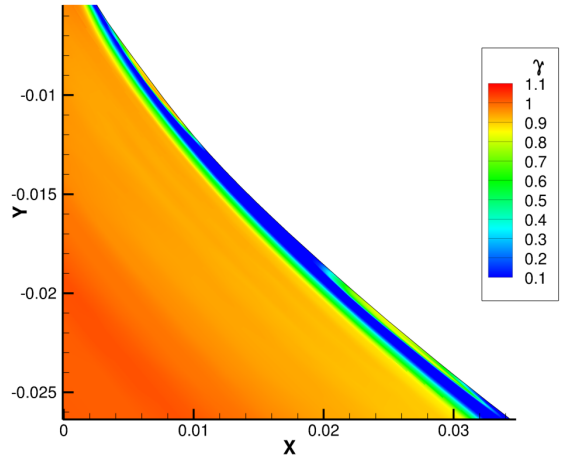

(n) *γ (intermittency) contour, $\alpha = -6^\circ$ ($C_l = -0.55$), lower side, AFT transition model*

Figure 5.22: *(concluded)*

5.6.3 S827 airfoil at $Re = 4$ x 10^6

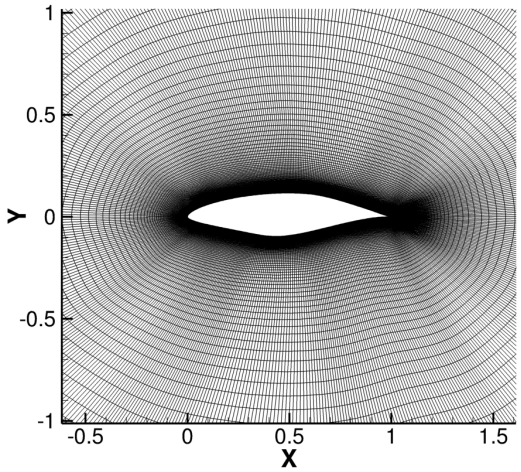

Figure 5.23: *S827 airfoil mesh*

The S827 airfoil is used in stall-regulated wind turbines and is designed to deliberately stall beyond a prescribed angle of attack. The airfoil was measured by D. Somers [7] at $Re = 4$ x 10^6, $Ma_\infty = 0.1$ and $Tu_\infty < 0.05\%$. For these flow conditions, the angle in which stall occurs is $\approx 4°$. A distinct feature of this airfoil is the two lift slopes [153], one corresponding to angles below stall and the other to the post stall region which begins at $\alpha \approx 5°$. Ambient turbulence production terms were: $Tu_{amb} = 0.05\%$, $\omega_{amb} = 50\frac{U_\infty}{c}$.

Computational results for the region between -5 and 16 degrees are presented in fig. 5.24. As shown in fig. 5.24c, predicted transition locations remain unchanged for angles between $-4°$ and $4°$. In this respect, lift is expected to vary linearly and drag to remain approximately constant as seen in the measurements and predicted by the transition models in fig. 5.24b, with the slight exception of the γ model which predicts upstream transition and earlier onset of drag bucket corners. The C_l slope is slightly over-predicted by all transition models and the first peak value differs when compared to the experiment (fig. 5.24a). This behavior is common and is attributed to the two-dimensional simulation that delays the onset of stall. The angle where the peak occurs varies between the transition models; for the e^N method it is shifted by $1°$, appearing at $\alpha = 5°$, in contrast to the experimental angle of $4°$. The γ-Re_θ model has a slight drop in lift at $4°$ caused by the corresponding transition location shift on the upper side (fig. 5.24c). However, the shift in transition location between $4°$ and $5°$ is not big enough and thus the C_l drop from the γ-Re_θ model is not as steep as the experiment. The γ model predicts transition shift at $3°$ and thus exhibits earlier stall than the experiment accompanied by a lower C_l peak value. Overall, the best agreement is observed using the AFT model, even though the shift in transition location starts at $6°$. Nevertheless, the AFT model predicts the drop in lift coefficient between $5°$ and $6°$ with good accuracy and has similar trend to the one observed in the experiments. The separation locations for the upper side are plotted in fig. 5.24d, where it is evident that the onset of transition alters the point of separation. The fully turbulent simulation exhibits trailing edge separation from $\alpha = -2°$, and thus has a completely different lift slope than the transitional simulations in low angles of attack.

C_p values are also compared in fig. 5.24e-5.24h. For $\alpha = -4°$ and $4°$, the predictions are close to the experimental measurements, even though there is a slight difference in overall C_p levels on both sides. Nevertheless, fig. 5.24f shows that both fully turbulent and γ simulations predicts separation close to the trailing edge, in contrast to what is observed in the experiments and the other three transition models. At $\alpha = 8°$, transition locations on the upper side are predicted close to the leading edge (fig. 5.24c). Separation, however, is delayed in the simulations when compared to the experiment (fig. 5.24g), leading to higher suction peak levels. The predicted transition locations could be different than those present in the experiment, although separation onset delay could also be caused by the turbulence model. Lacking experimental transition locations, it is not possible to further analyze why these deviations occur. For the case of $\alpha = 14°$, where the transition locations are all predicted at the leading edge, predicted C_p is closer to the experiments. The separated region is similar, suggesting that different C_p levels on the upper sided are probably caused by the turbulence model.

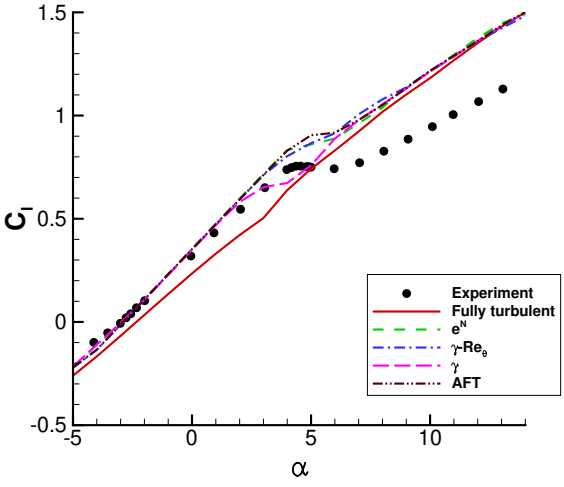

(a) C_l *vs* α

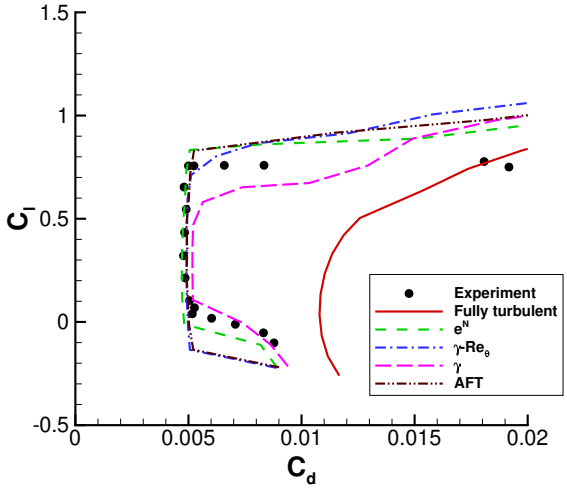

(b) C_l *vs* C_d

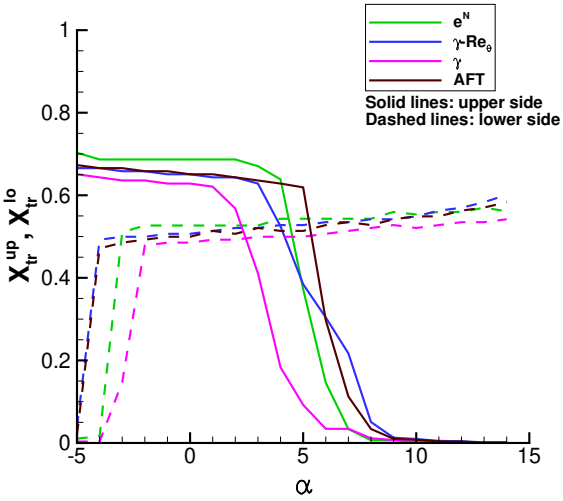

(c) *Transition locations*

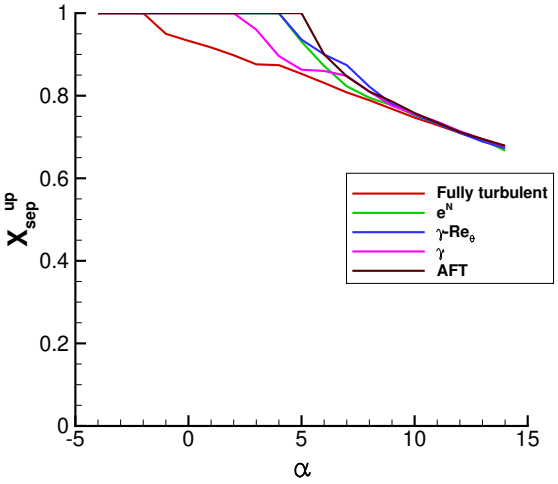

(d) *Trailing edge separation locations on the upper side*

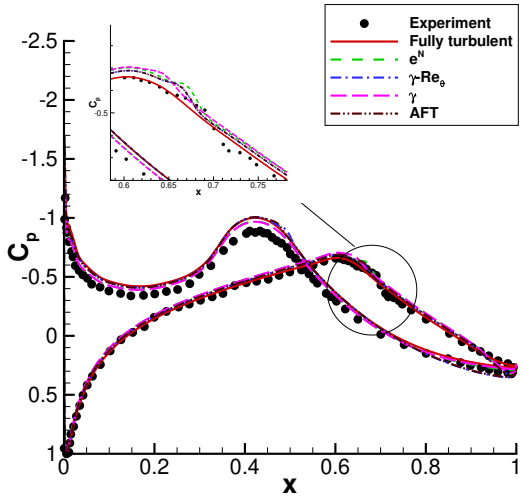

(e) C_p, $\alpha = -4°$

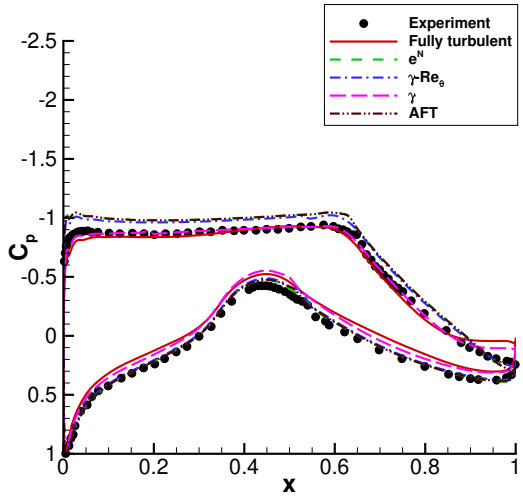

(f) C_p, $\alpha = 4°$

Figure 5.24: *Free-transition simulations for the S827 airfoil at* $Re = 4\ x\ 10^6$, $Ma_\infty = 0.1$, $Tu_{amb} = 0.05\%$, $\omega_{amb} = 50\frac{U_\infty}{c}$. *Comparison with experimental data [7].*

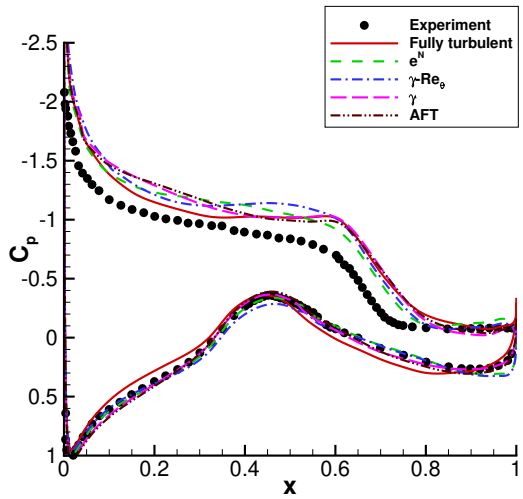

(g) C_p, $\alpha = 8°$

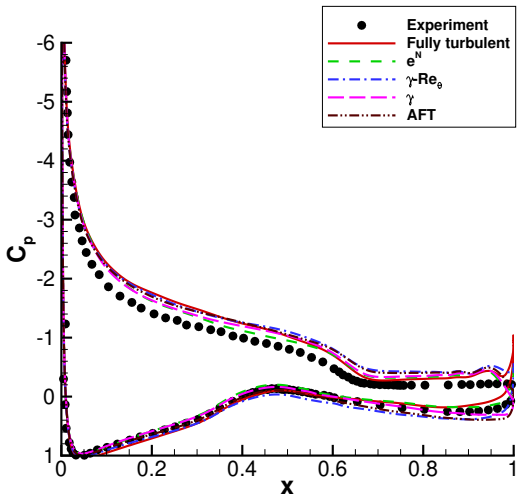

(h) C_p, $\alpha = 14°$

Figure 5.24: *(concluded)*

5.6.4 DU-00-W212 airfoil at $Re = 3$ to 15 x 10^6

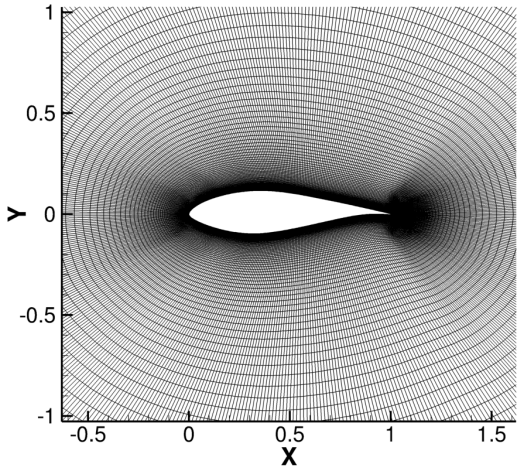

Figure 5.25: *DU-00-W212 airfoil mesh*

This airfoil was recently measured by O.Ceyhan and O. Pires [5] in the DNW-HDG Wind Tunnel at Goettingen. The flow conditions are presented in Table 5.5. Experimental data are available for various Reynolds numbers, and thus a direct evaluation of how Reynolds affects the performance of transition models is possible. Since the comparison focuses on the behavior of transition effects, angles beyond stall are omitted.

Table 5.5: *DU-00-W212 flow conditions*

Re (millions)	3	9	15
Ma_∞	0.075	0.082	0.08
$Tu_\infty = Tu_{amb}$ (%)	0.0864	0.1988	0.3346
$\omega_\infty = \omega_{amb}$	50 $\frac{U_\infty}{c}$	50 $\frac{U_\infty}{c}$	50 $\frac{U_\infty}{c}$
N_{crit}	8.50	6.60	5.25
$\alpha(^\circ)$	-10 to 10	-10 to 10	-10 to 10

Computational results are presented in fig. 5.26. For Reynolds numbers higher than 3 x 10^6, the $\gamma - Re_\theta$ model predicts higher drag levels inside the laminar drag bucket, with the difference becoming even higher as Re rises. The model also fails to capture the drag increase trends near the bucket corner. On the contrary, at $Re = 3$ x 10^6 the behavior is different, with the $\gamma - Re_\theta$ model giving lower drag values inside the bucket.

The e^N method and the AFT model are both in good agreement with the experiments at all Reynolds numbers, with the AFT model giving slightly higher drag levels inside the bucket at $Re = 9$ and 15 x 10^6. Predicted laminar bucket corners are also very similar for these two transition approaches, with the only notable difference being the corner on the negative angles at $Re = 3$ x 10^6, which the e^N predicts earlier than the AFT model.

Focusing on the sensitivity of the $\gamma - Re_\theta$ model, it is evident that the discrepancies between the experimental data and the computational results become larger as Re increases. At $Re = 3$ x 10^6, the $\gamma - Re_\theta$ model predicts transition downstream and thus yields lower drag values, whereas at $Re = 9$ and 15 x 10^6, besides predicting earlier transition, the model also exhibits a significant, early upstream jump in transition onset, behavior that is not observed with the e^N method and the AFT model (fig. 5.26e- 5.26f). Moreover, fig. 5.26d shows that when using the γ-Re_θ model the predicted minimum drag coefficient increases with increasing Re, behavior which disagrees with the trends in the experiments and both the e^N and AFT predictions. This deviation is caused by the upstream transition onset prediction.

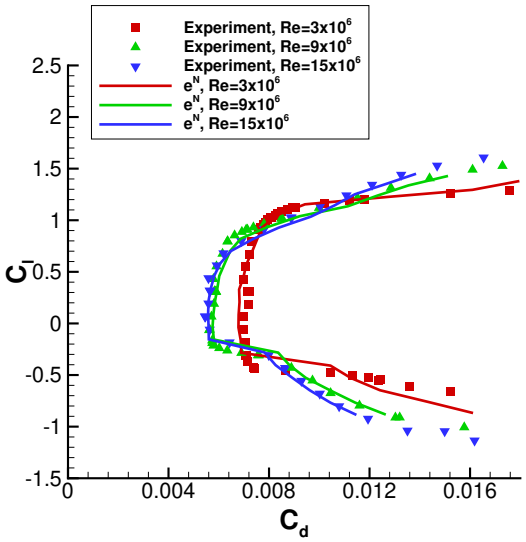

(a) e^N *method,* C_l *vs* C_d

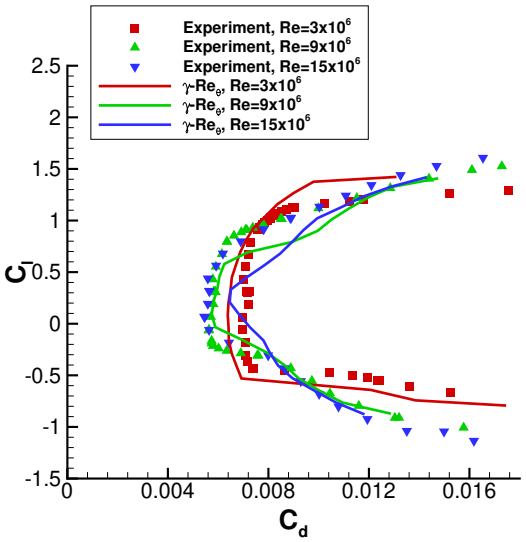

(b) $\gamma - Re_\theta$, C_l *vs* C_d

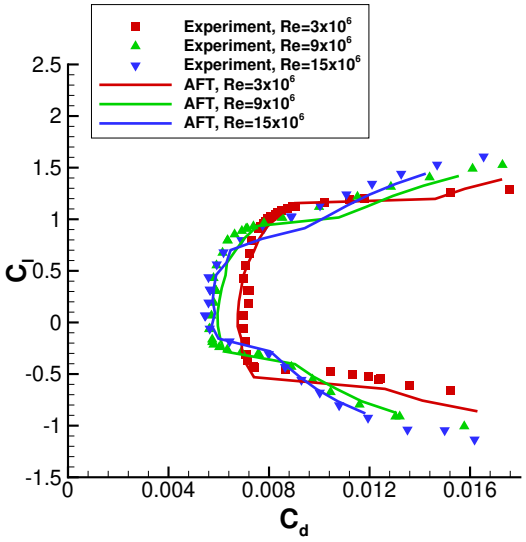

(c) *AFT,* C_l *vs* C_d

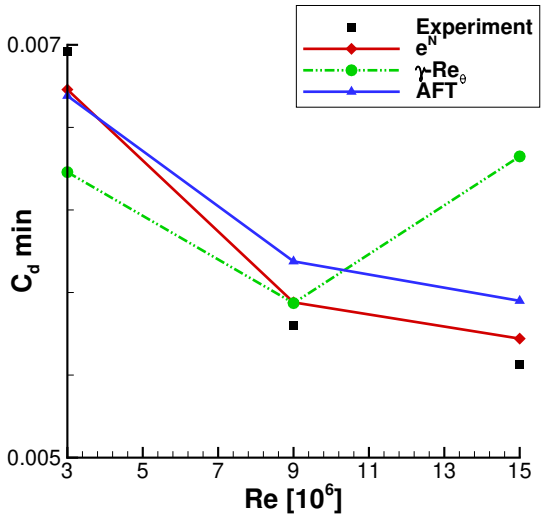

(d) *Predicted minimum drag coefficient for varying Reynolds number for the three transition models*

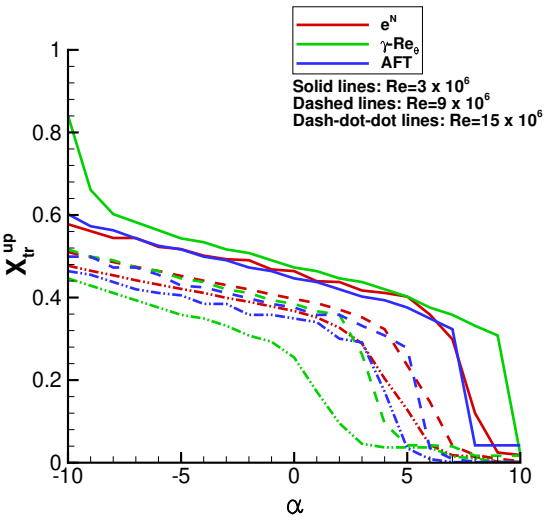

(e) *Upper side transition locations*

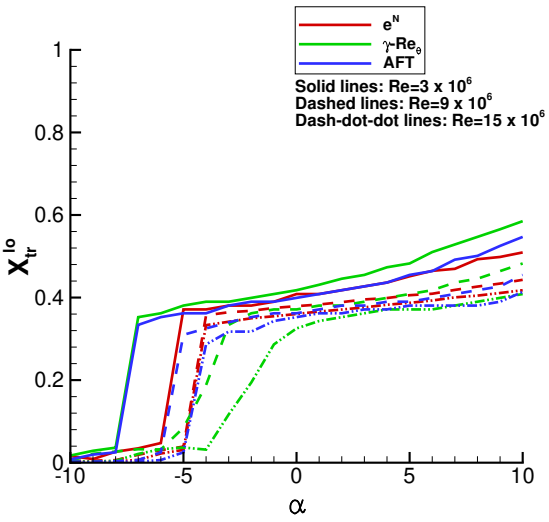

(f) *Lower side transition locations*

Figure 5.26: *Free transition simulations for the DU-00-W212 airfoil, flow conditions described in table 5.5. Comparison with experimental data [5].*

5.6.5 Aerospatiale-A airfoil at $Re = 2.1$ x 10^6

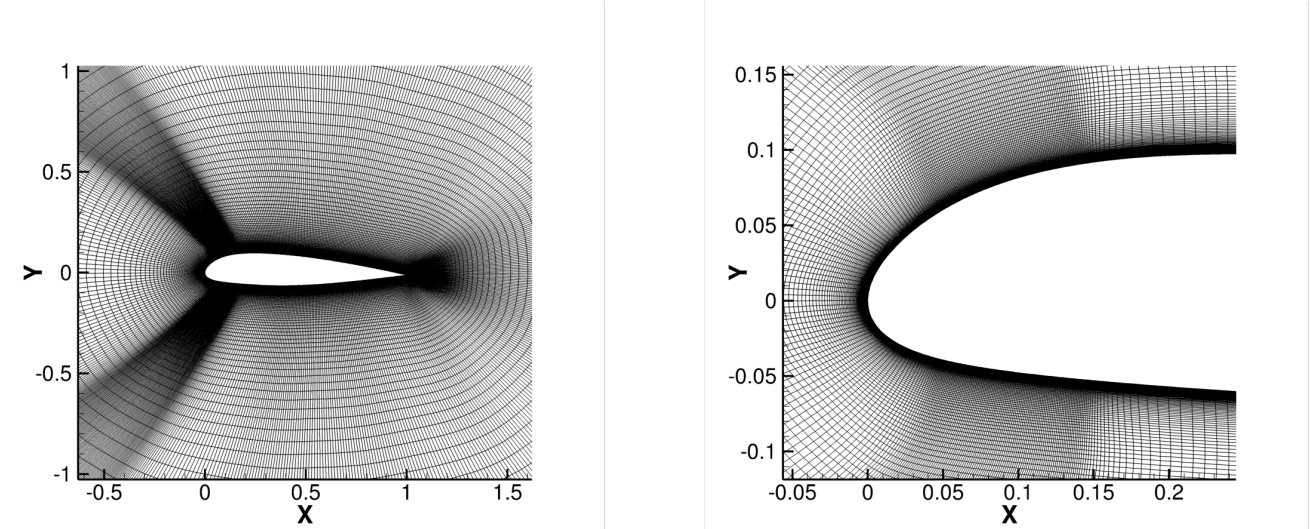

(a) *Full view* **(b)** *Refined region close-up*

Figure 5.27: *Aerospatiale-A airfoil mesh*

The Aerospatiale-A airfoil was designed in 1986 and tested in different wind tunnels. The experimental results used here are from the Onera F2 wind tunnel [8]. This particular airfoil has been used as a validation case by many reasearchers [91][154]. Flow conditions for the experiment were $Re = 2.1$ x 10^6 and $Ma_\infty = 0.15$, with turbulence levels being in the range of $Tu_\infty \approx 0.07\%$ ($N_{crit} = 9$). The simulations were unsteady, using a timestep of 0.002 nondimensional time units. Ambient turbulence production terms were: $Tu_{amb} = 0.07\%$, $\omega_{amb} = 50\frac{U_\infty}{c}$.

The pressure and skin friction coefficients were measured at $\alpha = 13.1°$. At this angle, laminar separation occurs on the upper side of the airfoil. The turbulent reattachment is located at $x/c \approx 12\%$. Additionally, the flow separates at the trailing edge due to the adverse pressure gradient. In the experiment, this occurs at $x/c \approx 82\%$. In order to capture the laminar bubble with sufficient accuracy, a modified baseline mesh was created, shown in fig. 5.27a-5.27b. This mesh is refined in the region where laminar separation is detected in the experiment. This refinement was carried out according to Menter [94], who suggests placing at least 20 elements in the streamwise direction of the bubble in order to have adequate resolution to resolve the separation induced transition.

The computational results are compared to experimental data and to results using LES (Mary et al [9]). The pressure and friction coefficients are shown in fig. 5.28. The fully turbulent simulation deviates from the experiments significantly, especially close to the trailing edge (fig. 5.28e). This is expected, as the absence of laminar flow on the airfoil leads to earlier trailing edge separation. The fully turbulent simulation is also not able to predict the laminar bubble in the leading edge (fig. 5.28c). Regarding transitional simulations, all employed models predict trailing edge separation at $x/c \approx 82\%$, which agrees with the experiment. In addition, all transition models predict C_f levels close to the experimental data (fig. 5.28b). However, the results differ close to the leading edge. The e^N method predicts transition at $x/c \approx 11\%$ and subsequently does not predict laminar separation. The AFT and γ models predict transition slightly upstream than $x/c = 12\%$ and exhibit only a small laminar bubble. The best agreement is achieved with the γ-Re_θ model which predicts turbulent reattachment at $x/c = 12.5\%$, which is adequately close to the experimental location of $x/c = 12\%$. The laminar bubble predicted by the γ-Re_θ model is also similar to the one predicted by the LES of Mary et al, although the latter is significantly bigger. However, since no experimental C_f data are available for this region, these deviations cannot be further evaluated.

Velocity profiles at various positions on the upper side are compared in fig. 5.29. The fully turbulent simulation again deviates significantly, even in regions with turbulent flow. On the contrary, the transitional simulations are very close to the experiment and to LES, showing that the laminar-turbulent transition is the driving mechanism in this particular flow case. The only notable difference between LES and current URANS with transition modeling is observed at the $x/c = 0.15$ and 0.2 profiles. Even though boundary layer thickness is similar, the velocity profiles differ. This suggests that the flow in the URANS simulation is not fully developed yet, in contrast to turbulent velocity profiles present in the LES simulation. Further downstream at $x/c = 0.3$ the profiles are again similar. As for the profiles close to the trailing edge (fig. 5.29), the transitional simulations are almost identical to the LES ones. However, both approaches slightly deviate from the experimental data

for the positions between $x/c = 0.825$ and $x/c = 0.93$. Nevertheless, given the low computational cost of the transitional simulations, the comparisons are very favorable.

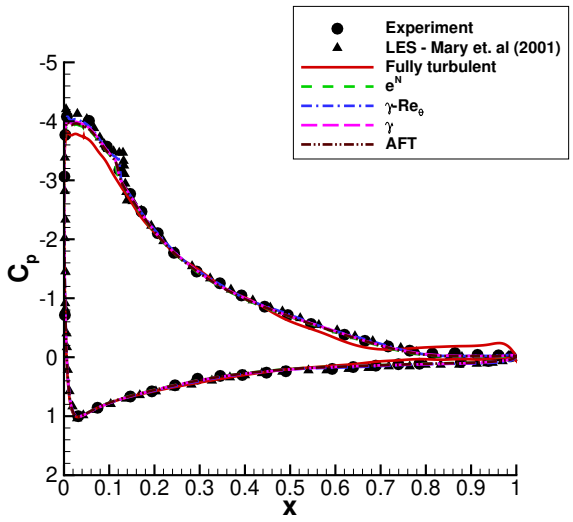

(a) C_p

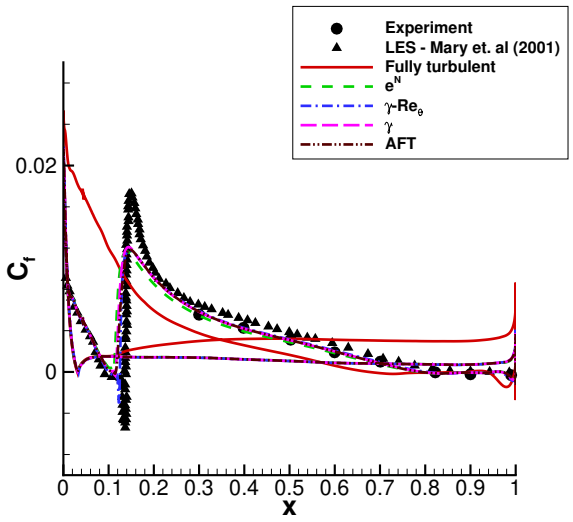

(b) C_f

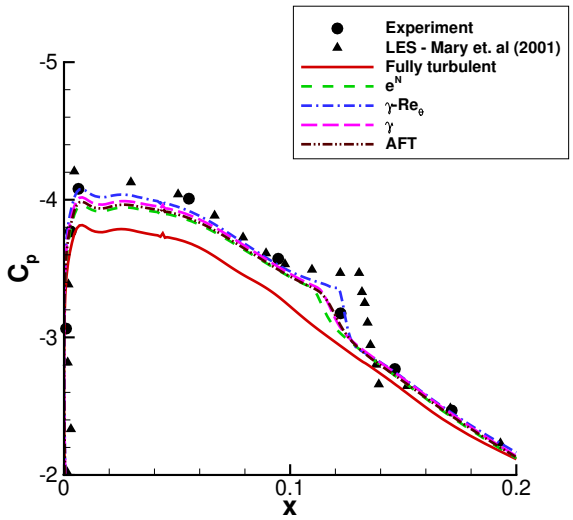

(c) C_p, *leading edge detail*

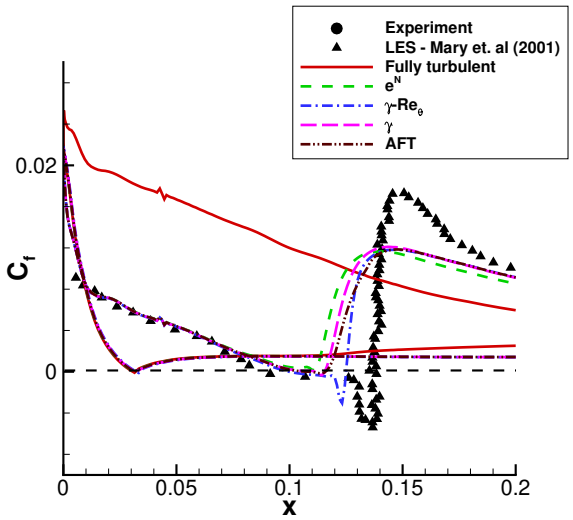

(d) C_f, *leading edge detail*

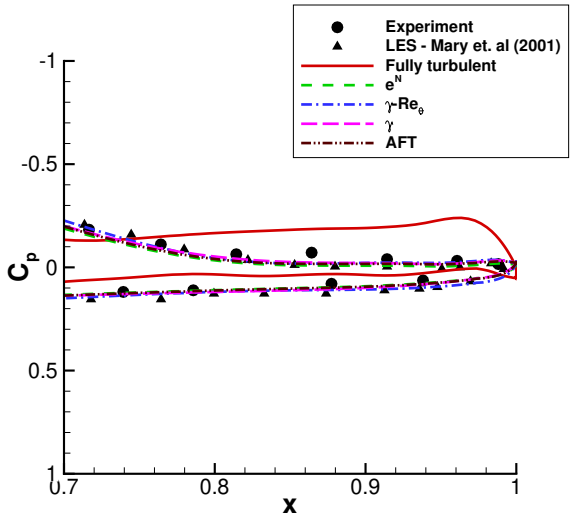

(e) C_p, *trailing edge detail*

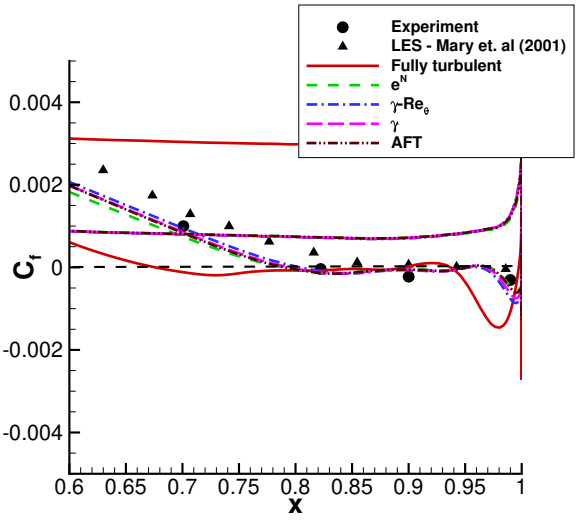

(f) C_f, *trailing edge detail*

Figure 5.28: *Free-transition simulations for the Aerospatiale-A airfoil at* $Re = 2.1\ x\ 10^6$, $Ma_\infty = 0.15$, $\alpha = 13.1°$, $Tu_{amb} = 0.07\%$, $\omega_{amb} = 50\frac{U_\infty}{c}$. *Comparison with experimental data [8] and LES computations [9].*

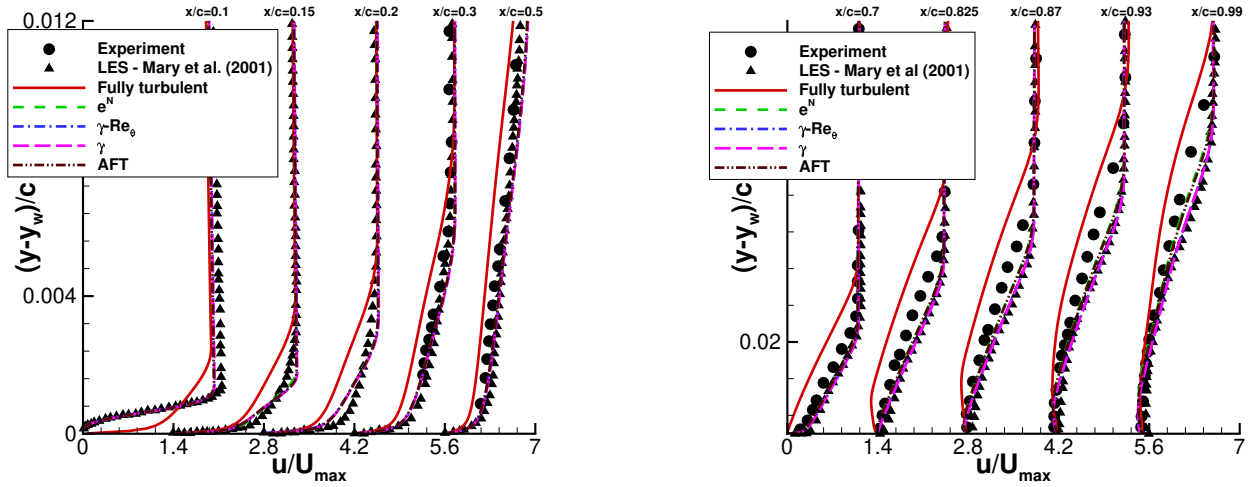

(a) *x/c=0.1-0.5*

(b) *x/c=0.7-0.99*

Figure 5.29: *Free-transition simulations for the Aerospatiale-A airfoil at* $Re = 2.1\ x\ 10^6$, $Ma_\infty = 0.15$, $\alpha = 13.1°$, $Tu_{amb} = 0.07\%$, $\omega_{amb} = 50\frac{U_\infty}{c}$. *Mean streamwise velocity profiles vs normalized wall distance. The individual x/c positions are separated by a horizontal offset of 1.4 with the corresponding zero lines being located at* 0, 1.4, 2.8, 4.2, 5.6. *Comparison with experimental data [8] and LES computations [9].*

5.6.6 NLR-7301 airfoil with flap at $Re = 2.51$ x 10^6

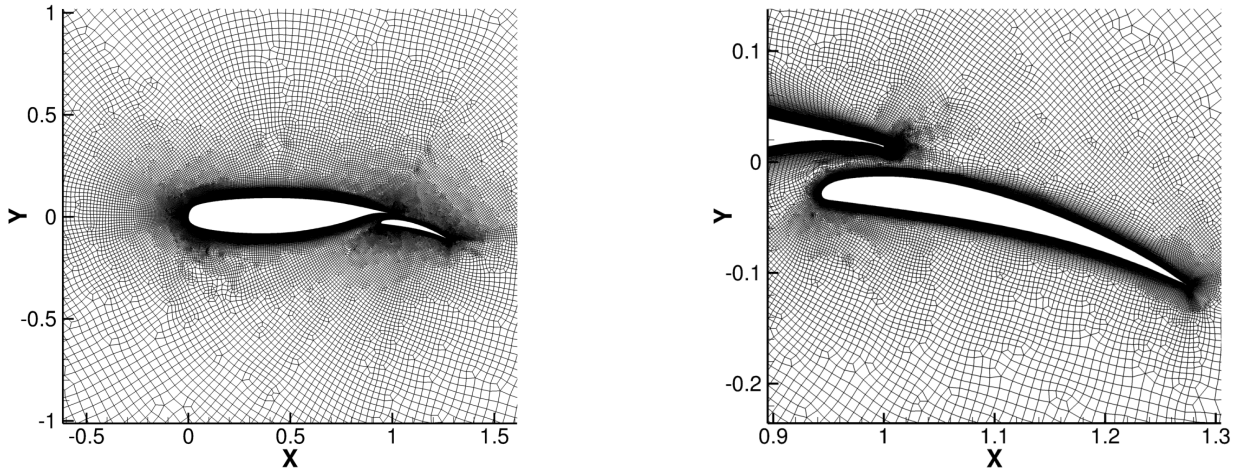

(a) *Full view* **(b)** *Flap close-up*

Figure 5.30: *NLR-7301 airfoil with flap mesh*

The NLR-7301 multi-element airfoil was measured by B. Van Der Berg et al at the NLR LST [10]. This case tests the capabilities of the transition models in multi-body transition predictions. Flow conditions were $Re = 2.51$ x 10^6, $Ma_\infty = 0.185$, $Tu_\infty = 0.2\%$ ($N_{crit} = 6.5$). The experimental measurements were carried out for $\alpha = 6°$ and $13°$. Only the case of $6°$ is considered because velocity profile measurements are also available, in contrast to the case of $13°$. Ambient turbulence production terms were: $Tu_{amb} = 0.2\%$, $\omega_{amb} = 50\frac{U_\infty}{c}$.

C_p and transition locations are compared in fig. 5.32. Overall, all simulations are close to the experimental C_p values for the main element (fig. 5.32a). In fig. 5.32b it is shown that the transport equation models predict a similar laminar bubble as the one in the experiment. However, this does not hold true for the e^N method, which exhibits a significantly oversized bubble due to predicting the transition location further downstream. The C_p levels for the flap are captured relatively well. However, the suction peak level is not well predicted by any simulation (fig. 5.32d). Higher suction levels in the experiment suggest that the mass flow between the main and flap elements is less than the computations. Comparing the transition locations on the upper sides of the main element and the flap (fig. 5.32e-5.32f), the results from all models are adequate. The overall best agreement for this problem is observed with the AFT model, however the deviations between different models are small.

Comparison with experimental boundary layer measurements is given in fig. 5.33. The location of the measuring stations is shown in fig. 5.31. At stations 1-8 (fig. 5.33a), the transitional simulations are very close to the experiments, whereas the fully turbulent simulation deviates slightly. The transitional simulations are also close to the experimental data at stations 9-11 (fig. 5.33b). The only notable difference is at station 10, where the predicted boundary layer profile from the transition models is not as turbulent as the experimental. This may occur because the flow in the simulation has not fully developed yet; station 10 is the first station downstream from the transition point on the lower side. This could also explain the difference in suction levels observed in fig. 5.32d. Lower velocity in the simulations decreases the mass flow rate between the main element and the flap, leading to higher pressure levels in the stagnation region of the latter. For stations 12 and 13 the results are close to the experiments, whereas for station 14 deviations occur (fig. 5.33c-5.33d). At station 14, which is located at the flap trailing edge, predicted boundary layer profile is not well developed in the region close to the wall surface (fig. 5.33d). At station 16, which is located in the separated shear layer, there is qualitative agreement with the experiments, even though the results deviate slighlty (fig. 5.33e).

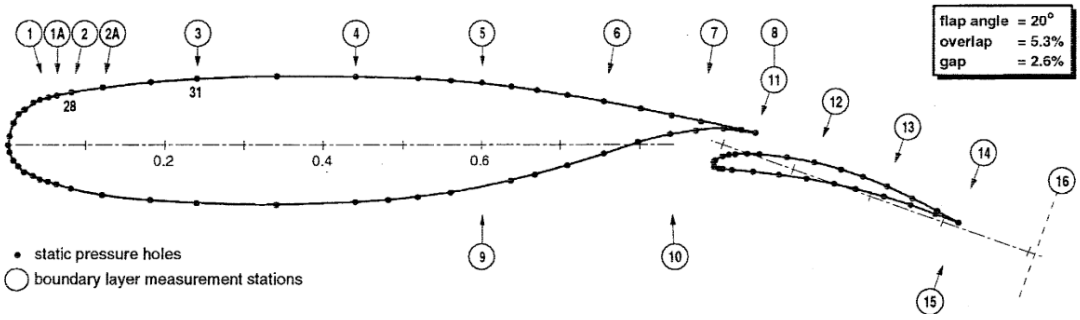

Figure 5.31: *NLR-7301 airfoil and flap section with the locations of static-pressure holes and boundary layer measuring stations (reproduced from [10])*

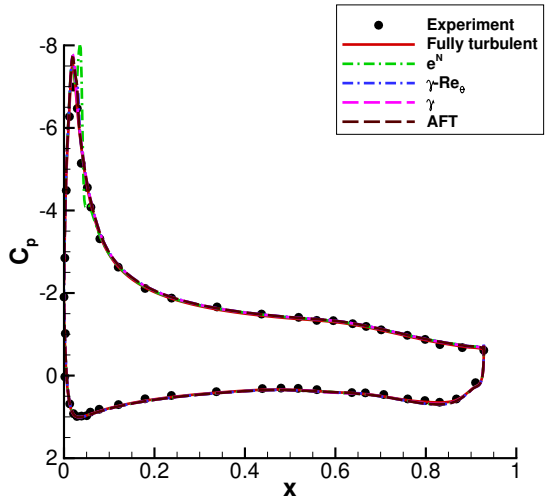

(a) C_p, *main element*

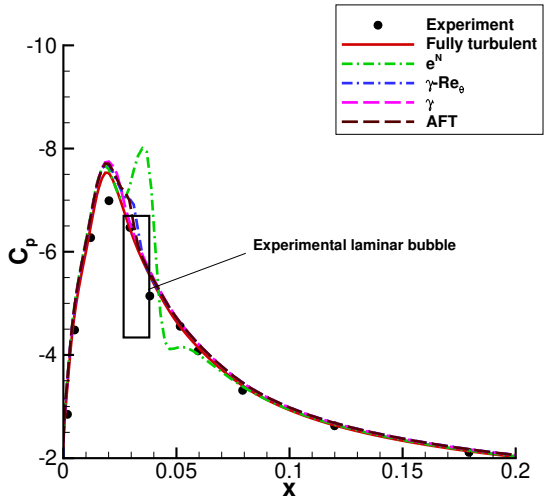

(b) C_p, *main element, leading edge detail*

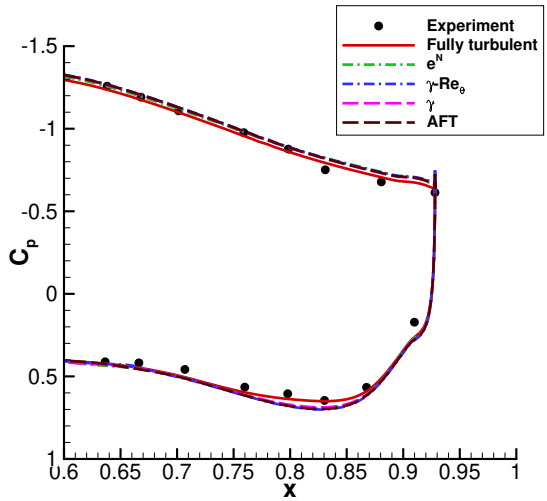

(c) C_p, *main element, trailing edge detail*

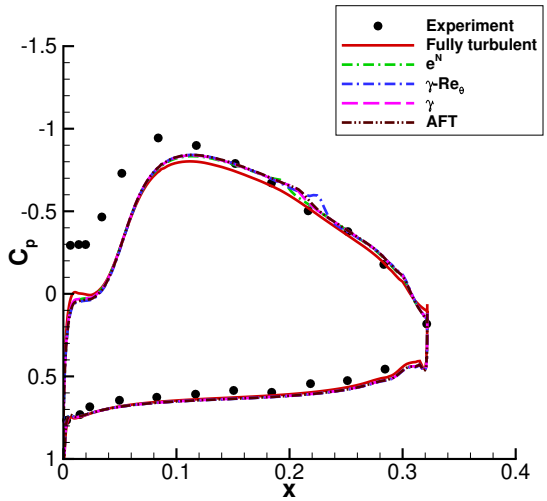

(d) C_p, *flap*

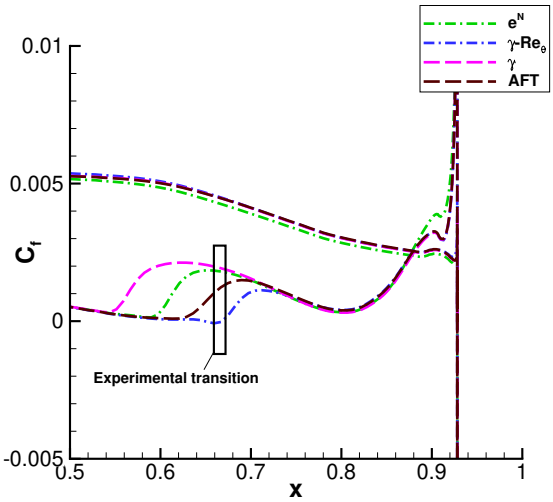

(e) C_f, *main element, trailing edge detail*

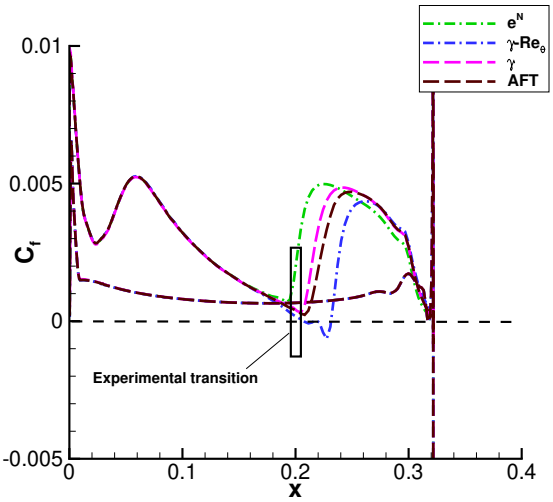

(f) C_f, *flap*

Figure 5.32: *Free-transition simulations for the NLR-7301 airfoil with flap at* $Re = 2.51\ x\ 10^6$, $\alpha = 6°$, $Ma_\infty = 0.185$, $Tu_{amb} = 0.2\%$, $\omega_{amb} = 50\frac{U_\infty}{c}$, $\alpha = 6°$. *Comparison with experimental data [10].*

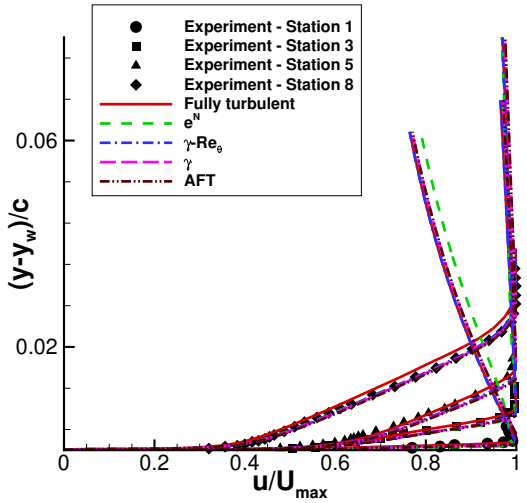

(a) *Stations 1, 3, 5 and 8*

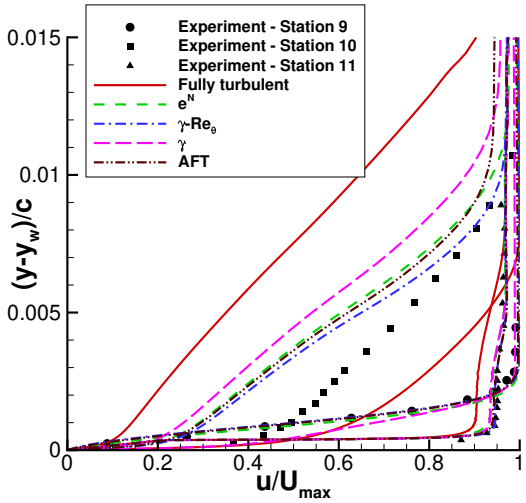

(b) *Stations 9, 10 and 11*

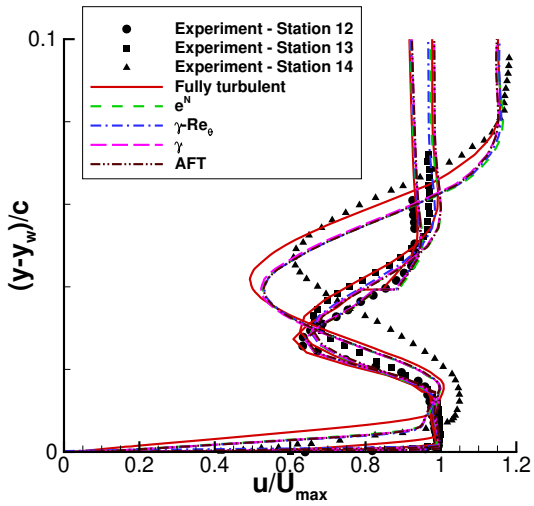

(c) *Stations 12, 13 and 14*

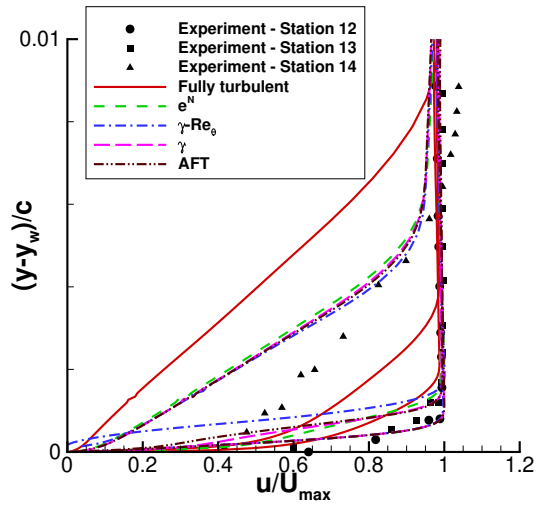

(d) *Stations 12, 13 and 14, detail*

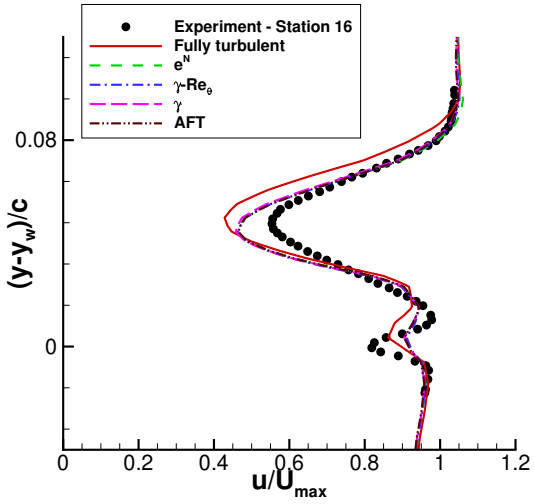

(e) *Station 16*

Figure 5.33: *Free-transition simulations for the NLR7301 multi-element airfoil at* $Re = 2.51\ x\ 10^6$, $Ma_\infty = 0.185$, $Tu_{amb} = 0.2\%$, $\omega_{amb} = 50\frac{U_\infty}{c}$. *Comparison with experimental data [10].*

5.6.7 Eppler e387 airfoil at $Re = 3$ x 10^5

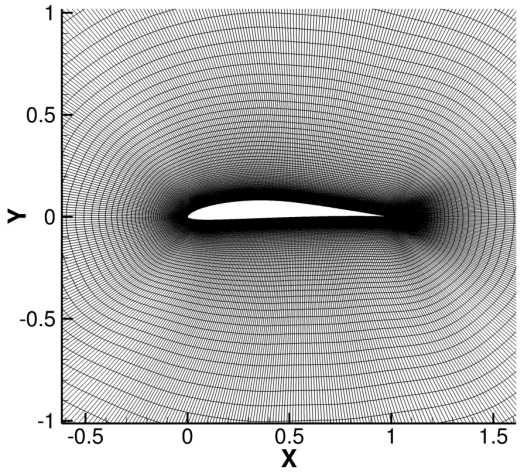

Figure 5.34: *Eppler E387 airfoil mesh*

The Eppler e387 airfoil was measured by McGhee [11] in the NASA Langley low turbulence pressure tunnel. This airfoil is characterized by the presence of laminar separation bubbles which induce transition, and thus has been used as a validation case for transition models (Crivellini et al [124]). The measurements were carried out for $Re = 0.3$ x 10^6 and $Tu_\infty < 0.07\%$, which corresponds to $N_{crit} = 9$ for the e^N methods. For the simulations, Ma_∞ was set to 0.075. Ambient turbulence production terms were: $Tu_{amb} = 0.07\%$, $\omega_{amb} = 50\frac{U_\infty}{c}$.

Computational results are presented in fig. 5.35. Lift and drag coefficients are compared in fig. 5.35a and fig. 5.35b. The lift curve is captured with good accuracy up to the point of stall. The laminar drag bucket is also well predicted in regards to drag level in the low-drag region and to drag bucket corner location. Overall, the e^N method predicts upstream transition on the upper side, as seen in fig. 5.35c. The transition point jumps to the leading edge at $\alpha = 7°$, which is 1° earlier than the jump observed in all other transition models. This early jump is responsible for the increase in drag just after $C_l = 1$, whereas the other models predict the bucket corner on the same C_l as the experiment (fig. 5.35b).

C_p values are also compared at three different angles, shown in fig. 5.35d-5.35f. Both the cases of $\alpha = -2°$ and 4° show that all transport equation transition models are better than the e^N method at capturing the laminar separation effect on the C_p. The comparison for these two angles is very favorable. For the case of 10° however, the comparison shows that the simulations have mild stall, contrary to the experiment which has not stalled yet. This difference is also visible in the lift polar fig. 5.35a, where it is clear that the simulations start developing trailing edge separation at $\alpha \approx 8°$ whereas the experiment starts at $\alpha = 10°$.

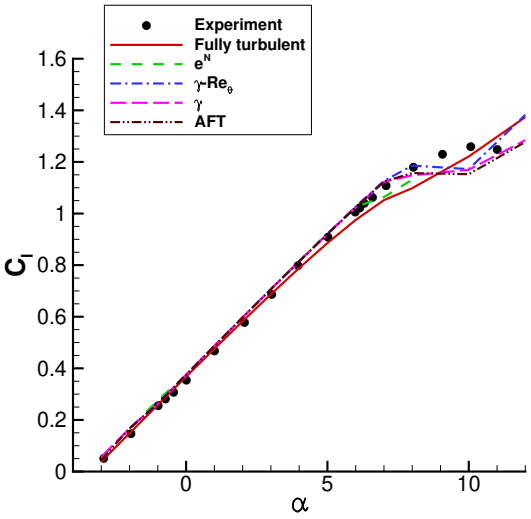

(a) C_l *vs* α

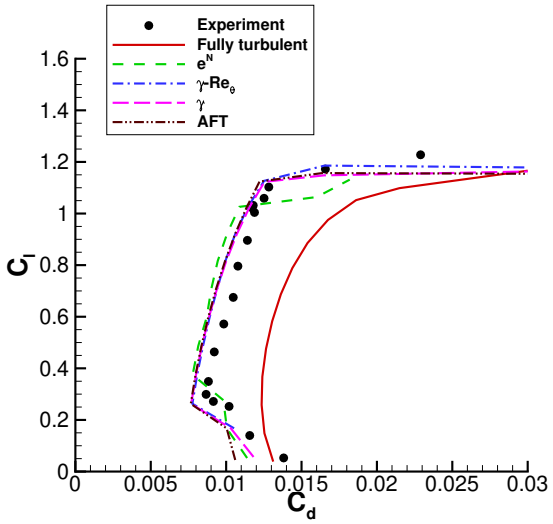

(b) C_l *vs* C_d

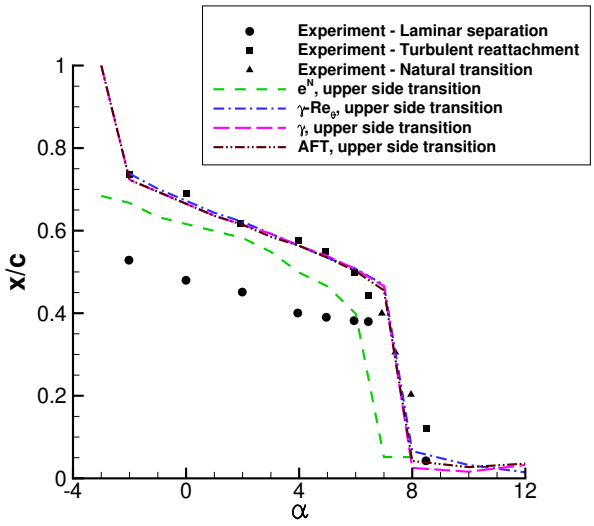

(c) *Laminar separation, turbulent reattachment, and transition locations on the upper side*

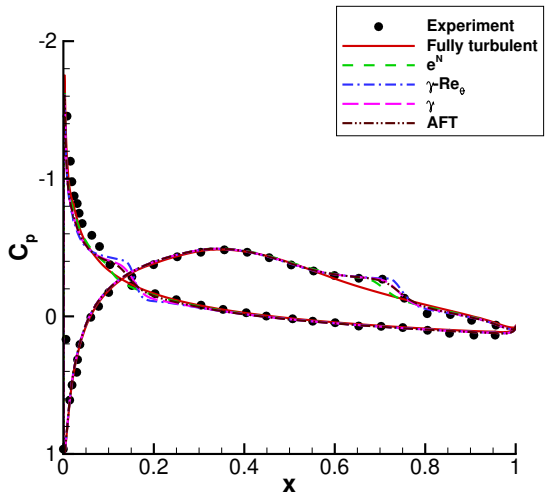

(d) C_p, $\alpha = -2°$

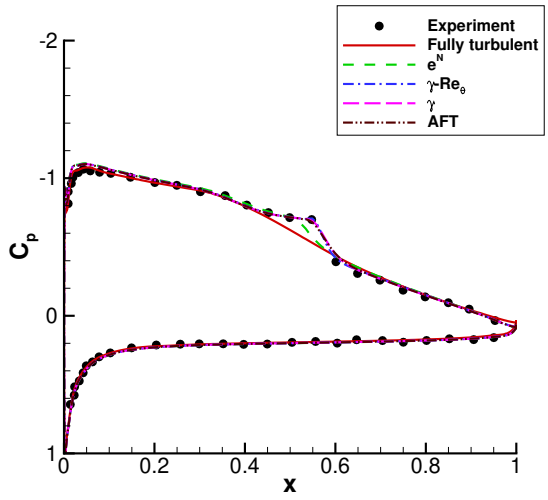

(e) C_p, $\alpha = 4°$

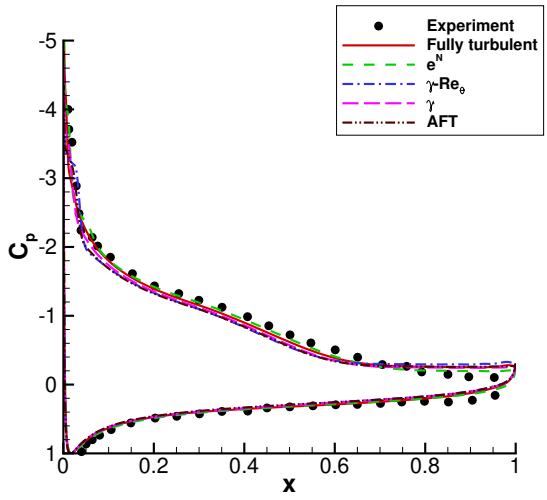

(f) C_p, $\alpha = 10°$

Figure 5.35: *Free-transition simulations for the Eppler e387 airfoil at* $Re = 0.3\ x\ 10^6$, $Ma_\infty = 0.075$, $Tu_{amb} = 0.07\%$, $\omega_{amb} = 50\frac{U_\infty}{c}$. *Comparison with experimental data [11].*

5.6.8 NACA64$_2$015 airfoil at $Re = 10$ to 40 x 10^6

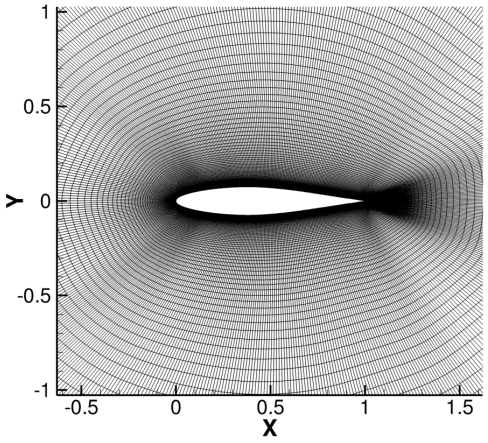

Figure 5.36: *NACA64$_2$015 airfoil mesh*

The next case concerns the NACA64$_2$015 airfoil at high Re numbers. This airfoil was measured in the NASA Ames 12-Foot Pressure Tunnel [12] at Reynolds numbers ranging from 10 x 10^6 to 40 x 10^6, $Ma_\infty = 0.27$ and angles $\alpha = 0°$ and $1°$. Since turbulence levels are not mentioned in the experimental reference, three different freestream turbulence levels were considered, namely $Tu_\infty = 0.1\%$, 0.07% and 0.045%, which correspond to $N_{crit} = 8$, 9 and 10. This case has also been studied by H. Stock in [155]. In regards to the computational mesh, different first layer spacings were used for the different Re numbers in order to ensure that $y^+ < 1$ for all simulations. Ambient turbulence production terms were $Tu_{amb} = 0.1\%$, 0.07% and 0.045% respectively, with $\omega_{amb} = 50\frac{U_\infty}{c}$ for all three cases.

For this particular airfoil, the boundary layer e^N method was used with both the database approach of Stock [156] and the approximate envelope approach of Drela [98]. This was chosen in order to evaluate more transition models at these high Reynolds numbers. Results presented in fig. 5.37 show that the e^N database approach predicts transition locations with great accuracy at both angles and at all Re. At $a = 0°$, best agreement is observed for $Tu_\infty = 0.07\%$ whereas at $a = 1°$ best agreement is observed for $Tu_\infty = 0.045\%$, However, lacking additional experimental data, it is currently not possible to further investigate why different Tu values lead to better agreement for different angles. Transition locations from the AFT model at $1°$ are very close to the experimental data, although at $0°$ the predicted transition location slopes are different than the experiments. At $Re <$ 16 x 10^6 the predicted transition locations are located upstream whereas for $Re >$ 16 x 10^6 they are located downstream. The approximate e^N approach has similar behavior for the higher Re numbers at $0°$. For the case of $a = 0°$, the database e^N method for $Tu_\infty = 0.045\%$ and the Drela e^N method for $Tu_\infty = 0.1\%$ predict the same transition locations. On the other hand, both $\gamma - Re_\theta$ and γ models predict transition too early at all Re numbers. However, the slope of the transition locations vs Re is similar to that predicted by the other transition models.

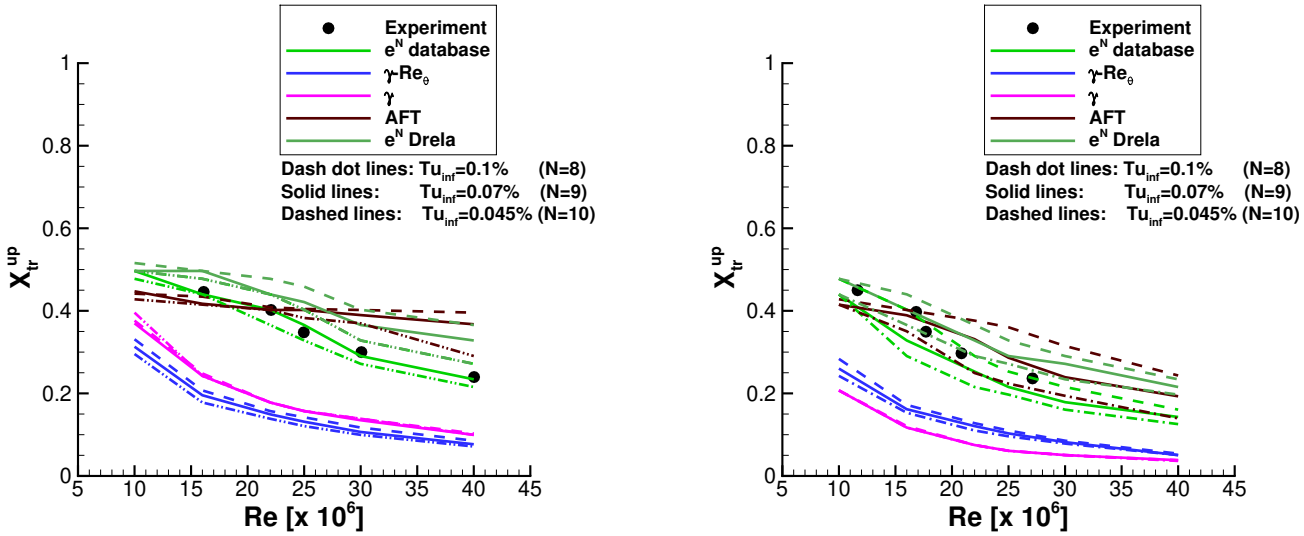

(a) *Transition locations, upper side,* $\alpha = 0^\circ$

(b) *Transition locations, upper side,* $\alpha = 1^\circ$

Figure 5.37: *Free transition simulations for the NACA* 64_2015 *airfoil at* $Re = 10 - 40\ x\ 10^6$, $Ma_\infty = 0.27$, $Tu_\infty = 0.045 - 0.1\%$, $\omega_\infty = 50\frac{U_\infty}{c}$. *Comparisons with experimental data [12].*

5.7 Three-dimensional test cases

5.7.1 6:1 prolate spheroid at Re=6.5 x 10^6

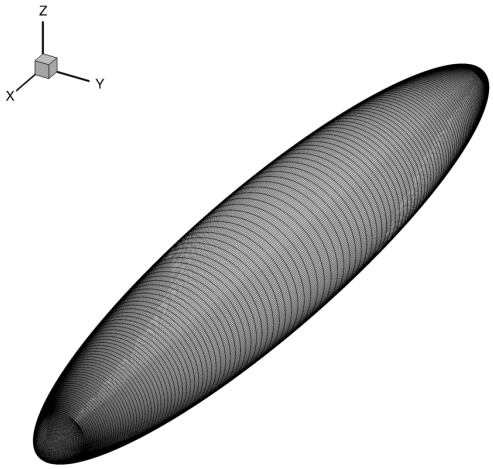

Figure 5.38: *6:1 prolate spheroid surface mesh*

The flow around the 6:1 prolate spheroid was measured by Kreplin et al in the DFVLR low speed wind tunnel [121]. The experiment was carried out at Reynolds number 6.5 x 10^6 (based on spheroid length), whereas M_∞ was 0.136. Turbulence intensity was about 0.2%. Three angles of attack were considered: 5°, 15° and 20°. Ambient turbulence source terms were: $Tu_{amb} = 0.2\%$, $\omega_{amb} = 50\frac{U_\infty}{L}$, with L being the length of the spheroid.

This case is of particular interest because the three-dimensional nature of the flow around spheroids leads to strong crossflow instabilities that dominate the transition process, which makes it a solid validation case for transition models that try to capture crossflow effects. First efforts (Nebel et al [157], Stock [158]) considered boundary layer transition using the e^N method, whereas more recently the focus has shifted towards the available transport equation transition models (Langtry et al [92], Grabe et al [115][13], Denison et al [159], Vallinayagam Pillai et al [160], Choi et al [116][117], Vizinho et al[161]). Due to the presence of crossflow effects, this case has also been suggested as a standard transition model validation case [149].

The generated computational mesh had 256 cells in the wrap-around, 128 in the normal, and 128 in the spanwise directions, resulting in approximately 5 million cells. The domain extent was set to 100 spheroid lengths. The γ-Re_θ model is used in the computations in its baseline version (Section 3.3), as well as equipped with two different crossflow transition variants (specifically discussed in Section 3.3.5). The surface roughness of the spheroid is not known, and thus for the crossflow model of Langtry a value of $10\mu m$ was assumed, which corresponds to a rough painted surface finish.

Computational results for the friction coefficient are compared with experiments in fig. 5.39-5.41. Simulations without crossflow terms are unable to produce results that resemble the experimental data. When using either of the crossflow models the results are significantly improved, especially at the two higher angles. The only exception is the case of 5°, where the crossflow models fail to give results that resemble the experiments. Similar deviations from the experimental data at this particular angle have also been noted by other researchers [13][161]. Between the Langtry and CFHE crossflow models, performance of both is comparable, with the latter having a slight edge in this particular case.

The extracted C_p distributions are compared in fig. 5.42. For the case of $\alpha = 5°$, results from all models are similar. This is expected, as the angle is relatively low and the crossflow is weak and manifests itself upon exit. For the cases of $\alpha = 15°$ and 20°, the differences start to apppear. At $\alpha = 15°$, where both crossflow models give results that are close to the experimental C_f, the upper side of the spheroid exhibits higher suction levels towards the trailing edge. Moving to the case of $\alpha = 20°$, the same behavior is observed; however this time only for the CFHE crossflow model, since the Langtry crossflow model deviates from the experiment. In the simulations where transition is predicted further downstream, larger regions of laminar flow on the upper side allow for higher pressure levels towards the trailing edge. This occurs because the laminar boundary layer does not dissipate energy as fast as the turbulent boundary layer. When comparing C_p distributions on the pressure side, the results are almost identical among the three models. This is expected, as the flow on the lower side for increasing α is mostly laminar.

Contours of z-axis vorticity on the $y/L = 0$ plane and x-axis vorticity on the $x/L = 0.7$ plane are presented

in fig. 5.43-5.44 for $\alpha = 5^\circ$ and 20°. The three approaches have similar patterns, however at 20° the CFHE model produces slightly bigger z-axis and x-axis structures (fig. 5.43f and fig. 5.44f) due to upstream transition prediction.

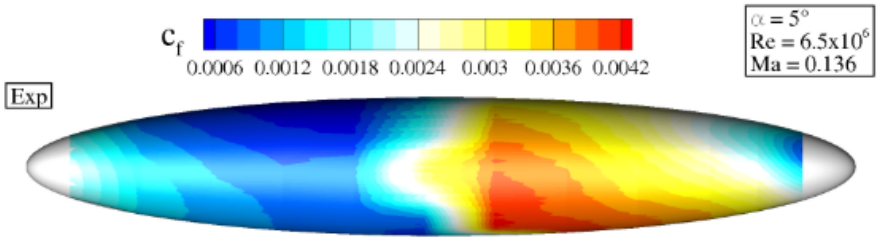

(a) *Experiment*

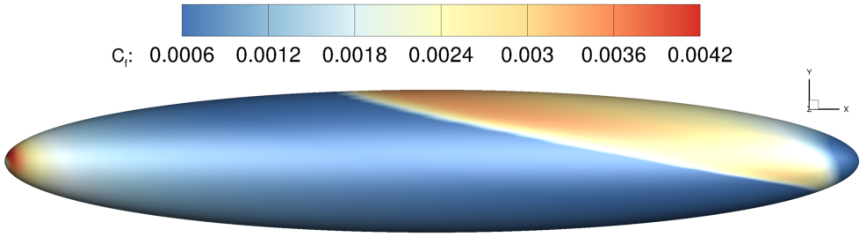

(b) *Free transition using the γ-Re_θ model without crossflow terms.*

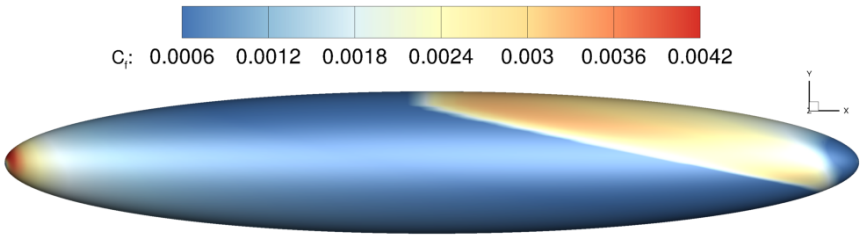

(c) *Free transition using the γ-Re_θ model with crossflow terms. Langtry crossflow model.*

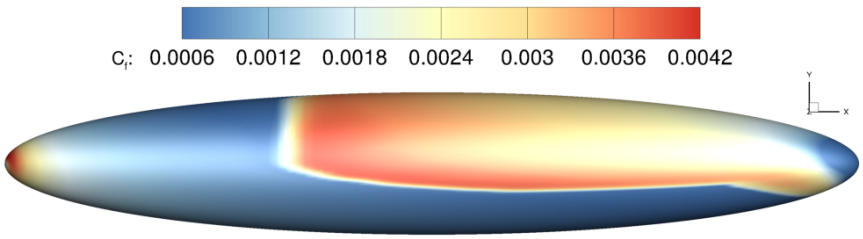

(d) *Free transition using the γ-Re_θ model with crossflow terms. CFHE crossflow model.*

Figure 5.39: *Free-transition simulations for the 6:1 prolate spheroid at $Re = 6.5\ x\ 10^6$, $Ma_\infty = 0.136$, $Tu_{amb} = 0.2\%$, $\omega_{amb} = 50\frac{U_\infty}{L_{spheroid}}$. Comparison of computational C_f contour to experimental data (reproduced from [13]) at $\alpha = 5^\circ$.*

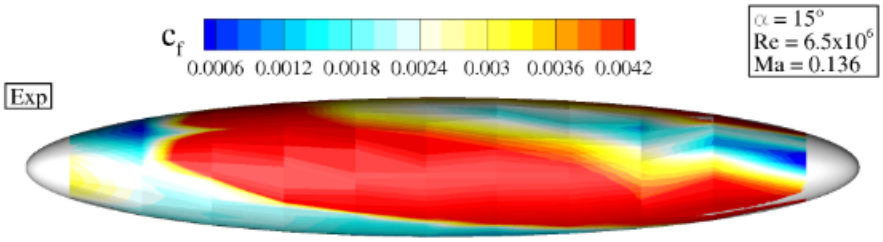

(a) *Experiment*

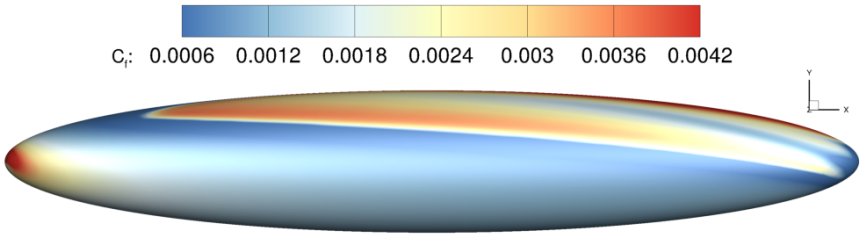

(b) *Free transition using the γ-Re_θ model without crossflow terms.*

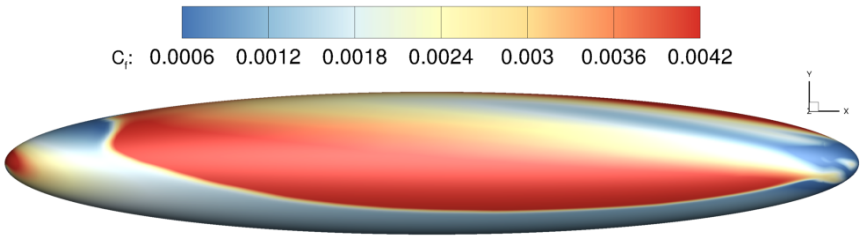

(c) *Free transition using the γ-Re_θ model with crossflow terms. Langtry crossflow model.*

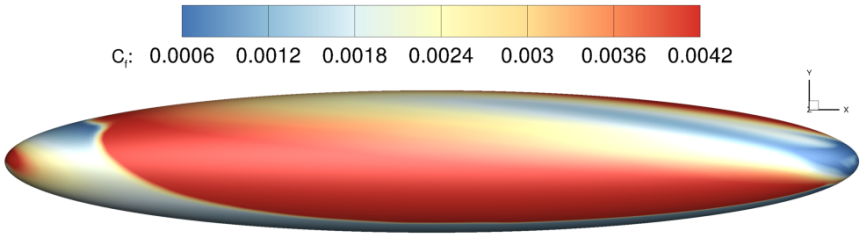

(d) *Free transition using the γ-Re_θ model with crossflow terms. CFHE crossflow model.*

Figure 5.40: *Free-transition simulations for the 6:1 prolate spheroid at $Re = 6.5\ x\ 10^6$, $Ma_\infty = 0.136$, $Tu_{amb} = 0.2\%$, $\omega_{amb} = 50\frac{U_\infty}{L_{spheroid}}$. Comparison of computational C_f contour to experimental data (reproduced from [13]) at $\alpha = 15°$.*

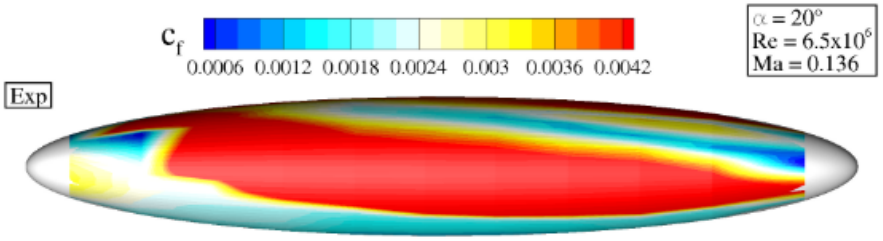

(a) *Experiment*

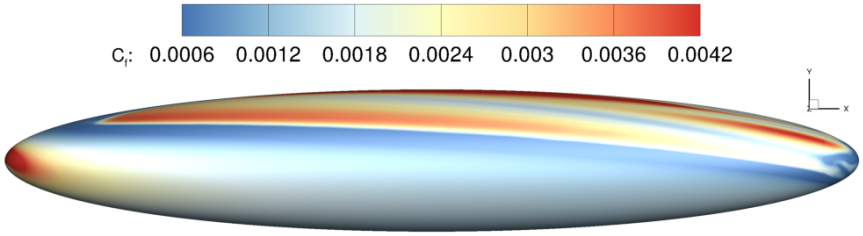

(b) *Free transition using the γ-Re_θ model without crossflow terms.*

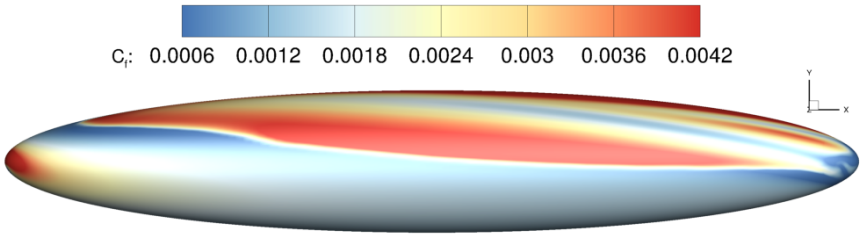

(c) *Free transition using the γ-Re_θ model with crossflow terms. Langtry crossflow model.*

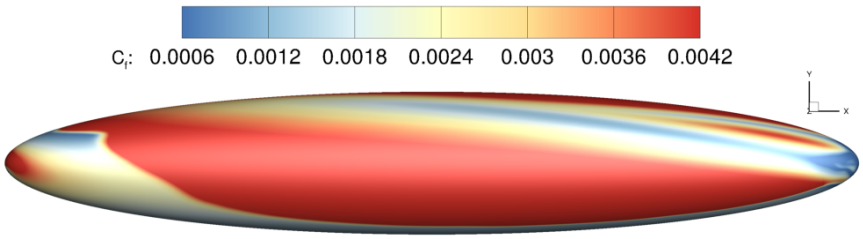

(d) *Free transition using the γ-Re_θ model with crossflow terms. CFHE crossflow model.*

Figure 5.41: *Free-transition simulations for the 6:1 prolate spheroid at $Re = 6.5\ x\ 10^6$, $Ma_\infty = 0.136$, $Tu_{amb} = 0.2\%$, $\omega_{amb} = 50\frac{U_\infty}{L_{spheroid}}$. Comparison of computational C_f contour with experimental data (reproduced from [13]) at $\alpha = 20°$.*

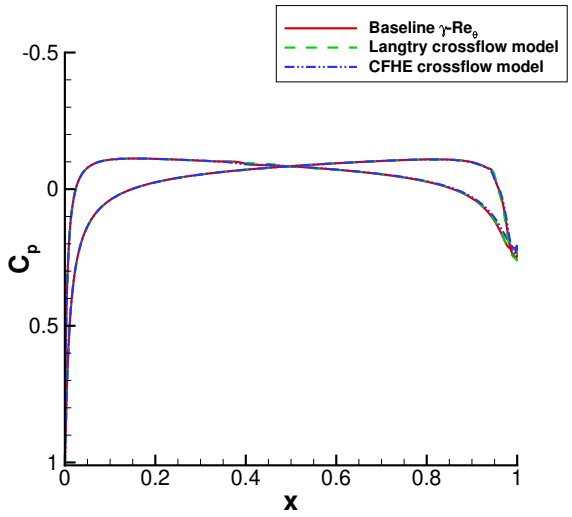

(a) $\alpha = 5^\circ$

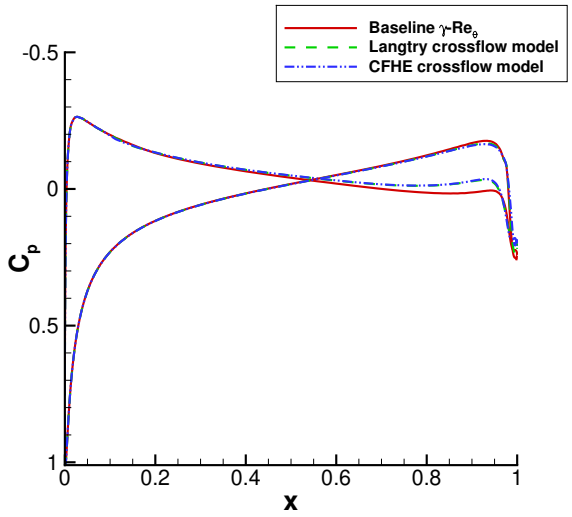

(b) $\alpha = 15^\circ$

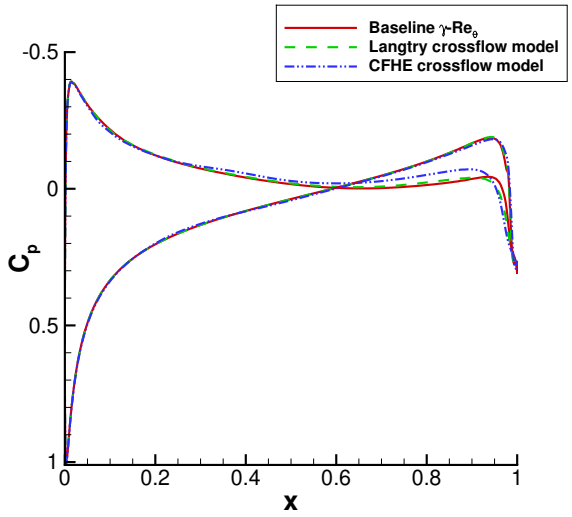

(c) $\alpha = 20^\circ$

Figure 5.42: *Free-transition simulations for the 6:1 prolate spheroid at* $Re = 6.5\ x\ 10^6$, $Ma_\infty = 0.136$, $Tu_{amb} = 0.2\%$, $\omega_{amb} = 50\frac{U_\infty}{L_{spheroid}}$. *Comparison of computational* C_p *distributions.*

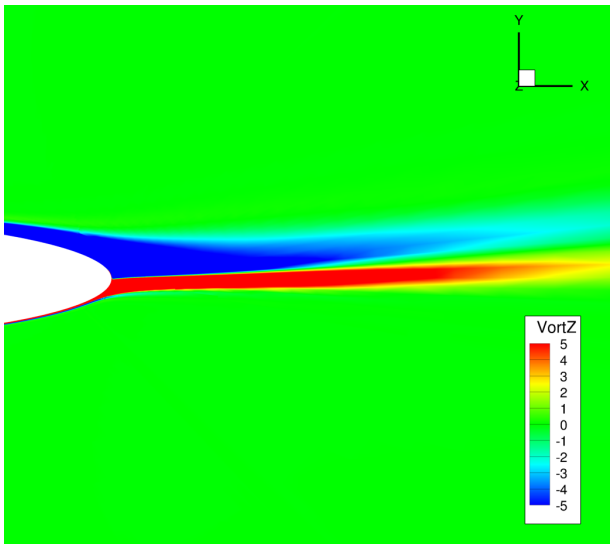

(a) $\alpha = 5°$, *γ-Re_θ model without crossflow terms*

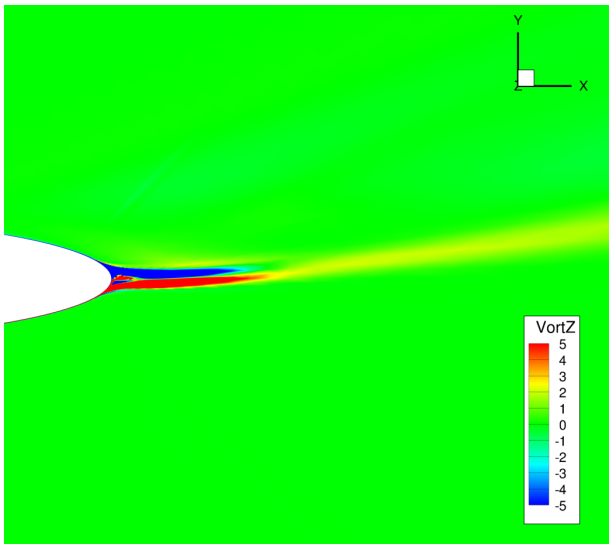

(b) $\alpha = 20°$, *γ-Re_θ model without crossflow terms*

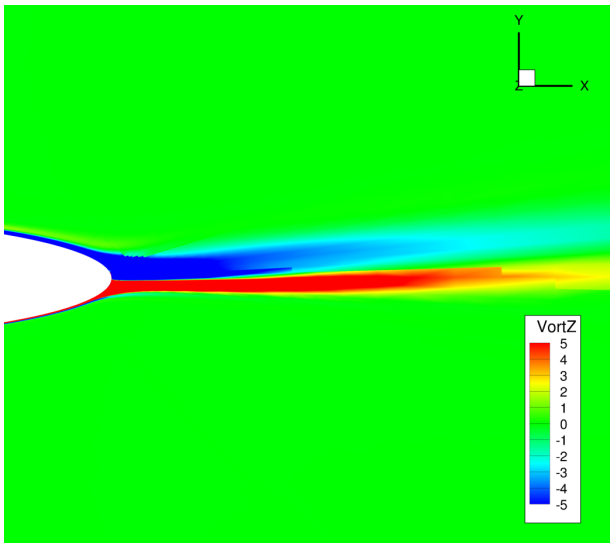

(c) $\alpha = 5°$, *Langtry crossflow model*

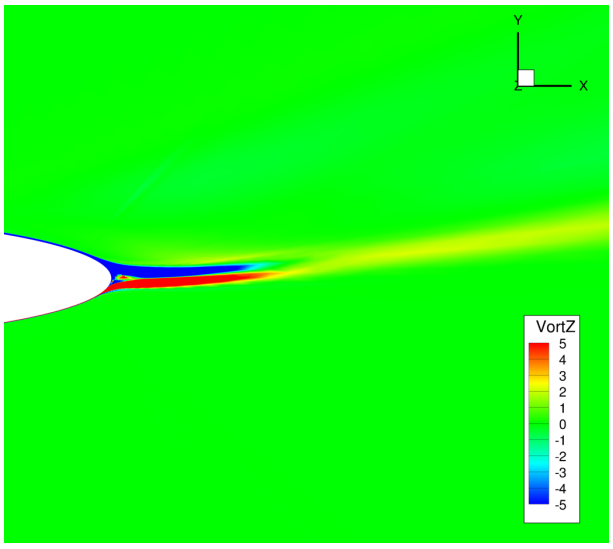

(d) $\alpha = 20°$, *Langtry crossflow model*

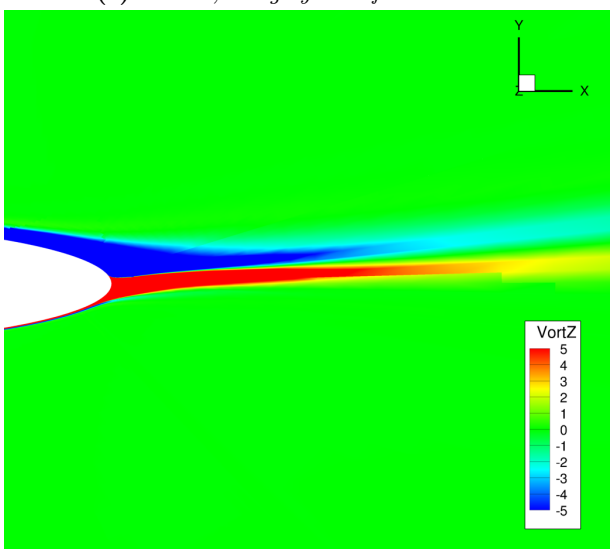

(e) $\alpha = 5°$, *CFHE crossflow model*

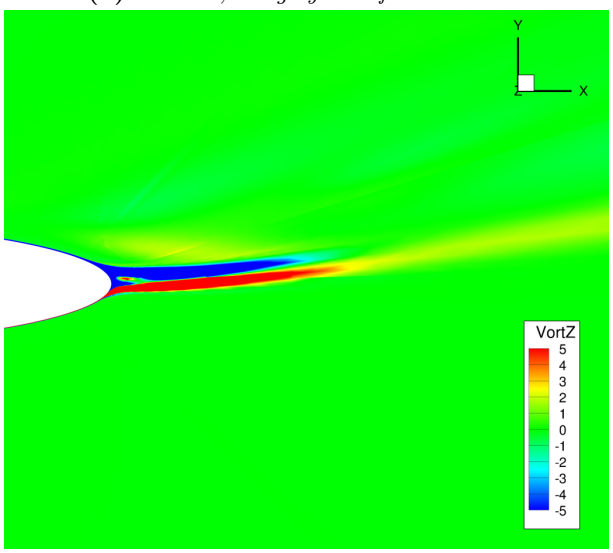

(f) $\alpha = 20°$, *CFHE crossflow model*

Figure 5.43: *Free-transition simulations for the 6:1 prolate spheroid at* $Re = 6.5\ x\ 10^6$, $Ma_\infty = 0.136$, $Tu_{amb} = 0.2\%$, $\omega_{amb} = 50\frac{U_\infty}{L_{spheroid}}$. *Contours of computational z-axis vorticity on the* $y/L = 0$ *plane.*

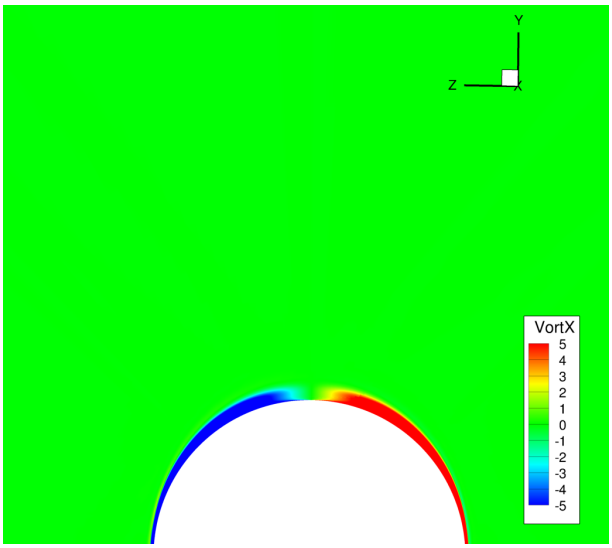

(a) $\alpha = 5°$, *γ-Re_θ model without crossflow terms*

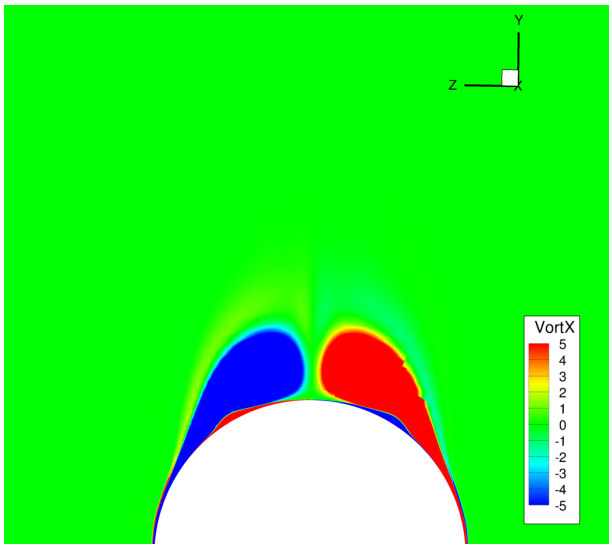

(b) $\alpha = 20°$, *γ-Re_θ model without crossflow terms*

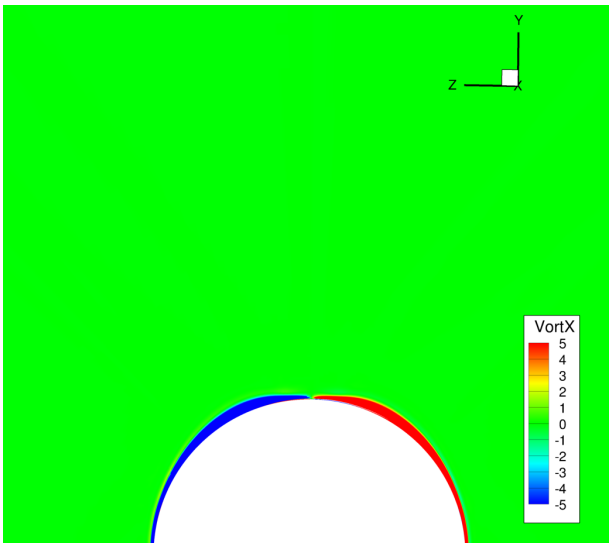

(c) $\alpha = 5°$, *Langtry crossflow model*

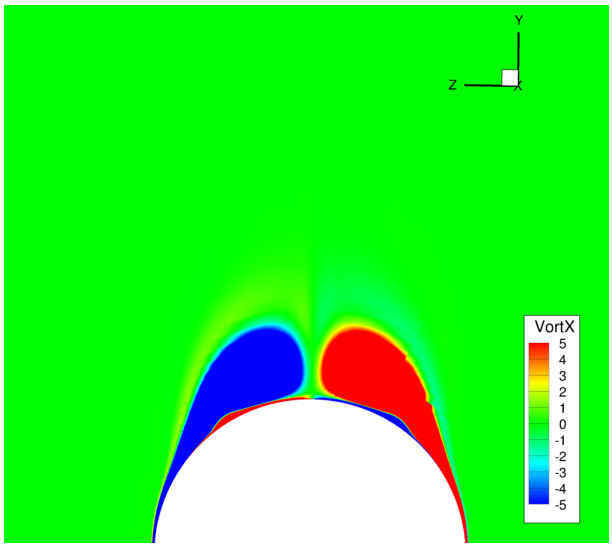

(d) $\alpha = 20°$, *Langtry crossflow model*

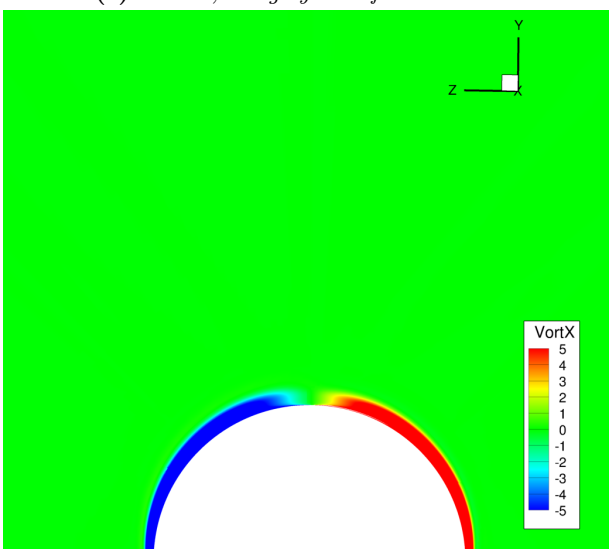

(e) $\alpha = 5°$, *CFHE crossflow model*

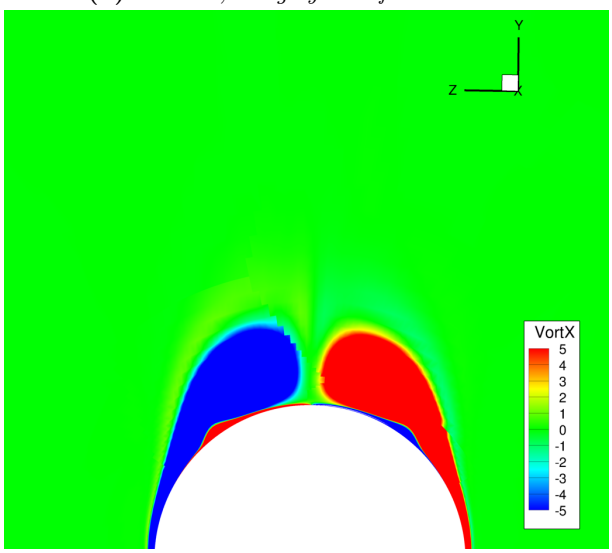

(f) $\alpha = 20°$, *CFHE crossflow model*

Figure 5.44: *Free-transition simulations for the 6:1 prolate spheroid at* $Re = 6.5\ x\ 10^6$, $Ma_\infty = 0.136$, $Tu_{amb} = 0.2\%$, $\omega_{amb} = 50\frac{U_\infty}{L_{spheroid}}$. *Contours of computational x-axis vorticity on the* $x/L = 0.7$ *plane.*

5.7.2 ONERA M6 wing at Re=3.5 x 10^6

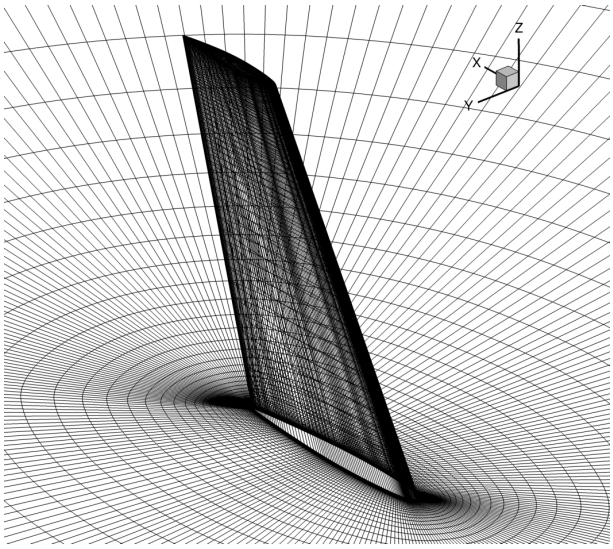

Figure 5.45: *ONERA M6 wing computational mesh*

The ONERA M6 wing is a widely used three-dimensional aerodynamic case. The design of the wing is based on a symmetric ONERA D airfoil section perpendicular to the 40% line. It is a single element semi-span swept, tapered wing with an aspect ratio of 3.8 and a taper ratio of $\lambda = 0.562$. The leading edge sweep angle is $\phi_{LE} = 30°$ whereas the trailing edge sweep angle is $\phi_{TE} = 15.8°$.

The flow around the wing has been measured for various operational conditions. The simulations in this thesis are based on the experiments presented in [14], which were performed in the ONERA S2Ch (Chalais-Meudon) wind tunnel. Re was 3.5 x 10^6, Ma 0.262. The freestream turbulence intensity of the wind tunnel was about $Tu_\infty = 0.2\%$. Laminar regions on the surface of the wing were visualized using sublimation of naphthalene.

The generated computational mesh had 256 wrap-around, 128 normal and 64 spanwise cells, resulting total number of approximately 3 million. Domain extent was set to 1000 root chords. First layer spacing was set to 5 x 10^6 root chords, which yielded $y^+ < 1$ at all times. The γ-Re_θ model is used, both without crossflow treatment and with two different crossflow transition models (see Section 3.3.5). For the Langtry crossflow model, surface roughness was set to $5\mu m$. Ambient turbulence production terms were: $Tu_{amb} = 0.2\%$, $\omega_{amb} = 50\frac{U_\infty}{c_{root}}$.

The experimental visualizations are compared to results from transitional simulations in fig. 5.46. Without crossflow transition modeling, the predicted transition locations are located far downstream at all angles considered (fig. 5.46b). For the case of 0° the inclusion of crossflow terms improves the results significantly. When compared to the results without crossflow transition modeling, the transition locations on both sides are located close to the leading edge (fig. 5.46c-5.46d) and they agree with the experimental visualizations (fig. 5.46a). At 5° the agreement was not as good, as both crossflow models deviated from the experimental transition locations on the lower side. At 20°, results from the CFHE crossflow model were accurate, whereas the Langtry crossflow model predicted transition downstream.

Integrated loads are also presented in fig. 5.47. Simulations with crossflow terms predict upstream transition, which raises predicted sectional C_d. On the contrary, the effect on C_l is negligible.

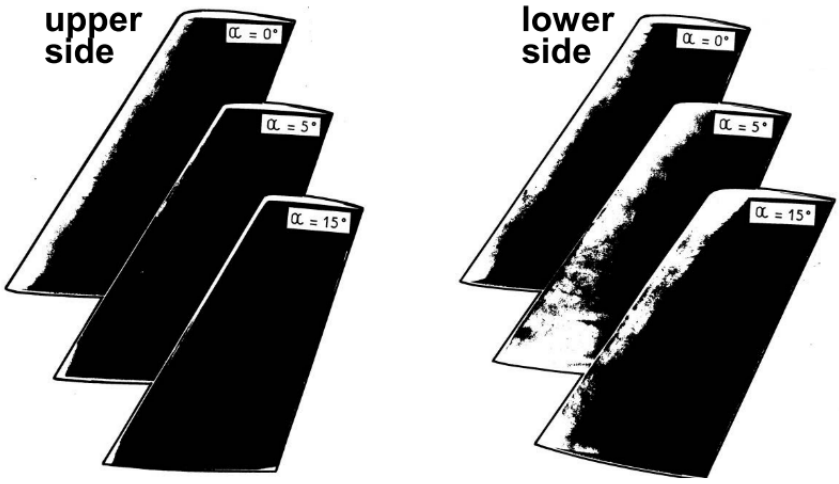

(a) *Experimental transition locations (sublimation of naphthalene).*

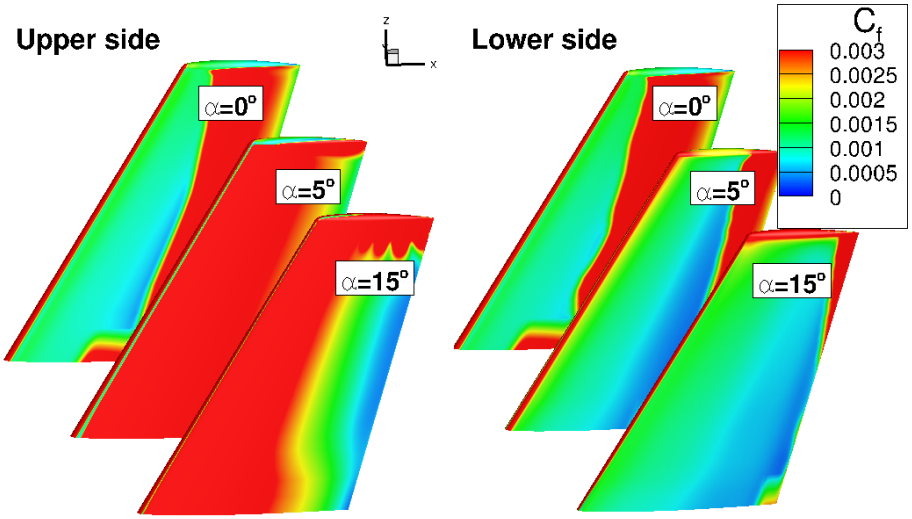

(b) *C_f visualization, γ-Re_θ model without crossflow terms.*

Figure 5.46: *Free-transition simulations for the ONERA M6 wing at $Re_{root} = 3.5\ x\ 10^6$, $Ma_\infty = 0.262$, $Tu_{amb} = 0.2\%$, $\omega_{amb} = 50\frac{U_\infty}{c_{root}}$. Laminar-turbulent region visualization. Comparison with experimental data [14].*

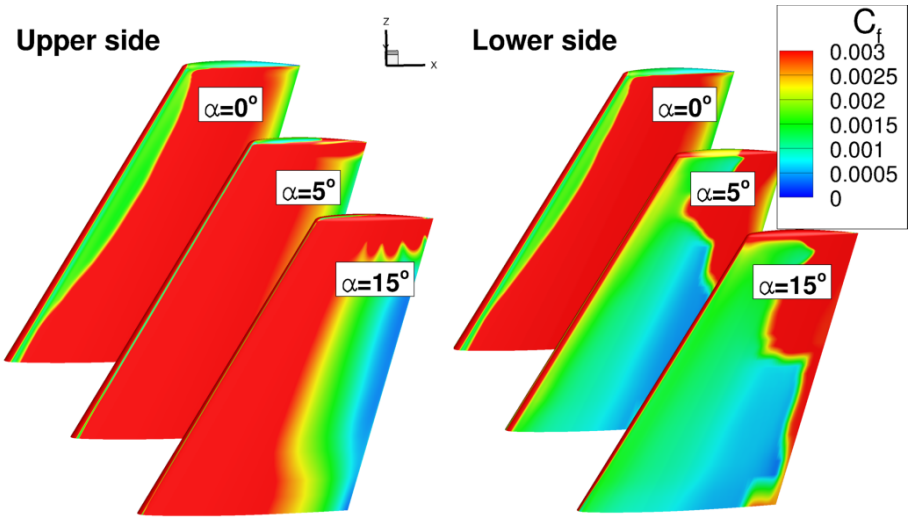

(c) *C_f visualization, γ-Re_θ model with crossflow terms using the crossflow model of Langtry et al.*

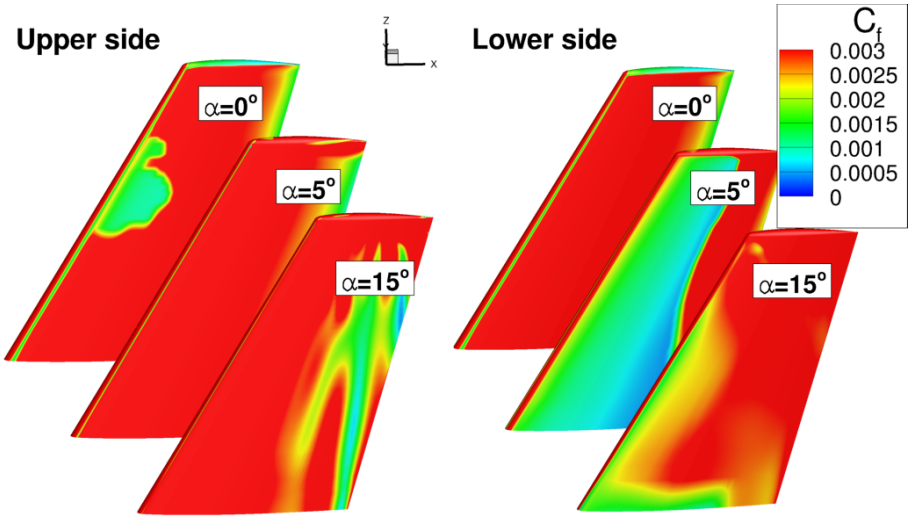

(d) *C_f visualization, γ-Re_θ model with crossflow terms using the CFHE model.*

Figure 5.46: *(concluded)*

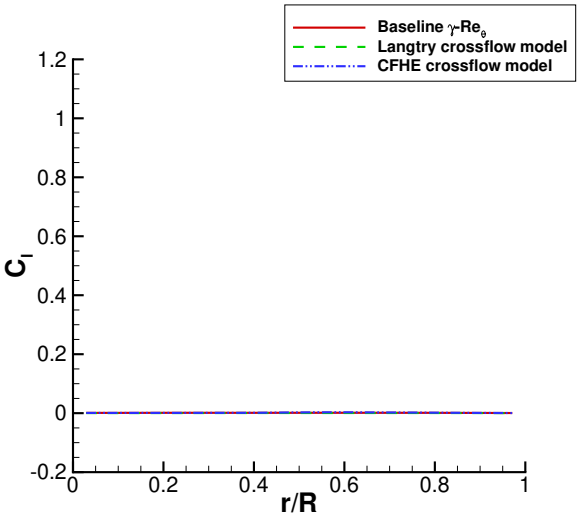

(a) $\alpha = 0°$, C_l

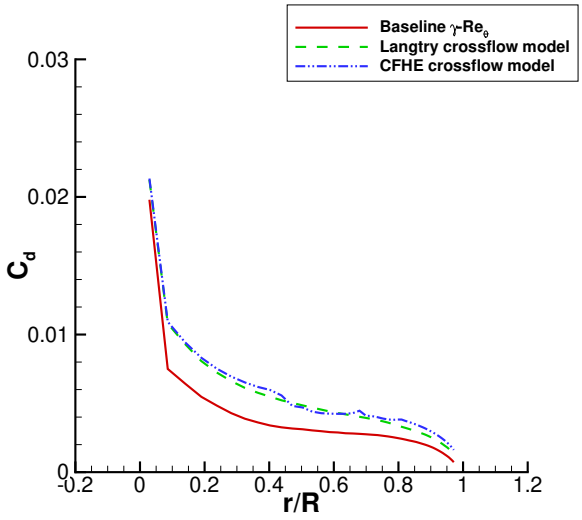

(b) $\alpha = 0°$, C_d

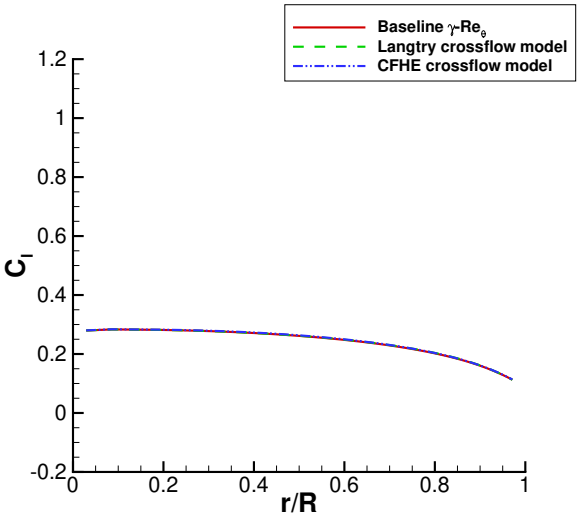

(c) $\alpha = 5°$, C_l

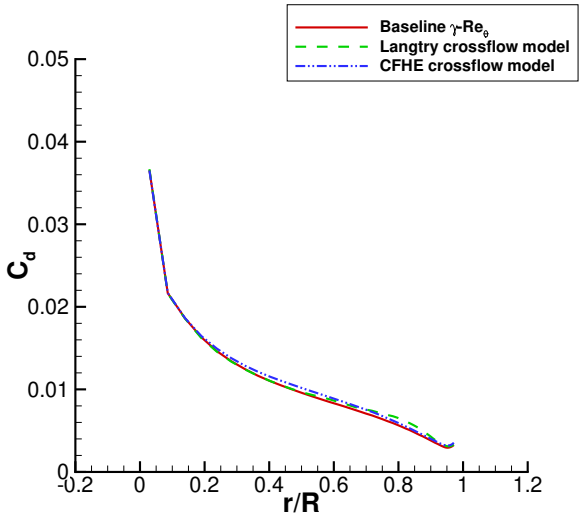

(d) $\alpha = 5°$, C_d

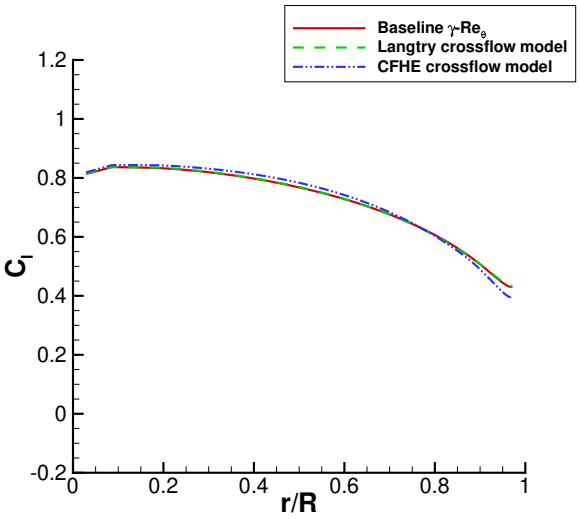

(e) $\alpha = 15°$, C_l

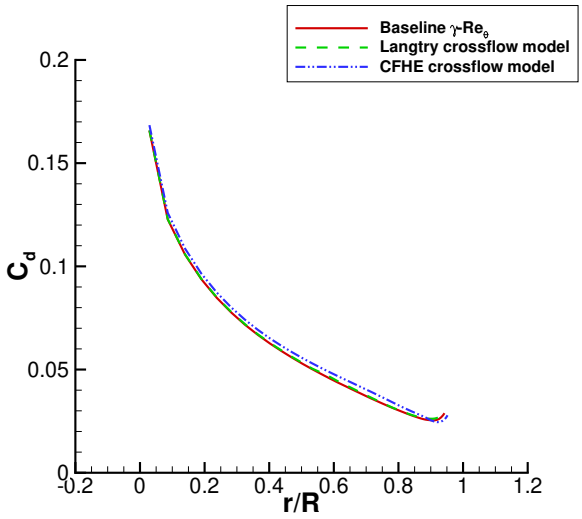

(f) $\alpha = 15°$, C_d

Figure 5.47: *Free-transition simulations for the ONERA M6 wing at* $Re_{root} = 3.5\ x\ 10^6$, $Ma_\infty = 0.262$, $Tu_{amb} = 0.2\%$, $\omega_{amb} = 50\frac{U_\infty}{c_{root}}$. *Computational* C_l *and* C_d *along the spanwise axis.*

5.7.3 AVATAR Wind Turbine Rotor Blade

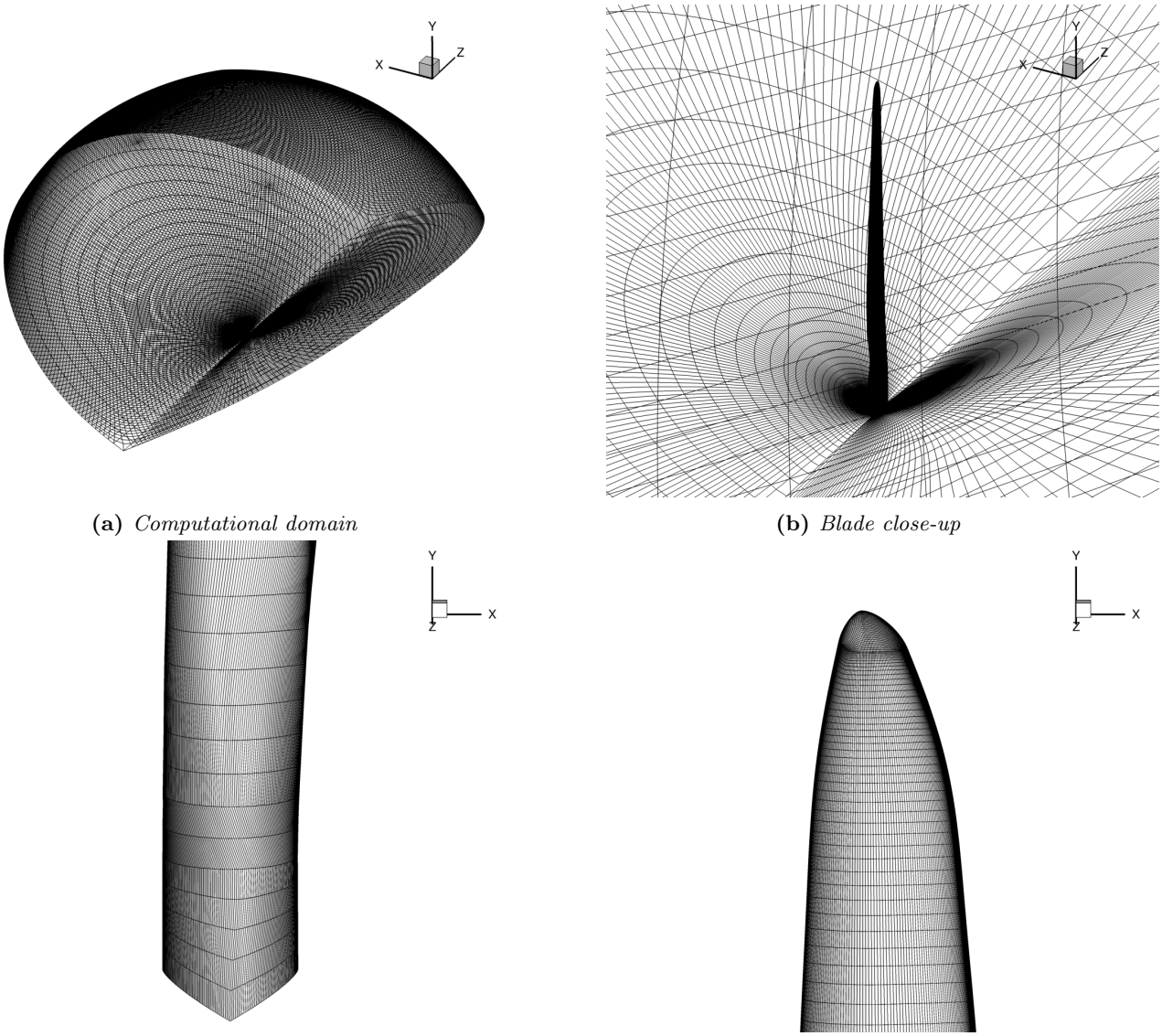

(a) *Computational domain*

(b) *Blade close-up*

(c) *Root surface mesh*

(d) *Tip surface mesh*

Figure 5.48: *AVATAR W/T Rotor Blade computational mesh*

The AVATAR Wind Turbine was employed in the AVATAR Project [15]. It consists of three blades and has a rotor diameter of 205 m. Operating conditions are given in Table 5.6. Experimental measurements have not been carried out, therefore comparison with experimental data is not possible. However, the results are compared to those of other researchers who participated in the AVATAR project. The goal is to assess the effect of transition on integrated blade loads.

The computational mesh was generated by DTU-Risoe and was freely available to the contributors of the AVATAR project. It consisted of 256 wrap-around, 128 normal and 128 spanwise cells, resulting in a total number of approximately 5 million (fig. 5.48). Only one blade was simulated, using 120° periodic conditions. Regarding transitional simulations, the e^N method with the approximate envelope approach was used. Natural transition was assumed ($N_{crit} = 9$). A sectional approach was adopted for the boundary layer, which means that the boundary layer was solved separately in each 2D airfoil section of the blade. Ambient turbulence production terms were not used, since they are not necessary for boundary layer transition methods.

Computational mechanical power and thrust are compared to those of other researchers in fig. 5.49, where it is shown that fully turbulent and transitional curves agree. As expected, the presence of laminar regions raises both power and thrust. The presence of laminar regions is able to harness more energy from the wind flow. However, the increase in power comes with an increase in construction cost, as higher levels of thrust will require a tower that is able to withstand the increased loads.

Table 5.6: *AVATAR W/T operating conditions*

$U_{wind}(m/s)$	RPM	Pitch (°)
4	6.0000	0
5	6.0000	0
6	6.0000	0
7	6.0146	0
8	6.8738	0
9	7.7330	0
10	8.5922	0
10.5	9.0218	0

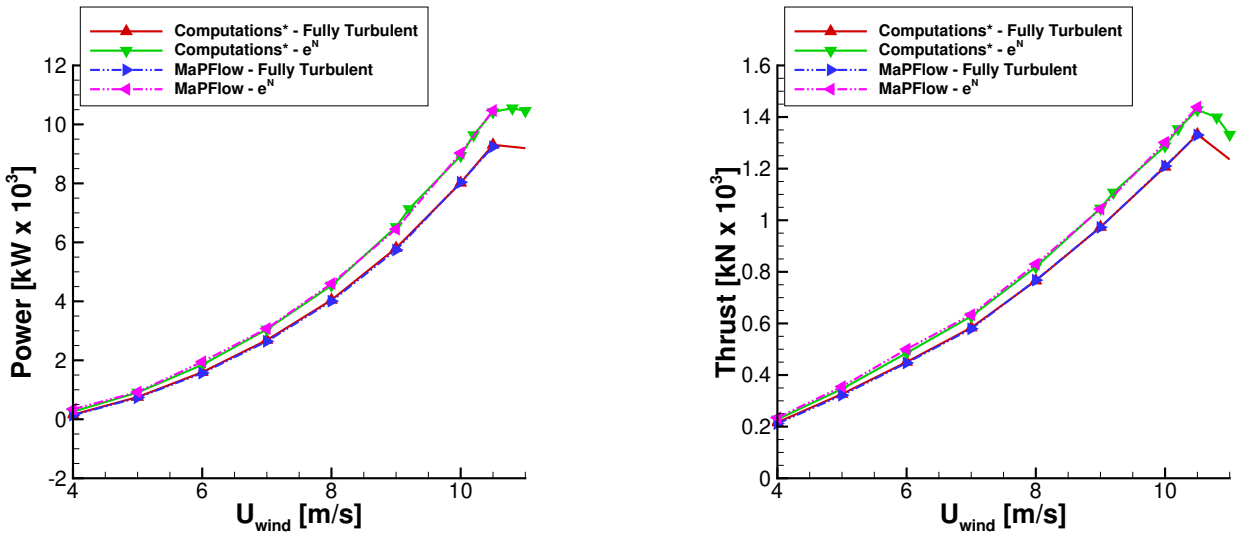

(a) *Mechanical Power vs Wind Speed*

(b) *Thrust vs Wind Speed*

Figure 5.49: *Simulations for the AVATAR W/T Rotor Blade. Flow conditions listed in Table 5.6. Comparison with computational data from [15].*

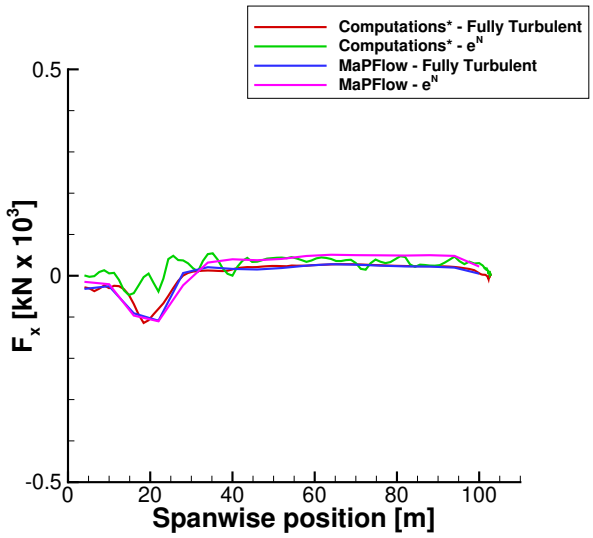

(a) *Wind speed 4 m/s, F_x*

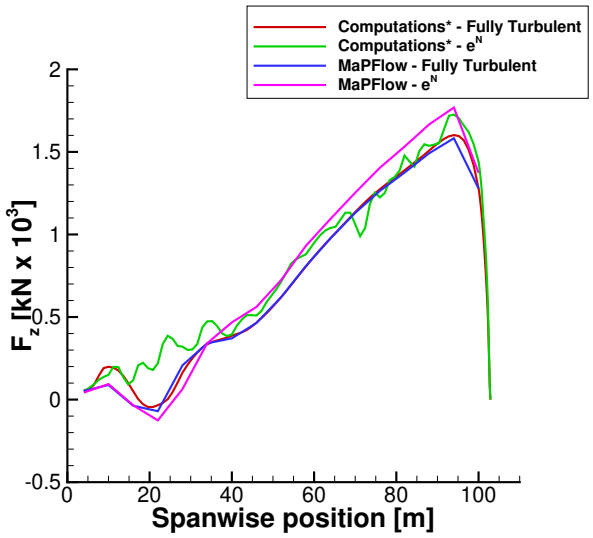

(b) *Wind speed 4 m/s, F_z*

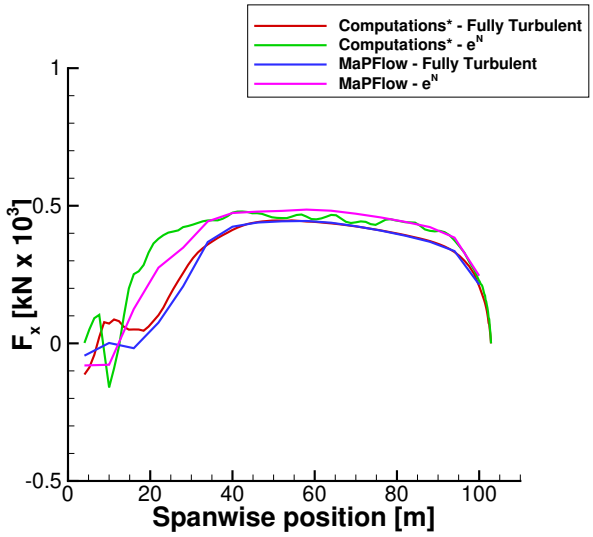

(c) *Wind speed 8 m/s, F_x*

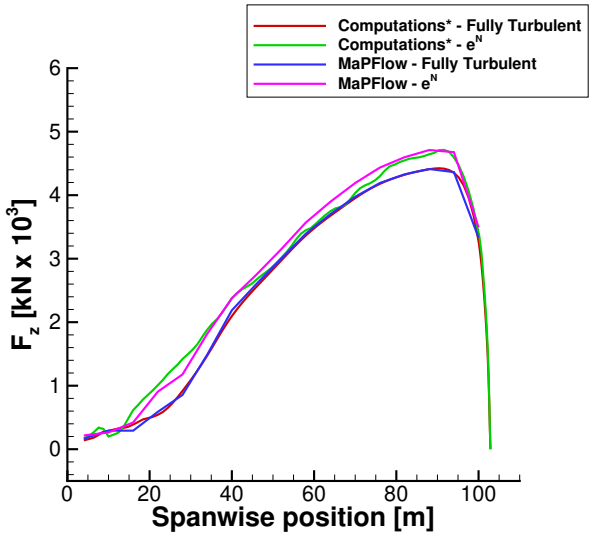

(d) *Wind speed 8 m/s, F_z*

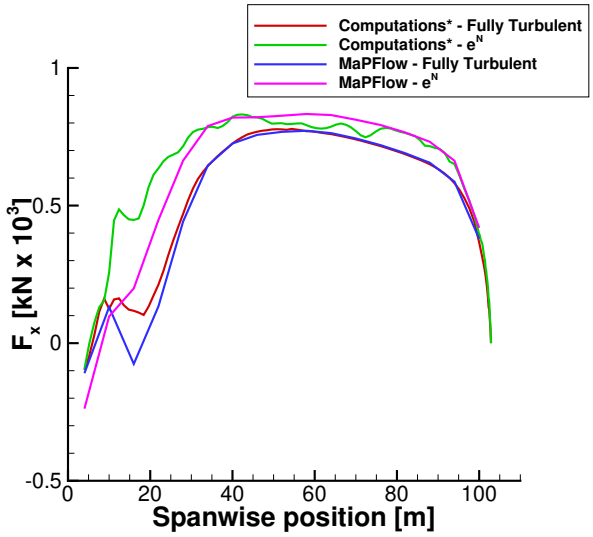

(e) *Wind speed 10.5 m/s, F_x*

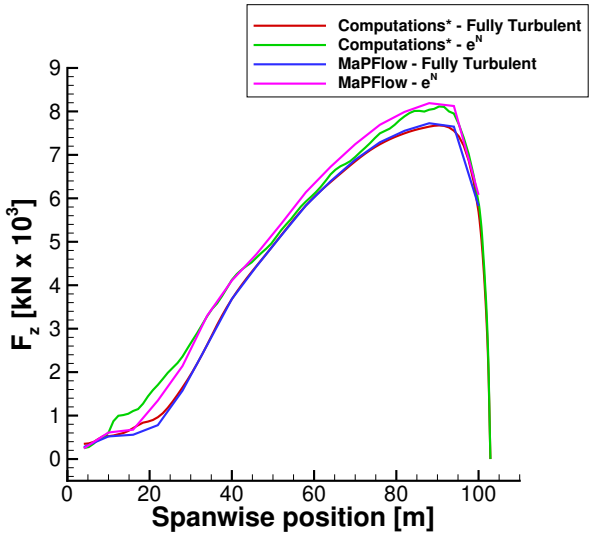

(f) *Wind speed 10.5 m/s, F_z*

Figure 5.50: *Simulations for the AVATAR W/T Rotor Blade. Flow conditions listed in Table 5.6. Comparison with computational data from [15].*

5.8 Discussion

In this Chapter, the results from transitional simulations have been presented. The focus was on external aerodynamic flows around airfoils, wings, and a generic fuselage configuration (spheroid). The initiative and background of the analysis was always in reference to aerodynamic loads and transition locations (where available), as well as to boundary layer velocity profiles for some cases.

In the two-dimensional test cases, different types of airfoils were tested in a wide range of Re numbers and freestream turbulence levels. The boundary layer transition approach paired with the e^N method provided accurate results for the aerodynamic loads and transition locations in the majority of cases, especially when Re numbers higher than 9 x 10^6 were considered. However, in cases with laminar separation (see Section 5.6.5, Section 5.6.7) the agreement with experiments in regards to bubble location and size was not always as good. On the other hand, the γ-Re_θ model rivaled the boundary layer e^N method for Re numbers up to 4 x 10^6, providing accurate results for both aerodynamic loads and transition locations. However, its accuracy deteriorated significantly for Re higher than 4 x 10^6 (Section 5.6.4, Section 5.6.8), as it always predicted early transition. This behavior had a significant effect on the produced aerodynamic loads. On the contrary, in cases with laminar separation (see Section 5.6.5, Section 5.6.7) the γ-Re_θ model provided more accurate results, predicting laminar separation locations and bubble sizes that closely resembled the measurements and reference computations. The γ model most often predicted transition upstream from other models and experimental data, resulting in higher C_d values. Large discrepancies were observed in cases with low freestream turbulence levels and $Re = 2 - 4$ x 10^6 (Section 5.6.1, Section 5.6.2, Section 5.6.3). For Re numbers higher than 4 x 10^6 (Section 5.6.4, Section 5.6.8), its accuracy also deteriorated in a similar fashion to the γ-Re_θ model. The AFT model was in good agreement with the experimental data for all examined cases and, unlike γ-Re_θ and γ models, its accuracy did not deteriorate drastically in the high Re cases (Section 5.6.4, Section 5.6.8). However, despite being based on the e^N method, for the majority of cases it yielded results that resembled those from the other transport equation transition models.

In the context of two-dimensional airfoil polars, which is what was examined in most cases considered in this thesis, the focal points are drag level inside the laminar bucket and location of laminar bucket corners. In most examined cases, the boundary layer e^N method predicted corners earlier than the γ-Re_θ and AFT models, which often coincided with the experiments. The γ-Re_θ and AFT models usually exhibited a delay of $1 - 2^\circ$ with respect to the e^N method in both positive and negative angles, which in some cases brought the results closer to the experimental data than the e^N method. The γ model usually predicted earlier laminar bucket corners caused by upstream transition predictions.

In the three-dimensional test cases, two configurations with strong crossflow transition effects were assessed (Section 5.7.1, Section 5.7.2). The γ-Re_θ model was used for transition prediction, with and without crossflow treatment. In the latter cases, two different crossflow models were considered. The transition locations from simulations that accounted for crossflow effects were significantly more accurate with respect to experimental data. Out of the two crossflow models, the CFHE model was able to give more accurate results than the Langtry model for both cases. Lastly, the boundary layer e^N method was used in a rotating wind turbine rotor blade simulation (Section 5.7.3), where the resulting integrated loads highlighted the importance of transition in aerodynamic simulations.

However, for transition predictions in three dimensions boundary layer definition and calculation can become quite complex. In such cases, the boundary layer e^N method is not always easy to implement, because it requires both a boundary layer and a streamline calculation interface. Nevertheless, the three-dimensional boundary layer can be approximated by two-dimensional sections, skipping the need for an explicit streamline interface. However, this assumption is case specific and is not always valid. Furthermore, the integral boundary layer equations are inherently two-dimensional and cannot solve three-dimensional boundary layers. This leaves Direct CFD integration as the only viable approach for crossflow transition prediction, as the latter requires boundary layer parameters in the crossflow direction. Due to all these reasons, transport equation transition models have a clear advantage in three dimensional simulations. as they do not require boundary layer and streamline calculation interfaces and, by including the corresponding modeling terms, can be used to predict crossflow transition without additional modifications.

Based on the results and the discussion in this Chapter, the following are derived:

- If two-dimensional simulations are considered, the boundary layer e^N method and the AFT transport equation model are recommended. These two approaches were able to provide accurate results for all examined cases.
- For two-dimensional simulations at Re numbers not higher than $\approx$ 6 x 10^6, the γ-Re_θ model is also a viable option. However, for Re number beyond this limit the prediction accuracy of the model deteriorates.
- The γ model behaves similarly to the γ-Re_θ model, however it predicts upstream transition in most cases. For Re numbers beyond 4 x 10^6, the prediction accuracy of the model also deteriorates.

- If the γ-Re_θ and γ models are considered, inflow turbulence should be defined appropriately (as discussed in Section 5.5.1).
- In three-dimensional simulations, the implementation of boundary layer methods is complicated, therefore transport equation models have a clear advantage because they are significantly easier to implement.
- If crossflow transition prediction is important, then the γ-Re_θ model with crossflow terms is the only viable option.

This page intentionally left blank

Chapter 6

LES-DES verification and validation

6.1 Introduction

In this chapter the results from simulations using LES and DES are presented. The focus is cases that exhibit massive separation, in which URANS predictions are expected to deviate from experimental data. The aim is to compare different approaches on the same mesh and using same arithmetic parameters, in order to focus on the effect of turbulence modeling on the produced results. The classic case of a circular cylinder at critical Reynolds number is discussed in Section 6.2.1 using Spalart-Allmaras (S-A) URANS, S-A DDES and LES equipped with the Smagorinsky subgrid model. In Section 6.2.2 the flow around the S809 airfoil at angles up to $\alpha = 90°$ is considered using S-A URANS and S-A IDDES. The classic validation case of the periodic hills is discussed in Section 6.2.3 using Smagorinsky LES whereas in Section 6.2.4 the flow through the Sexbierum rotor with Smagorinsky LES, using turbulent inflow and actuator methods, is considered.

6.2 Test cases

6.2.1 Circular cylinder at $Re = 3900$ using 3D URANS, DDES and LES

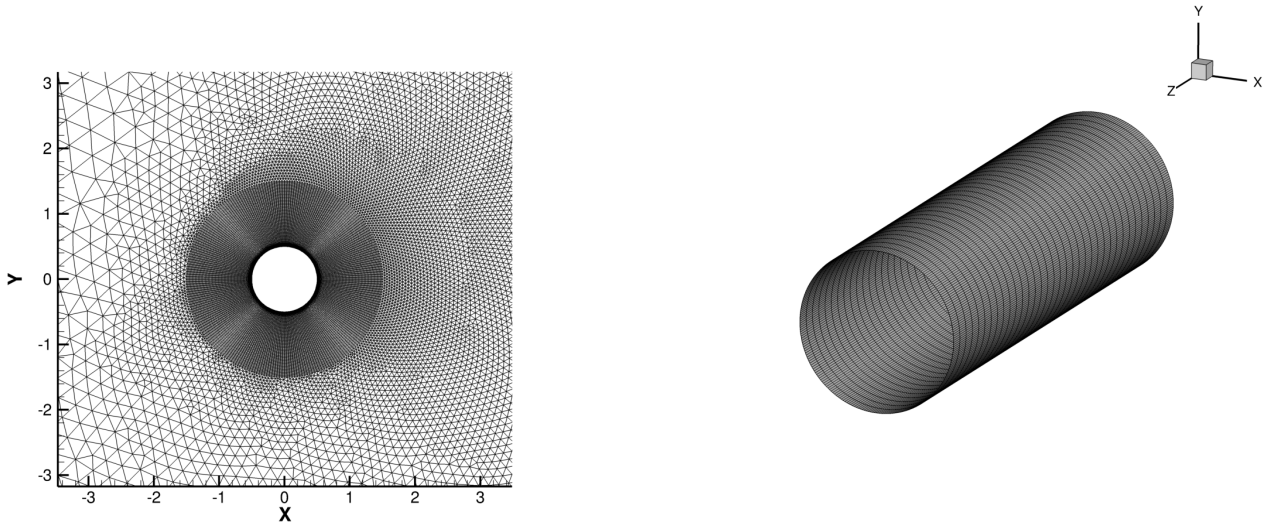

(a) *2D hybrid mesh*

(b) *3D surface mesh with AR=3.2 and 32 layers on the spanwise direction*

Figure 6.1: *Computational mesh for the circular cylinder*

The flow around circular cylinders is a classic test for turbulence modeling validation and assessment. Due to the separated nature of the flow, conventional RANS turbulence models are not able to produce accurate results when compared to experimental data. This occurs because the separated flow exhibits strong vortex shedding, which RANS models fail to capture adequately. The use of LES or DES is expected to give a better representation of the turbulent characteristics in the near wake region, which is the most active region in regards to the presence of turbulence structures.

A critical Reynolds number of 3900 is considered. At this Reynolds number, the wake is fully turbulent but the boundary layer remains laminar. Experimental results are taken from Nordberg [16], Lourenco et al [17] (data taken from [34]) and Ong et al [19]. This specific case has also been numerically studied by Blackburn et al [18], Breuer [35] and Beaudan et al [34].

3D Unsteady RANS using the S-A model, S-A DDES and LES with the Smagorinskgy subgrid model are considered. Laminar to turbulent transition is not considered in this case. The simulations are carried out on the same hybrid mesh, consisting of 280 wrap-around elements, 60 elements in the region up to 0.1 cylinder diameters and 60 elements in the region from 0.1 to 1 diameter. The rest of the mesh was unstructured using triangles. The aspect ratio is 3.2 based on what was discussed in [18], where an aspect ratio of at least π is suggested. The spanwise direction had 32 layers, resulting in a total of approximately 2 x 10^6 elements for the 3D mesh. A timestep of 0.001 nondimensional time units was used.

For the comparisons, the computational results have been averaged over more than 30 shedding cycles. C_p and C_f distributions are compared to experiments in fig. 6.2a-6.2b. Both LES and DDES are able to capture the experimental pressure coefficient, in contrast to URANS which predicts a lower suction level after the 50° position. The C_f distribution is not available from the experiments. However, the experimental separation point is located at approximately 88° [18]. Both LES and DES capture the separation location with good accuracy, whereas the URANS solution predicts separation slightly downstream at 95°.

Results on the wake centerline are compared to experimental data and to LES results from [18] in fig. 6.3. Both LES and DES are closer to measurements (fig. 6.3a) than URANS. Mean stresses are compared to results from [18] in fig. 6.3b-6.3d. LES and DDES give similar results which are close to the results from [18]. Regarding $u'u'$ and $v'v'$, URANS predicts slightly higher values and a smoother distribution overall. However, URANS predicts very small $w'w'$ values when compared to all other methods, suggesting that the 3d character of the separated flow is significantly suppressed.

In fig. 6.4-6.7 computational results are compared to experimental data at various x/D wake positions. At $x/D = 1.06$ (fig. 6.4a), URANS captures the mean U distribution well, but both DDES and LES are closer to the experiments. For the mean V distribution, URANS fails to capture the variations that are present in the experiments. It is noted that the experimental values for V on the edge of both distributions do not approach 0, contrary to what is expected. Therefore, a straight comparison for the mean V distribution cannot be made. However, a qualitative comparison shows that both DDES and LES resemble the experimental variation pattern, in contrast to URANS.

At the $x/D = 1.54$ position (fig. 6.5), URANS overpredicts the mean U value and LES slightly underpredicts it, whereas the results from DDES are very accurate (fig. 6.5a). In regards to the mean V distribution (fig. 6.5b), the experimental data again do not approach 0 over the edges. However, all three simulations predict similar variation patterns. No variations of mean V are present on the experimental data at this position. However, URANS slightly underpredicts mean V when compared to DDES and LES. Normal stresses $u'u'$, $v'v'$ and shear stress $u'v'$ are compared in fig. 6.5c-6.5e. DDES results are very close to the experiment. URANS underpredicts the normal $u'u'$ stress and the shear $u'v'$ stress, whereas it overpredicts the normal $v'v'$ stress. LES underpredicts all three stresses, with the most notable deviation being noted for the $v'v'$ stress. It is possible that this was caused by insufficient mesh resolution in the near wall region, which led to higher diffusion. Since the RANS mode of DDES is active within the boundary layers, DDES is able to perform well even with coarser meshes in the wall region. However, for a wall resolved LES (as is the one considered here) a higher resolution for the boundary layer is probably needed.

At the $x/D = 3$ position (fig. 6.6), the comparison of the results from DDES, LES and URANS have similar trends to those at the $x/D = 1.54$ position. Two different sets of experimental results are available [17][19], which deviate from each other significantly. For the mean U distribution (fig. 6.6a), LES and DDES agree with the experimental results from [17], whereas the results using URANS seem to agree with the experimental results from [19]. However, the latter agreement is probably coincidental. For the mean V distribution (fig. 6.6b), no fluctuations are present in the experimental data. All three simulation predict similar trends, albeit with different values than the experiments. For the normal and shear stresses (fig. 6.6c-6.6e), comparisons of computational results to experimental data vary in trend. DDES results for the normal $u'u'$ stress are closer to the experimental data from [17] whereas LES results are closer to the data from [19]. For the normal $v'v'$ stress, the experimental data from the two sources are similar and LES is able to give better results. On the contrary, for the $u'v'$ shear stress the experimental results again deviate from each other; LES and DES are close to the data from [17] whereas URANS is close to the data from [19].

Moving on, comparison of the $u'u'$ stress with experimental data at $x/D = 6$, 7, and 10 (fig. 6.7) shows that URANS always predicts a symmetrical distribution around the $y/D = 0$ axis. On the contrary, both DDES and LES predict variations and exhibit non-symmetric distributions. The comparison of DDES and LES results to the experiments is favorable. However, LES always gives lower levels of the normal stress.

Overall, the comparisons show that simulations using URANS cannot provide accurate results for this flow case. The averaged nature of the URANS approach produces almost symmetrical distributions, which do

not agree with the experimental findings. On the other hand, DDES and LES seem to agree more with the experiments. However, the comparisons presented here are not conclusive as to which of the two methods is better. The LES simulation may not have sufficient resolution inside the boundary layer region. This could explain some of the deviation between LES and DDES in the near wake region, although at some positions the results using LES were closer to the experimental findings. In addition, the Smagorinsky subgrid model may be too dissipative for this particular flow case. Perhaps a different subgrid model could provide more accurate results.

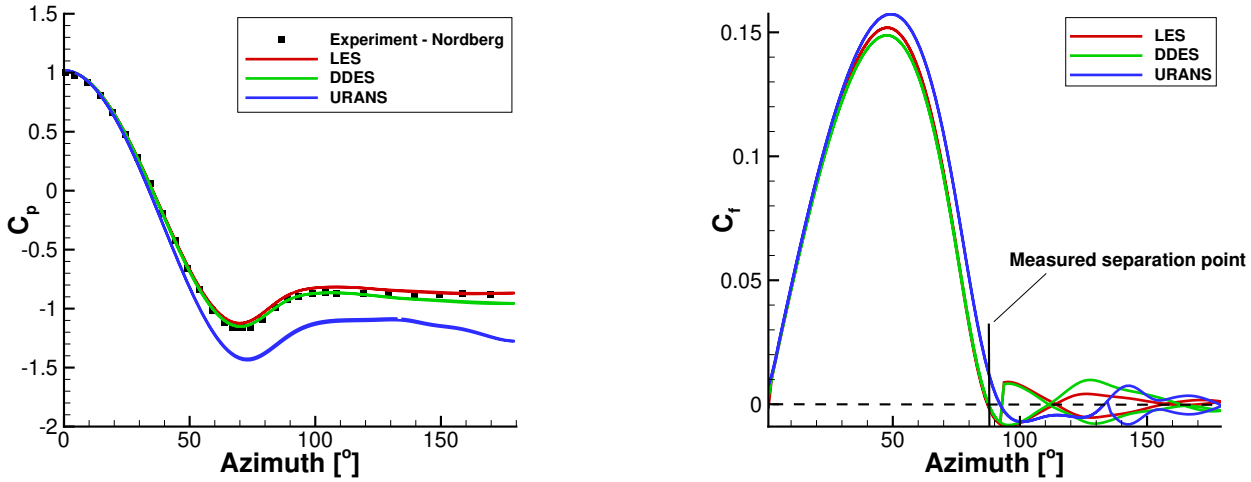

(a) C_p *distribution*

(b) C_f *distribution*

Figure 6.2: *Flow past a circular cylinder at* $Re = 3900$, $Ma_\infty = 0.08$. *Comparison with experiments [16].*

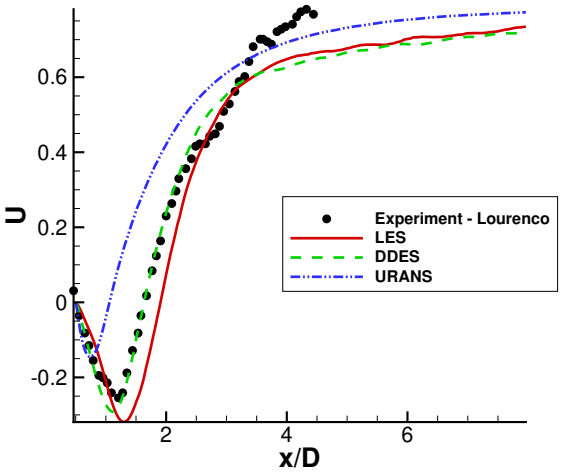

(a) *Mean U*

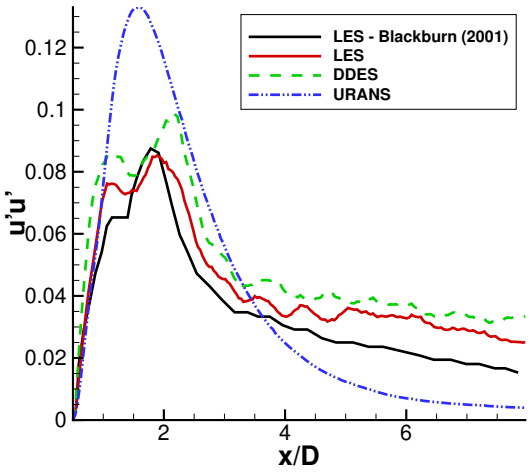

(b) *Mean $u'u'$*

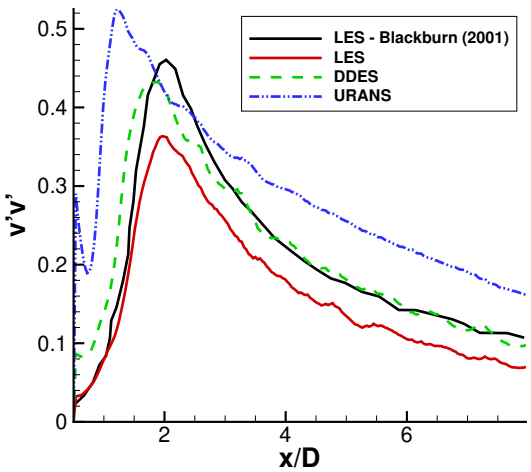

(c) *Mean $v'v'$*

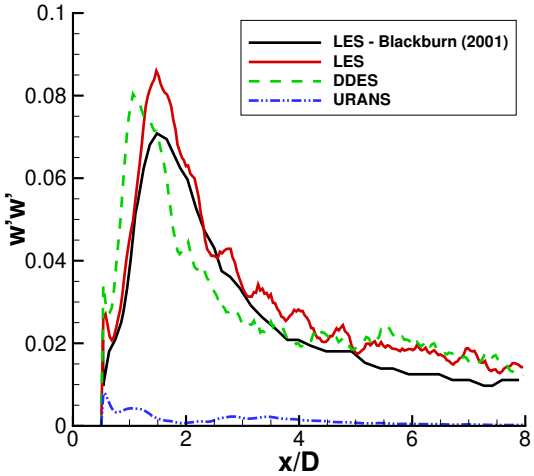

(d) *Mean $w'w'$*

Figure 6.3: *Flow past a circular cylinder at $Re = 3900$, $Ma_\infty = 0.08$. Values on the near wake centerline ($y/D = 0$). Comparison with experiments [17] and computational results [18].*

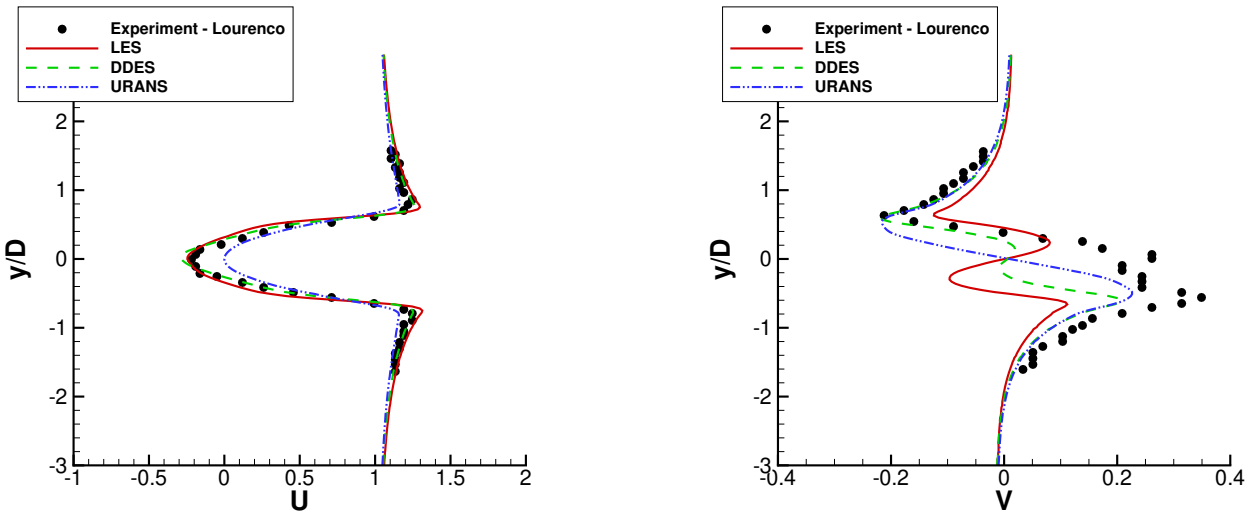

(a) *Mean U* **(b)** *Mean V*

Figure 6.4: *Flow past a circular cylinder at* $Re = 3900$, $Ma_\infty = 0.08$. *Values on the* $x/D = 1.06$ *plane. Comparison with experiments [17].*

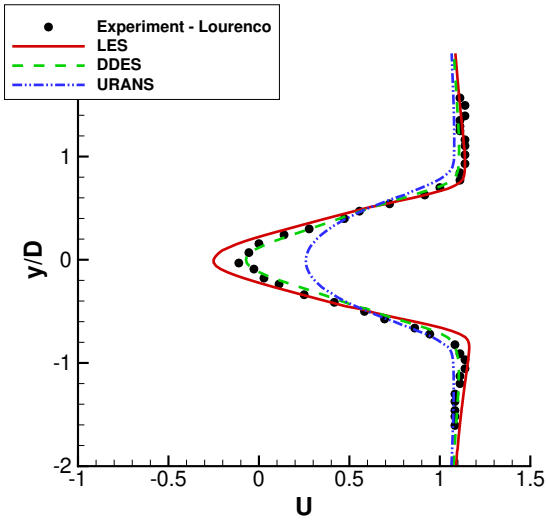

(a) *Mean U*

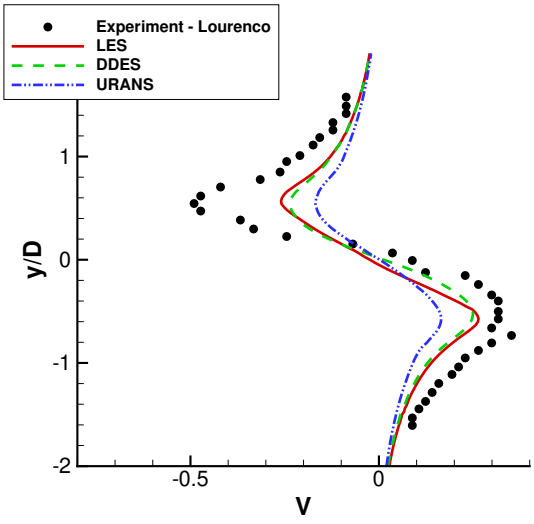

(b) *Mean V*

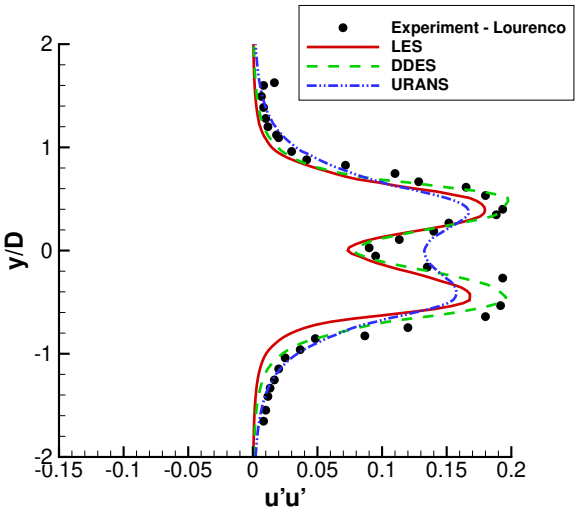

(c) *Mean $u'u'$*

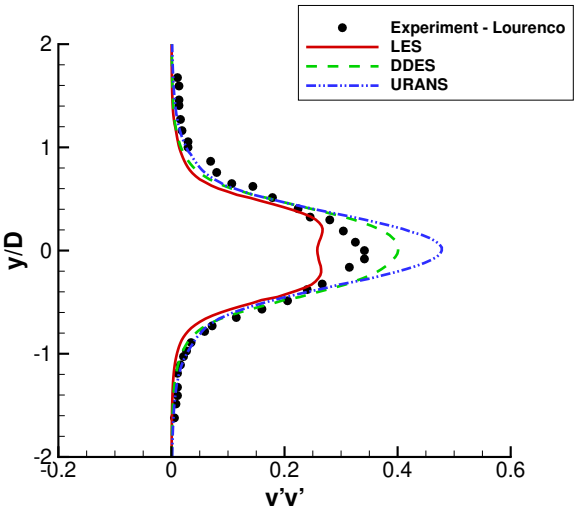

(d) *Mean $v'v'$*

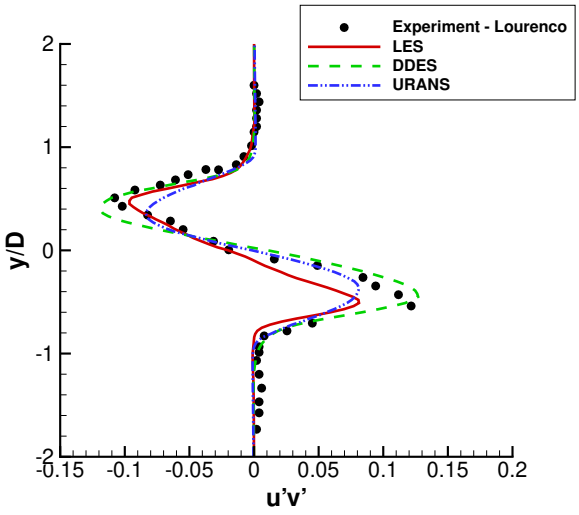

(e) *Mean $u'v'$*

Figure 6.5: *Flow past a circular cylinder at $Re = 3900$, $Ma_\infty = 0.08$. Values on the $x/D = 1.54$ plane. Comparison with experiments [17].*

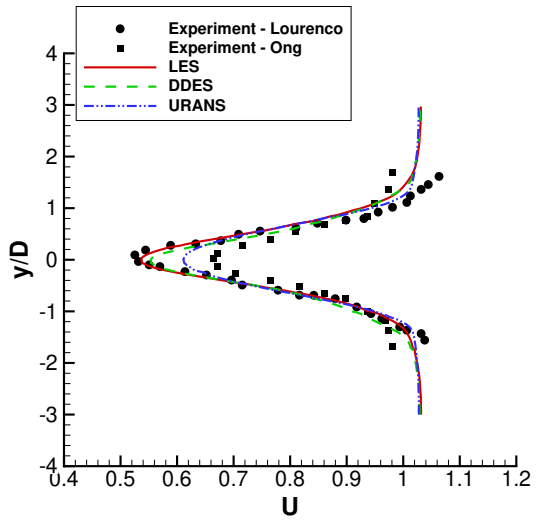

(a) *Mean U*

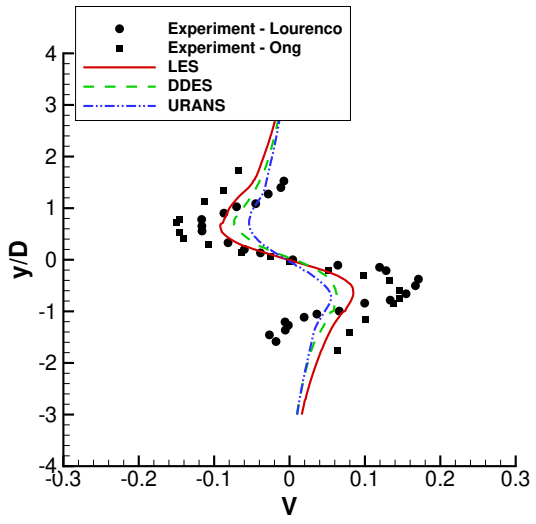

(b) *Mean V*

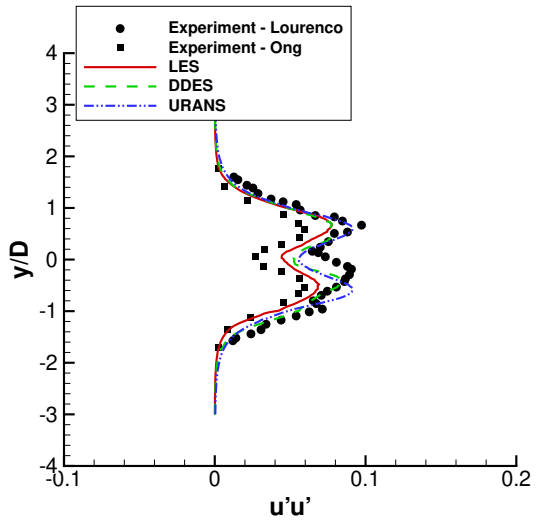

(c) *Mean $u'u'$*

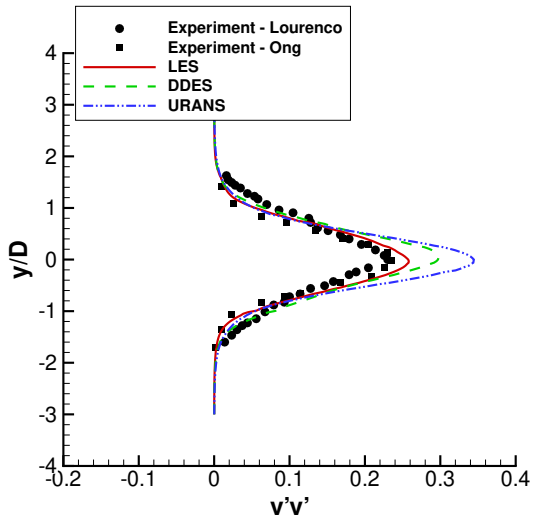

(d) *Mean $v'v'$*

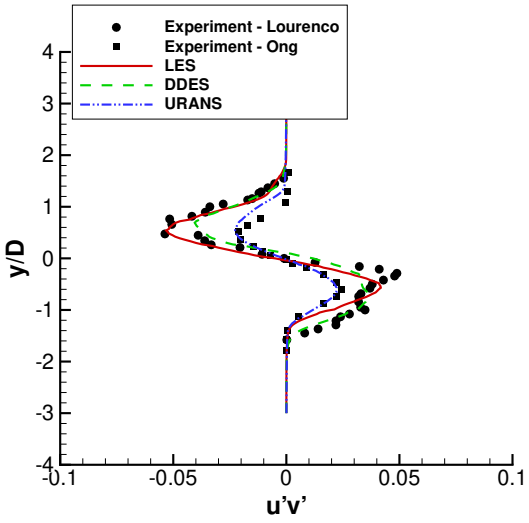

(e) *Mean $u'v'$*

Figure 6.6: *Flow past a circular cylinder at $Re = 3900$, $Ma_\infty = 0.08$. Values on the $x/D = 3.00$ plane. Comparison with experiments [17][19].*

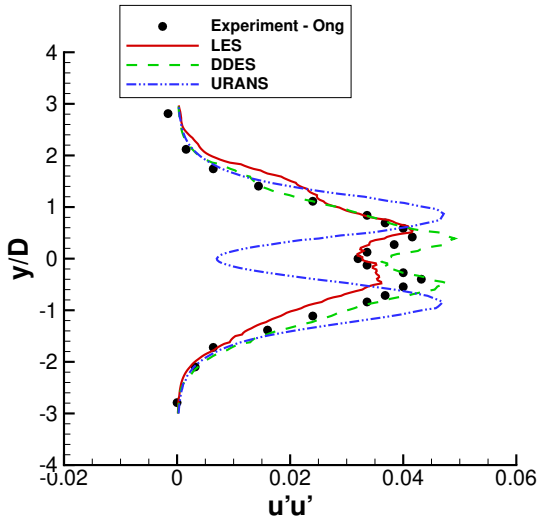

(a) *Mean* $u'u'$, $x/D = 6.00$

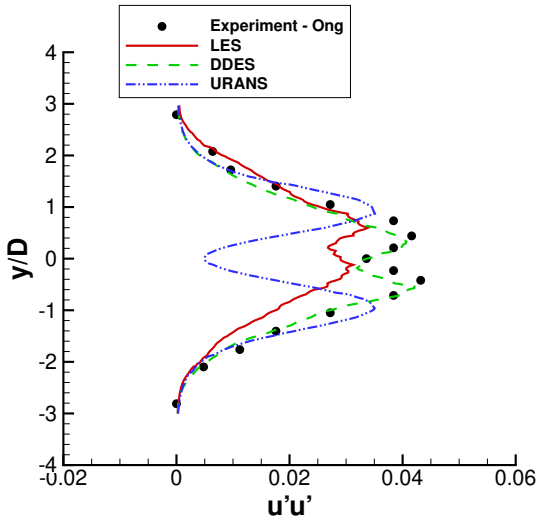

(b) *Mean* $u'u'$, $x/D = 7.00$

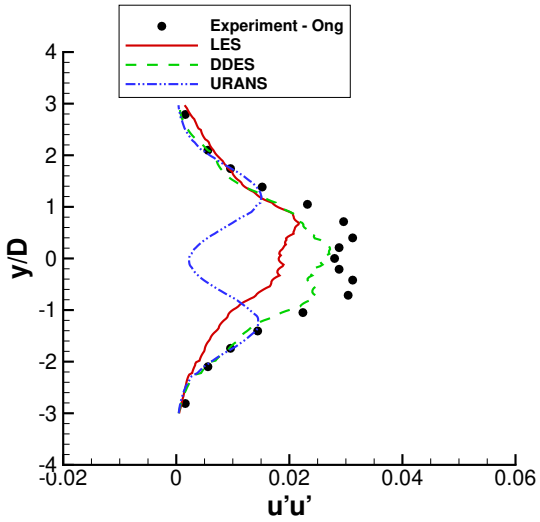

(c) *Mean* $u'u'$, $x/D = 10.00$

Figure 6.7: *Flow past a circular cylinder at* $Re = 3900$, $Ma_\infty = 0.08$. *Values on the* $x/D = 6.00, 7.00, 10.00$ *planes. Comparison with experiments [19].*

6.2.2 S809 airfoil at $Re = 0.6$ x 10^6 using 3D URANS and DDES

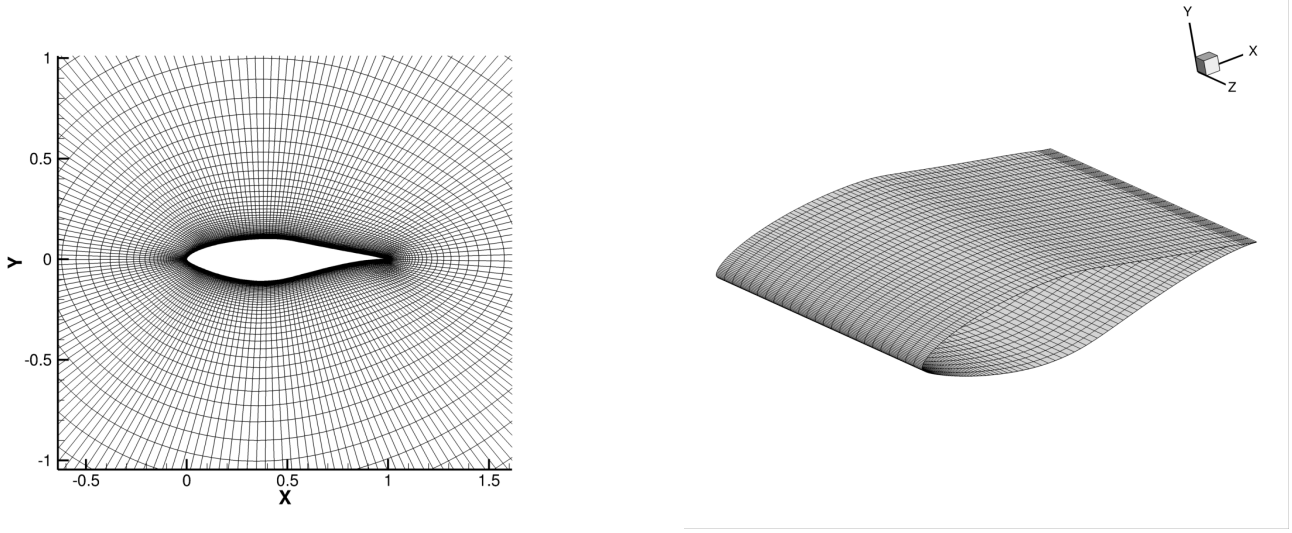

(a) *200 wrap-around x 100 normal element 2D mesh*

(b) *3D surface mesh, AR=1c, 25 spanwise layers*

Figure 6.8: *S809 airfoil mesh for the high angle study*

The S809 airfoil was measured by Butterfield et al [20] in the Colorado State University (CSU). The experiment covers a wide range of angles of attack up to 90°, at freestream Re 0.65 x 10^6 and freestream Ma 0.076. The wide range of angles covers all flow regimes; attached flow, mildly separated flow and massively separated flow. This case has also been numerically studied by Xu et al in [32].

The employed mesh is shown in fig. 6.8. The 2D mesh consisted of 200 wrap-around and 100 normal elements (fig. 6.8a). For the 3D simulations, the 2d mesh was extruded in the lateral direction. The aspect ratio of the 3d configuration was equal to 1 chord and had 25 layers (fig. 6.8b), which brought the 3d mesh to a total of 500 thousand elements. Symmetry conditions were used on the lateral boundaries. For the employed timestep, according to what was suggested in [32], a value of 0.01 nondimensional time units was used. The simulations utilized the Spalart-Allmaras (S-A) turbulence model.

The simulations presented here aim at capturing the effect of large turbulence structures. Therefore, angles located in the mild separation regime (below 20°) are omitted. Below 20°, trailing edge separation is caused by the development of small turbulent scales inside the boundary layer, where DDES will be on the RANS mode (Section 4.3). Therefore, separation prediction is greatly dependent on the underlying turbulence model capabilities. In order to capture the effect of these small scales, a finer mesh than the one utilized here is required, which will enable DDES to switch on the LES mode inside the boundary layer and resolve the LES flow content. On the contrary, at higher angles of attack separation on the upper side occurs near the leading edge of the airfoil and is not dependent on the turbulence model. Due to the development of large turbulent structures on the separated region, DDES will utilize the LES mode and is expected to yield different results than the baseline URANS.

Computational results are compared to experimental data in fig. 6.9. For the 3D URANS and 3D DDES simulations, both PLR and MUSCL schemes are used (Section 2.3). For the cases of 20° and 30°, the DDES results are similar to those using 3D URANS, with the MUSCL scheme being overall closer to the experiment. For angles greater than 45°, where the flow is massively separated, 3D URANS and DDES results differ, especially with respect to the predicted C_d. The presence of large turbulent structures in the flow gives way to the LES mode of the DDES model. The DDES results are very close to the experimental data, in contrast to the 2D and 3D URANS results which overpredict both lift and drag coefficients in all cases. Especially at 90°, 3D URANS overpredicts the drag coefficient significantly, as expected. At 90° the airfoil behaves like a bluff body and the measured drag coefficient is close to the value of 0.2 which is also the value for a flat plate at 90°.

Instantaneous spanwise-axis vorticity contours are shown in fig. 6.10 and 6.11 for the 2D and 3D simulations, respectively. Contours are plotted at three different spanwise locations, namely $z/c = 0.25$, 0.50 and 0.75. It is evident that the vorticity structures in 3D URANS are similar to the 2D results and they do not exhibit significant variations in the spanwise direction. The structures in DDES results on the other hand are more chaotic and exhibit significantly different structures at the three spanwise planes. Suppression of the 3D character of the flow is typical in 3D URANS, as also discussed in Section 6.2.1.

In fig. 6.12 averaged pressure coefficient contours using 3D URANS are compared to those using DDES at $\alpha = 45°$ and 90°. Three different spanwise positions are presented. 3D URANS underpredicts C_p on the suction

side, especially at 90°. This explains the differences in fig. 6.9a-6.9d.

Mean normal and shear stresses using URANS and DDES are compared in fig. 6.13 and 6.14. 3D URANS is able to give results that resemble those from DDES only for the normal $u'u'$ and $v'v'$ stresses (fig. 6.13a and 6.13c) and the $u'v'$ shear stress (6.14a). For all other stresses, results from URANS deviate from DDES significantly. Due to the suppressed 3D character in 3D URANS, the predicted levels of the spanwise velocity w are relatively low. Therefore, normal and shear stresses involving the spanwise velocity are equally low when compared to those using DDES.

This flow case shows that when massively separated flows are considered, the accuracy of the URANS predictions is compromised. Especially at angles higher than $\alpha = 45°$, DDES is able to give significantly more accurate results than URANS even when the same mesh is used.

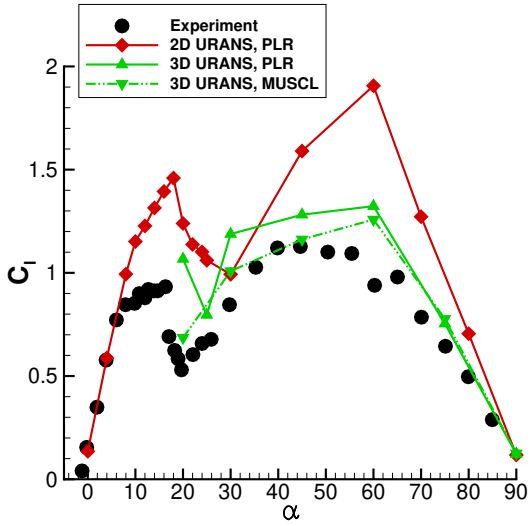

(a) *URANS, C_l vs α*

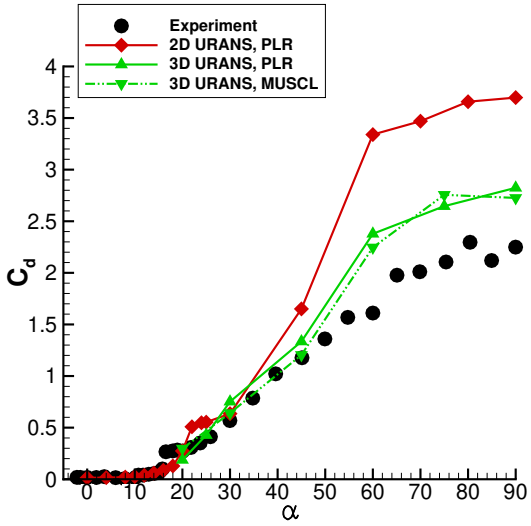

(b) *URANS, C_d vs α*

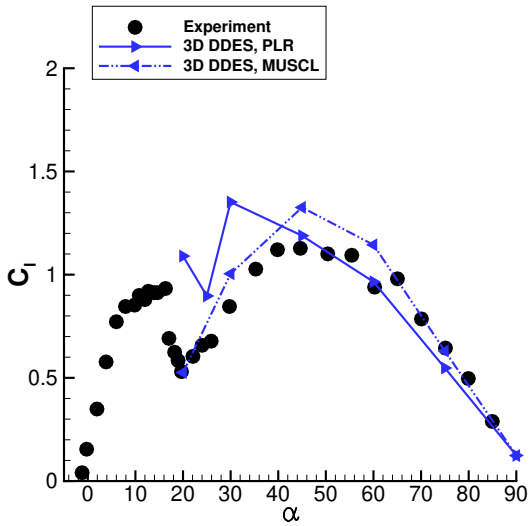

(c) *DDES, C_l vs α*

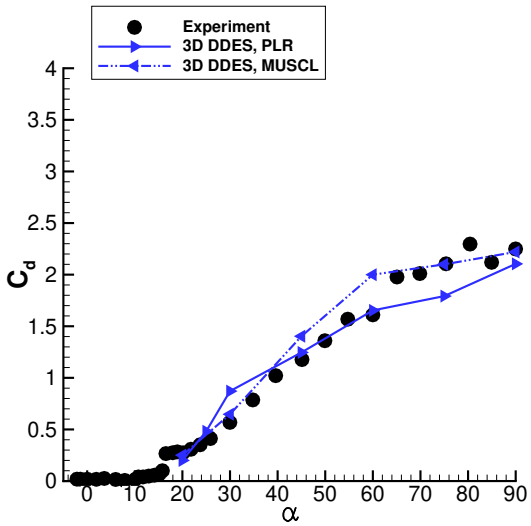

(d) *DDES, C_d vs α*

Figure 6.9: *Simulations on the S809 airfoil using 2D URANS, 3D URANS and 3D DDES at $Re = 0.65\ x\ 10^6$, $Ma_\infty = 0.075$. Comparison with experimental data [20].*

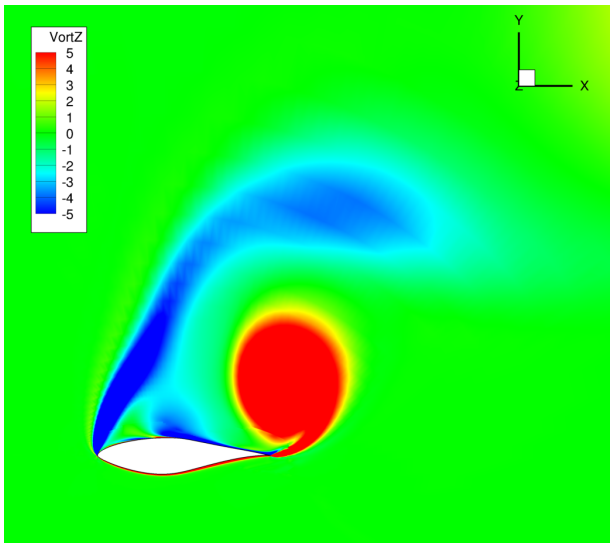

Figure 6.10: *Simulations on the S809 airfoil using 2D URANS (2^{nd} order PLR scheme) at* $Re = 0.65\ x\ 10^6$, $Ma_\infty = 0.075$, $\alpha = 45°$. *Instantaneous z-axis vorticity.*

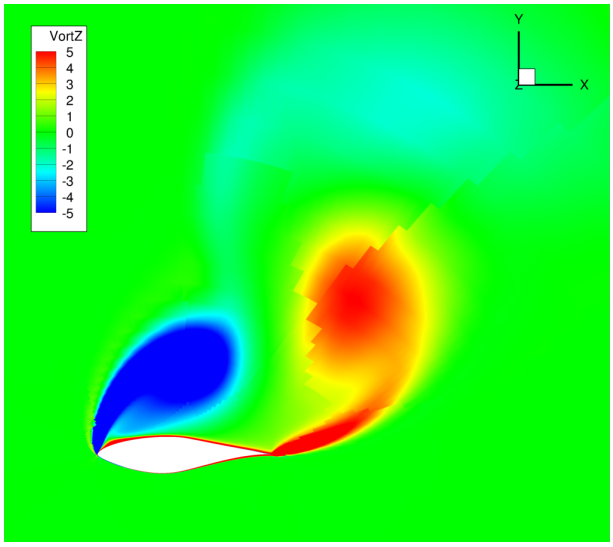

(a) *3D URANS,* $z/c = 0.25$

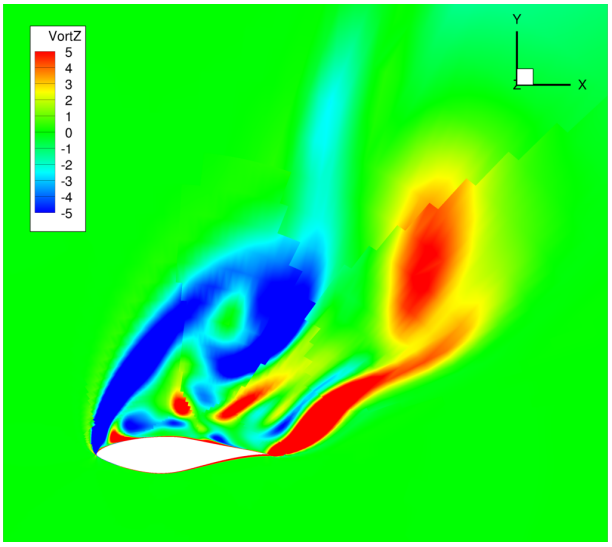

(b) *DDES,* $z/c = 0.25$

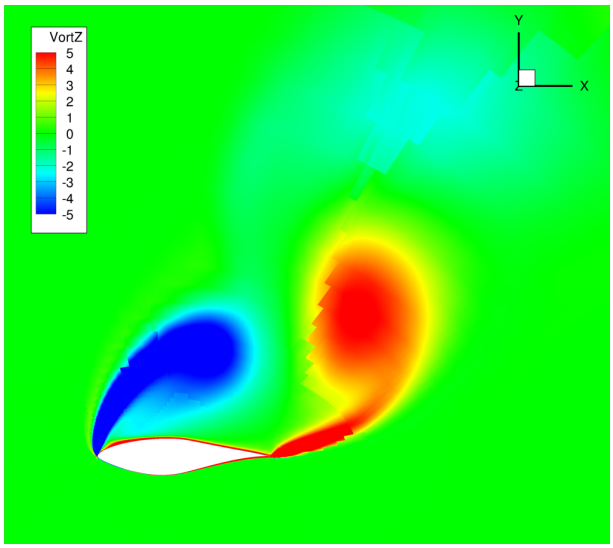

(c) *3D URANS,* $z/c = 0.50$

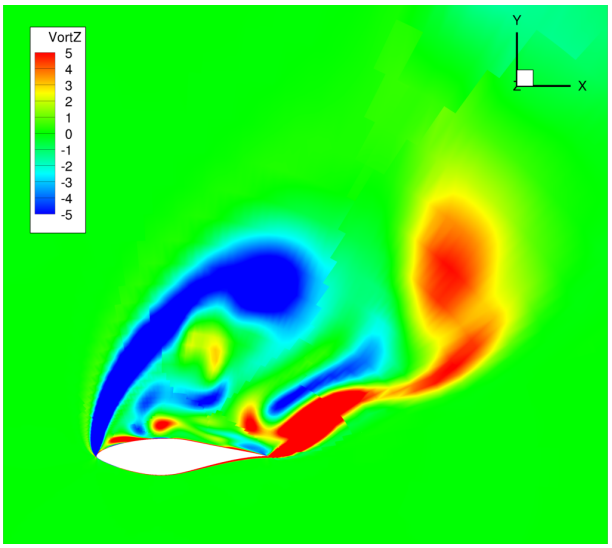

(d) *DDES,* $z/c = 0.50$

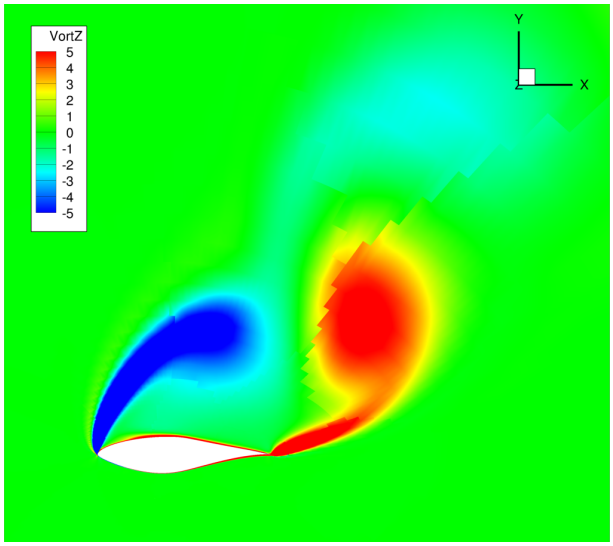

(e) *3D URANS,* $z/c = 0.75$

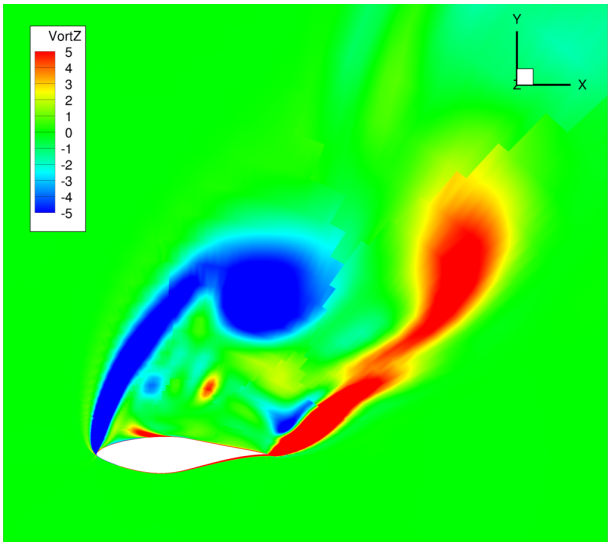

(f) *DDES,* $z/c = 0.75$

Figure 6.11: *Simulations on the S809 airfoil using 3D URANS and DDES (2^{nd} order PLR scheme) at* $Re = 0.65\ x\ 10^6$, $Ma_\infty = 0.075$, $\alpha = 45°$. *Instantaneous z-axis vorticity at three spanwise locations.*

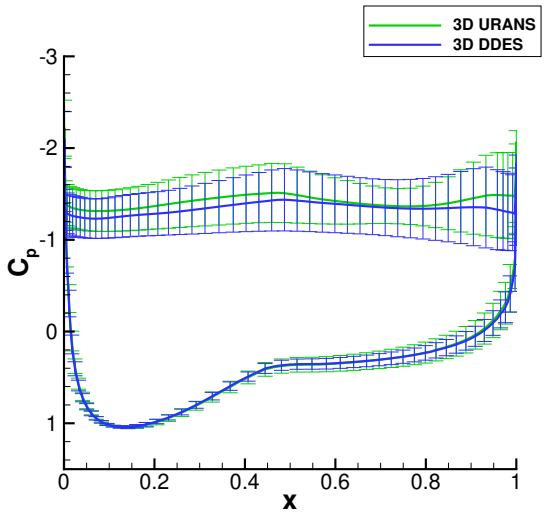

(a) $\alpha = 45°$, $z/c = 0.25$

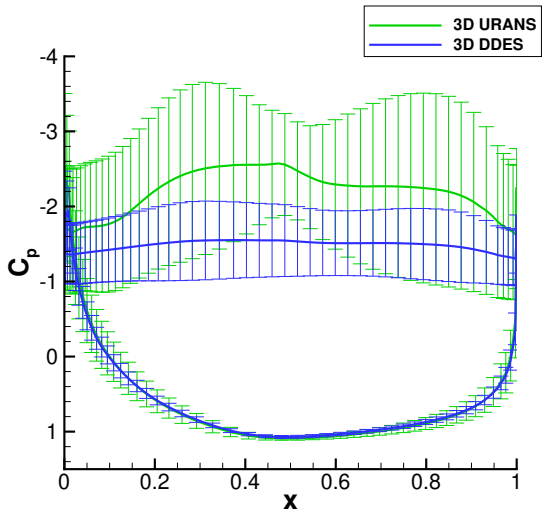

(b) $\alpha = 90°$, $z/c = 0.25$

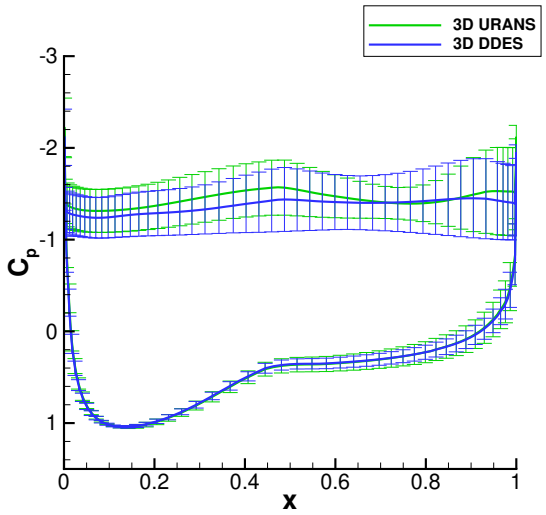

(c) $\alpha = 45°$, $z/c = 0.50$

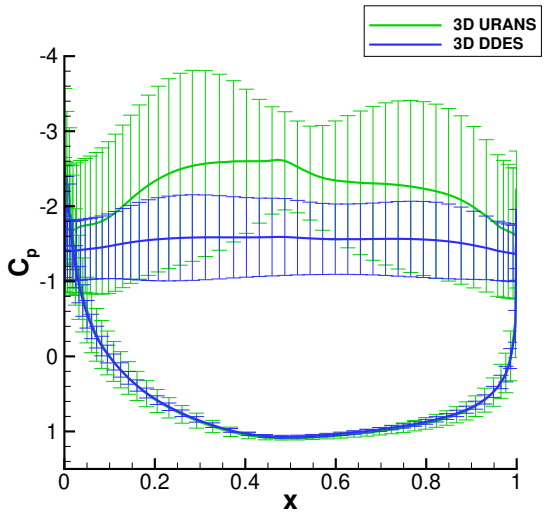

(d) $\alpha = 90°$, $z/c = 0.50$

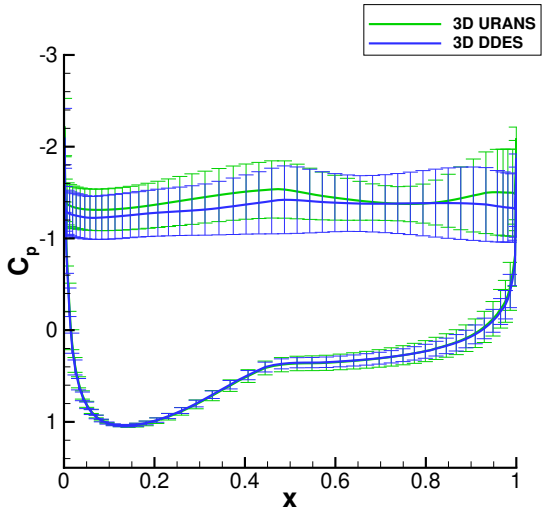

(e) $\alpha = 45°$, $z/c = 0.75$

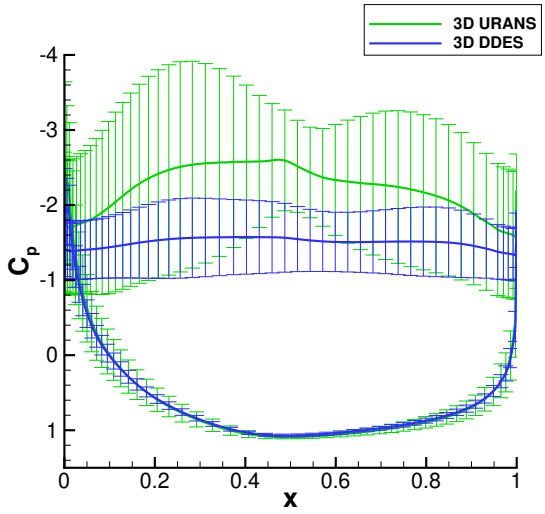

(f) $\alpha = 90°$, $z/c = 0.75$

Figure 6.12: *Simulations on the S809 airfoil using 3D URANS and DDES (2^{nd} order PLR scheme) at $Re = 0.65\ x\ 10^6$, $Ma_\infty = 0.075$. Mean C_p contours and standard deviations at three spanwise locations for $\alpha = 45°$ and* $90°$.

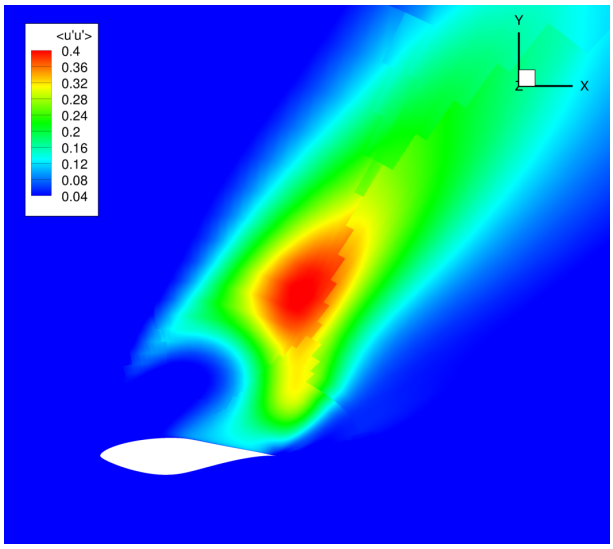

(a) *3D URANS, mean $u'u'$*

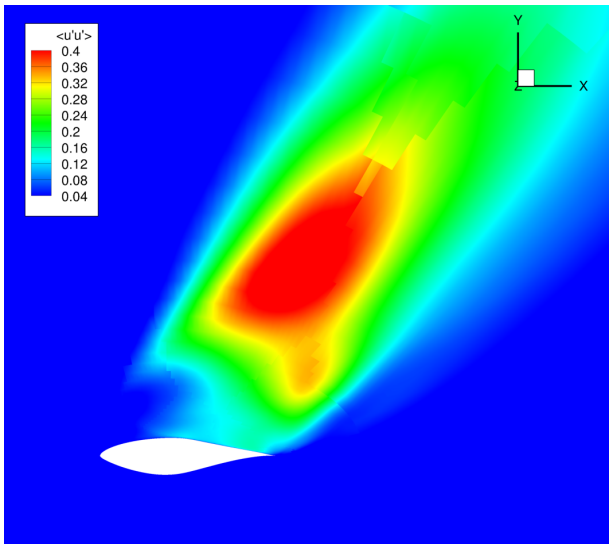

(b) *DDES, mean $u'u'$*

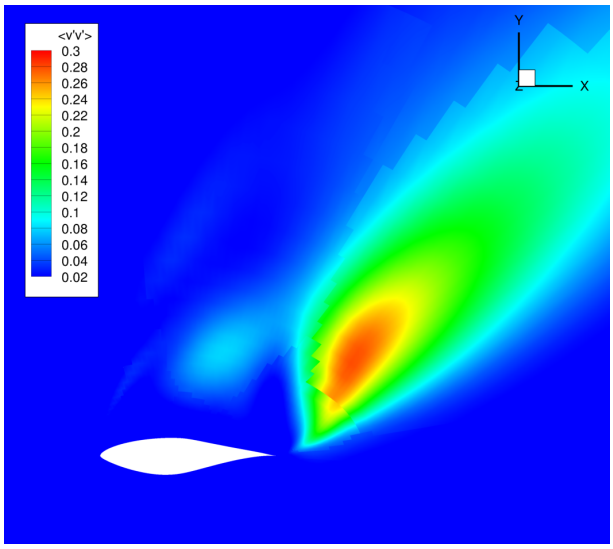

(c) *3D URANS, mean $v'v'$*

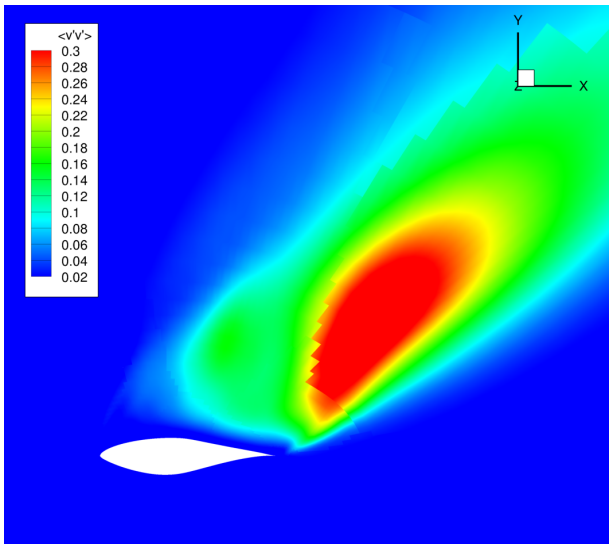

(d) *DDES, mean $v'v'$*

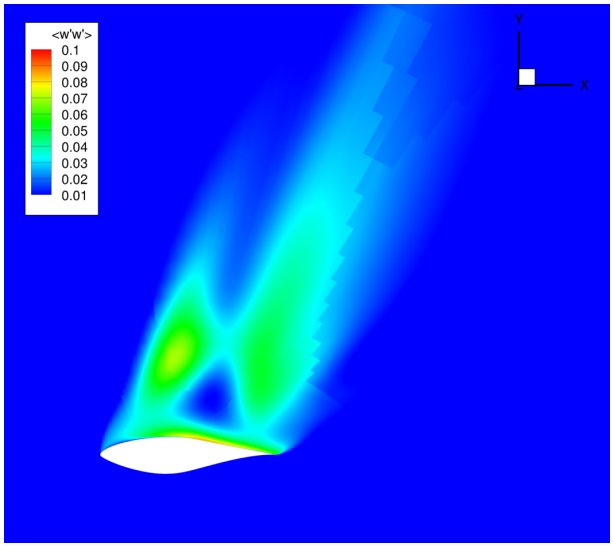

(e) *3D URANS, mean $w'w'$*

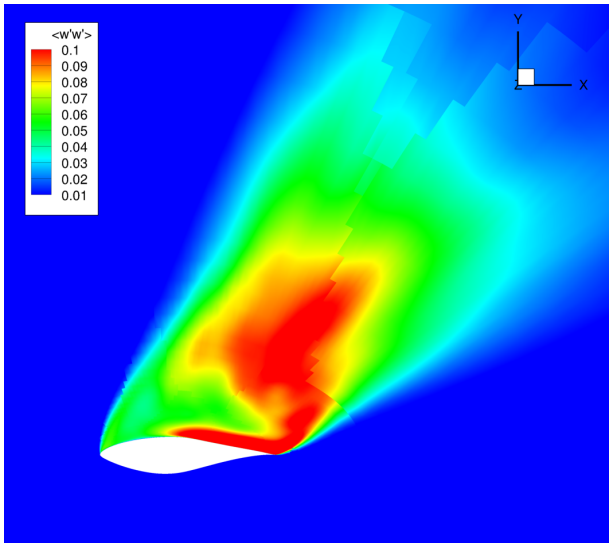

(f) *DDES, mean $w'w'$*

Figure 6.13: *Simulations on the S809 airfoil using 3D URANS and DDES (2^{nd} order PLR scheme) at $Re = 0.65\ x\ 10^6$, $Ma_\infty = 0.075$, $\alpha = 45°$. Mean normal stress contours at the $z/c = 0.5$ position.*

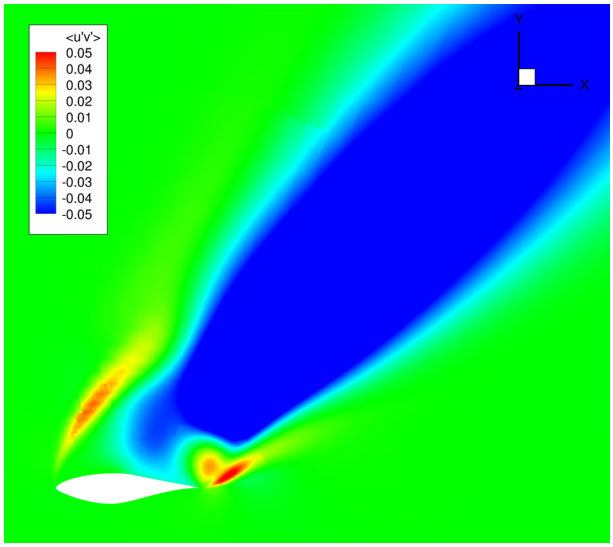

(a) *3D URANS, mean $u'v'$*

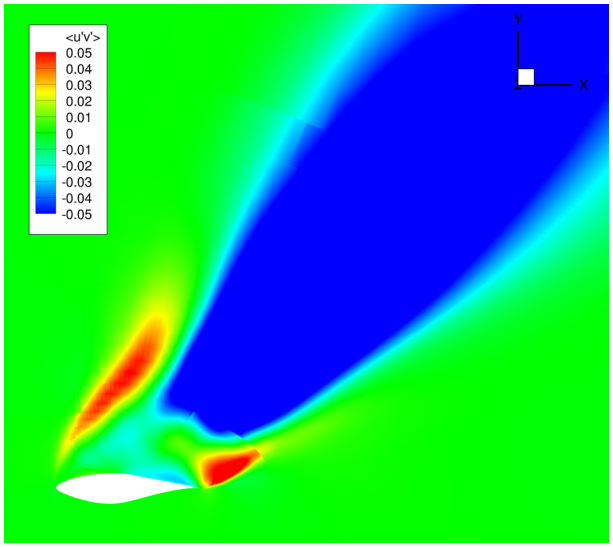

(b) *DDES, mean $u'v'$*

Figure 6.14: *Simulations on the S809 airfoil using 3D URANS and DDES (2^{nd} order PLR scheme) at $Re = 0.65\ x\ 10^6$, $Ma_\infty = 0.075$, $\alpha = 45°$. Mean $u'v'$ shear stress contours at the $z/c = 0.5$ position.*

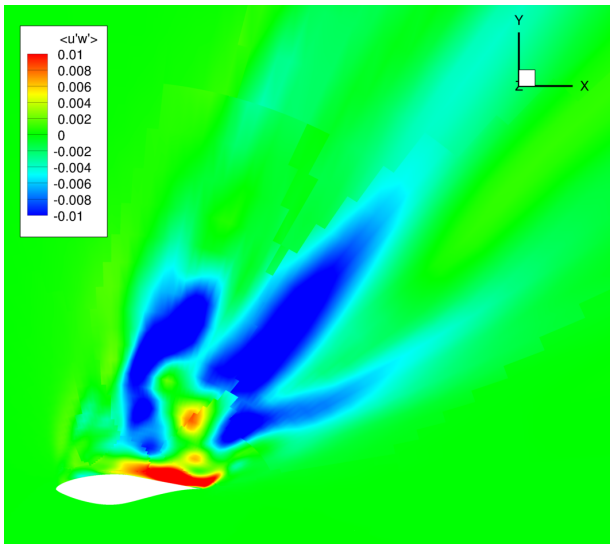

(a) *DDES, mean $u'w'$*

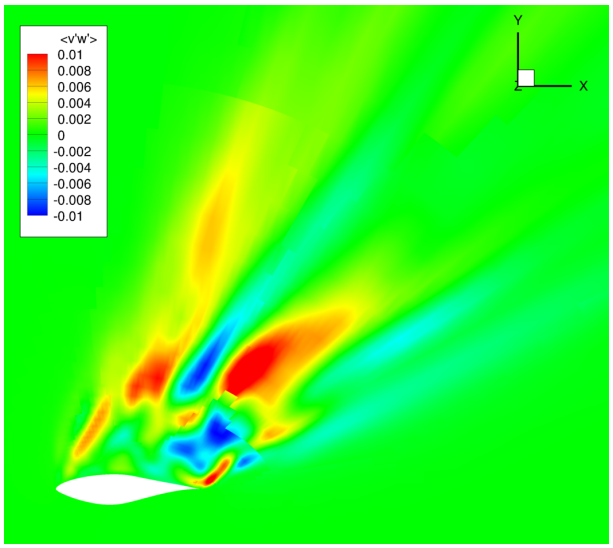

(b) *DDES, mean $v'w'$*

Figure 6.15: *Simulations on the S809 airfoil using DDES (2^{nd} order PLR scheme) at $Re = 0.65\ x\ 10^6$, $Ma_\infty = 0.075$, $\alpha = 45°$. Mean $u'w'$ and $v'w'$ shear stress contours at the $z/c = 0.5$ position.*

6.2.3 Flow past periodic hills at $Re = 10596$ using LES

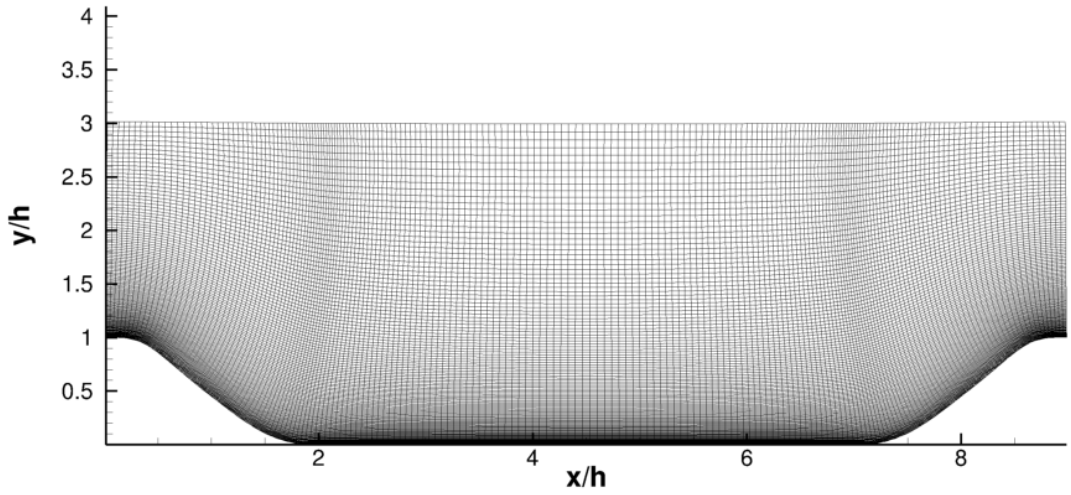

Figure 6.16: *2D mesh for the periodic hill*

The flow past periodic 2D hills is a popular test case for validating turbulence models in regards to separation and reattachment predictions. The present study follows the experiment of Breuer et al [162]. The Reynolds number based on the hill crest height, h, and the bulk velocity, U_b, is equal to 10596. The length of the domain is equal to $9h$ and the spanwise direction size is $4.5h$. This flow case is also computationally studied by Balakumar et al [28], Frolich et al [163] and Gritskevich et al [146].

LES using the Smagorinsky model is considered. The computational mesh consisted of 196 x 128 elements on the xy plane. In the spanwise direction 128 layers were used, bringing the 3D mesh to 4.7 million elements. A timestep of 0.002 nondimensional time units was used. The lower wall was fully resolved whereas wall functions were used for the upper wall.

The streamwise periodicity suggests that the inlet mass flow rate must be constant. If no external forces are used, inlet mass flow rate cannot remain constant in the simulation. It will instead decrease in value due to the presence of surface friction on viscous walls. There should be a pressure gradient that drives the flow and enables the conservation of mass flow rate. Following Xu [164], the pressure is decomposed into periodic and aperiodic components as:

$$\bar{p}(x, y, z, t) = \beta x + \bar{p}_p(x, y, z, t) \tag{6.1}$$

where β is the average streamwise pressure gradient. The constitutive equation of state thus becomes:

$$\bar{\rho} = \frac{\bar{p}}{R\bar{T}} = \frac{\beta x}{R\bar{T}} + \frac{\bar{p_p}}{R\bar{T}} \tag{6.2}$$

For moderate Reynolds numbers, the pressure gradient term is much smaller than the periodic pressure and therefore $\frac{\beta x}{R\bar{T}}$ is negligible compared to $\frac{\bar{p_p}}{R\bar{T}}$. The density can thus be approximated as:

$$\bar{\rho} \approx \frac{\bar{p_p}}{R\bar{T}} \tag{6.3}$$

The periodic component $\bar{p}_p$ replaces $\bar{p}$ in the governing equation and the streamwise pressure gradient is added as a body force term in the right hand side of the u-momentum equation. The periodic assumption for pressure is thus satisfied and the periodic pressure component is determined in the simulation by requiring that the mean mass flow rate be constant. The average streamwise pressure gradient is dynamically calculated in each physical time step in order to provide the desired mass flow rate as:

$$\beta^{n+1} = \beta^n - \frac{1}{\Delta t}\left[\left(\frac{\dot{m}}{A_c}\right)^0 - 2\left(\frac{\dot{m}}{A_c}\right)^n + \left(\frac{\dot{m}}{A_c}\right)^{n-1}\right] \tag{6.4}$$

where A_c is the crossflow area of the computational domain and Δt is the physical timestep. The average mass flow rate, $\dot{m}/A_c$, is defined as:

$$\frac{\dot{m}}{A_c} = \frac{1}{A_c}\int < \rho u >_s \, dA \tag{6.5}$$

where $<>_s$ denotes an ensemble average along the normal and spanwise direction and $(\dot{m}/Ac)^0$ is the desired mass flow rate which was set equal to a non-dimensional value of 1.0 for the simulation.

Computational results are compared to LES results available from the NASA turbulence modeling database [21] in fig. 6.17-6.22. Mean u contours differ slightly in the region close to the upper wall (fig. 6.17). This may be attributed to different wall modeling between the two simulations. However, moving away from the upper wall the contours become similar. Similarities are also observed for the mean v (fig. 6.18). The presence of small contour fluctuations close to the lower wall when compared to the reference results suggests that a smaller time averaging period was used. Slight differences observed in the mean $u'u'$ contour (fig. 6.19) also imply that a larger time-averaging frame is needed.

According to the experimental measurements, separation occurs near $x/h = 0.2$ and reattachment near $4.6 - 4.7h$. In fig. 6.20-6.22 it is shown that both separation and reattachment locations are captured well. The tail of the recirculation region is slightly different in MaPFlow when compared to the reference results (fig. 6.21b), exhibiting lower mean u values. The reattachment point is located slightly downstream at $x/h \approx 5$. Separation is predicted very close to the experimental value of 0.2 (fig. 6.22b).

Overall, the present results are very close to the reference ones. The discrepancies could be caused by different subgrid models. Unfortunately, the subgrid model employed in the reference computations is not known. In addition, usage of longer time averaging periods than the one considered here will produce results that will be closer to the reference data. The averaging period used in this work was $T_{avg} = 360$ nondimensional time units, whereas Breuer et al [162] used a value of $T_{avg} = 1277$. However, such a long time-averaging period was beyond our computational capabilities.

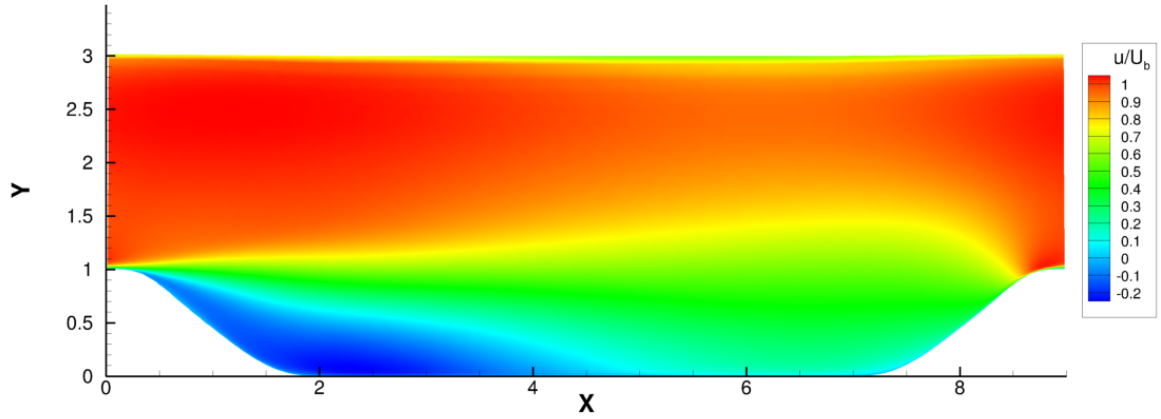

(a) *Mean u/U_b, NASA, LES*

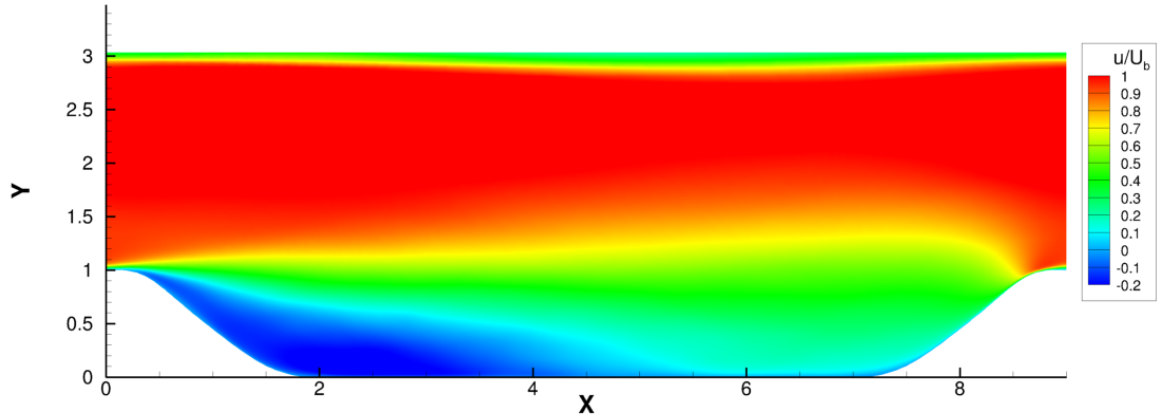

(b) *Mean u/U_b, MaPFlow, LES, Smagorinsky*

Figure 6.17: *Flow around periodic hills. h is the height of the hill crest. Distance between hill crests $L_x = 9h$, channel height $L_y = 3.035h$. Spanwise depth $L_z = 4.5h$. $Re = 10596$, based on h and on bulk velocity U_b at the crest of the first hill. Comparison with computations from the NASA turbulence database [21].*

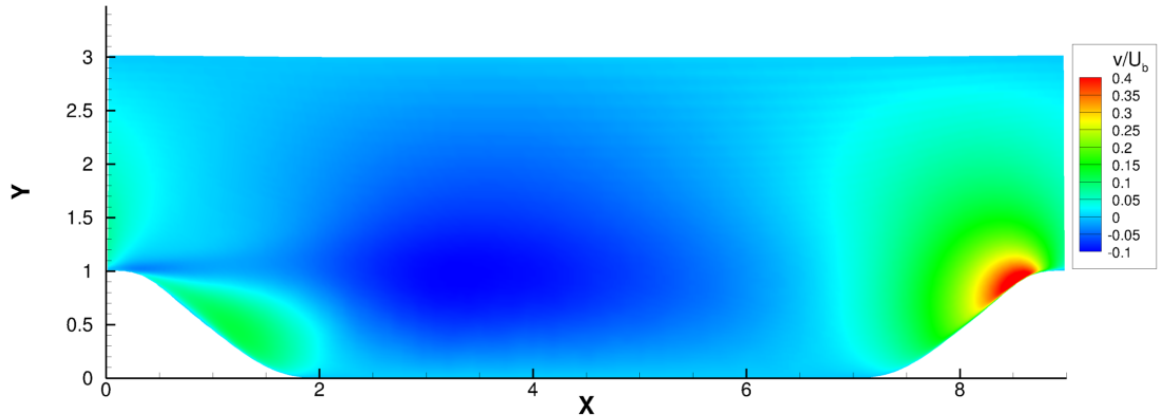

(a) *Mean v/U_b, NASA, LES*

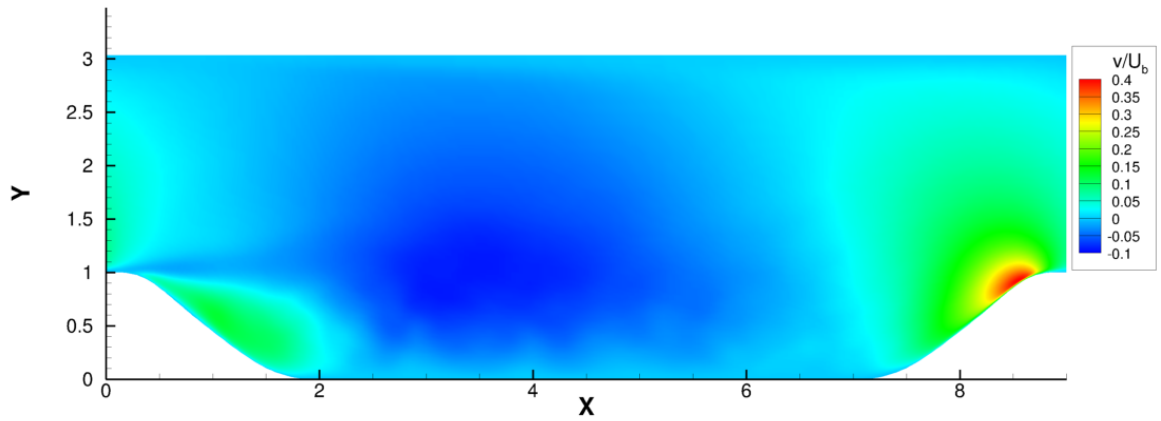

(b) *Mean v/U_b, MaPFlow, LES, Smagorinsky*

Figure 6.18: *Flow around periodic hills. h is the height of the hill crest. Distance between hill crests $L_x = 9h$, channel height $L_y = 3.035h$. Spanwise depth $L_z = 4.5h$. $Re = 10596$, based on h and on bulk velocity U_b at the crest of the first hill. Comparison with computations from the NASA turbulence database [21].*

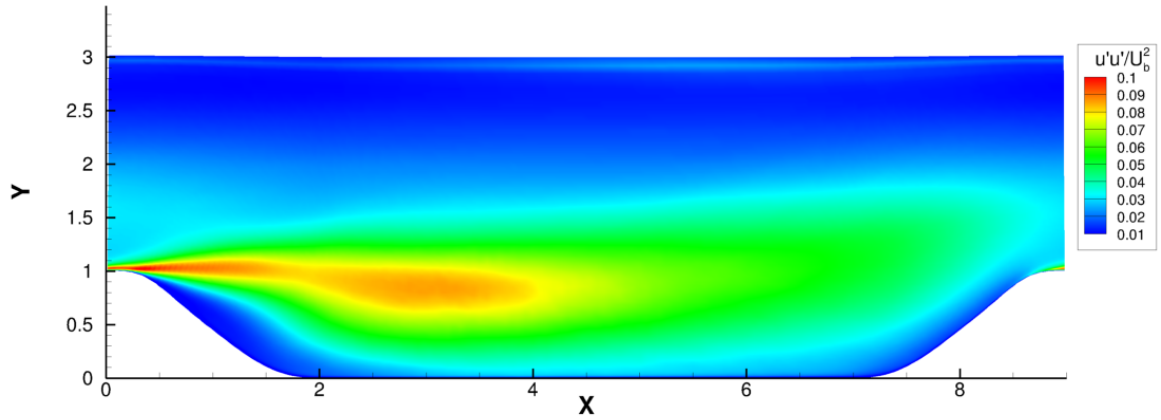

(a) *Mean $u'u'/U_b^2$, NASA, LES*

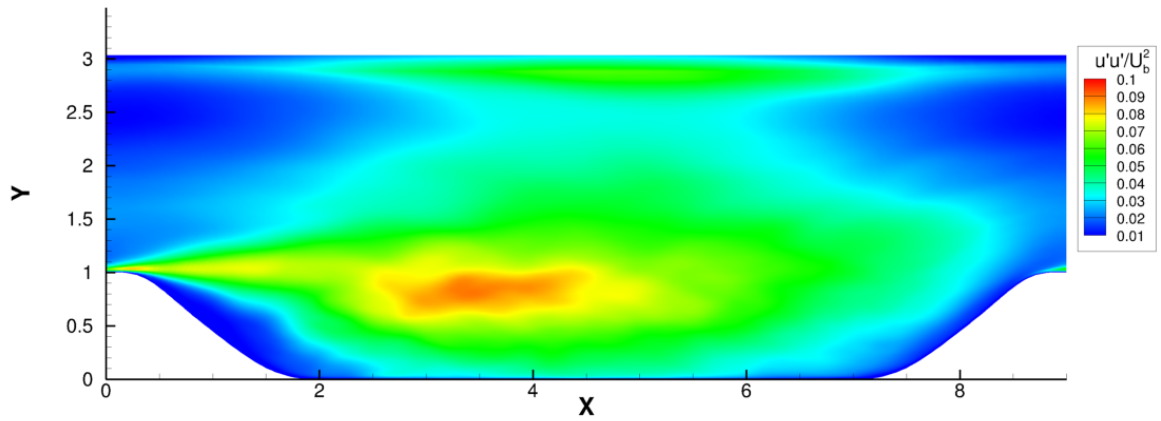

(b) *Mean $u'u'/U_b^2$, MaPFlow, LES, Smagorinsky*

Figure 6.19: *Flow around periodic hills. h is the height of the hill crest. Distance between hill crests $L_x = 9h$, channel height $L_y = 3.035h$. Spanwise depth $L_z = 4.5h$. $Re = 10596$, based on h and on bulk velocity U_b at the crest of the first hill. Comparison with computations from the NASA turbulence database [21].*

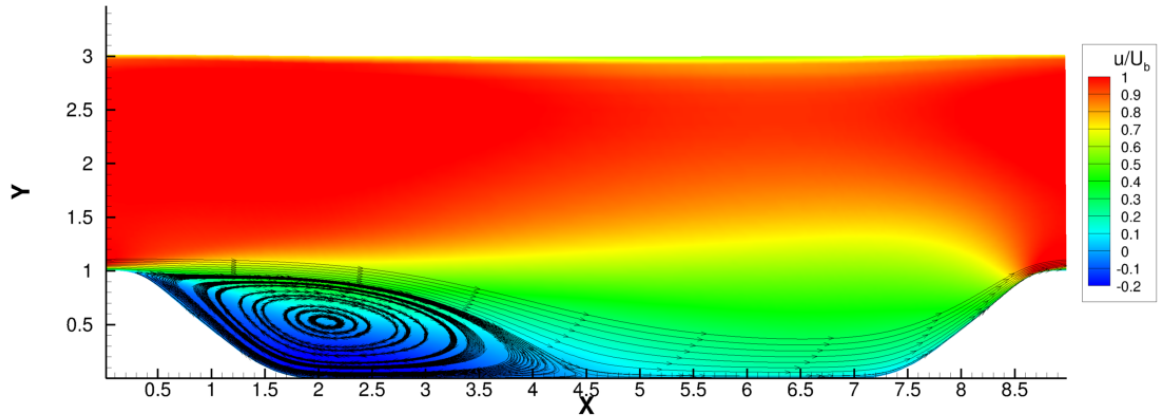

(a) *Recirculation region, NASA, LES*

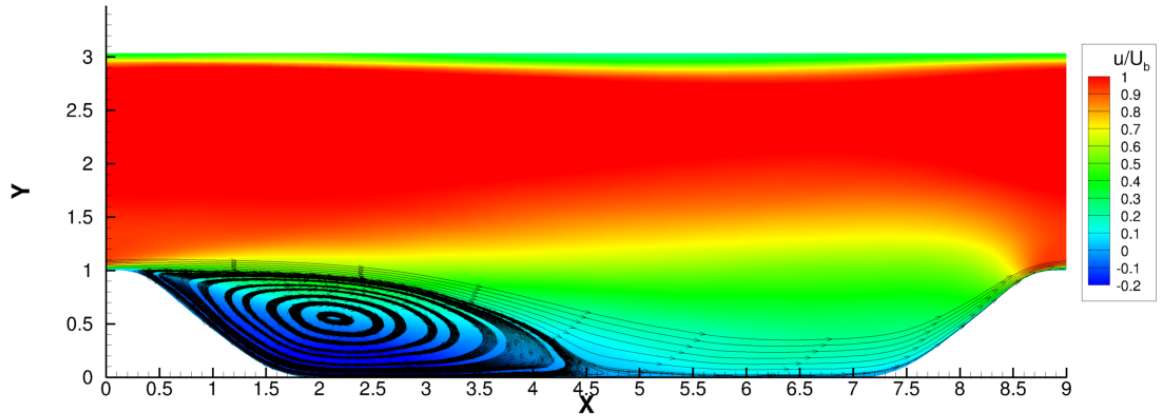

(b) *Recirculation region, MaPFlow, LES, Smagorinsky*

Figure 6.20: *Flow around periodic hills. h is the height of the hill crest. Distance between hill crests $L_x = 9h$, channel height $L_y = 3.035h$. Spanwise depth $L_z = 4.5h$. $Re = 10596$, based on h and on bulk velocity U_b at the crest of the first hill. Comparison with computations from the NASA turbulence database [21].*

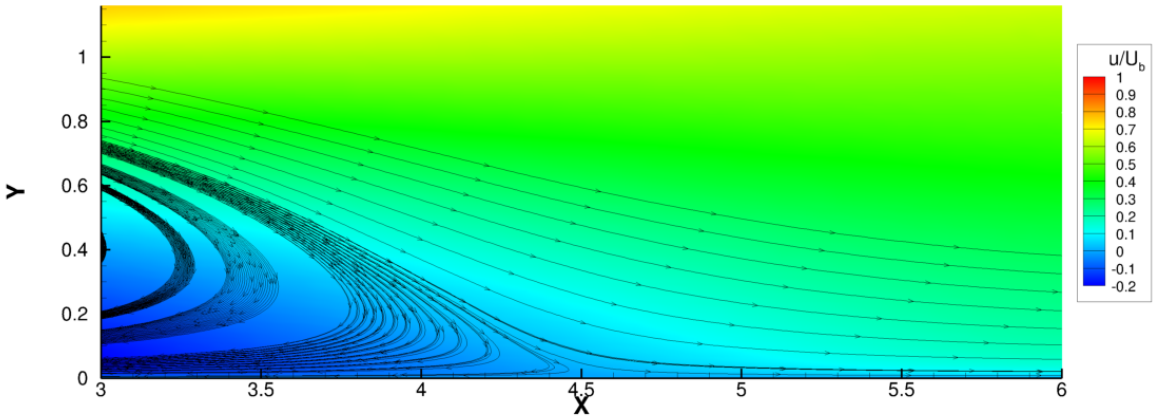

(a) *Reattachment, NASA, LES*

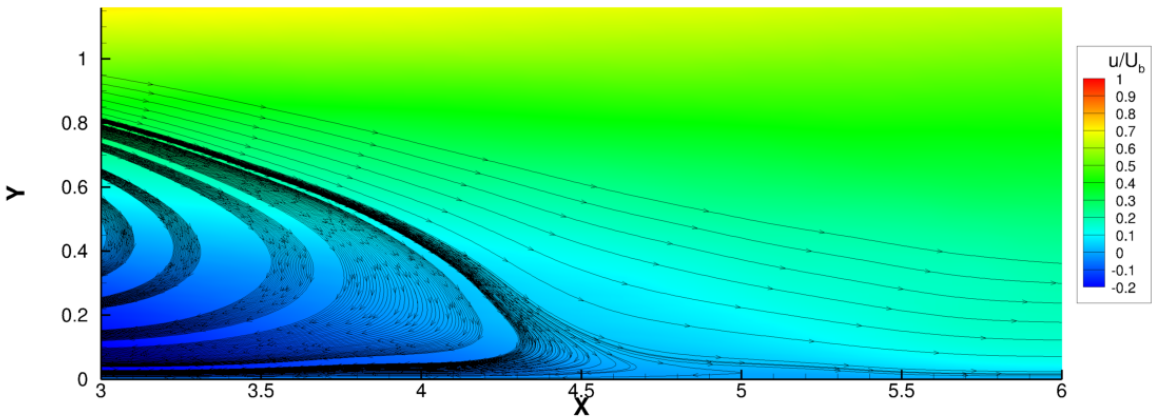

(b) *Reattachment, MaPFlow, LES, Smagorinsky*

Figure 6.21: *Flow around periodic hills. h is the height of the hill crest. Distance between hill crests $L_x = 9h$, channel height $L_y = 3.035h$. Spanwise depth $L_z = 4.5h$. $Re = 10596$, based on h and on bulk velocity U_b at the crest of the first hill. Comparison with computations from the NASA turbulence database [21].*

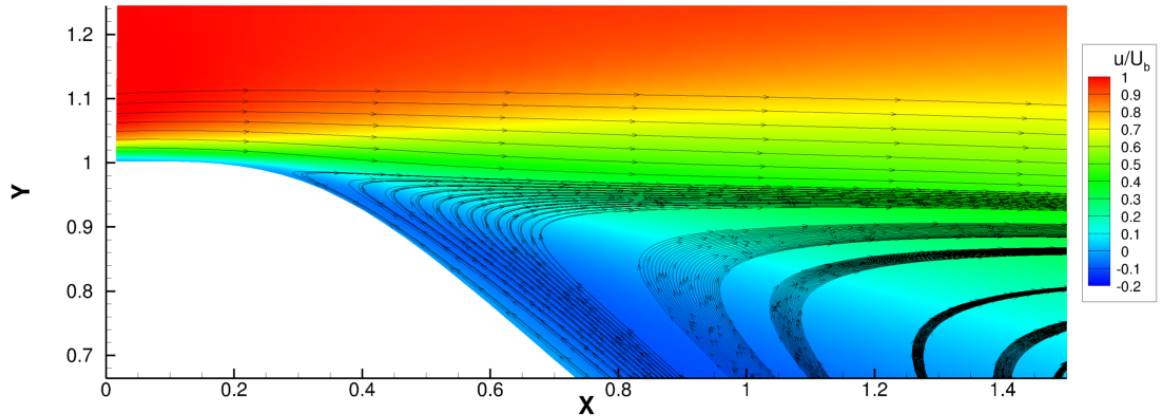

(a) *Separation, NASA, LES*

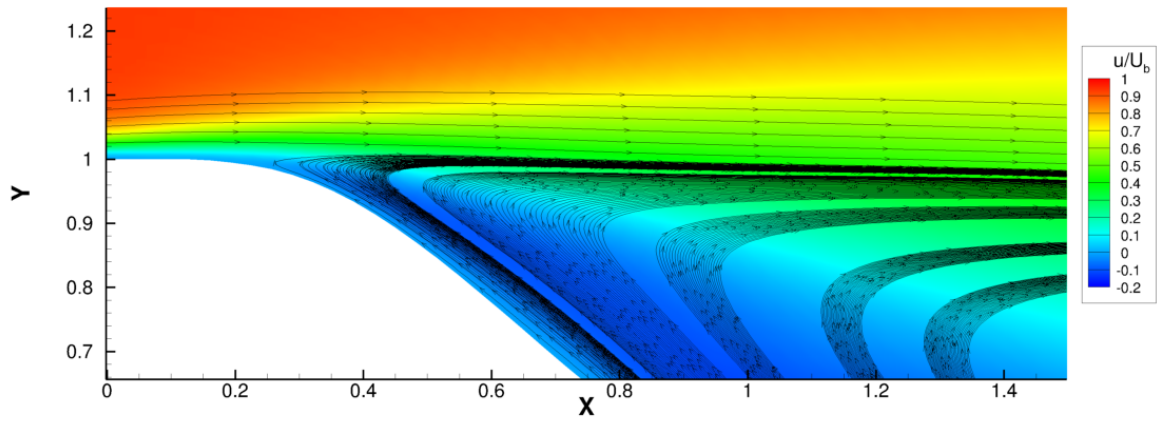

(b) *Separation, MaPFlow, LES, Smagorinsky*

Figure 6.22: *Flow around periodic hills. h is the height of the hill crest. Distance between hill crests $L_x = 9h$, channel height $L_y = 3.035h$. Spanwise depth $L_z = 4.5h$. $Re = 10596$, based on h and on bulk velocity U_b at the crest of the first hill. Comparison with computations from the NASA turbulence database [21].*

6.2.4 Atmospheric flow past the Sexbierum rotor using turbulent inflow and LES

The Sexbierum wind turbine was measured by Cleijne [22] in the Sexbierum Wind farm. Flow and turbulence quantities at various wake positions were measured. The availability of such data renders this case suitable for the validation and assessment of higher fidelity turbulence models. Smagorinsky LES is performed under turbulent inflow conditions using the Mann Box generator (Section 4.4), which is representative of a real atmospheric turbulent spectrum including all three velocity components and spatial variation. The wind velocity at hub height is $U_{hub} = 8m/s$, whereas the diameter D is $30m$ and the hub height H is $35m$. Turbulence intensity at hub height is $Tu_{hub} = 13.5\%$. The rotor is rotating with rotational speed $\omega = 4.1rad/s$. The employed timestep was $0.08513s$, which corresponds to 180 timesteps per rotor rotation.

The Wind turbine rotor is simulated using two approaches: a) a simple actuator disk and b) an actuator line considering each blade as a rotating line along which loading is distributed through blade element theory. The implemented actuator line theory is presented in [39]. In order to capture the whole range of turbulent eddies and the formation of tip vortices, mesh spacing should be really small and as uniform in all directions as possible, which results in very dense meshes. The results using LES are compared to 3D Unsteady RANS predictions using the k-ω SST turbulence model in order to assess the prediction capabilities of both methods. The results are distinguished in three different categories according to the successive steps taken.

Wind turbine simulation in the absence of turbulent inflow

The first step aims at evaluating the formation of vortex structures in the wake and assess the effect of shear imposed by the presence of ground. Both uniform and sheared inflow simulations were performed at this step. The computational domain extend was $-8D$ to $16D$ in the main flow direction (x-axis) and $-12D$ to $12D$ in the lateral direction (y-axis). For uniform inflow, domain dimensions in z and y axis remain the same whereas for sheared inflow the z (vertical) dimension is extended to $30D$ in order to avoid flow blockage. The mesh is equidistant for $x \in [-2D, 8D]$ and $y \in [-D, D]$, with a $D/60$ spacing. Outside this refined region, the spacing increases following a geometric progression.

The magnitude of vorticity on the rotor plane is presented in fig. 6.23, showing the mesh density and the increased vorticity close to the blade tips. In fig. 6.25, contours in the wind turbine wake for the averaged vorticity magnitude (fig. 6.25a) and the averaged x-axis vorticity (fig. 6.25b), whereas fig. 6.24 contains the velocity deficits at three wake positions. The velocity deficit remains significant in the far wake. There is also an artificial acceleration in the wake center due to the modeling of the blade root as a cylinder. This acceleration remains high due to the absence of turbulent inflow. Overall, the effect of sheared inflow is the decrease of the off-center velocity deficit in the far wake.

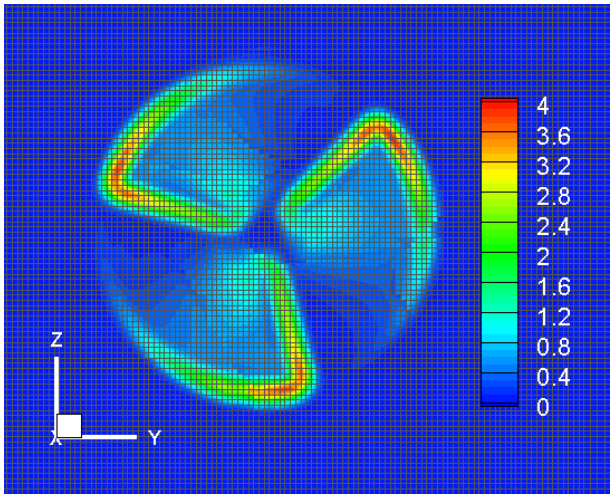

Figure 6.23: *LES on the Sexbierum Wind Turbine rotor [22]. Actuator line in the absence of turbulent inflow. Contours of vorticity magnitude on the rotor plane.*

Turbulent inflow simulation in the absence of wind turbine

The second step is to check the evolution of turbulent inflow along an empty computational domain. Both uniform and sheared inflow are again considered. The Mann box has a discretization of 2m using 64 points in all directions. The input parameters correspond to neutral atmospheric conditions in the case of the Sexbierum blade (see Table 6.1).

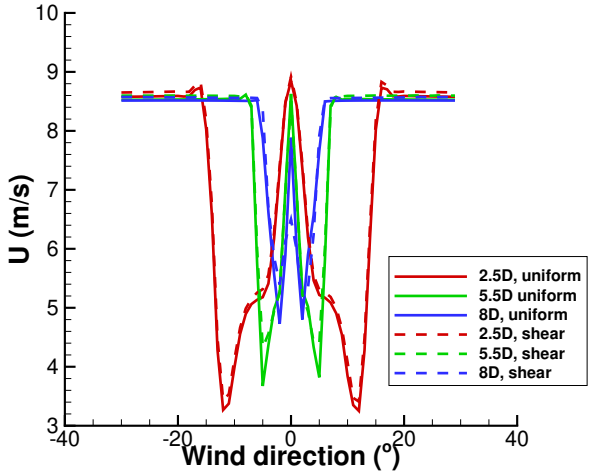

Figure 6.24: *LES on the Sexbierum Wind Turbine rotor [22]. Actuator line in the absence of turbulent inflow. Streamwise velocity deficit at various positions on the wake.*

Table 6.1: *Input parameters for the Mann turbulence generator*

Parameter of the sheared spectral tensor, Γ	3.7
Length scale of the spectral velocity tensor, L	19.6 m
Product of the Kolmogorov constant (α) and the dissipation of turbulent kinetic energy (ϵ), $\alpha\epsilon^{2/3}$	0.072

In order to assess the effect of mesh density on the evolution of turbulent inflow, two different computational meshes with spacings $0.5m$ and $1m$ are compared. The resulting U velocity time series and turbulence spectra are presented in fig. 6.26 for positions $x = -1D$, $3D$ and $7D$. It is evident that the time variations using the coarser mesh are smoother, which explains why high frequencies are not reproduced (fig. 6.26a, 6.26c, 6.26e). This is confirmed by analyzing the turbulence spectra in fig. 6.26b, 6.26c and 6.26f. It is shown that the spectral density is retained for frequencies up to $1Hz$ when the fine mesh is used. On the contrary, there is a significant reduction in turbulent kinetic energy when using the coarse mesh, suggesting that the high frequency part of the spectra has been eliminated due to increased diffusion.

Wind turbine simulation with turbulent inflow

The third step is the simulation of the wind turbine using turbulent inflow. Both uniform and sheared inflow were considered, using the actuator disk and actuator line approaches. Results from this step are compared to URANS results and experimental data [22].

Based on the analysis from the previous step, a mesh spacing of $0.5m$ is used in order to properly maintain the frequency spectrum of the turbulent inflow. This spacing was used for simulations using the actuator disk approach. However, for this mesh spacing the actuator line approach exhibited numerical instabilities, especially for sheared inflow. For the uniform flow case, the alternative of resolving the turbulent inflow field upstream of the rotor with a $1m$ mesh spacing while retaining the 0.5 spacing in the wake was investigated.

In fig. 6.27a-6.27b, velocity contours for the mean and instantaneous flow fields using LES with the actuator disk approach and turbulent inflow are presented. The velocity deficit is clearly visible. However, the instantaneous field also exhibits the variations caused by the turbulent inflow. In fig. 6.28a, 6.28c and 6.28e the wind speed deficits at distance $x = 2.5D$, $5.5D$ and $8D$ downstream of the rotor are compared. The URANS predictions have been obtained using the actuator line approach and sheared inflow, whereas the LES predictions assume uniform inflow for both actuator disk and actuator line approaches. In addition, LES utilizes turbulent inflow. In the vertical direction the mesh spacing equals $0.5m$ up to $1.6D$ above ground level. In the x and y directions the minimum mesh spacing equals $0.5m$ in the rotor region and increases following a geometric progression outwards. In the near wake, it is evident that LES gives better predictions of the wind speed deficit, even when utilizing a simpler actuator disk approach and assuming uniform inflow. In the far wake, both LES and URANS predictions are similar and are able to give adequate predictions of the wind speed deficit. Similar observations can be made for the turbulent kinetic energy predictions, shown in fig. 6.28b, 6.28d and 6.28f. The differences between fig. 6.28c and fig. 6.28e at the $x = 2.5$ position are due to less turbulent mixing in the case of LES. It is also noted that the presence of ground reduces the wake speed and therefore results in a better

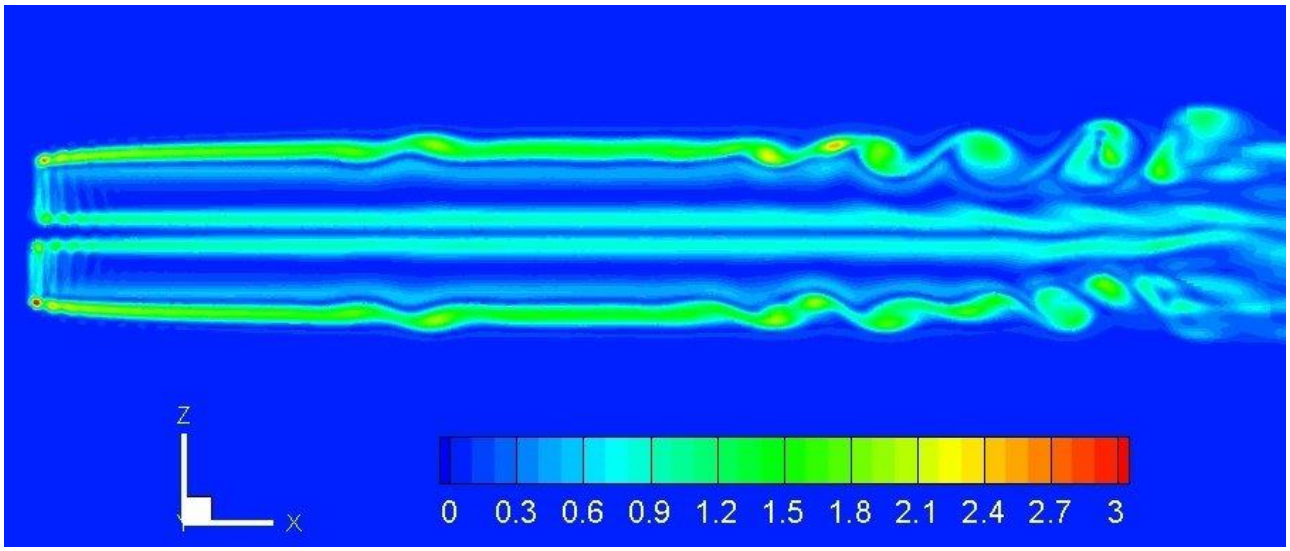

(a) *Averaged vorticity magnitude on the xz plane.*

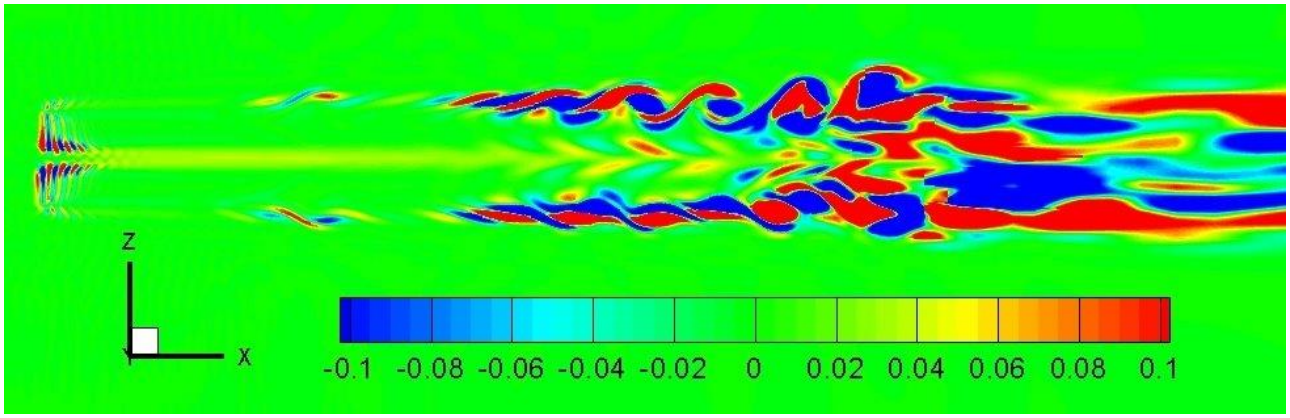

(b) *Averaged x-axis vorticity on the xz plane.*

Figure 6.25: *LES on the Sexbierum Wind Turbine rotor [22]. Actuator line in sheared flow, without turbulent inflow.*

prediction of the off-center deficit when compared to the experiments. The Q criterion iso-surfaces in the wake ($Q = 0.1$) are presented in section 6.2.4, without and with turbulent inflow. The simulation without turbulent inflow used a finer mesh, as discussed in the first paragraph of this section. When comparing the two figures, it is shown that even for the coarser mesh the presence of turbulent inflow has a significant effect on the turbulent structures past the wind turbine rotor.

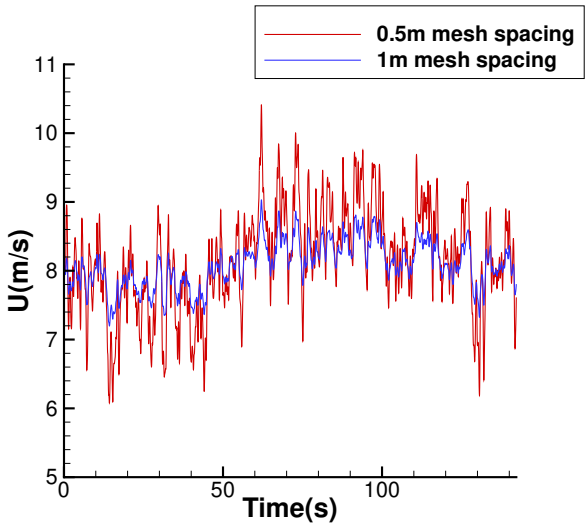

(a) *Streamwise velocity time series, $x = -1D$.*

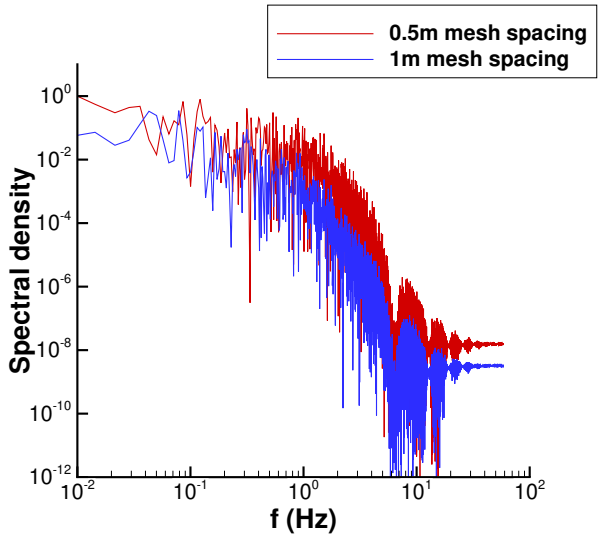

(b) *Streamwise velocity variations spectrum, $x = -1D$.*

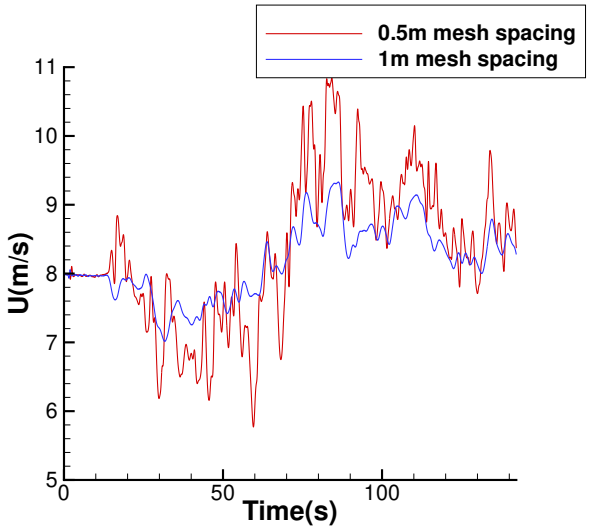

(c) *Streamwise velocity time series, $x = 3D$.*

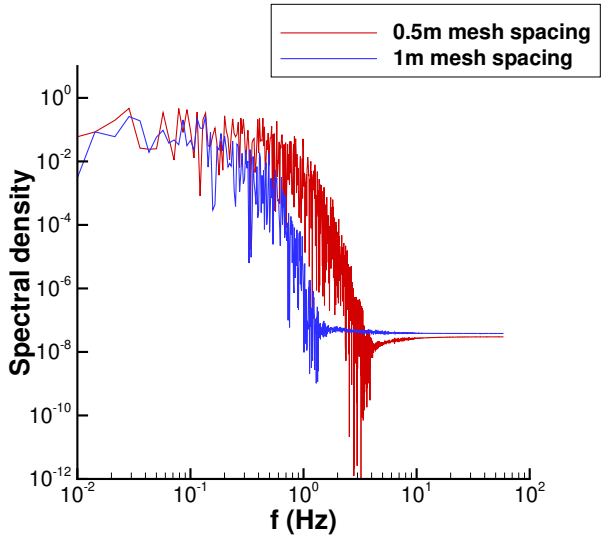

(d) *Streamwise velocity variations spectrum, $x = 3D$.*

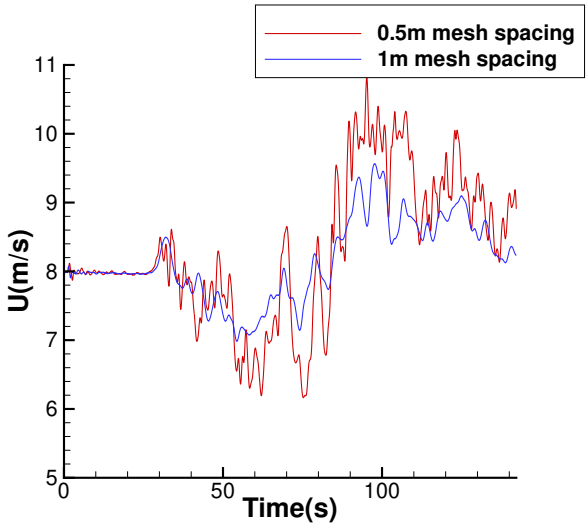

(e) *Streamwise velocity time series, $x = 7D$.*

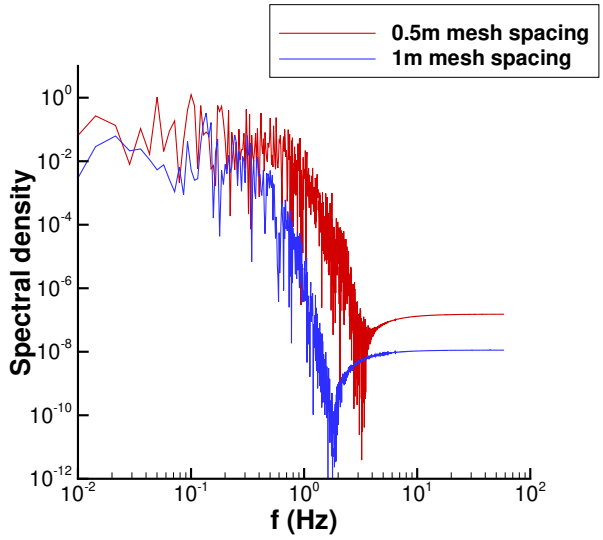

(f) *Streamwise velocity variations spectrum, $x = 7D$.*

Figure 6.26: *Sheared flow with turbulent inflow (see Table 6.1) in the absence of wind turbine. U velocity time series and corresponding spectrum of the velocity variations using two different mesh spacings.*

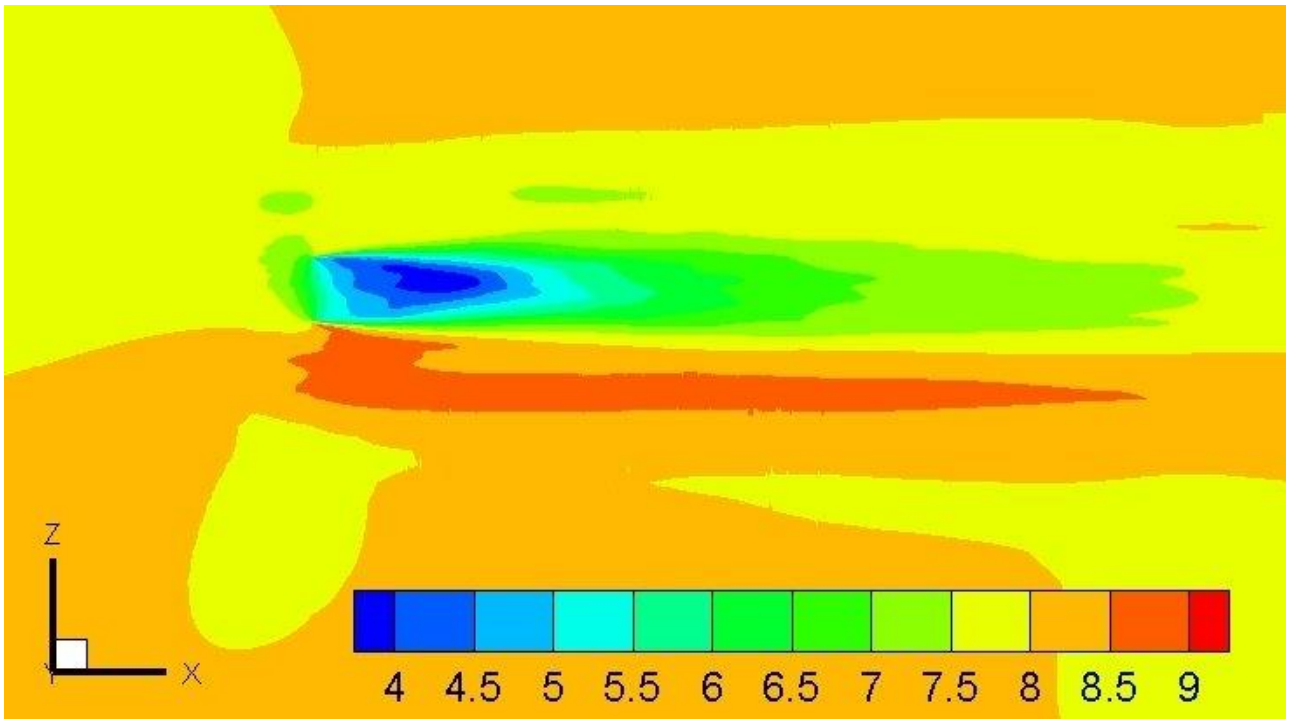

(a) *Mean U contour*

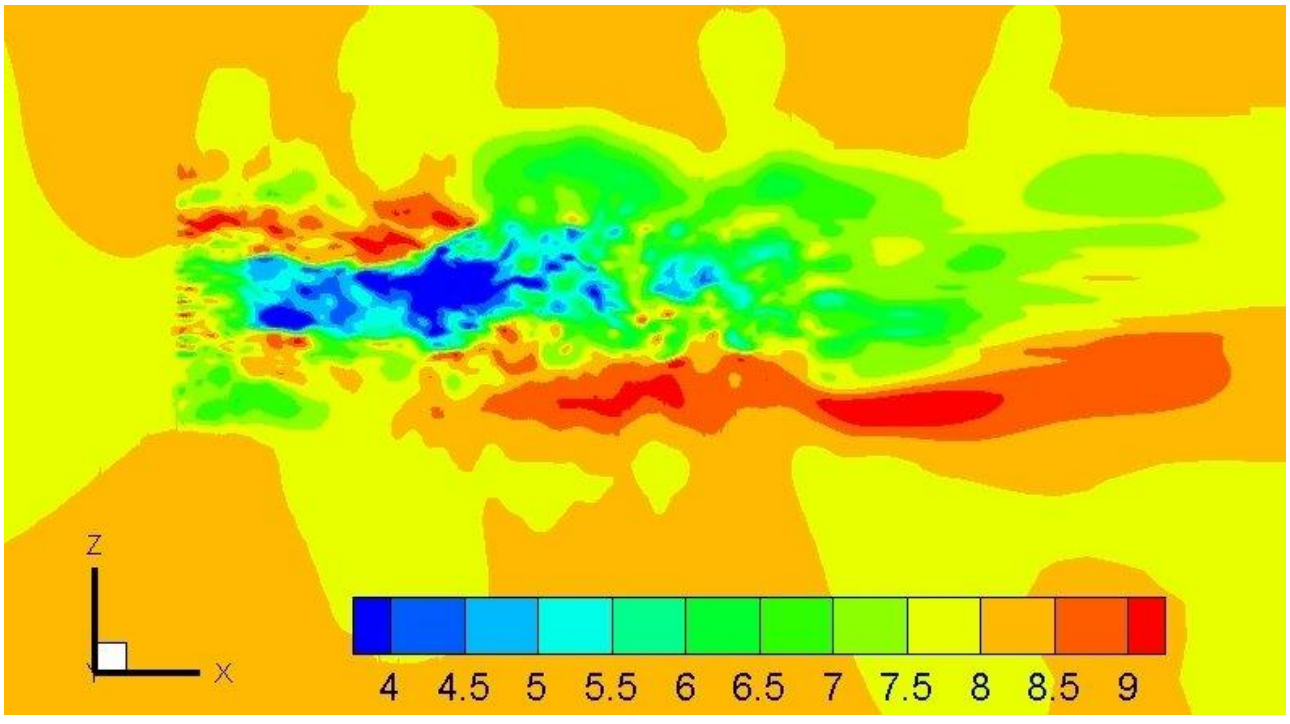

(b) *Instantaneous U contour*

Figure 6.27: *LES on the Sexbierum Wind Turbine rotor [22]. Actuator disk with turbulent inflow (see Table 6.1).*

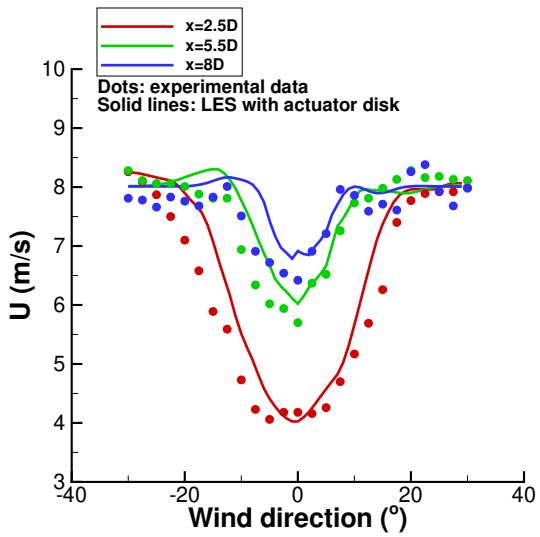

(a) *LES, actuator disk, wind velocity deficit*

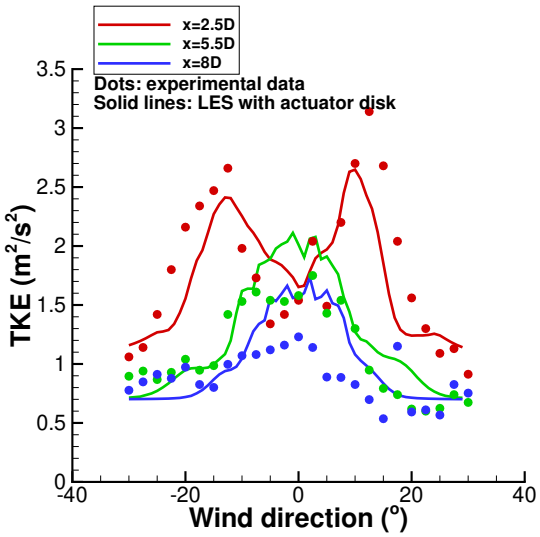

(b) *LES, actuator disk, turbulent kinetic energy*

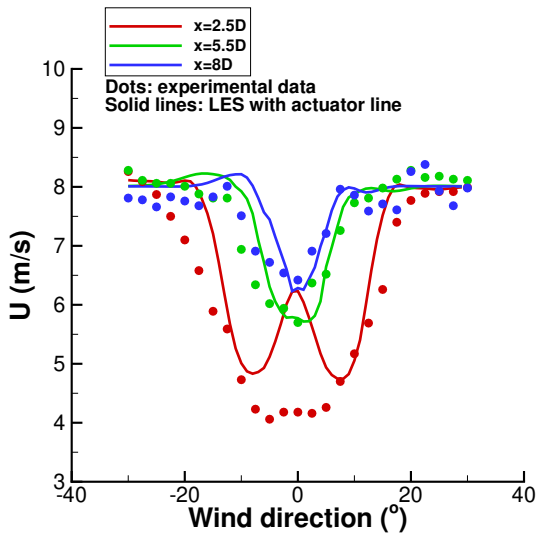

(c) *LES, actuator line, wind velocity deficit*

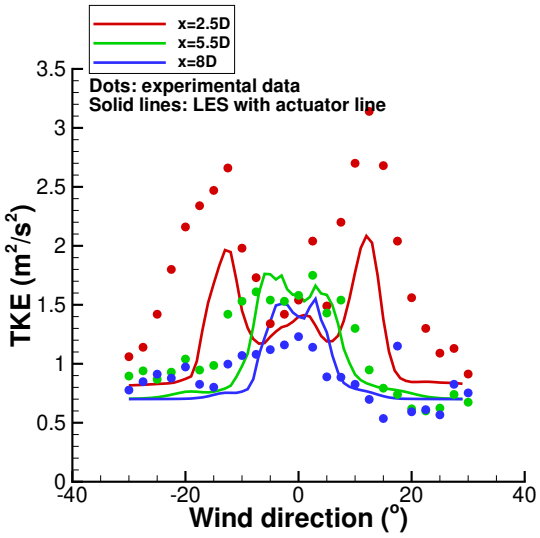

(d) *LES, actuator line, turbulent kinetic energy*

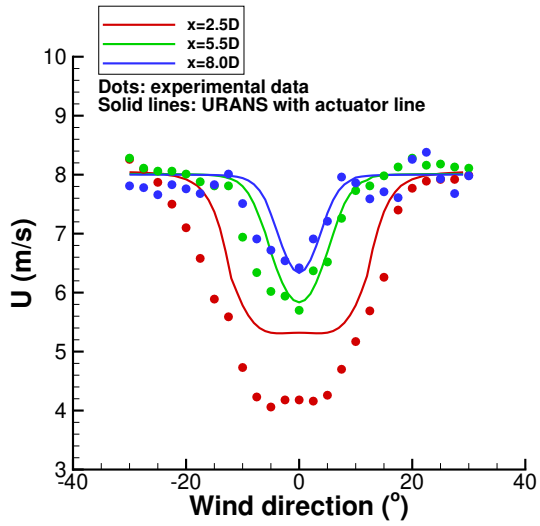

(e) *URANS, actuator line, wind velocity deficit*

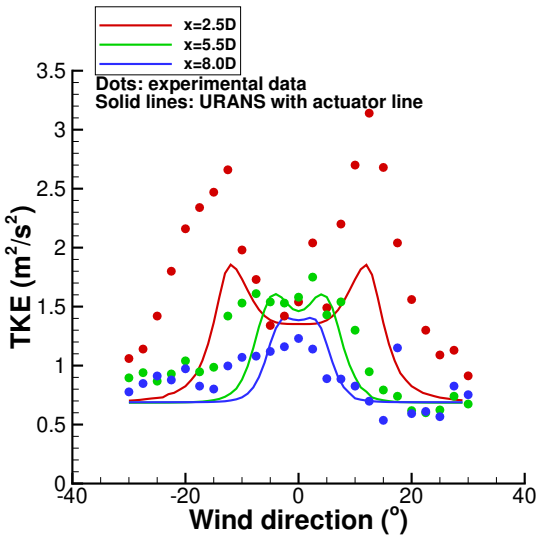

(f) *URANS, actuator line, turbulent kinetic energy*

Figure 6.28: *LES and URANS on the Sexbierum Wind Turbine rotor [22]. LES utilizes both actuator disk and actuator line approaches in sheared flow with turbulent inflow (see Table 6.1). URANS utilizes the actuator line approach in sheared flow without turbulent inflow. Wind speed deficits and turbulent kinetic energy in various wake positions.*

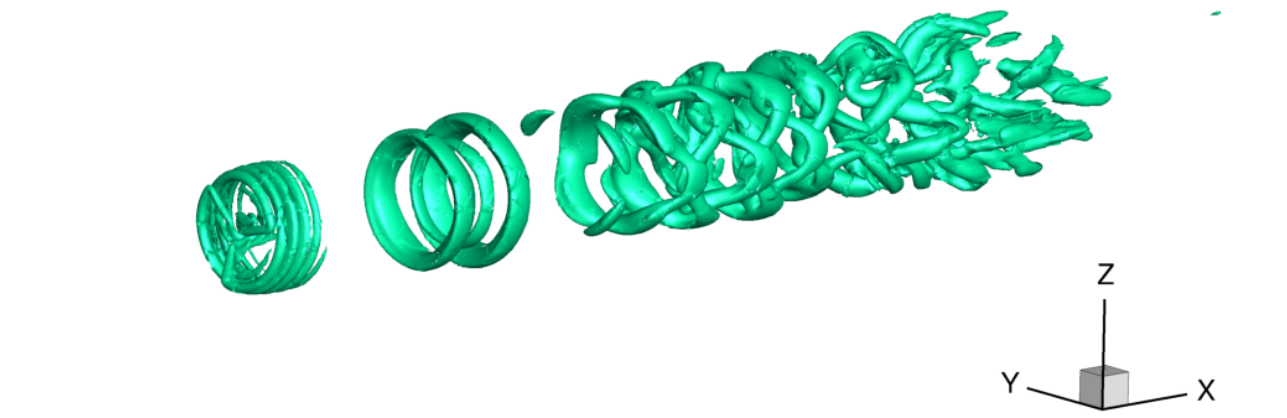

(a) *Without turbulent inflow.*

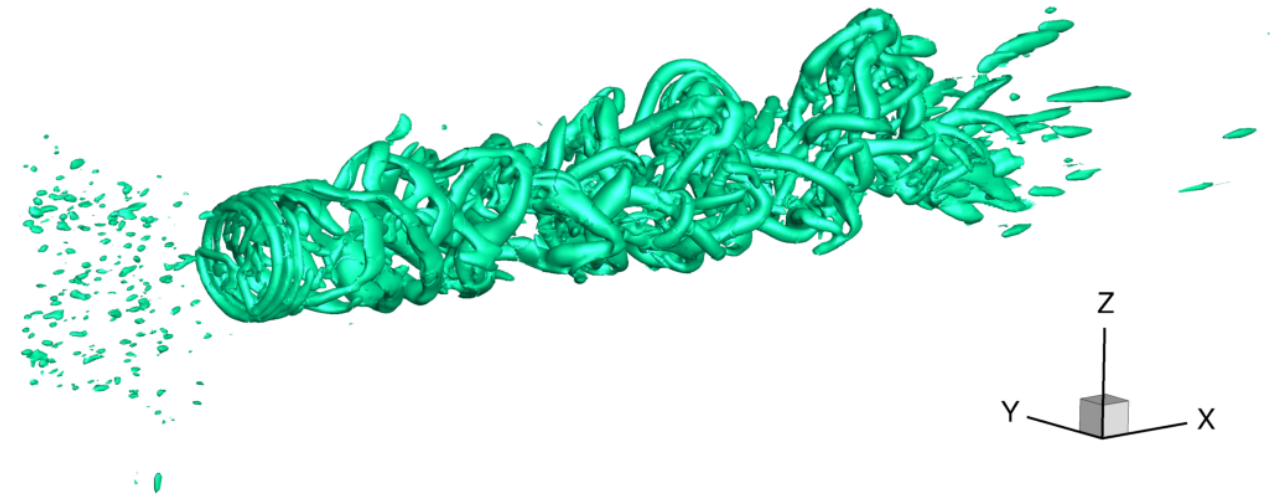

(b) *With turbulent inflow.*

Figure 6.29: *LES on the Sexbierum Wind Turbine rotor [22]. Actuator line without and with turbulent inflow (see Table 6.1). $Q = 0.1$ iso-surfaces on the wind turbine wake.*

6.3 Discussion

In this Chapter, the results from simulations with LES and DDES have been presented. The comparisons were mostly carried out in locations away from the solid surface, with an emphasis on various positions on the wake. However, some cases included integrated load measurements, which were also compared.

For the classic case of circular cylinder (Section 6.2.1), both LES and DDES outperform URANS on the same computational mesh, providing more accurate predictions when compared to experimental data. URANS suppressed the three-dimensional character of the flow in the simulations, behavior which was not observed with LES or DDES. The case of the S809 airfoil (Section 6.2.2) showed that DDES outperforms URANS at very high angles of attack with massive separation, especially when approaching 90°. Aerodynamic results from DDES were in very good agreement with the experiments, whereas URANS seemed to overpredict both C_l and C_d. Suppression of the three-dimensional character was again observed when using URANS. The simulation of flow past periodic hills with LES (Section 6.2.3) gave results that were in very good agreement with reference computations. However, some deviations highlighted the importance of a sufficient time-averaging period. Lastly, a wind turbine with turbulent inflow was simulated using LES and actuator methods (Section 6.2.4). Velocity deficits at the wake were compared to experimental data, showing good agreement. The effect and importance of turbulent inflow in aerodynamic simulations with LES was also highlighted.

Based on the results and the discussion in this Chapter, the following are derived:

- Regarding the implementation of LES and DES, simulations with finer meshes will yield more accurate results. Due to the nature of both approaches, a true mesh independent solution cannot be obtained.
- Increasing Re will require higher mesh resolution, therefore a mesh that is able to provide accurate results for a given case will not necessarily have the same prediction accuracy for cases with higher Re. For a given mesh, its capability to simulate a particular flow problem should thus be assessed appropriately.
- For the cases that involved both LES and DES, both approaches utilized the same computational mesh. Neither LES nor DES were pushed to their limits.
- LES was not further refined in order to assess how it performs according to literature. The use of finer meshes will improve the accuracy of the results.
- In the test cases considered in this thesis, LES proved to be operational. The general know-how has been implemented and the results presented here were in good agreement with reference data. Therefore, LES can be used in aerodynamic problems.
- Due to not having an underlying RANS mode, the computational cost of LES is considered higher than that of DES. This also means that insufficient mesh resolution may lead to inaccurate results.
- For the simulations presented in this thesis, the utilized computational meshes and the simulated physical time really tested our available resources. Therefore, if a large number of simulations for practical or engineering applications are considered, use of LES is unrealistic.
- DES proved to be a very honest compromise. For the examined cases, comparison of computational results on the wake to measurements was favorable. This means that the underlying Spalart-Allmaras turbulence model was able to predict the boundary layer with good accuracy, which led to good results on the wake.
- DES is not expected to give accurate results for flows with mild stall (i.e. below 20°), because at those angles the separation point will be mostly defined by the underlying RANS model and not by the development of small scales inside the boundary layer. In practice, the results from DES at those angles will closely resemble those from URANS.
- For flows with massive separation, DES has a clear advantage over URANS.
- Overall, the lower computational cost of DES renders it a viable option when a large number of simulations are considered, especially if cases with massive separation are of interest.

Chapter 7

Concluding remarks

7.1 Synopsis

The first objective of the present work concerned transitional simulations which were carried out in a wide range of test cases from the wind energy and aeronautics sectors. Boundary layer and transport equation approaches were both considered. Regarding boundary layer transition, different ways to obtain the boundary layer parameters in a Navier-Stokes solver were discussed and evaluated. The complete module that couples the transition prediction algorithm with the Navier-Stokes simulation was discussed in detail. Regarding transport equation transition, three different models were discussed and suggested practice guidelines were given. The computational results were compared to available experimental data in order to assess the performance of each model. The comparisons focused on integrated loads (C_l-C_d curves), transition locations, and boundary layer velocity profiles. The prediction accuracy of the models with increasing Re number was also assessed.

The second objective of the present work concerned simulations with massive separation. The Large Eddy Simulation (LES) and Detached Eddy Simulation (DES) approaches were implemented. Simulations with LES utilized the Smagorinsky subgrid scale model. Regarding simulations with DES, the Spalart-Allmaras turbulence model was used. The objective was to assess the prediction accuracy of both approaches by comparing to available experimental data. In some cases, computational results from LES and DES were also compared to those from baseline URANS, in an effort to highlight notable differences. Turbulent inflow capabilities were also implemented, in order to have more realistic simulations of cases with atmospheric flows.

In the context of two-dimensional transitional simulations, the boundary layer e^N method and the AFT transport equation transition model proved reliable for all examined cases. Regarding airfoil polars, the focal points are drag levels inside the laminar bucket as well as laminar bucket extent (location of laminar bucket corners), which are both greatly affected by the transition locations. The e^N method and the AFT model were able to accurately predict transition locations, therefore leading to very good agreement with experimental data. The γ-Re_θ model was also able to provide accurate results for cases up to 4 x 10^6. However, its accuracy was significantly compromised for Re numbers beyond this limit as it always predicted transition locations significantly upstream, leading to higher drag levels inside the bucket. The overall upstream transition prediction also caused the laminar bucket corners to appear earlier, thus decreasing the extent of the laminar bucket. The γ model exhibited similar behavior to the γ-Re_θ model, as it also predicted transition upstream for Re numbers beyond 4 x 10^6. However, some notable deviations in predicted transition locations were also noted in cases with Re number lower 4 x 10^6.

In the context of three-dimensional transitional simulations, application of boundary layer transition methods is complex. The integral equations cannot be used to solve three-dimensional boundary layers. This leaves direct CFD integration as the only approach that can provide the required boundary layer parameters. Moreover, application of specific transition criteria (such as the e^N method) in three dimensional boundary layers will require the calculation of streamlines on the solid surface. This problem does not exist in two-dimensional simulations, where the solid surface has a single stagnation point and the boundary layer can only march towards the trailing edge on the two sides of the wall surface. In three-dimensional simulations, the calculation of streamlines must be repeated at every iteration, thus raising the overall computational cost of the boundary layer transition module. In some cases, the three dimensional boundary layer can be approximated by two-dimensional sections, each treated as a separate, two-dimensional boundary layer. However, this approach cannot be applied to arbitrary geometries (i.e. spheroids) and is greatly dependent on the flow characteristics. Streamlines on the solid surface must be approximately parallel to the two-dimensional sections of the geometry. This assumption is valid on rotating wind turbine blades, where rotation causes the boundary layer to be parallel to the two-dimensional sections at least up to the point of separation. In swept wings, however, the boundary layers have a strong three-dimensional character that cannot be approximated by solving the boundary layer

on two-dimensional sections. For flow cases and geometries which hinder the application of boundary layer methods, usage of transport equation models is more favorable, as they bypass the need for additional boundary layer integration and streamline calculation interfaces. In their baseline versions, all transport equation models account only for natural transition in the streamwise direction. However, accurate prediction of crossflow transition can be quite important, as was highlighted from the results in this thesis. This can be achieved by the inclusion of additional terms which aim at including the effect of crossflow instabilities on the transition models. Such terms were implemented in the γ-Re_θ transport equation model. For the examined three-dimensional cases with crossflow transition, which were carried out at Re numbers up to 6.5 x 10^6, comparisons of computational results to experimental data were favorable.

Regarding LES and DES approaches, both were able to give results that closely resembled the available experimental data, and, in addition, outperformed baseline URANS. The presence of inflow turbulence was also found to be important, as it had significant impact on the produced results on the near wake. It should be noted that for the case of circular cylinder, in which both LES and DES approaches were considered, the same computational mesh was used in all simulations. Deviations between the results of LES and DES were probably caused by insufficient mesh resolution. LES does not model the boundary layer, and thus requires a relatively fine mesh in order to accurately resolve all turbulent scales. The resolution must be fine enough for LES to resolve the relevant scales and not rely on the Smagorinsky subgrid scale model, as the latter was not designed and calibrated to model boundary layers. On the contrary, DES utilizes the underlying Spalart-Allmaras turbulence model, which is known to be reliable for the modeling of attached boundary layers. Therefore, it is able to give accurate predictions of the boundary layer even in cases which utilize a relatively coarse mesh.

It should also be noted that, in comparison to RANS, mesh dependence in both LES and DES approaches has a different meaning. With continuing mesh refinement, a larger percentage of turbulent scales will be resolved and not modeled. Therefore, a truly mesh independent solution of LES and DES will practically reach Direct Numerical Simulation (DNS) levels, although it is possible to obtain mesh independent results for the mean values of the simulations. However, even when similar mean values are obtained, simulations with varying mesh refinement will have significantly different subgrid scale content. In this thesis, the considered cases utilized the finer meshes possible. Usage of even finer meshes would definitely improve the results, however this was not possible due to both limited computational resources and time constraints. For these types of simulations, access to supercomputing platforms is necessary. Proposals for such platforms are submitted once or twice per year. Therefore, there may be a big downtime period during which the development of the solver has finished but simulations are not yet possible.

In regards to overall computational cost, application of LES is prohibitively expensive if a large number of cases is considered, since it requires meshes that are fine enough to fully resolve the boundary layer. For the cases presented in this thesis, LES was used in relatively low Re numbers (3900 for the cylinder and 10596 for the periodic hills). In order to use LES in flow cases with $Re \sim 1$ x 10^6, the required mesh for the solution of the boundary layer would greatly increase the computational cost. On the contrary, the fact that DES utilizes boundary layer modeling lowers the computational cost and renders it a more viable approach for practical applications, provided that Re numbers do not exceed $1 - 2$ x 10^6. DES is better suited for massively separated flows, where the separation locations are driven by the geometry and not by the solution of the boundary layer. For flows with mild trailing edge separation (i.e. airfoil at $\alpha = 12^\circ$), the predicted separation locations will depend on the capabilities of the underlying RANS turbulence model. Therefore, results from DES will be similar to those from 3D URANS. At those cases, separation onset is caused by the development of small scales inside the boundary layer and therefore only LES with fine enough meshes is expected to be able to provide accurate results.

Lastly, it is possible to combine higher fidelity turbulence modeling and transition modeling within the same simulation. These types of simulations most often utilize DES paired with a transport equation transition model. Transition modeling and higher fidelity turbulence modeling were not combined in this thesis due to limited computational resource availability. In addition, the focus of the LES and DES cases was on massively separated flows, which are not significantly affected by the presence of transition.

7.2 Main conclusions

Transition modeling

- In regards to two-dimensional transitional simulations, the e^N method and the AFT transport equation model are recommended, as they proved to be reliable for all examined cases.
- In three-dimensional simulations, prediction of crossflow transition is important. It is difficult to apply boundary layer transition methods in such flow cases, because they require the calculation of streamlines. Usage of transport equation models augmented with crossflow terms is thus recommended in order to predict crossflow transition.

- Calculating boundary layer parameters directly from the CFD solution requires finer meshes near the wall surface. Therefore, in cases where integral boundary layer equations can be used, direct CFD integration is not recommended.
- Comparisons of transition models in the literature are most often carried out up to moderate Re numbers (4×10^6). However, it is also necessary to assess the validity of the models in higher Re ($> 20 \times 10^6$).
- Mesh requirements for two-dimensional simulations are in the order of 100 thousand elements, whereas for three-dimensional simulations are in the order of 4 million elements.

Higher fidelity turbulence modeling

- DES is a decent approach with manageable computational cost. It is considerably more accurate than RANS and therefore is a viable option for engineering purposes.
- LES is a better choice than DES for cases where flow details are important. However, the computational requirements are considerably higher when compared to those of DES.

7.3 Future work recommendations

In regards to transition modeling, the AFT model should be extended to include prediction capabilities for crossflow transition. Based on the results presented in this thesis, when flow cases with Re numbers higher than 6.5×10^6 are considered, the AFT model is a more suitable candidate than the γ-Re_θ model, as in such cases the prediction accuracy of the latter was found to deteriorate significantly. By including crossflow transition prediction in the AFT model, three-dimensional transitional simulations for a wide range of Re numbers will be made possible. Moreover, the different models should be assessed in cases with bypass transition, as this thesis focused only on natural, crossflow, and separation induced transition. When comparing the accuracy of different models in flow cases with bypass transition, one could end up in completely different conclusions than what was discussed in this thesis, due to the fact that bypass transition is a notably different transition mechanism.

When it comes to LES and DES, it is clear that neither method was pushed to its limits in this thesis. Additional test cases should be considered in order to acquire more experience on the application range of both methods, as well as in their computational requirements. In the context of LES, this work focused solely on the baseline Smagorinsky subgrid scale model. Even though this model is popular, it does have its limitations. Different subgrid models should, thus, also be assessed. Among others, the first one that should be tested is the dynamic Smagorinsky model, in which the Smagorinsky constant varies in space and time.

Regarding the MaPFlow solver itself, the effect of arithmetic parameters such as difference schemes should be assessed in the context of LES and DES. Different schemes were only used in the case of the S809 airfoil, which was simulated using 3D DDES and 3D URANS, and it was shown that they can impact the produced results. Future work will include a more rigorous analysis of higher order schemes, such as MUSCL and QUICK. Moreover, for simulations with LES and DES, which both can have high computational cost, implementation of acceleration techniques can be quite important. One such technique is multigrid, which will enable the simulations to converge significantly faster. The solver should also be further optimized in regards to parallelization performance, especially for simulations with LES and DES which are very computationally demanding.

This page intentionally left blank

Bibliography

[1] Y. Zhiyin, Large-eddy simulation: Past, present and the future, Chinese Journal of Aeronautics 28 (2015) 11–24. URL: https://linkinghub.elsevier.com/retrieve/pii/S1000936114002064. doi:10.1016/j.cja.2014.12.007.

[2] D. Simms, S. Schreck, M. Hand, L. J. Fingersh, NREL Unsteady Aerodynamics Experiment in the NASA-Ames Wind Tunnel: A Comparison of Predictions to Measurements (2001).

[3] M. Drela, XFOIL: An Analysis and Design System for Low Reynolds Number Airfoils 54 (1989). URL: http://link.springer.com/10.1007/978-3-642-84010-4. doi:10.1007/978-3-642-84010-4.

[4] D. M. Somers, Design and Experimental Results for a Natural-Laminar-Flow Airfoil for General Aviation Applications, Technical Report June 1981, NASA, 1981.

[5] O. Pires, X. Munduate, O. Ceyhan, M. Jacobs, H. Snel, Analysis of high Reynolds numbers effects on a wind turbine airfoil using 2D wind tunnel test data, Journal of Physics: Conference Series 753 (2016). doi:10.1088/1742-6596/753/2/022047.

[6] D. M. Somers, Design and Experimental Results for the S809 Airfoil, Technical Report, NREL, 1997.

[7] D. M. Somers, Design and Experimental Results for the S827 Airfoil, Technical Report January, NREL, 2005.

[8] C. Gleyzes, Operation Decrochage- Resultats des Essais a la Souflerie F2, Technical Report, ONERA, 1988.

[9] I. Mary, P. Sagaut, Large Eddy Simulation of Flow around an Airfoil, AIAA 40 (2001).

[10] B. van den Berg, J. H. M. Gooden, Low-Speed Surface and Boundary Layer Measurement Data for the NLR-7301 Airfoil Section with Trailing Edge Flap, Technical Report, 1979.

[11] R. McGhee, B. Walker, B. Millard, Experimental Results for the Eppler 387 Airfoil at Low Reynolds Numbers in Langley Low - Turbulence Pressure Tunnel, Nasa 4062 (1988) 238. URL: https://ntrs.nasa.gov/archive/nasa/casi.ntrs.nasa.gov/19890001471.pdf.

[12] F. W. Boltz, G. C. Kenyon, C. Q. Allen, Effects of Sweep Angle on the Boundary Layer Stability Characteristics of an Untapered Wing at Low Speeds, Technical Report, 1960.

[13] C. Grabe, N. Shengyang, A. Krumbein, Transport Modeling for the Prediction of Crossflow Transition, AIAA Journal 56 (2018) 3167–3178. doi:10.2514/1.j056200.

[14] V. Schmitt, B. Monneris, G. Dorey, C. Capelier, Etude de la couche limite tridimensionelle sur une aile en fleche, Rapport Technique No 14/1713 AN (1975).

[15] AVATAR, Project fp7-energy-2013-1/n608396, 2016. URL: www.eera-avatar.eu.

[16] C. Norberg, Effects of Reynolds Number and Low-Intensity Freestream Turbulence on the Flow Around a Circular Cylinder, 1987.

[17] L. Lourenco, C. Shih, Characteristics of the plane turbulent near wake of a circular cylinder; a particle image velocimetry study (1993).

[18] H. Blackburn, S. Schmidt, Large-eddy simulation of flow past a circular cylinder, 14th Australisian Fluid Mechanics Conference (2001) 3–6.

[19] L. Ong, J. Wallace, The velocity field of the turbulent very near wake of a circular cylinder, Experiments in Fluids 20 (1996) 441–453. doi:10.1007/BF00189383.

[20] C. Butterfield, G. Scott, W. Musial, Comparison of Wind Tunnel Airfoil Performance Data With Wind Turbine Blade Data, Journal of Solar Energy Engineering 114 (1992) 119–124. doi:10.1109/IECEC.1990.747950.

[21] NASA, Turbulence modeling resource, 2018. URL: https://turbmodels.larc.nasa.gov/Other_LES_Data/2dhill_periodic.html.

[22] J. W. Cleijne, Results of Sexbierum wind farm, volume 92, 1992.

[23] G. Papadakis, S. Voutsinas, In view of accelerating cfd simulations through coupling with vortex particle approximations, The Science of Making Torque from Wind Journal of Physics: Conference Series (2014).

[24] H. Schlichting, Boundary-Layer Theory (1979). URL: http://link.springer.com/10.1007/978-3-662-52919-5. doi:10.1007/978-3-662-52919-5. arXiv:arXiv:1011.1669v3.

[25] M. Morkovin, On the many faces of transition, Viscous Drag Reduction, edited by C.S. Wells (1969) 1–31. doi:10.1053/jhin.2001.1053. arXiv:arXiv:1011.1669v3.

[26] E. Malkiel, R. E. Mayle, Transition in a Separation Bubble, Journal of Turbomachinery 118 (1996) 752. doi:10.1115/1.2840931.

[27] R. E. Mayle, The Role of Laminar-Turbulent Transition in Gas Turbine Engines, Journal of Turbomachinery 113 (1991). doi:10.1115/1.2929223.

[28] P. Balakumar, G. I. Park, B. Pierce, DNS , LES , and wall-modeled LES of separating flow over periodic hills, Center for Turbulence Research Proceedings of the Summer Program 2014 (2014) 407–415.

[29] H. Choi, P. Moin, Grid-point requirements for large eddy simulation: Chapman's estimates revisited, Physics of Fluids 24 (2012) 1–6. doi:10.1063/1.3676783.

[30] D. R. Chapman, Computatisnal Aerodynamics Development and Outlook, AIAA Journal 17 (1979) 1293–1313. URL: http://arc.aiaa.org/doi/abs/10.2514/3.61311. doi:10.2514/3.61311.

[31] M. Strelets, Detached eddy simulation of massively separated flows, 39th Aerospace Sciences Meeting and Exhibit (2001). URL: http://arc.aiaa.org/doi/10.2514/6.2001-879. doi:10.2514/6.2001-879.

[32] H. Y. Xu, C. L. Qiao, H. Q. Yang, Z. Y. Ye, Delayed detached eddy simulation of the wind turbine airfoil S809 for angles of attack up to 90 degrees, Energy 118 (2017) 1090–1109. URL: http://dx.doi.org/10.1016/j.energy.2016.10.131. doi:10.1016/j.energy.2016.10.131.

[33] L. Gilling, Airfoils in Turbulent Inflow, Dce thesis, no. 23, Aalborg University, 2009.

[34] P. Beaudan, P. Moin, Numerical experiments on the flow past a circular cylinder at sub-critical Reynolds number, Stanford University (1994) 1–262.

[35] Breuer M, A challenging test case for large eddy simulation: high Reynolds number circular cylinder flow, International Journal of Heat and Fluid Flow 21 (2000) 648–654.

[36] A. Travin, M. Shur, M. Strelets, P. Spalart, Detached-Eddy Simulations Past a Circular Cylinder, Flow, Turbulence and Combustion 63 (1999) 293–313. URL: http://www.pubmedcentral.nih.gov/articlerender.fcgi?artid=192295{&}tool=pmcentrez{&}rendertype=abstract. doi:10.1023/A:1009901401183.

[37] M. Galbraith, M. Visbal, Implicit Large Eddy Simulation of Low Reynolds Number Flow Past the SD7003 Airfoil, 46th AIAA Aerospace Sciences Meeting and Exhibit (2008) 1–17. URL: http://arc.aiaa.org/doi/10.2514/6.2008-225. doi:10.2514/6.2008-225.

[38] N. Troldborg, J. N. Sorensen, R. F. Mikkelsen, Actuator line modeling of wind turbine wakes, 2008. URL: http://orbit.dtu.dk/en/publications/actuator-line-modeling-of-wind-turbine-wakes(5ba63e95-7f74-4e6c-82b8-9f497315a664).html.

[39] N. Troldborg, J. N. Sorensen, R. Mikkelsen, Numerical simulations of wake characteristics of a wind turbine in uniform inflow, Wind Energy 13 (2010) 86–99. URL: http://doi.wiley.com/10.1002/we.345. doi:10.1002/we.345.

[40] N. Troldborg, J. Sørensen, A simple atmospheric boundary layer model applied to large eddy simulations of wind turbine wakes, Wind Energy 17 (2014) 657–669. URL: http://onlinelibrary.wiley.com/doi/10.1002/we.1608/full. doi:10.1002/we. arXiv:arXiv:1006.4405v1.

[41] M. Breuer, N. Jovicic, K. Mazaev, Comparison of DES, RANS and LES for the separated flow around a flat plate at high incidence, International Journal for Numerical Methods in Fluids 41 (2003) 357–388. URL: http://doi.wiley.com/10.1002/fld.445. doi:10.1002/fld.445.

[42] B. A. Toms, Large-eddy Simulation of Flow Over a Backward Facing Step: Assessment of Inflow Boundary Conditions, Eddy Viscosity Models and Wall Functions, Journal of Applied Mechanical Engineering 4 (2015) 1–6. doi:10.4172/2168-9873.1000169.

[43] M. V. Salvetti, R. Damiani, F. Beux, Three-dimensional coarse large-eddy simulations of the flow above two-dimensional sinusoidal waves, International Journal for Numerical Methods in Fluids 35 (2001) 617–642. doi:10.1002/1097-0363(20010330)35:6<617::AID-FLD104>3.0.CO;2-M.

[44] C. Hirsch, Numerical computation of internal and external flows (1990). doi:10.1007/978-3-662-52919-5.

[45] Y. H. Choi, C. Merkle, The Application of Preconditioning in Viscous Flows, Journal of Computational Physics 105 (1993) 207–223. URL: https://linkinghub.elsevier.com/retrieve/pii/S0021999183710697. doi:10.1006/jcph.1993.1069.

[46] E. Turkel, V. N. Vatsa, Local preconditioners for steady and unsteady flow applications, ESAIM: Mathematical Modelling and Numerical Analysis 39 (2005) 515–535. URL: http://www.esaim-m2an.org/10.1051/m2an:2005021. doi:10.1051/m2an:2005021.

[47] L.-E. Eriksson, A preconditioned navier-stokes solver for low mach number flows, Computers and Fluids (1996) 199–205.

[48] V. G. Asouti, D. I. Papadimitriou, D. G. Koubogiannis, K. C. Giannakoglou, Low Mach Number Preconditioning for 2D and 3D Upwind Flow Solution Schemes on Unstructured Grids, Control (2005).

[49] Y. Colin, H. Deniau, J.-F. Boussuge, A robust low speed preconditioning formulation for viscous flow computations, Computers & Fluids 47 (2011) 1–15. URL: https://linkinghub.elsevier.com/retrieve/pii/S0045793011000223. doi:10.1016/j.compfluid.2011.01.015.

[50] R. Biedron, J. Thomas, Recent Enhancements to the FUN3D Flow Solver for Moving-Mesh Applications, in: 47th AIAA Aerospace Sciences Meeting including The New Horizons Forum and Aerospace Exposition, January, American Institute of Aeronautics and Astronautics, Reston, Virigina, 2009, pp. 1–19. URL: http://arc.aiaa.org/doi/10.2514/6.2009-1360. doi:10.2514/6.2009-1360.

[51] R. K. Agarwal, J. E. Deese, Euler calculations for flowfield of a helicopter rotor in hover, Journal of Aircraft 24 (1987) 231–238. URL: http://arc.aiaa.org/doi/10.2514/3.45431. doi:10.2514/3.45431.

[52] V. Venkatakrishnan, On the accuracy of limiters and convergence to steady state solutions, AIAA Paper 93-0880 (1993).

[53] B. van Leer, Towards the ultimate conservative difference scheme. V. A second-order sequel to Godunov's method, Journal of Computational Physics 32 (1979) 101–136. doi:10.1016/0021-9991(79)90145-1.

[54] S. K. Godunov, A difference method for numerical calculation of discontinuous solutions of the equations of hydrodynamics, Math-Net.Ru (translated) 47 (1959) 271–306. doi:10.18287/0134-2452-2015-39-4-459-461.

[55] P. L. Roe, Characteristic-Based Schemes for the Euler Equations, Annual Review of Fluid Mechanics 18 (1986) 337–365. doi:10.1146/annurev.fluid.18.1.337.

[56] G. D. van Albada, B. van Leer, W. W. Roberts, A Comparative Study of Computational Methods in Cosmic Gas Dynamics, Astronomy and Astrophysics 108 (1982).

[57] B. P. Leonard, A stable and accurate convective modelling procedure based on quadratic upstream interpolation, Computer Methods in Applied Mechanics and Engineering 19 (1979) 59–98. doi:10.1016/0045-7825(79)90034-3.

[58] B. P. Leonard, Simple highaccuracy resolution program for convective modelling of discontinuities, International Journal for Numerical Methods in Fluids 8 (1988) 1291–1318. doi:10.1002/fld.1650081013.

[59] A. Jameson, W. Schmidt, E. Turkel, AIAA 1981 1259 Numerical Solution of the Euler Equations by Finite Volume Methods Schemes AIAA 14th Fluid and Plasma Dynamic Conference Palo Alto , California, Convergence M (1981) 1–19. URL: http://www.cs.tau.ac.il/{~}turkel/PSmanuscripts/jst.pdf.

[60] B. van Leer, Flux-vector splitting for the Euler equations, in: Computers & Fluids, volume 9, 1982, pp. 507–512. URL: https://linkinghub.elsevier.com/retrieve/pii/0045793081900177http://link.springer.com/10.1007/3-540-11948-5{_}66. doi:10.1007/3-540-11948-5_66.

[61] J. L. Steger, R. Warming, Flux vector splitting of the inviscid gasdynamic equations with application to finite-difference methods, Journal of Computational Physics 40 (1981) 263–293. URL: https://linkinghub.elsevier.com/retrieve/pii/0021999181902102. doi:10.1016/0021-9991(81)90210-2.

[62] P. Roe, Approximate riemann solvers, parameter vectors and difference schemes, Journal of Computational Physics, Volume 43, Pages 357-372 (1981).

[63] V. G. Asouti, Aerodynamic Analysis and Design Methods at High and Low Speed Flows on Multiprocessor Platforms, Ph.D. thesis, National Technical University of Athens, 2009.

[64] J. Blazek, Computational fluid dynamics:Principles of Grid Generation, 2001. doi:http://dx.doi.org/10.1016/B978-008044506-9/50013-8.

[65] R. Biedron, V. Vatsa, H. Atkins, Simulation of Unsteady Flows Using an Unstructured Navier-Stokes Solver on Moving and Stationary Grids, in: 23rd AIAA Applied Aerodynamics Conference, June, American Institute of Aeronautics and Astronautics, Reston, Virigina, 2005. URL: http://arc.aiaa.org/doi/10.2514/6.2005-5093. doi:10.2514/6.2005-5093.

[66] V. Vatsa, M. Carpenter, D. Lockard, Re-evaluation of an Optimized Second Order Backward Difference (BDF2OPT) Scheme for Unsteady Flow Applications, in: 48th AIAA Aerospace Sciences Meeting Including the New Horizons Forum and Aerospace Exposition, American Institute of Aeronautics and Astronautics, Reston, Virigina, 2010, pp. 1–15. URL: http://arc.aiaa.org/doi/10.2514/6.2010-122. doi:10.2514/6.2010-122.

[67] D. J. Mavriplis, V. Venkatakrishnan, Agglomeration Multigrid for Viscous Turbulent Flows, ICASE report 24 (1994) 553–570.

[68] D. J. Mavriplis, A. Jameson, Multigrid solution of the Navier-Stokes equations on triangular meshes, AIAA Journal 28 (1990) 1415–1425. URL: http://arc.aiaa.org/doi/10.2514/3.25233. doi:10.2514/3.25233.

[69] K. Hejranfar, R. Kamali-Moghadam, Preconditioned characteristic boundary conditions for solution of the preconditioned Euler equations at low Mach number flows, Journal of Computational Physics 231 (2012) 4384–4402. URL: http://dx.doi.org/10.1016/j.jcp.2012.01.040. doi:10.1016/j.jcp.2012.01.040.

[70] P. R. Spalart, S. R. Allmaras, J. Reno, One-Equatlon Turbulence Model for Aerodynamic Flows Boeing, Aiaa (1992) 23. doi:10.2514/6.1992-439.

[71] F. R. Menter, Two-equation eddy-viscosity turbulence models for engineering applications, AIAA Journal 32 (1994) 1598–1605. URL: http://arc.aiaa.org/doi/10.2514/3.12149. doi:10.2514/3.12149.

[72] D. C. Wilcox, Turbulence modeling for cfd, second edition (1998).

[73] F. Menter, Zonal Two Equation k-w Turbulence Models For Aerodynamic Flows, in: 23rd Fluid Dynamics, Plasmadynamics, and Lasers Conference, American Institute of Aeronautics and Astronautics, Reston, Virigina, 1993. URL: http://arc.aiaa.org/doi/10.2514/6.1993-2906. doi:10.2514/6.1993-2906.

[74] D. Koubogiannis, L. Poussoulidis, D. Rovas, K. Giannakoglou, Solution of flow problems using unstructured grids on distributed memory platforms, Computer Methods in Applied Mechanics and Engineering 160 (1998) 89–100. URL: https://linkinghub.elsevier.com/retrieve/pii/S0045782597002855. doi:10.1016/S0045-7825(97)00285-5.

[75] Y. Saad, Iterative Methods for Sparse Linear Systems Second Edition Yousef Saad (2003).

[76] A. Theofilopoulos, Numerical analysis of the dynamic behavior of airfoils with deformable and articulated trailing edge flap (2013).

[77] Y. Zhao, J. Tai, F. Ahmed, Simulation of micro flows with moving boundaries using high-order upwind FV method on unstructured grids, Computational Mechanics 28 (2002) 66–75. URL: http://link.springer.com/10.1007/s00466-001-0271-1. doi:10.1007/s00466-001-0271-1.

[78] P. D. Thomas, C. K. Lombard, Geometric Conservation Law and Its Application to Flow Computations on Moving Grids 17 (1979) 1030–1037.

[79] D. J. Mavriplis, Z. Yang, Construction of the discrete geometric conservation law for high-order time-accurate simulations on dynamic meshes, Journal of Computational Physics 213 (2006) 557–573. URL: https://linkinghub.elsevier.com/retrieve/pii/S002199910500392X. doi:10.1016/j.jcp.2005.08.018.

[80] H. T. Ahn, Y. Kallinderis, Strongly coupled flow/structure interactions with a geometrically conservative ALE scheme on general hybrid meshes, Journal of Computational Physics 219 (2006) 671–696. URL: https://linkinghub.elsevier.com/retrieve/pii/S0021999106001987. doi:10.1016/j.jcp.2006.04.011.

[81] R. Michel, Etude de la transition sur les profiles d'aile, ONERA Report 1/1578A (1951).

[82] J. Moran, An Introduction to Theoretical and Computational Aerodynamics, Dover Publications, Mineola, New York, 1984.

[83] J. Johansen, J. N. S-oacute, Rensen, Prediction of Laminar Turbulent Transition in Airfoil flows, 1999. URL: http://arc.aiaa.org/doi/abs/10.2514/2.2501?journalCode=ja. doi:10.2514/2.2501.

[84] R. Eppler, D. Somers, A Computer Program for the Design and Analysis of Low-Speed Airfoils, Nasa Technical Memorandum 81862 (1980).

[85] R. Abu-Ghannam, B. J., Shaw, Natural Transition of Boundary Layers - The Effects of Turbulence, Pressure Gradient, and Flow History, Journal Mechanical Engineering Science 22 (1980). doi:10.1243/JMES.

[86] P. Granville, Armed services technical information agency, Technical Report, United States Navy Department, 1953. doi:10.1002/asi.5090070303.

[87] E. D. Arnal, H. Habiballah, Theorie de linstabilite laminaire et criteres de transition en ecoulement bi et tridimensionnel, La Recherche Aerospatiale (1984).

[88] D. Arnal, R. Houdeville, O. Vermeersch, Overview of laminar-turbulent transition investigations at ONERA Toulouse, Data Base (2011) 1–13. doi:10.2514/6.2011-3074.

[89] A. Smith, N. Gamberoni, Transition, Pressure Gradient, and Stability Theory, 1956. doi:ES26388.

[90] J. L. Van Ingen, A suggested semi-empirical method for the calculation of the boundary layer transition region, 1956.

[91] F. Langtry, R. B., Menter, Transition Modeling for General CFD Applications in Aeronautics, AIAA 2005-522 (2005). doi:10.1515/text.2001.007.

[92] R. B. Langtry, F. R. Menter, Correlation-Based Transition Modeling for Unstructured Parallelized Computational Fluid Dynamics Codes, AIAA Journal 47 (2009) 2894–2906. URL: http://arc.aiaa.org/doi/10.2514/1.42362. doi:10.2514/1.42362.

[93] F. R. Menter, R. B. Langtry, S. R. Likki, Y. B. Suzen, P. G. Huang, S. Volker, A Correlation-Based Transition Model Using Local Variables - Part I: Model Formulation, Journal of Turbomachinery 128 (2006) 413. doi:10.1115/1.2184352.

[94] F. R. Menter, P. E. Smirnov, T. Liu, R. Avancha, A One-Equation Local Correlation-Based Transition Model, Flow, Turbulence and Combustion 95 (2015). doi:10.1007/s10494-015-9622-4.

[95] J. G. Coder, M. D. Maughmer, Computational Fluid Dynamics Compatible Transition Modeling Using an Amplification Factor Transport Equation, AIAA Journal 52 (2014) 2506–2512. URL: http://arc.aiaa.org/doi/10.2514/1.J052905. doi:10.2514/1.J052905.

[96] J. G. Coder, T. H. Pulliam, J. C. Jensen, Contributions to HiLiftPW-3 Using Structured, Overset Grid Methods, 2018 AIAA Aerospace Sciences Meeting (2018) 1–41. URL: https://arc.aiaa.org/doi/10.2514/6.2018-1039. doi:10.2514/6.2018-1039.

[97] J. G. Coder, Further Development of the Amplification Factor Transport Transition Model for Aerodynamic Flows (2019) 1–24. doi:10.2514/6.2019-0039.

[98] M. Drela, M. B. Giles, Viscous-inviscid analysis of transonic and low Reynolds number airfoils, AIAA Journal 25 (1987) 1347–1355. URL: http://arc.aiaa.org/doi/10.2514/3.9789. doi:10.2514/3.9789.

[99] D. K. Walters, D. Cokljat, A Three-Equation Eddy-Viscosity Model for Reynolds-Averaged NavierStokes Simulations of Transitional Flow, Journal of Fluids Engineering 130 (2008) 121401. URL: http://fluidsengineering.asmedigitalcollection.asme.org/article.aspx?articleid=1478203. doi:10.1115/1.2979230.

[100] V. M. Falkner, S. W. Skan, Aeronautical Research Council Reports and Memoranda, Technical Report 1314, Advisory Committee for Aeronautics, 1930.

[101] J. Johansen, J. N. S-oacute, Rensen, Prediction of Laminar Turbulent Transition in Airfoil flows, Journal of Aircraft 36 (1999) 731–734. URL: http://arc.aiaa.org/doi/abs/10.2514/2.2501?journalCode=ja. doi:10.2514/2.2501.

[102] P. Granville, The calculation of viscous drag of bodies of revolution, DTMB Report No. 849 (1953).

[103] J. L. V. Ingen, Historical review of work at TU Delft, 38th Fluid Dynamics Conference and Exhibit (2008) 1–49. doi:AIAA2008-3830.

[104] H. W. Stock, E. Degenhart, A simplified en method for transition predictions in two-dimensional, incompressible boundary layers, Z. Flugwiss. Weltraumforsch 13 (1989) 16–30.

[105] K. K. Chen, N. A. Thyson, Extension of Emmons' spot theory to flows on blunt bodies, AIAA Journal 9 (1971) 821–825. URL: http://arc.aiaa.org/doi/10.2514/3.6281. doi:10.2514/3.6281.

[106] R. Narasimha, K. J. Devasia, G. Gururani, M. A. B. Narayanan, Experiments in Fluids © 176 (1984) 171–176.

[107] F. R. Menter, R. Langtry, S. Völker, P. G. Huang, Transition Modelling for General Purpose CFD Codes, Engineering Turbulence Modelling and Experiments 6 (2005) 31–48. doi:10.1016/B978-008044544-1/50003-0.

[108] F. R. Menter, R. B. Langtry, S. R. Likki, Y. B. Suzen, P. G. Huang, S. Volker, A Correlation-Based Transition Model Using Local VariablesPart I: Model Formulation, Journal of Turbomachinery 128 (2006) 413. URL: http://turbomachinery.asmedigitalcollection.asme.org/article.aspx?articleid=1467239. doi:10.1115/1.2184352.

[109] E. R. Van Driest, C. B. Blumer, Boundary layer transition: Freestrean turbulence and pressure gradient effects, AIAA Journal 1 (1963) 1303–1306.

[110] F. Menter, T. Esch, S. Kubacki, Transition modelling based on local variables, Proceedings of the 5th International Symposium on Engineering Turbulence Modelling and Measurements, Elsevier (2002) 555–564.

[111] K. Suluksna, P. Dechaumphai, E. Juntasaro, Correlations for modeling transitional boundary layers under influences of freestream turbulence and pressure gradient, International Journal of Heat and Fluid Flow 30 (2009) 66–75. URL: http://dx.doi.org/10.1016/j.ijheatfluidflow.2008.09.004. doi:10.1016/j.ijheatfluidflow.2008.09.004.

[112] P. Malan, K. Suluksna, E. Juntasaro, Calibrating the gamma-Re-omega Transition model for commerical CFD, Aiaa (2009) 1–14.

[113] C. Sinclair, C. Wells Jr, Effects of freestream turbulence on boundary-layer transition, AIAA Journal, Vol. 5, No. 1 (1967).

[114] S. Medida, J. Baeder, A New Crossflow Transition Onset Criterion for RANS Turbulence Models (2013) 1–11. doi:10.2514/6.2013-3081.

[115] C. Grabe, A. Krumbein, Correlation-Based Transition Transport Modeling for Three-Dimensional Aerodynamic Configurations, Journal of Aircraft 50 (2013) 1533–1539. doi:10.2514/1.c032063.

[116] J. H. Choi, O. J. Kwon, Enhancement of a Correlation-Based Transition Turbulence Model for Simulating Crossflow Instability, AIAA Journal 53 (2015) 3063–3072. doi:10.2514/1.j053887.

[117] J. H. Choi, O. J. Kwon, Recent Improvement of a Correlation-Based Transition Model for Simulating Three-Dimensional Boundary Layers, AIAA Journal 55 (2017) 2103–2108. doi:10.2514/1.j055182.

[118] J. C. Cooke, L. Howarth, The boundary layer of a class of infinite yawed cylinders, Mathematical Proceedings of the Cambridge Philosophical Society 46 (1950) 645. URL: http://www.journals.cambridge.org/abstract{_}S0305004100026220. doi:10.1017/S0305004100026220.

[119] R. B. Langtry, K. Sengupta, D. T. Yeh, A. J. Dorgan, Extending the γ-Reθt local correlation based transition model for crossflow effects, 45th AIAA Fluid Dynamics Conference (2015) 1–12. URL: http://arc.aiaa.org/doi/10.2514/6.2015-2474. doi:10.2514/6.2015-2474.

[120] R. Radeztsky, JR., M. Reibert, W. Saric, S. Takagi, Effect of micron-sized roughness on transition in swept-wing flows, in: 31st Aerospace Sciences Meeting, American Institute of Aeronautics and Astronautics, Reston, Virigina, 1993. URL: http://arc.aiaa.org/doi/10.2514/6.1993-76. doi:10.2514/6.1993-76.

[121] H. P. Kreplin, H. Vollmers, H. Meier, Wall shear stress measurements on an inclined prolate spheroid in the DFVLR 3m x 3m low speed wind tunnel, Technical Report report ID 22-84, DFVLR-AVA, 1985.

[122] J. Cliquet, R. Houdeville, D. Arnal, Application of Laminar-Turbulent Transition Criteria in Navier-Stokes Computations, AIAA Journal 46 (2008) 1182–1190. URL: http://arc.aiaa.org/doi/10.2514/1.30215. doi:10.2514/1.30215.

[123] S. Medida, J. D. Baeder, Application of the Correlation-based $\gamma Re\theta t$ Transition Model to the Spalart-Allmaras Turbulence Model, 20th AIAA Computational Fluid Dynamics Conference (2011) 1–21.

[124] A. Crivellini, V. D. Alessandro, D. Di, L. Binci, G. Clementi, G. V. Iungo, F. Viola, A Spalart Allmaras local correlation based transition model for Thermo uid dynamics (2017).

[125] S. Colonia, V. Leble, R. Steijl, G. Barakos, Assessment and Calibration of the γ-Equation Transition Model at Low Mach, AIAA Journal 55 (2017) 1126–1139. URL: https://arc.aiaa.org/doi/10.2514/1.J055403. doi:10.2514/1.J055403.

[126] J. G. Coder, Development of a CFD-Compatible Transition Model Based on Linear Stability Theory, Ph.D. thesis, 2014.

[127] J. G. Coder, M. D. Maughmer, Application of the Amplification Factor Transport Transition Model to the Shear Stress Transport Model, 53rd AIAA Aerospace Sciences Meeting (2015) 1–16. URL: http://arc.aiaa.org/doi/10.2514/6.2015-0588. doi:10.2514/6.2015-0588.

[128] J. G. Coder, Enhancement of the Amplification Factor Transport Transition Modeling Framework, 55th AIAA Aerospace Sciences Meeting (2017) 1–14. URL: http://arc.aiaa.org/doi/10.2514/6.2017-1709. doi:10.2514/6.2017-1709.

[129] D. C. Wilcox, Turbulence Modeling for CFD, DCW Industries, 1995. URL: http://ebooks.cambridge.org/ref/id/CBO9781107415324A009. doi:10.1017/CBO9781107415324.004. arXiv:arXiv:1011.1669v3.

[130] B. Launder, D. Spalding, The numerical computation of turbulent flows, Computer Methods in Applied Mechanics and Engineering 3 (1974) 269–289. URL: https://linkinghub.elsevier.com/retrieve/pii/0045782574900292. doi:10.1016/0045-7825(74)90029-2.

[131] B. Baldwin, H. Lomax, Thin-layer approximation and algebraic model for separated turbulentflows, in: 16th Aerospace Sciences Meeting, American Institute of Aeronautics and Astronautics, Reston, Virigina, 1978. URL: http://arc.aiaa.org/doi/10.2514/6.1978-257. doi:10.2514/6.1978-257.

[132] NASA, Turbulence modeling resource, 2018. URL: https://turbmodels.larc.nasa.gov/.

[133] C. Seyfert, A. Krumbein, Evaluation of a Correlation-Based Transition Model and Comparison with the eN Method, Journal of Aircraft 49 (2012) 1765–1773. URL: http://arc.aiaa.org/doi/10.2514/1.C031448. doi:10.2514/1.C031448. arXiv:arXiv:1011.1669v3.

[134] J. Smagorinsky, Monthly weather review, Volume 91, Number 3, Washington, D.C. (1963).

[135] P. R. Spalart, W.-H. Jou, M.Strelets, S. R. Allmaras, Comments on the feasibility of LES for wings, and on a hybrid LES/RANS approach, Proceedings of the First AFOSR International Conference on DNS/LES (1997) 137–147.

[136] F. R. Menter, M. Kuntz, Adaptation of Eddy-Viscosity Turbulence Models to, Lecture Notes in Applied and Computational Mechanics 19 (2004) 339–352. doi:10.1007/978-3-540-44419-0_30.

[137] P. R. Spalart, S. Deck, M. L. Shur, K. D. Squires, M. K. Strelets, A. Travin, A new version of detached-eddy simulation, resistant to ambiguous grid densities, Theoretical and Computational Fluid Dynamics 20 (2006) 181–195. doi:10.1007/s00162-006-0015-0.

[138] E. Lenormand, P. Sagaut, L. T. Phuoc, P. Comte, Subgrid-Scale Models for Large-Eddy Simulations of Compressible Wall Bounded Flows, AIAA Journal 38 (2000) 1340–1350. URL: http://arc.aiaa.org/doi/10.2514/2.1133. doi:10.2514/2.1133.

[139] D. K. Lilly, The Representation of Small-Scale Turbulence in Numerical Simulation Experiments., Technical Report November, National Center for Atmospheric Research, Boulder, Colorado, 1966.

[140] M. Germano, U. Piomelli, P. Moin, W. H. Cabot, A dynamic subgrid-scale eddy viscosity model, Physics of Fluids A 3 (1991) 1760–1765. doi:10.1063/1.857955.

[141] P. R. Spalart, Trends In Turbulence Treatments, AIAA Paper 2000-2306 (2000).

[142] P. R. Spalart, Strategies for turbulence modelling and simulations, International Journal of Heat and Fluid Flow 21 (2000) 252–263. doi:10.1016/S0142-727X(00)00007-2.

[143] J. Johansen, N. N. Sorensen, J. A. Michelsen, S. Schreck, Detached-Eddy Simulation of Flow Around the NREL Phase-VI Blade, ASME 2002 Wind Energy Symposium 197 (2002) 106–114. URL: http://proceedings.asmedigitalcollection.asme.org/proceeding.aspx?articleid=1572085. doi:10.1115/WIND2002-32.

[144] N. N. Sørensen, A. Bechmann, F. Zahle, 3D CFD computations of transitional flows using des and a correlation based transition model, Wind Energy 14 (2011) 77–90. doi:10.1002/we.404.

[145] M. L. Shur, P. R. Spalart, M. Strelets, A. Travin, A hybrid RANS-LES approach with delayed-DES and wall-modelled LES capabilities, International Journal of Heat and Fluid Flow 29 (2008) 1638–1649. URL: http://dx.doi.org/10.1016/j.ijheatfluidflow.2008.07.001. doi:10.1016/j.ijheatfluidflow.2008.07.001.

[146] M. S. Gritskevich, A. V. Garbaruk, J. Schütze, F. R. Menter, Development of DDES and IDDES formulations for the k-ω shear stress transport model, Flow, Turbulence and Combustion 88 (2012) 431–449. doi:10.1007/s10494-011-9378-4.

[147] R. Menter, F. R., Kuntz, M., Langtry, Ten Years of Industrial Experience with the SST Turbulence Model F., Turbulence, Heat and Mass Transfer 4 (2003). URL: http://www.scientific.net/AMR.576.60. doi:10.4028/www.scientific.net/AMR.576.60.

[148] J. Mann, Wind field simulation, Probabilistic Engineering Mechanics 13 (1998) 269–282. doi:10.1016/s0266-8920(97)00036-2.

[149] J. G. Coder, Standard Test Cases for CFD-Based Laminar-Transition Model Verification and Validation, 2018 AIAA Aerospace Sciences Meeting (2018) 1–16. URL: https://arc.aiaa.org/doi/10.2514/6.2018-0029. doi:10.2514/6.2018-0029.

[150] M. Kato, B. E. Launder, The modelling of turbulent flow around stationary and vibrating cylinders, Ninth Symposium on Turbulent Shear Flows (1993).

[151] P. R. Spalart, C. L. Rumsey, Effective Inflow Conditions for Turbulence Models in Aerodynamic Calculations, AIAA Journal 45 (2007) 2544–2553. URL: http://arc.aiaa.org/doi/10.2514/1.29373. doi:10.2514/1.29373.

[152] C. M. Langel, R. Chow, C. C. P. Van Dam, A Comparison of Transition Prediction Methodologies Applied to High Reynolds Number External Flows, 54th AIAA Aerospace Sciences Meeting (2016) 551. doi:10.2514/6.2016-0551.

[153] A. Aranake, V. Lakshminarayan, K. Duraisamy, Assessment of Transition Model and CFD Methodology for Wind Turbine Flows, 42nd AIAA Fluid Dynamics Conference and Exhibit (2012) 1–22. URL: http://arc.aiaa.org/doi/10.2514/6.2012-2720. doi:10.2514/6.2012-2720.

[154] C. Seyfert, A. Krumbein, Comparison of a Local Correlation-Based Transition Model with an eN-Method for Transition Prediction, New Results in Numerical and Experimental Fluid Mechanics VIII 121 (2013) 541–548. URL: http://link.springer.com/10.1007/978-3-642-35680-3. doi:10.1007/978-3-642-35680-3.

[155] H. Stock, Airfoil Validation Using Coupled Navier-Stokes and e Transition Prediction Methods, Journal of aircraft 39 (2002). URL: http://arc.aiaa.org/doi/pdf/10.2514/2.2894.

[156] H. W. Stock, W. Haase, Feasibility Study of e N Transition Prediction in Navier Stokes Methods for Airfoils, Aiaa Journal 37 (1999). doi:10.2514/2.612.

[157] C. Nebel, R. Radespiel, T. Wolf, Transition prediction for 3D flows using a reynoldsaveraged Navier-Stokes code and n-factor methods, 33rd AIAA Fluid Dynamics Conference and Exhibit (2003) 1–11. URL: http://www.scopus.com/inward/record.url?eid=2-s2.0-84883623959{&}partnerID=tZOtx3y1.

[158] H. W. Stock, eN Transition Prediction in Three-Dimensional Boundary Layers on Inclined Prolate Spheroids, AIAA Journal 44 (2008) 108–118. doi:10.2514/1.16026.

[159] M. Denison, T. H. Pulliam, Implementation and Assessment of the Amplification Factor Transport Laminar-Turbulent Transition Model, 2018 Fluid Dynamics Conference (2018) 1–27. URL: https://arc.aiaa.org/doi/10.2514/6.2018-3382. doi:10.2514/6.2018-3382.

[160] S. Vallinayagam Pillai, S. Lardeau, Accounting Crossflow Effects in One-Equation Local Correlation-Based Transition Model, 8th AIAA Theoretical Fluid Mechanics Conference (2017) 1–13. URL: https://arc.aiaa.org/doi/10.2514/6.2017-3159. doi:10.2514/6.2017-3159.

[161] R. Vizinho, J. Morgado, J. Páscoa, M. Silvestre, Analysis of transitional flow in 3D geometries using a novel phenomenological model, Aerospace Science and Technology 45 (2015) 431–441. URL: http://dx.doi.org/10.1016/j.ast.2015.06.018. doi:10.1016/j.ast.2015.06.018.

[162] M. Breuer, N. Peller, C. Rapp, M. Manhart, Flow over periodic hills - Numerical and experimental study in a wide range of Reynolds numbers, Computers and Fluids 38 (2009) 433–457. URL: http://dx.doi.org/10.1016/j.compfluid.2008.05.002. doi:10.1016/j.compfluid.2008.05.002.

[163] J. Frohlich, C. P. Mellen, W. Rodi, L. Temmerman, M. A. Leschziner, Highly resolved large-eddy simulation of separated flow in a channel with streamwise periodic constrictions, Journal of Fluid Mechanics 526 (2005) 19–66. URL: http://www.journals.cambridge.org/abstract{_}S0022112004002812. doi:10.1017/S0022112004002812.

[164] X. Xu, Large eddy simulation of compressible turbulent pipe flow with heat transfer, Ph.D. thesis, Iowa State University, 2003.

This page intentionally left blank

Appendices

Appendix A

Influence of numerical scheme

The DU-00-W212 airfoil is considered at $Re = 3$ x 10^6, $Ma_\infty = 0.75$, $Tu_\infty = 0.086\%$. The simulations assumed fully turbulent flow using the baseline SST k-ω turbulence model as presented in [71]. Four different meshes were used, with resolutions ranging from 96 (chordwise) x 48 (normal) to 800 (chordwise) x 500 (normal) elements.

The results are presented in fig. A.1. It is shown that the 3$^{\text{rd}}$ order schemes converge faster towards a mesh independent solution. Deviations between the 256 x 128 and 512 x 256 meshes are higher when using the 2$^{\text{nd}}$ PLR scheme whereas for the 3$^{\text{rd}}$ order MUSCL and QUICK schemes the three finer meshes yield very similar results.

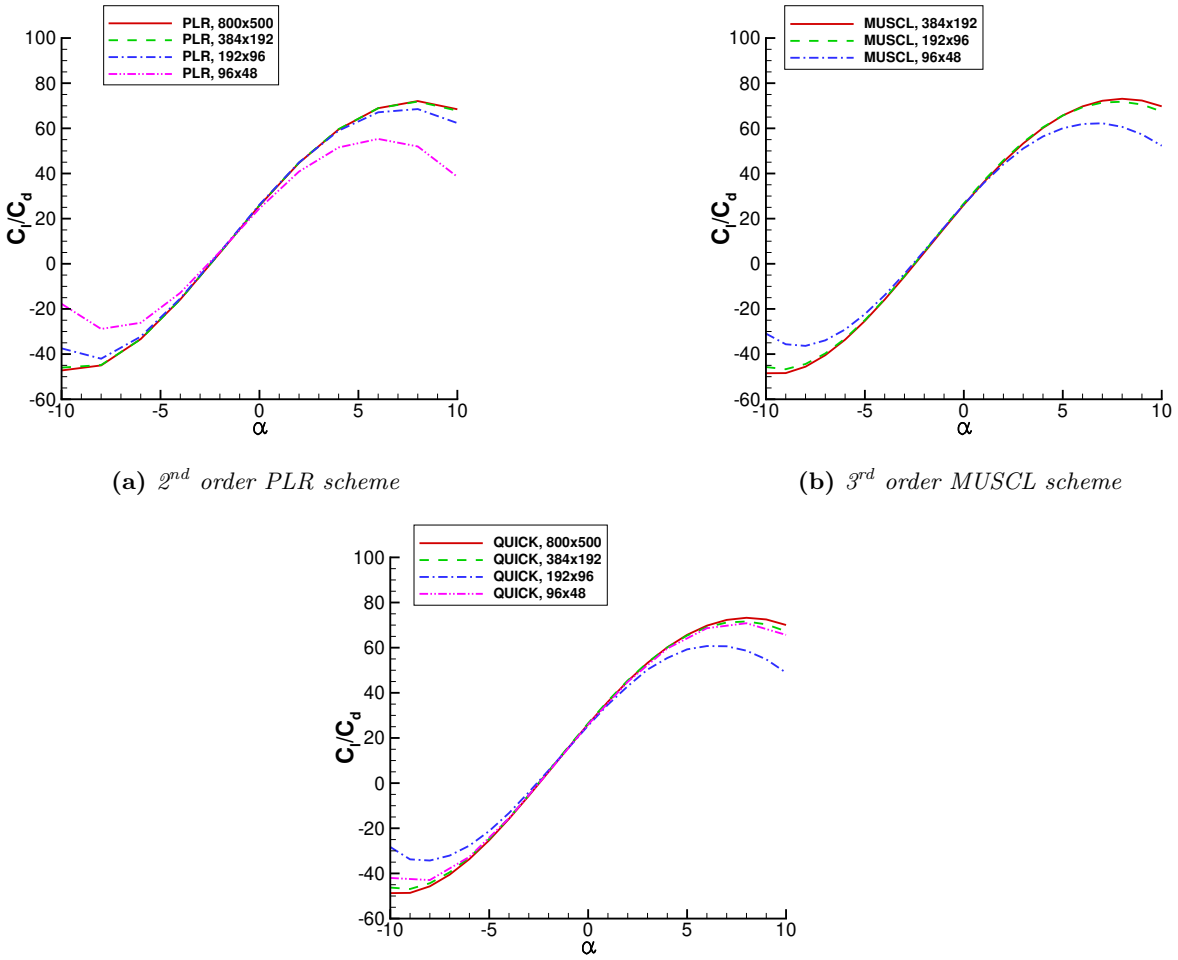

(a) *2nd order PLR scheme*

(b) *3rd order MUSCL scheme*

(c) *3rd order QUICK scheme*

Figure A.1: *Effect of numerical scheme. Fully turbulent simulations for the DU-00-W212 airfoil, $Re = 3$ x 10^6, $Ma_\infty = 0.75$, $Tu_\infty = 0.086\%$.*

This page intentionally left blank

Appendix B

Influence of numerical limiter

The DU-00-W212 airfoil is considered at $Re = 3$ x 10^6, $Ma_\infty = 0.75$, $Tu_\infty = 0.086\%$. The simulations assumed fully turbulent flow using the baseline SST k-ω turbulence model as presented in [71]. Four different meshes were used, with resolutions ranging from 96 (chordwise) x 48 (normal) to 800 (chordwise) x 500 (normal) elements.

The 2nd order PLR scheme is used. Simulations with limiter utilized Venkatakrishnan's limiter [52]. The results are presented in fig. B.1. For the simulations with limiter (fig. B.1a), results from the two finer meshes have some deviations on the higher and lower angles. On the contrary, if the limiter is turned off (B.1b) the results from the two finer meshes are almost identical. In addition, the 192x96 and 96x48 meshes give results that are closer to those from the finer meshes.

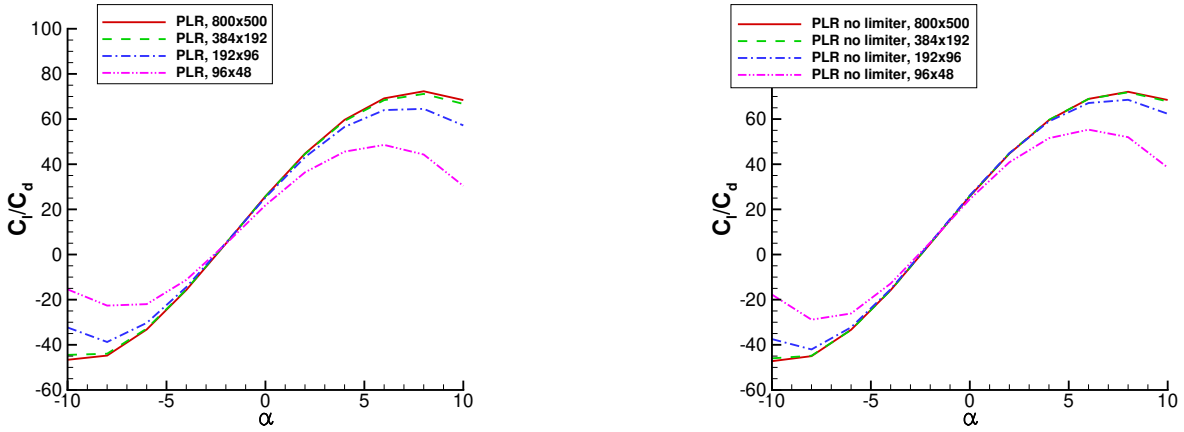

(a) *2^{nd} order PLR scheme, Venkatakrishnan's limiter*

(b) *2^{nd} order PLR scheme, no limiter*

Figure B.1: *Effect of numerical limiter on the 2^{nd} order PLR scheme. Fully turbulent simulations for the DU-00-W212 airfoil, $Re = 3$ x 10^6, $Ma_\infty = 0.75$, $Tu_\infty = 0.086\%$.*